Improved Particle Method with High-Resolution and Computational Stability for Solid-Liquid Two-Phase Flows

2013

Naoki Tsuruta

Abstract

The aim of this study is to establish and improve comprehensive solid-liquid two-phase flow models for practical applications with the reliable accuracy, stability and ease by high-resolution tracking. In this study, some particle-based solutions, namely the Distinct Element Method (DEM; Cundall and Strack, 1979) and the Moving Particle Semi-implicit (MPS; Koshizuka and Oka, 1996) method characterized by the User-friendly frameworks with the good robustness are chosen as the DEM-MPS method (Gotoh et al., 2003) in order to track unsteady solid motions under various complicated boundary conditions including violent free-surface flows. As for the significant problems of the DEM-MPS method is as follows:

1. Up to now, the DEM-MPS framework does not have plenty candidates, applications and their verifications, particularly with a high-resolution coupling of solid-liquid phases.

2. As a general problem, particle-based Navier-stokes solutions with Lagrangian tracking involve perturbations of pressure causing numerical instability.

Resolving these problems, the follows are achieved:

I. Development of the high-resolution DEM-MPS methods:

Four DEM-MPS methods are proposed. Each DEM-MPS coupling scheme is based on different concepts. **First proposed model** is based on the two-fluid-based model with introduction of the accurate particle methods. **Second model** is composed of two separated discretization space accommodating each phase with the solid-liquid interaction based on the momentum. This model is improved further as **third proposed model** in consideration of consistency in additional physical quantities except the momentum with the mass conservation. **Fourth model** improves the first model to resolve a problem related to the computational space resolution to reproduce the solid shape.

II. Improvement of the MPS method for unsteady flow around solid phase:

Novel schemes are proposed for the MPS method to enhance the numerical stability and accuracy.

[Dynamic Stabilization] A new stabilizing scheme is developed. This scheme gives the minimally requisite repulsive force based on the Newton's third law of motion for both compressive and tensile stress states. It is shown to stabilize and adjust the disorder of calculation points for comprehensive MPS applications with more accurate velocity fields.

[Space Potential Particles] A new free-surface boundary condition is proposed to keep consistency of definition of the free surface in its mathematical and physical properties. This scheme presents a new virtual particle given the free-surface boundary for unphysical void space in consideration of a potential of interactions from void space. In a Karman vortex simulation, it is shown that this proposed scheme effectively suppresses the familiar unphysical-voids occurring in particle-based simulations. In addition, it gains a significant enhancement of the numerical stability and saves computational costs remarkably.

[Introduction of the Wendland kernel] The convergence of the kernel function is investigated and a higher order kernel function, namely the Wendland kernel is introduced to suppress the pressure perturbation effectively.

Enhanced performance of these proposed schemes are demonstrated through some benchmarks. For accurate simulations, enormous computational costs are required for 3D solid-liquid two-phase flows with high space-resolution. The prominent advantage of the proposed schemes is particularly characterized by their performance to enhance the numerical stability. The property contributes to saving the computational cost by its applicability to lower time resolution with more accurate results.

Acknowledgements

The completion of my present study could not have been accomplished without the help and support of several people.

I owe my deepest and sincerest gratitude to my supervisor, Professor Hitoshi Gotoh, for his continuous support, insightful guidance and inestimable advice throughout the present study. I have been benefited immensely from Professor Gotoh's erudite knowledge and his wide view on research with honorable responsibility. His noble character together with his earnest attitude towards the scientific research have made an everlasting impression on my life.

I would like to express my acknowledgments to the member of my thesis committee, Professor Takashi Hosoda for his constructive comments during the refereeing phase of this thesis. Besides, I am grateful to Dr. Abbas Khayyer, the member of my thesis committee and my supervisor for the present study related to the particle method, for his tremendous support and extensive discussion as well as his genuine kindness.

I would also like to take this opportunity to express my gratitude to Professor Seiichi Koshizuka, developer of MPS method from the University of Tokyo, for his kind comments and encouragements.

I am indebted to my supervisor for the coastal engineering and the computational physics from the beginning of my research journey, Dr. Eiji Harada, for his incisive guidance and tremendous support in every respect. He has offered me the delight of the scientific research. Besides, I would also like to express my sincere appreciation to Dr. Hiroyuki Ikari for his constructive advice and heartfelt kindness. My sincere thanks go to Dr. Dongfang Liang, the University of Cambridge, UK, for his constructive discussion and invaluable advice. I should thank all current and former members of our laboratory particularly Mr. Hiroki Kubota for his supportive attitude.

Special and sincere thanks should go to my precious friends, Mr. Hidekazu Shirai, Nobuhiro Takenaka and Mr. Satoshi Kusaka, for all their kindness and positive attitude.

Finally, my infinite gratitude goes to my parents, my dearest father and mother, for their unconditional love and continuous support; to my brothers, Takeshi and Shinji, for their warm encouragement.

List of Figures and Tables

Contents

3. Development of the High-resolution DEM-MPS methods

II Improved MPS method for unsteady flow around solid phase

4. Dynamic Stabilization of Moving Particle Semi-implicit Method

CHAPTER 1

INTRODUCTION

Since the 2011 Great East Japan Earthquake and Tsunami, it is a matter of great emergency to reevaluate durability of coastal structures for violent flows over the conventional expectation. Surroundings of structures, such as rubble-mounds, covering blocks or caissons, dynamically change the states by tsunami hitting repeatedly. The suffering processes are enumerated as follows; scouring grounds by the waves dropping down over caissons, a destruction of structures by floating matters hitting it, deformation of foundations through a moving of rubble-mounds or covering blocks, a tumbling or slide of structures by the violent flows, etc. Such suffering processes by terrible disasters get all the more complicated and outstanding matters increase. Therefore, wider viewpoints and a further comprehensive and accurate prediction tool based on a highly developed physics model is absolutely necessary to catch the faithful boundary condition to the real phenomenon. However, such unsteady suffering mechanisms are difficult to be grasped through experimental measurements due to the intricacy, consequently, it has not yet been comprehend sufficiently up to now. For this reason, in recent years, numerical simulation is studied extensively as an assistant or alternative approach to experiment and observation. In particular, the Japan coastal engineering committee found a subcommittee attempting to establish and systematize reliable numerical frameworks for reproduction of the physical fluid behaviors as the so-called numerical wave flume. In these numerical frameworks for tracking details of fluid motions, the Navier-Stokes equation is commonly adopted as the governing equation. However, the Navier-Stokes equation originally corresponds to a description of a fluid motion at a local point, and thus, it is a crucial issue how the formula is discretized and applied to the infinite calculation points or grids. Up to now, the numerical models varies depending on purposes from various viewpoints and they mutually complement each other - the details of the numerical models are explained in the second section of this chapter. Due to the brisk advancement of numerical tools and their applications, in recent years, comprehension of the suffering mechanisms progresses rapidly from various angles via each numerical model [1-7]. In particular, since the 2011 Great East Japan Earthquake and Tsunami, numerical analysis about the huge tsunami is studied actively.

Incidentally, it is essential for coastal engineering problems to consider various boundary conditions comprehensively to accommodate each changeable circumstances not merely for terrible disasters represented by a huge tsunami, but also for general purposes as e.g. designs of common constructions or prediction of long-term phenomenon, such as tidal waves or changes of environment like a sediment transportation by ordinary waves. Therefore, in order to establish comprehensive solvers, the coastal engineering field regularly approaches unrelated phenomenon as a benchmark, which is targeted mainly in other engineering fields. In contrast, a wave behavior with experimental-channel-scale; relative small-scale but violent state, is taken up as a general problem for examinations of numerical models by other engineering fields, such as the mechanical engineering. Extending over several fields, a foundation of numerical approach to complicated fluid flows is laid. Therefore, development or improvement of numerical schemes for the coastal engineering problems would contribute to other engineering fields. So is the same with converse. The significance of development of comprehensive, accurate and practical

numerical models is not only for the coastal problems specialized in the urgent problems like a huge tsunami, but also for various problems including that of other engineering fields.

1.1 Background and Motivation

As for application of numerical models to prediction or examination of a suffering mechanism with a big disaster like a huge tsunami, the following cautions and problems are decisive.

I. **Violent free surface of flow**:
Wave flows with a complicated boundary condition are usually categorized as unsteady flows. They change their free-surface configurations violently, and as a result, are apt to bring about the numerical instability. Reliable numerical stability, namely the robustness and adaptability to various situations are vital for practical use, not to mention the accuracy. However, the so-far numerical models are mostly specialized for each own original targets, and a prudent setting of calculation condition is necessary for extension to the other targets.

II. **Moving boundary**:
Wave flows change the states responding to the circumstances. However, the numerical wave flume particularly focuses on reproducibility of the behavior of flows with an assumption of experimental channel flows under a simple condition, and thus, development of multi-phase flow models accommodating a moving boundary does not advance sufficiently.

III. **Boundary between phases**:
Accuracy of evaluation of flows around solid elements depends on handling the solid-liquid boundary, whose shape is not straight definitely. Therefore, it is required a flexible computational setting of calculation points or grids to track the dynamical and elaborated boundary, which is usually troublesome.

IV. **Calculation coast**:
Numerical stability and accuracy depend on the calculation resolution of both time and space. For practical use, such a calculation coast should be reduced as much as possible. If it is possible to enhance the stability and have a rough time resolution, the calculation cost can be saved keeping the accuracy. However, the coastal engineering problems usually include violent flows with instability, and result in making it exceedingly challenging.

V. **User-friendly**:
In many cases, advanced numerical models have a tendency to require laborious procedures and proficiency in program code and numerical schemes. Considering propagation of the numerical model, it is significant to keep it simple. The ease would assist users to progress engineering projects smoothly, too.

Even recent accurate models cannot capture the whole picture of the physical suffering processes due to the above problems. At present, most studies of the numerical wave flumes concentrate improvements of the reproducibility of violent flows without the moving boundary. Nevertheless, trials of multi-phase flow simulation are implemented by degrees despite the relatively scarce candidates of the models, such as

[8-11]. As one of the cause of the present circumstance, the treatment of multi-phase flow accompanies with a computational arduousness mainly caused by the difference of the governing equations between each phase. It is significant that the solid phase has a disparate property and mathematical description of its behavior from the other phases corresponding to the continuum; liquid and gas. Therefore, coupling schemes of solid-liquid or solid-gas phases involve convoluted procedures as a weakly-coupling and may bring about a confusion to most users with requirement of a special proficiency in the models. In addition, the manners of coupling schemes are miscellaneous depending on the solid scale to the resolution of the continuum. The coastal engineering problems usually target on enormous calculation domains and violent states in need of a high resolution for flows around structures, and worse than that, the scale of solid elements varies. Consequently, multi-phase flow simulations in the coastal engineering field are restricted due to the calculation cost.

However, in these days, a computer performance advances rapidly and brings about a period of transition for numerical models. By making full use of the computer performance, it is expected that an achievement of the high-resolution solid-liquid two-phase simulation would be realized for the coastal problems. The aim of this study is to improve the solid and liquid two-phase flow model for practical application with a reliable accuracy and stability by a relative high-resolution.

Firstly, the so-far schemes are overviewed to settle on the target for the trial of improvement in this study.

1.2 An overview of numerical solvers for violent free-surface flows

Here, the so-far numerical solvers of the Navier-Stokes equation for free-surface flows are reviewed. Numerical models have been developed from the various approaches. The detail of the outline can be referred to Gotoh et al. (2005) [12] or Sethian and Smereka (2003) [13]. Paying attention to the Navier-Stokes solvers for free-surface fluid flows, it can be classified into two groups. The first is the interface-tracing method and the second is the interface-capturing method. The difference of them comes from the usage of the flows by the Lagrangian solvers or the Eulerian solvers. In addition, means of the discretization of the governing equation is also classified into two groups as the Grid-based method or the Gridless method.

1.2.1 Grid-based solvers of Navier-Stokes equation

As the most popular method, Grid-based solvers have numerous achievements. This direct discretization of the space or materials with distributed grids make its physical meaning clearly comparing with the Gridless solvers.

1.2.1.1 Eulerian Grid-based solvers

Eulerian Grid-based solver corresponds to the interface capturing method. The grid-based solvers settle the fixed grids in the domain, and the mass and momentum flux is calculated across the cell boundary through Eulerian observation. In this method, the interface between different phases is captured indirectly by

calculating the advection term of some indexes. As most popular models for capturing free-surface, the MAC (Harlow and Welch, 1965) [14] or the VOF (Hirt and Nichols, 1981) methods [15] are employed. In the MAC method, moving particles are distributed in the cell and free surface is tracked through the position of the particles. While, the VOF method utilizes a volumetric occupation rate of fluid, which requires calculation of the advection term causing the numerical diffusion. The prominent advantage of these solvers is the tenacious robustness to violent free-surface flows with its applicability for various actual phenomenon. However, the process of the free-surface capturing necessarily contains a drawback of numerical diffusion dulling the free-surface tracking function in the cell, particularly in a large deformation of free surface with an acute angle. As a successor model to suppress the numerical diffusion, CIP method (Yabe et al., 2001) [16] is developed to calculate the advection term clearly and is improved more to grasp forms of free surface as e.g. an introduction of the Immersed-Boundary method (Perkin et al., 1989) [17] utilizing an interpolated interaction associated with interfaces, IDO (Aoki, 1997) [18] as a higher order scheme for the diffusion term, etc. As for the other scheme, Level-set method is proposed to track the interface sharply via the Level-set function. Nevertheless, theses precise models would require the complicated calculation procedures increasingly.

1.2.1.2 Lagrangian Grid-based solvers

As another tracking method, Lagrangian Grid-based solver is cited. This corresponds to the tracking interface method. The conspicuous advantage of this is the accuracy of expression of free-surface flows. The interface of the targeted material or the free-surface boundary is tracked by the grids directly, consequently, it has no relation with the numerical diffusion caused in the interface capturing method. In addition, the grids are set only within computational domain where the fluid or some other element exists. It is able to save a computational storage space. In contrast, the disadvantage is the vulnerable robustness caused by the large deformation of a grid. For example, the Space-time FEM (Behr and Tezduyar, 1994) [19] was proposed, which applies the FEM scheme (Turner et al., 1956) [20] to both space and time, and succeeded to keep an acceptable stability and accuracy, however, it needs a nuisance remeshing procedure and a relative large computational cost. Moreover, as thought, a large deformation of an interface impedes its smooth calculation. ALE method (Huerta et al., 1974) [21] was developed to resolve the problem about robustness related to the deformation. The ALE method utilizes a special grid, which moves voluntarily and independently on the fluid motions tracked by an Eulerian gird and solid element motions by a Lagrangian grid. If the ALE grid is moved following interfaces, it is possible to implement calculation stably without remeshing procedures. As for another approach by the CIP method, the CIVA method (Tanaka, 1999) [22] was proposed on the basis of unstructured grids as a modified scheme of CIP method. However, these modified models have a perturbation of velocity due to the phase of the grids, and need a high resolution of time fitting the smallest grid size. In either case, an adequate and prudent calculation setting is necessary.

1.2.2 Gridless solvers of Navier-Stokes equation

In the Grideless solvers, the estimation of physical quantities are based on interactions between distributed calculation points (nodes or particles). Although it requires operators to express the interactions in some forms, it is unnecessary to adjust a physical connectivity between each points typically required for the usual Grid-based solvers possibly distorted, and is expected the possibility of the more flexible applicability

for any complicated boundary condition.

1.2.2.1 Eulerian Gridless solvers

In the Eulerian Gridless solvers, fixed nodes are arbitrarily distributed over the computational domain and the derivative of the governing equation is approximated by the neighboring nodes in a finite effective domain or a cloud of nodes. Firstly, method of least squares was introduced into the Gridless framework for the function of the approximation of variables (Batina, 1993) [23]. However, the numerical diffusion arise in the process of the approximation, therefore, some attempts to suppress it by improvement of approximation was implemented, such as an introduction of CIP method with a highly accurate interpolation (Tanaka, 1999) [24], an introduction of the Galerkin method (Belytschko et al., 1994) [25], or the Meshless Local Petrov-Galerkin method: MLPG (Fries and Matthises, 2005) [26]. Nonetheless, they still remain the strong numerical diffusion through e.g. the artificial stabilizing force. To resolve this problem, newly higher accurate Gridless scheme; MPS-MAFL method was proposed as a Lagrangian-Eulerian method. This is composed of a combination of grid and particle, namely MPS with a Meshless Advection using Flow directional Local grid. In the Lagrangian phase, the original MPS differential operators are utilized for the pressure gradient, diffusion and compressibility. While, the convection of flows are calculated by the flow-directional 1st dimension grid generated locally at each calculation steps.

1.2.2.2 Particle method: Lagrangian Gridless solvers

Particle method is the fully Lagrangian Gridless method. This can be categorized by two classifications. First, it is categorized in accordance with the length scale of each models. Fluid flow can be regarded as the continuum from a macroscopic viewpoint, and simultaneously an aggregation of molecules from a microscopic viewpoint. Models to calculate the motions of each molecules corresponding to the microscopic model has examples as Molecular dynamics or direct simulation Monte Calro (DSMC: Bird, 1987) [27]. On the other hand, macroscopic model is represented by the Smoothed Particle Hydrodynamics: SPH (Lucy, 1977 [28]; Gingold and Monaghan, 1977 [29]), the Moving Particle Semi-implicit model: MPS (Koshizzuka and Oka, 1995) [30] method. The microscopic model tracks motions of molecules by e.g. the potential energy between the molecules, and the fluid motion is estimated statically through them. Therefore, this model needs enormous computational coast comparing the macroscopic model. Secondly, particle methods are categorized by the mathematical system to approach the fluid motions as the probabilistic model or the deterministic model. The probabilistic model is applied to probabilistic phenomenon based on the static principles, and it has examples as DSMC or lattice gas automaton (Frisch et al., 1987) [31]. As a matter of course, this model requires numerous calculation points as the microscopic model for the calculation of the statics. While, usual solvers of the Navier-Stokes equation are classified into the deterministic phenomenon with a macroscopic treatment (e.g. SPH, MPS, PIC: Particle In Cell method; Harlow, 1988) [32]. PIC method was proposed to avoid numerical diffusion associated with the advection term by setting both grids and particles. Particles are distributed for calculation of advection of flows, while grids are used for the other term. This was improved as FLIP: fluid-implicit particle method (Brackbill et al, 1988) [33] to suppress the numerical diffusion related to the interpolation of the particles. The SPH method was developed for compressible flows in the astronomy field. In the SPH method, physical quantities are distributed with the kernel function. The SPH is applied to incompressible flows also with treatment of flows as a weakly-compressible flow (WSPH; Morris et al., 1997) [34] or strictly-incompressible flows (ISPH; Shao and Lo, 2003) [35].

The advantages of particle method are as follows;

i. It has a capability to handle interfaces without any deformation of grids, and as a result, it keeps a robust numerical stability comparing with the Grid-based solvers.
ii. It is dispensable with a nuisance reconstruction or relocation of grids for deformed interface only if tracking the particles.
iii. Advection term is needless, and thus, it results in no relation with numerical diffusion.
iv. It secures ease of setting an initial condition. Only putting particles on the objectives is satisfactory.

While, the disadvantage of particle method is;

i. It requires a huge computational storage in memorizing relations of connection for neighboring particles. In addition, due to the large number of the connections, the load of computational cost increases.
ii. The inherent perturbation of motions of particles may cause the numerical instability and inaccuracy.
iii. Some contrivance is required for the outlet/inlet boundary due to the unphysical free-surface definition given to particles at the edge of the domain.

1.3 An overview of solid-liquid two-phase solvers for moving boundary condition

The so-far solid and liquid two-phase coupling models are reviewed here. Up to now, various numerical models are proposed and they vary for each purposes or targets. They are categorized by the degrees to distinguish the solid phase form the liquid phase as; mixture model, two-fluid model and particle tracking model. Mixture model takes motions of solid and liquid phases as integrated one phase flow with the constitutive low. Two-fluid model also regards a solid motion as fluid flow, but the fundamental equations are separated between solid and liquid phases. Mixture model and two-fluid model are usually employed with a condition that solid elements are adequately small and it can be applied the constitutive low, such as sediment transportation and debris flows. Such a simulation focuses on states of the mixture flows in proper perspective. Meanwhile, for a simulation of such unsteady flows that solid-solid interactions are significant, some models to calculate solid motions separately from fluid motions are necessary. Particle tracking model is effective to resolve this issue. In the model, solid particles are tracked by Lagrangian observation and the interactions between solid particles are calculated individually as an impact force by separating the discrete domains between solid and liquid phases. In widely common methods, particle size is set smaller than that of liquid resolution, namely width of grids (or interval of nodes or particles) of flows. In the fundamental equation of fluid flows with Reynolds averaging procedure, each phases are connected physically through the interaction between solid and liquid by introduction of e.g. PSI-cell model [36] or some models based on semi-empirical coefficients of added mass. Then, since the solid particles are handled directly by Lagrangian tracking, an approximation of the diffusion and gradient for the interaction is needles. All the solid particles are not targeted for estimation of their motions considering the computational cost in many case, however, the number of observed particles should be secured over the reliance amount definitely. Therefore, its application to unsteady flows is difficult due to the possible maldistribution of particles. In

addition, considering the diverse length-scales in a practical site associated with the coastal engineering problems, such as sand, rubble-mound, covering block and caisson, some comprehend frameworks to cope with the different scales of solid elements is indispensable. Currently, owing to the advance of the performance of computer, although it is limited to small domains and calm flows, a great resolution model, namely a DNS-based model is applied to multi-phase flow simulations with a precise capture of flows. A size of solid element is set as larger than captured scale of liquid motions in this model. The driving force of the solid element is evaluated by integration of the STERESS on the surface of the targeted element. For the evaluation, it is needed extremely minute grids (or nodes, particles) distributed around the particle for the evaluation of driving force. As an ideal approach to this, BEM [37] consummately matches the concept, however, many studies utilize fixed grids due to the computational cost for a remeshing procedure. These are basically adopt IBM (Peskin, 2002) [38] concept, so that fluid flows are handled as multiphase flows through projection of interactions between each phases evaluated by the variation of the momentums of the phases. In most precedents of the high-resolution simulation of solid and liquid two-phase flow, though such a procedure of connection between each phase is identical, the solver of the Navier-Stokes equation for the fluid flows varies. Equally to single phase flow models mentioned in the section 2, DNS-based solid and liquid two-phase models are also roughly classified into two groups as Euler-Lagrange coupling model and Lagrange-Lagrange coupling model. In either case, solid phase is tracked by Lagrangian method as a discrete element. The efficacy of the models for the boundary between the solid and liquid phases corresponds to the usage of free surface of flows.

1.4 Objective

From now on, it is supposed that required accuracy of numerical models would get all the more escalated in accordance with high-level demands. Considering the situation, following factors would be desirable for a future model.

i. Comprehension of models to accommodate with various complicated boundary conditions including violent free-surface flows.
ii. User-friendly scheme to apply practical engineering problems easily.

As for issue i, comprehension of models for complicated boundary is mainly decided by the accuracy of tracking interfaces. As stated before, the accuracy is refined by various methods through ingenious devices. However, focusing on the grid-based models, they inevitably involve the numerical instability caused by distortion of grids, moreover, they generally requires troublesome remeshing procedures. As a solution of these, the grids are meshed minutely as ordinal DNS-based models with fixed grids and projection of interactions between phases. Meanwhile, gridless-particle methods track free-surface flows directly by the calculation particles without any ambiguousness and annoying procedures, surely the distortion of particles also. Therefore, particle method is expected its satisfactory potential to be applied to the DNS-based high-resolution framework for both interface of different phases and free surface with an acceptable accuracy and stability by plain handling. However, particle method is a relatively fresh model and does not have affluent verifications about its validity. In particular, scheme with high-resolution

coupling of solid-liquid phase has few candidates and few pragmatic uses in particle method. As a further problem, precedent studies commonly report a burdensome problem about the unphysical perturbation of pressure involved in the particle method as a general issue. However, in recent years, accurate particle methods were developed so that such pressure perturbations have been obviously suppressed, and as a result, earnest introduction of particle method into a simulation of precise flows is being fulfilled. The aim of this study is to develop and improve high-resolution solid-liquid multi-phase flow models based on the particle method so that complicated boundary condition including violent free-surface flows can be simulated accurately and stably with ease.

1.5 Major Findings

The target of this study is development of particle-based high-resolution solid-liquid multi-phase flow model. To begin with, the following objectives are designed as main concerns and challenges to be accommodated for optimum solutions of a practical use.

I. Developing an accurate DEM-MPS method for high-resolution simulation.
II. Securing the well-reproducibility in flows around solid phase
III. Securing the numerical stability for practical applications to the coastal engineering problems

As for issue i., several DEM-MPS models are developed [39], and their validities are examined by comparison with experimental results as shown in **Fig. 1.5.1**. Coupling schemes of each model are based on different concepts. First, referring to the two-fluid-based model shown in some studies, the framework is improved by introduction of accurate particle methods for numerical stability and accuracy, and the Passively Moving Solid model is applied to solid particles for high-resolution expression of rigid solid structures. Second model is composed of two separated domains accommodating different phases; solid particles and liquid particles, and they are connected to each other through interactions of each phases based on the momentum quantity. This model is improved further as third model i consideration of physical quantities, namely velocity, viscosity and density by projecting them between the calculation domains allocated to each phases for conservation of mass. Fourth model improves the first model to resolve a problem related to the calculation resolution.

For issue ii and iii, novel schemes are proposed for the MPS method. As for the enhancement of the stability, new stabilizing scheme, namely the Dynamic stabilization [40] is invented. This scheme assists reproduction of physical velocity of flows and motion of solids. Owing to this scheme, applicability of the so-far accurate particle method is enhanced. This scheme is introduced into the DEM-MPS frameworks and its validity is verified by some benchmarks (refer to **Fig. 1.5.2**).

As for the numerical accuracy, a consistency of a definition of particles in the mathematical and physical properties is investigated. Up to now, free surface of flows is tracked obscurely by the particle methods in a single-phase flow simulation due to their usages of free-surface particles in the Poisson Pressure Equation. To resolve this problem, new virtual particle given the free-surface boundary is introduced in consideration of a potential of interactions from void space. This scheme shows well-reproductions in some benchmarks with effective suppression of unphysical voids and keeping

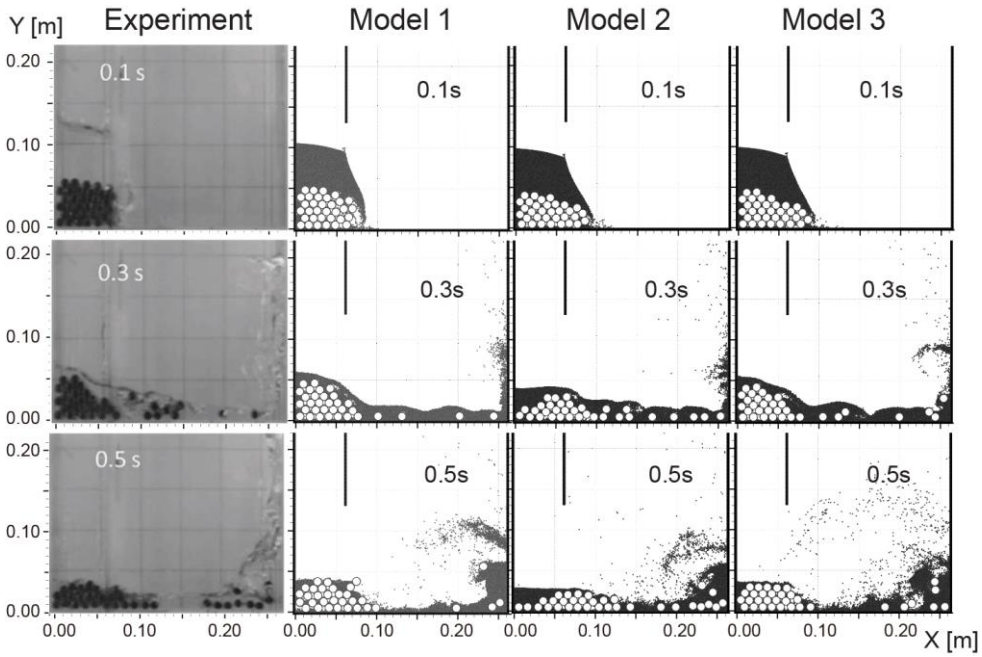

Fig. 1.5.1 Snapshots of experiment and simulation results by the proposed DEM-MPS methods in solid-liquid two-phase dam breaking

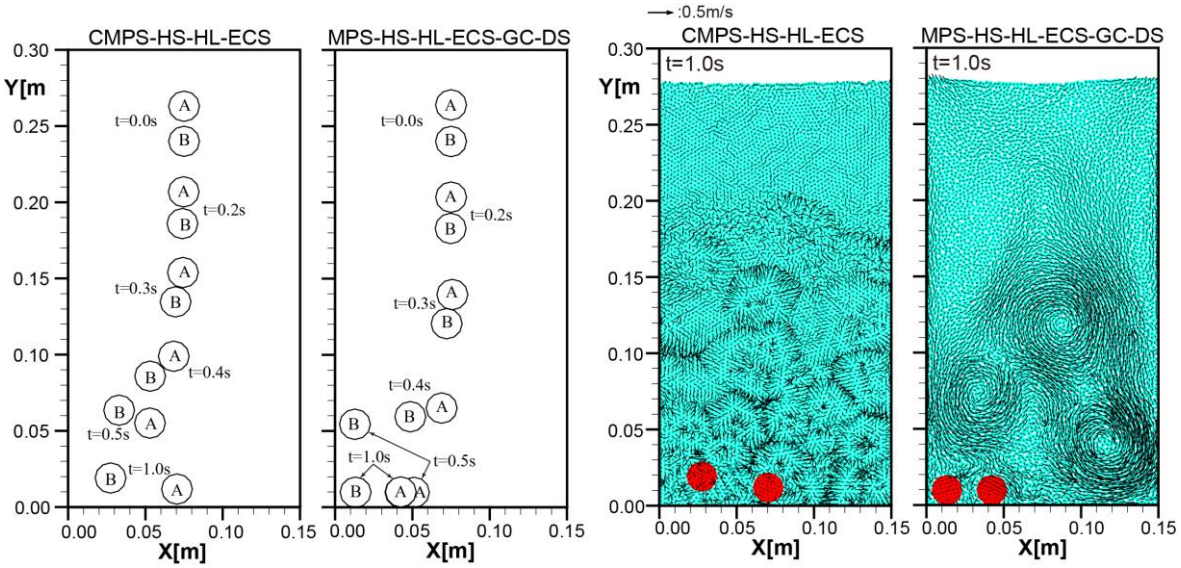

Fig. 1.5.2 Snapshots of the simulation results with velocity fields by DEM-MPS methods with so-far stabilizer and the Dynamic Stabilization

continuity of free-surface flows (refer to **Fig. 1.5.3**). In addition, it gains supplementally a considerable enhancement of numerical stability.

Finally, the function is reconsidered and a higher order kernel function is introduced. Improvement of numerical stability about pressure perturbation is shown in several benchmarks as shown in **Fig. 1.5.4**.

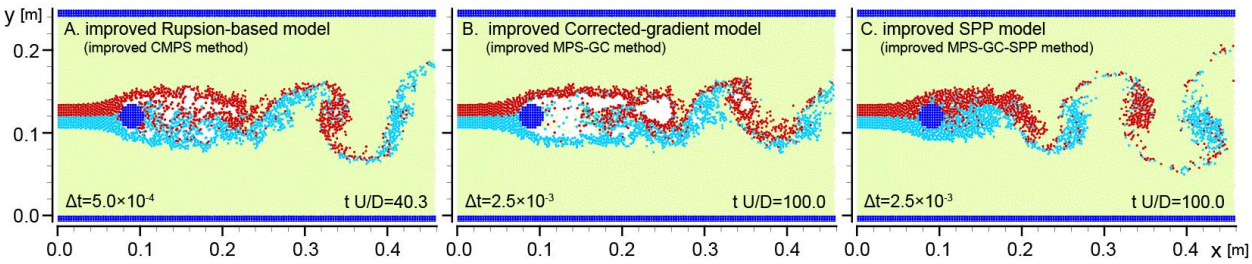

Fig. 1.5.3 Snapshots of the simulation results by Repulsion-based model, Corrected-gradient model and proposed SPP model

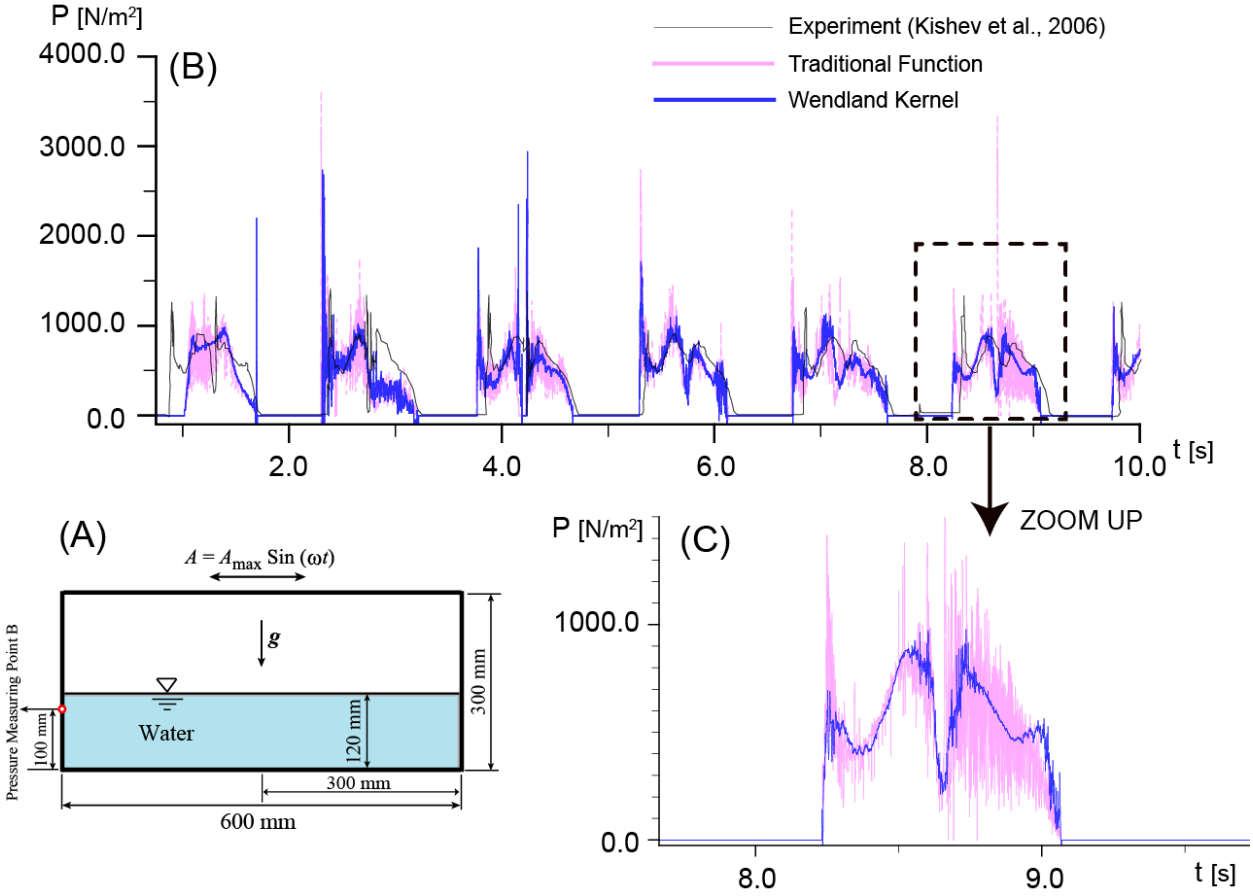

Fig. 1.5.4 (A)illustration of the simulation condition and (B)time series of pressure at a measurement point in sloshing simulation by the traditional function and the Wendland kernel

1.6 Thesis outlines

This dissertation is organized into seven chapters.

Chapter 2 overviews the so-far particle methods for solid-liquid two-phase flow. In addition, a solid model and a liquid model; DEM for tracking solid elements and MPS method for tracking fluid

motions including accurate particle methods, are explained as components of proposed multi-phase models in this study. The effectiveness of accurate particle methods are examined through simple benchmarks.

Chapter 3 aims to develop solid-liquid two-phase flow models with DEM and MPS method (accurate particle method) for high-resolution simulation, namely the accurate DEM-MPS methods. Firstly, three DEM-MPS methods are proposed. The validity of each model is examined by comparison with an experimental result targeting on a solid-liquid two-phase dam breaking. Secondly, one of proposed models is improved further and applied to a three dimensional simulation for a sedimentation process of numerous blocks with violent deformation of free-surface flows by dropping blocks.

From chapter 4, improvements of the MPS method are attempted to improve the numerical stability and accuracy for reproducibility of flows around solid structures.

Chapter 4 discusses the tensile instability of the so-far MPS method and unphysical consequences of solid motions, focusing on the pressure gradient term. A novel stabilizer scheme is proposed and applied to simple benchmark simulations. Well-reproductions of flows and effective stability are shown in the tests. Moreover, the proposed stabilizer is introduced into the accurate DEM-MPS methods. The universality of this problem in the MPS method is proved so that it does not depend on coupling schemes of DEM and MPS method by some benchmarks. Simultaneously, the effectiveness of the proposed stabilizing scheme is shown. Finally, reexamination of improvement of the DEM-MPS frameworks is implemented by comparison with the experimental results from a viewpoint of fundamental quantities in property of solid motions in flows.

Chapter 5 advances the discussion of reproducibility of flows around a solid boundary in the MPS method. A novel definition and usage of free surface are developed to keep consistency in both space and substance between mathematical property and physical property. A verification of the proposed scheme for reimposition of unphysical voids is examined through a benchmark with whir of water flow in a rotating tank. Secondly, the Karman vortex simulation is performed with the proposed scheme to show resolution of unphysical voids usually shown in the so-far MPS methods. Thirdly, continuity around free surface area is examined with free jet simulation in a vacuum domain and a dam breaking simulation.

Chapter 6 focuses on the kernel function for differential operations. This chapter highlights properties of some kernel functions widely used in the SPH method. And a higher order kernel function is introduced to improve the numerical stability related to a pressure perturbation. Its performance is shown in the some simple benchmarks including a sloshing flow.

Chapter 7 summarizes entirely all of the chapters, and the conclusions of this research will be made. At the same time, the recommendations for future research are also discussed.

REFERENCES

[1] Brocchini, M. R., Bernetti, A. Manchnelli and G. Albertini, "An efficient solver for nearshore flows based on the WAF method", *Coastal Engineering*, Vol.43, issue 2, pp.105-129, 2001

[2] Gotoh, H. and T., Sakai, "Key Issues in the Particle Method for Computation of Wave Breaking", *Coastal Engineering*., Vol. 53, No. 2-3, pp.171-179, 2006.

[3] B.H., Choia, D.C., Kima, E., Pelinovskyb and S.B., Wooc, "Three-dimensional simulation of tsunami run-up around conical island", *Coastal Engineering*, Vol.54, issue 8, pp.618-629, 2007

[4] Gotoh, H., "Lagrangian Particle Method as Advanced Technology for Numerical Wave Flume", *International Journal of Offshore and Polar Engineering*, Vol. 19, No.3, pp.161-167, 2009.

[5] Fuhrman, D.R. and P.A. Madsen, "Tsunami generation, propagation, and run-up with a high-order Boussinesq model", *Coastal Engineering*, Vol.56, issue 7, pp.745-758, 2009
[6] Hsiao, S.-C. and T.-C., Linb, "Tsunami-like solitary waves impinging and overtopping an impermeable seawall: Experiment and RANS modeling", *Coastal Engineering*, Vol.57, issue 1, pp.1-18, 2010
[7] Fuhrman, D.R. and P.A. Madsen, "Numerical simulation of waves generated by landslides using a multiple-fluid Navier–Stokes model", *Coastal Engineering*, Vol.57, issue 9, pp.779-794, 2010
[8] Mutsuda, H., Y., Shimizu and Y., Doi, "Numerical Study on Interaction between Violent Wave and Structure using SPH, Particle-Based Methods, Fundamentals and Applications", *PARTICLES 2009*, pp.266-269, 2009.
[9] Baso, Suandar., H., Mutsuda, T., Kurihara, T., Kurokawa, Y., Doi and J., Shi "An Eulerian Scheme With Lagrangian Particles For Evaluation of Seakeeping Performance of Ship In Nonlinear Wave", *Proc. International Journal of Offshore and Polar Engineering*, Vol. 21, No. 2, p.611, 2011.
[10] Harada, E., H., Gotoh and N., Tsuruta, "Numerical Simulation for Sedimentation Process of Blocks on a Sea Bed by High-Resolution Multi-Phase Model", *Coastal Eng. Jour.*, Vol. 53, No. 4, pp.343-364, 2011.
[11] Harada, E., N., Tsuruta and H., Gotoh, "Two-phase flow LES of the sedimentation process of a particle cloud", *Journal of Hydraulic Research*, First, pp.1-9, 2013.
[12] Gotoh, H., Ikari, H., Memita, T. and Sakai, T., "Lagrangian particle method for simulation of wave overtopping on a vertical seawall", *Coast. Eng. J.* 47(2 & 3), pp.157-181, 2005.
[13] Sethian, J. A. and Smereka, P., "Level set methods for fluid interfaces", *Annual Review of Fluid Mechanics*, Vol. 35, pp. 341-372, 2003.
[14] Harlow, F. H. and Welch, J. E., "Numerical calculation of time-dependent viscous incompressible flow of fluid with free surface", *Phys. Fluid*, vol.8, pp.2182-2189, 1965.
[15] Hirt, C. and Nichols, B. D., "Volume of fluid (VOF) method for the dynamics of free boundaries", *J. Comput. Phys*. Vol.39, pp.201-225, 1981. Osher, S., et al. : Fronts Propagating with Curvature-Dependent Speed : Algorithms Based on Hamilton-Jacobi Formulations, *J. Comput. Phys*. Vol.79, pp.12-49, 1988.
[16] Yabe, T. and Wang, P.Y., "Unfied Numerical Procedure for Compressible and Incompressible Fluid, *J. Phys. Soc*. Japan, Vol.60, No.7, pp.2105-2108, 1991.
[17] Peskin, C. S. and David, M.M., "A Three-Dimensional Method for Blood Flow in the Heart I. Immersed Elastic Fibers in a Viscous Incompressible Fluid", *J. Comput. Phys*. Vol.81, pp.372-405, 1989.
[18] Aoki, T. "Interpolated Differential Operator (IDO) scheme for solving partial differential equations", *Computer Physics Communications*, Vol.102, No.1-3, pp.132–146, 1997.
[19] Behr, M. and TE., Tezduyar, "Finite element solution strategies for large-scale flow simulations", *Computer Methods in Applied Mechanics and Engineering*, vol.112 (1), pp.3-24, 1994.
[20] Turner, M. J., R.W., Clough, H.C., Martin, and L.J., Topp, "Stiffness and deflection analysis of complex structures," *Journal of Aerospace Science*, vol.23, article 805, 1956
[21] Huerta, A. and WK., Liu, "Viscous flow with large free surface motion", *Comput Methods Appl Mech Engrg*, vol.69: pp.277-324, 1988.
[22] N. Tanaka, "The CIVA method for mesh-free approaches: improvement of the CIP method for n-simplex", *Comput. Fluid Dyn. J*. vol. 8 (1), pp.121–127, 1999.
[23] Batina, J.T., "A Gridless Euler/Navier-Stokes Solution Algorithm for Complex-aircraft Applications", *Front Cover*. 13 pages, 1993.
[24] Tanaka, N., "Development of highly accurate interpolation method for mesh-free flow simulations II. Application of CIVA method to incompressible flow simulations", *International Journal for Numerical Methods in Fluids*, Volume.34, Issue.5, pp.403-424, 2000.
[25] Belytschko, T., Lu, Y. Y. and Gu, L., "Element-free Galerkin methods", *Int. J. Num. Meth. Eng*. Vol.37, pp.229-256, 1994.
[26] Fries, T.P. and Matthies, H.G., "A Stabilized and Coupled Meshfree/Meshbased Method for the Incompressible Navier-Stokes Equations - Parts I and II: Stabilization and Coupling", Informatikbericht-Nr. 2005.
[27] Bird G. A., Nonequilibrium Radiation During Reentry at 10 km/s, AIAA Paper 87-1543, 1987.
[28] Lucy, L. B., "A numerical approach to the testing of the fission hypothesis", *Astron. J*., vol.82, pp.1013-24, 1977.
[29] Monaghan, J. J., "Simulating free surface flows with SPH", *J. Comput. Phys*. Vol.110, pp.399-406, 1994.

[30] Koshizuka, S. and Oka, Y., "Moving particle semi-implicit method for fragmentation of incompressible fluid", *Nuclear Science and Engineering*, vol.123, pp.421-434, 1996.
[31] Frisch, U., d'Humi´eres, D., Hasslacher, B., Lallemand, P., Pomeau Y. and Rivet J-P., "Lattice gas hydrodynamics in two and three dimensions", *Complex Syst.* 1, pp.649–707, 1987.
[32] Harlow, F. H. and Welch, J. E., "Numerical calculation of time-dependent viscous incompressible flow of fluid with free surface," *Phys. Fluid*, vol.8, pp.2182-2189, 1965.
[33] Brackbill, J.U., D.B. Kothe, H.M. Ruppel, "Flip: A low-dissipation, particle-in-cell method for fluid flow", Computer Physics Communications, Vol.48, pp. 25-38, 1988.
[34] Morris J. P., Fox P. J. and Zhu, Y., "Modeling low Reynolds number incompressible flows using SPH", *J. Comput. Phys.*, vol.136, pp.214-226, 1997.
[35] Shao, S. D. and Lo, E. Y. M., "Incompressible SPH method for simulating Newtonian and non-Newtonian flows with a free surface", *Advanced Water Resources*, vol.26 (7), pp.787-800, 2003.
[36] Crowe, C.T., Sharma, M.P., and Stock, D.E., "The Particle-Source-in Cell method for gas droplet-flows". *Trans. ASME-J. Fluid Eng.*, 99, pp.325-332, 1977.
[37] Crouch SL, Starfield AM., "Boundary Element Methods in Solid Mechanics". *Unwin Hyman*: London, 1990.
[38] Peskin, C. S., "The immersed boundary method", *Acta Numerica*, 11, pp. 1-39, 2002.
[39] Gotoh, G., N., Tsuruta, E., Harada, H., Ikari, H., Kubota, "High-resolution DEM-MPS methods for solid-liquid multi-phase flow",Proc. JSCE, Vol. B2-68, No.2, pp.21-25.
[40] Tsuruta, N., A. Khayyer and H. Gotoh, "A Short Note on Dynamic Stabilization of Moving Particle Semi-implicit Method", *Computers & Fluids*, Vol. 82, pp.158–164, 2013.

Part I

High-resolution DEM-MPS method for solid-liquid two-phase flow

CHAPTER 2

Introduction of DEM and MPS method into solid-liquid two-phase flow model

In this chapter, particle methods for Lagrange-Lagrange tracking of solid and liquid phases are presented. Firstly, as a solid-phase tracking method, the Discrete Element Method abbreviated as DEM is explained. Secondly, the Moving Particle Semi-implicit (MPS) method is introduced as a basic model for tracking fluid motions. Finally, accurate particle methods are explained. As for the section of the accurate particle method, to begin, the precedents of the accurate particle method including the Smooth Particle Hydraulics (SPH) method are overviewed. Next, focusing on the part of them, which are introduced into this study, their details are explained and their effectiveness are examined by some benchmarks.

2.1 Discrete Element Method (DEM)

For estimation of solid motions in water, in addition to the governing equation of fluid flows for the drag force, the interactions between solid elements are also necessary. In particular, where the solid elements are markedly concentrated, plural collisions may occur acting on a same solid element synchronously, and thus, solutions to handle plural collisions comprehensively is required. The solutions of collisions of elements are roughly classified into two typical frameworks.

The first model is the so-called hard sphere model, which dynamically treats the collision process of rigid body (particle). The collision between particles is estimated through the repulsion coefficient and all the particles are expressed as isolated states after or before collision in outputs of the calculation (Campbell and Brennen, 1985) [1]. This model is an orthodox method to express the collision faithfully and physically along to the real phenomenon, however, as a drawback, it cannot handle the synchronized collisions acting on a same particle more than three impacts due to its excessive number of the unknown variables for the solution. Such a so-called three-body problem is familiar to the astrophysics and is known that it does not guaranteed the unique solution except particular conditions. To resolve this problem, it is effective to apply the event driven approach, which is a kind of interpolant technics by cutting a time step into minute sub time steps to estimate a collision at the missed moment. Nevertheless, the significantly minute time intervals may bring about increase of numerical errors and result in s tendency to lose the reliability of results. Moreover, the extra procedure for the sub time step requires a bothersome computational handling.

While, another solution type is the soft sphere model, which targets on both collision and contact between particles and allows particles to overlap each other to some extent. The interaction between overlapped particles is calculated through the overlapping amount with velocities and angular velocities of the particles. The remarkable advantage is that it can handle the synchronized collisions together, and thus, it has superiority in application to transportation phenomenon of highly concentrated solids. As a typical

model of this concept, the Distinct Element Method (DEM) is cited. The DEM was proposed by Cundall and Strack (1979) [2] as a particle method. The DEM method has a comprehensive applicability for states of collision, contact, detachment and re-contact of elements including capturing their rotational motions. In addition, this method can easily introduce external forces including the fluid driving force, therefore, it has an outstanding adaptability to coupling schemes with other frameworks, namely the Computational Fluid Dynamics. Accordingly, the DEM has been applied to various coastal engineering problems, such as sediment transportation, sedimentation process, and construction project with rigid bodies as i.e. blocks or caissons.

The DEM tracks particles individually with the explicit scheme. Therefore, the fine resolution of computational time is necessary for the accurate and stable calculation. For this issue, a looping calculation is usually implemented in a time step of calculation for fluid flows, which is constructed by the implicit or semi-implicit method.

2.1.1 Governing equations

In the Distinct Element Method (DEM), a spring-dashpot system modeling a mechanical structure is introduced. On the assumption that solid elements are in fluid flows, the governing equations of translational and rotational motions of the solid elements are described with each force as:

$$M\frac{d\boldsymbol{v}}{dt} = \boldsymbol{F}_{p\mathrm{int}} + \boldsymbol{F}_{flow} + \boldsymbol{F}_{g} \tag{2.1.1}$$

$$\boldsymbol{I}\frac{d\boldsymbol{\omega}}{dt} = \boldsymbol{T}_{p\mathrm{int}} + \boldsymbol{T}_{flow} \tag{2.1.2}$$

where M is the mass of the solid element, $\boldsymbol{v}$ is the velocity vector of the solid element, t is time, $\boldsymbol{F}_{pint}$ is the vector of the inter-element force, $\boldsymbol{F}_{flow}$ is the vector of hydrodynamic force, $\boldsymbol{F}_{g}$ is the vector of the body force (gravity acceleration), $\boldsymbol{I}$ is the inertia tensor, $\boldsymbol{\omega}$ *is* the angular velocity vector of elements, $\boldsymbol{T}_{pint}$ and $\boldsymbol{T}_{flow}$ are the vectors of the torque force by the inter-element force and the hydrodynamic force, respectably.

The solution of the hydrodynamic force varies mainly depending on the computational space resolution for solid elements to track the fluid flow. Particularly, in the high-resolution simulation of the solid elements, the hydrodynamic force is usually calculated by integral of fluid stress tensors over the surface of solid elements as:

$$\boldsymbol{F}_{flow} = \iint_{s} \boldsymbol{\tau}\cdot\boldsymbol{n}ds \tag{2.1.3}$$

$$\boldsymbol{T}_{flow} = \iint_{s} \boldsymbol{r}_{s}\times(\boldsymbol{\tau}\cdot\boldsymbol{n})ds \tag{2.1.4}$$

where $\boldsymbol{n}$ is the unit vector directing outward from the surface of the element, $\boldsymbol{\tau}$ is the fluid stress tensor, s is the surface of the element, and $\boldsymbol{r}_s$ is the relative positional vector from the centroid of the targeted solid element to its surface.

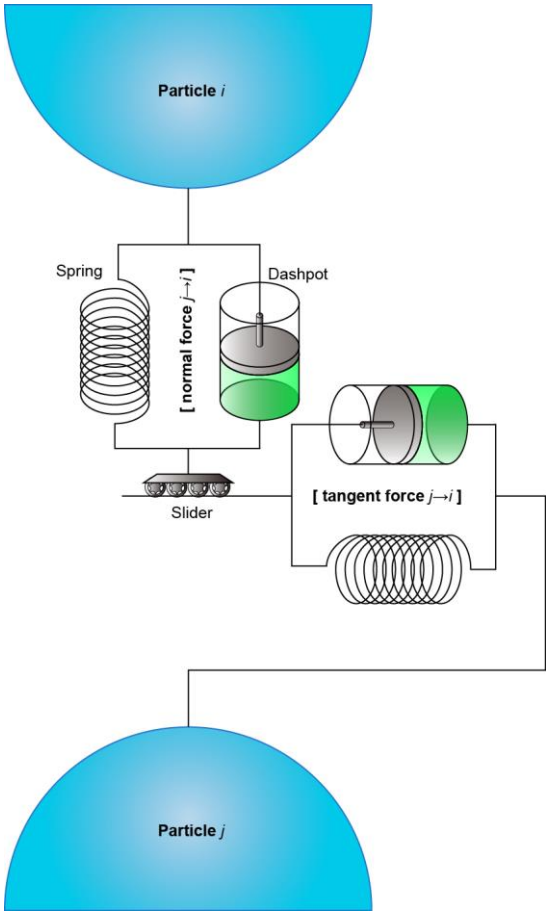

Fig. 2.1.1 Illustration of the spring-dashpot system

2.1.2 Numerical Solution

The interaction force between particles $\boldsymbol{F}_{pint}$ is given where particles overlap each other. Defining the diameter of targeted particle i and j as d_i and d_j, the collision interaction between them works when the distance between centroids of the particles $|\boldsymbol{r}_{ij}|$ is satisfied as:

$$\left|\boldsymbol{r}_{ij}\right| \le \frac{d_i + d_j}{2} \tag{2.1.5}$$

Modeling a mechanical joint as shown in **Fig. 2.1.1**, the magnitude of the interaction is decided in accordance with the overlapped amount of particles in the both normal and parallel direction between the particles and its fluctuation band. Relative displacements $\Delta\boldsymbol{x}_{ij}$ and $\Delta\boldsymbol{\xi}_{ij}$ in the global coordinate O-xyz and the local coordinate O-$\xi\eta\zeta$, respectably, are described as:

$$\Delta\boldsymbol{x}_{ij} = \left[(\boldsymbol{u}_p + \boldsymbol{\omega}_p \times \boldsymbol{r})\Delta t\right]_{i,j} \tag{2.1.6}$$

$$\Delta\boldsymbol{\xi}_{ij} = \left[\boldsymbol{T}_{GL}\right]\Delta\boldsymbol{x}_{ij} \tag{2.1.7}$$

where $\boldsymbol{r}$ is the relative coordinate vector from the centroid of the targeted particle i to its surface as $|\boldsymbol{r}| = d/2$ (d: diameter of particle), Δt is time interval, $[\boldsymbol{T}_{GL}]$ is the transformation matrix to change the global coordinate to the local coordinate. Then, $[\ ]_{i,j}$ denotes amount of relative displacement between the overlapped particle i and j. As shown in **Fig. 2.1.1**, the dynamic model is based on the so-called voight material with spring, dashpot and friction slider connected in parallel for expression of collisions of viscoelastic particles. The interaction force $\boldsymbol{F}_{pint,L}$ of particles in the local coordinate is defined as follows:

$$\boldsymbol{F}_{p\mathrm{int},L} = \underbrace{e^{pre} + k\Delta\boldsymbol{\xi}_{ij}}_{\boldsymbol{e}} + \underbrace{c\Delta\dot{\boldsymbol{\xi}}_{ij}}_{\boldsymbol{d}} \tag{2.1.8}$$

where $\boldsymbol{e}$ is the interaction force by the spring system, $\boldsymbol{d}$ is the interaction force by the dashpot system, k is the stiffness coefficient for an elastic spring, c is the damping coefficient for a buffering dashpot, subscript *pre* denotes the previous time step and the subscript L denotes the local coordinate. From Eq. (2.1.5), a negative value of e, namely tensile interaction in the normal direction is excluded by:

$$\langle e_n \rangle < 0 \quad then \quad \boldsymbol{F}_{p\mathrm{int},L} = 0 \tag{2.1.9}$$

where the subscript n denotes in the normal direction. Moreover, the slider system is introduced for a friction effect in the tangent direction as:

$$\left|\langle e_s \rangle\right| > k\langle e_n \rangle \quad then \quad \left\langle \boldsymbol{F}_{p\mathrm{int},L,s} \right\rangle = \mu \cdot Sign\left[\langle e_n \rangle,\ \langle e_s \rangle\right] \tag{2.1.10}$$

where the subscript s denotes to the tangent direction, μ is the friction coefficient, $Sign[A, B]$ represents an operation to give a sign of B to an absolute value of A, the bracket $\langle\ \rangle$ represents a component of a vector. From these, the total interaction force $\boldsymbol{F}_{pint}$ acting to the particle i in the global coordinate is written as:

$$\boldsymbol{F}_{p\mathrm{int}} = -\sum_j \left[\boldsymbol{T}_{GL}\right]^{-1} \boldsymbol{F}_{p\mathrm{int},L} \tag{2.1.11}$$

And, the total torque force $\boldsymbol{T}_{pint}$ for the targeted particle i is written as:

$$\boldsymbol{T}_{p\mathrm{int}} = -\sum_j \left[\boldsymbol{T}_{GL}\right]^{-1} \left(\boldsymbol{r}_L \times \boldsymbol{F}_{p\mathrm{int},L}\right) \tag{2.1.12}$$

Each particle is tracked by the forces $\boldsymbol{F}_{pint}$ and $\boldsymbol{T}_{pint}$ obtained from Eqs. (2.1.11) and (2.1.12) with time differential schemes, such as the Euler explicit method.

2.1.3 Tuning parameters of spring-dashpot system

Here, a widespread theory, namely the so-called Hertzian contact theory (refer to **Fig. 2.1.2**) to determine

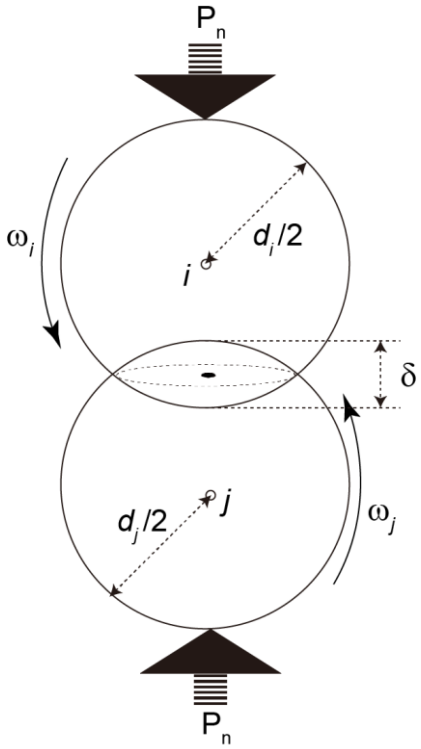

Fig. 2.1.2 Illustration of the Hertzian contact theory

the tuning parameters used in Eq. (2.1.8) for the spring-dashpot system is explained. In the Hertzian contact theory, the overlap amount δ between particle i and j has the following relation with diameters of particles, the Poisson's ratio ν, the Young's module E and the contact force P as:

$$\delta^3 = \frac{9}{2}\frac{d_i + d_j}{d_i d_j}\left(\frac{1-\nu^2}{E}\right)^2 P^2 \tag{2.1.13}$$

This equation is rewritten with a spring constant corresponding to the stiffness coefficient as:

$$P = k_n \delta^{3/2} \tag{2.1.14}$$

From this equation, the stiffness coefficient in the normal direction k_n is calculated as:

$$k_n = \frac{\sqrt{2}}{3}\frac{E}{1-\nu^2}\sqrt{\frac{d_i d_j}{d_i + d_j}} \tag{2.1.15}$$

While, in assumption of a pseudo linear relation, the overlap amount of particles and its contact force is expressed as:

$$P = k_n \delta \tag{2.1.16}$$

Similarly, the normal spring constant is written as:

$$k_n = \left\{ \frac{2}{9} \frac{d_i d_j}{d_i + d_j} \left(\frac{E}{1-\nu^2} \right)^2 \cdot P \right\}^{1/3} \tag{2.1.17}$$

Incidentally, the spring constant k corresponds to the normal interaction force e_n:

$$P = \langle e_n \rangle \tag{2.1.18}$$

The spring constant in the parallel direction k_s is constructed from the ration of the Young's module E to the shear model G as:

$$S_0 = \frac{k_s}{k_n} = \frac{G}{E} = \frac{1}{2(1+\nu)} \tag{2.1.19}$$

where s_0 is the damping rate. The damping coefficients C_n and C_s are deduced from the follow:

$$C_n = 2\sqrt{m_p k_n}\,; \qquad C_s = C_n \sqrt{S_0} \tag{2.1.20}$$

where m_p is the mass of the particle.

2.1.4 DEM-based rigid-body model

As an advantage of the DEM characterized by its superiority in comprehensive adaptability, the DEM can be easily applied to motions of non-sphere shaped rigid bodies also. By joining each particle as a structural component, the behavior of the rigid body can be tracked. This technique was proposed by Koshizuka et al. (1998) [3] as the so-called Passively Moving Solid (PMS) model and has been introduced into another particle method, such as MPS method and SPH method.

As for the numerical procedure, the motions of the structural components (particles) are firstly calculated by the standard DEM framework without the rigid connections. After that, the positions and velocities of the scattered particles are modified with the rigid connection in accordance with the state of the structure. The translational velocity vector $\boldsymbol{v}_g$ and rotational velocity vector $\boldsymbol{\omega}_g$ acting on the centroid of the structure are given as:

$$\boldsymbol{v}_g = \frac{1}{k} \sum_{i=1}^{k} \boldsymbol{v}_i \tag{2.1.21}$$

$$\boldsymbol{\omega}_g = \boldsymbol{I}_g^{-1} \sum_{i=1}^{k} (\boldsymbol{q}_i \times \boldsymbol{v}_i); \qquad \boldsymbol{q}_i = \boldsymbol{x}_i - \boldsymbol{x}_g \tag{2.1.22}$$

$$\boldsymbol{x}_g = \frac{1}{k}\sum_{i=1}^{k} \boldsymbol{x}_i \tag{2.1.23}$$

$\boldsymbol{x}_i$ is the auxiliary coordinate vector of a component (particle) i of the targeted structure, $\boldsymbol{v}_i$ is the auxiliary velocity vector of a component i, k is the number of components of the targeted structure and $\boldsymbol{I}_g$ is the inertia tensor of the structure. From these equations, the coordinate vector of the component i of the structure is updated as:

$$\boldsymbol{x}_i^t = \boldsymbol{x}_i^{t-\Delta t} + \left(\boldsymbol{v}_g + \boldsymbol{\omega}_g \times \boldsymbol{q}_i^{t-\Delta t}\right)\Delta t \tag{2.1.24}$$

This equation contains an undesirable possibility that components of different structured overlap each other as a numerical error due to a gap of the modifying magnitude of components which is decided independently within each structure. So is the relation of components in a same structure, too, due to accuracy of time differential schemes. Therefore, using the Passively Moving Solid model, prudent numerical setups with a minute time resolution is necessary. As another approach to the second issue about the gap between components of a same structure, a quaternion description based on the rotational angle is utilized with a more accurate consideration of relative positions of components.

2.2 Moving Particle Semi-implicit Method: Liquid phase model

The particle method is the fully Lagrangian Gridless method. As major particle methods for the Navier-Stokes equation, the Smoothed Particle Hydrodynamics (SPH) [4,5] method and the Moving Particle Semi-implicit (MPS) method [6] are employed in the engineering fields. The SPH method was originally developed for the astrophysics, and at present, its application has been extended to various engineering fields including the coastal engineering. The SPH method was developed by Lucy [4] and Monaghan [4,5] to compute compressible fluid flows by Lagrangian tracking with an explicit algorithm, and the SPH method has been applied to incompressible flows also by a treatment of flows as weakly-compressible flows (WSPH; Morris et al., 1997) [7]. On the other hand, the MPS method was originally proposed by Koshizuka and Oka (1996) [6] for incompressible flows with a semi-implicit algorithm. Owing to the semi-implicit algorithm with its compatibility of the Continuity equation, the MPS method reproduces suitably the volume conservation comparing with the WSPH method with rougher time resolutions. The semi-implicit framework was introduced into the SPH method also for incompressible flows as strictly-incompressible flows (ISPH; Shao and Lo, 2003) [8]. Considering the pragmatic use, the superior performance in the volume conservation and the adaptability to rough time resolutions are the remarkable advantages. In this study, the MPS method is adopted for the solid-liquid two-phase flow model. As mentioned in Chap.1, the particle method has advantages as follows: **1.** Robustness for violent deformations of interfaces, **2.** Needles of a terrible procedure for reconstruction of calculation grids, **3.** Needless of the advection term causing the numerical diffusion and a complicated discretization and **4.** Securing the ease of computational setups.

2.2.1 Governing equations

The motion of incompressible flow is described by the Continuity equation and the Navier-Stokes equation:

$$\frac{D\rho}{Dt} + \rho\nabla \cdot \boldsymbol{u} = 0 \tag{2.2.1}$$

$$\rho\frac{D\boldsymbol{u}}{Dt} = -\nabla p + \mu\nabla^2\boldsymbol{u} + \rho\boldsymbol{g} \tag{2.2.2}$$

where ρ is density, t is time, $\boldsymbol{u}$ is the velocity vector, p is pressure, $\boldsymbol{g}$ is the vector of gravity acceleration and μ is viscosity.

2.2.2 Integral interpolants and vector differential operators

In the MPS method, the incompressible continuum is expressed by the distributed particles which have the physical quantities representing the positions. Each term of the Navier-Stokes equation is approximated by kernel-based interpolants. The interpolants are expressed by modeled interactions between particles and are locally averaged in the influence area through a kernel function. In the MPS method, the following kernel function w is commonly used as:

$$w\left(\left|\boldsymbol{r}_{ij}\right|\right) = \begin{cases} \dfrac{r_e}{\left|\boldsymbol{r}_{ij}\right|} - 1 & if \quad \left|\boldsymbol{r}_{ij}\right| < r_e \\ 0 & if \quad r_e \le \left|\boldsymbol{r}_{ij}\right| \end{cases} \tag{2.2.3}$$

where the subscript i denotes the targeted particle, the subscript j is the neighboring particle, r_e is the radius of influence and $\boldsymbol{r}_{ij}$ is the relative coordinate vector as $\boldsymbol{r}_{ij} = \boldsymbol{r}_j - \boldsymbol{r}_i$ ($\boldsymbol{r}_i$, $\boldsymbol{r}_j$: the coordinate vector of particle i and neighboring particle j). From Eq. (2.2.3), the amount of the averaging weight is set as zero for particles outside the influence area, and as a result, the targeted neighboring particles are limited in a finite area. The illustration of the concept is shown in **Fig. 2.2.1**. The statistical volume of particle i representing its position is denoted by the so-called particle number density n_i defined as:

$$n_i = \sum_{j \neq i} w\left(\left|\boldsymbol{r}_{ij}\right|\right) \tag{2.2.4}$$

The kernel function is utilized for all the differentiation operators. The first order approximation of a gradient between particles i and j as shown in **Fig. 2.2.2** is written as:

$$\nabla\phi_{ij} = \frac{\phi_j - \phi_i}{\left|\boldsymbol{r}_{ij}\right|^2}\boldsymbol{r}_{ij} \tag{2.2.5}$$

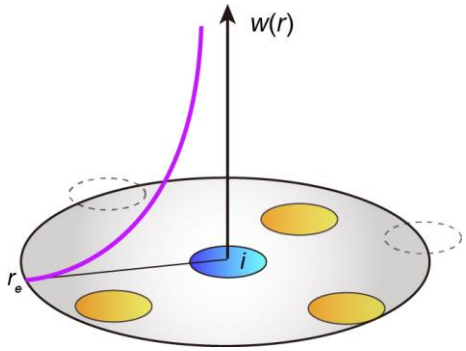

Fig. 2.2.1 Illustration of the traditional kernel function

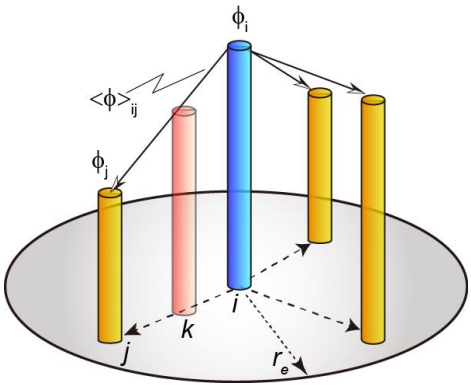

Fig. 2.2.2 Illustration of the gradient operation by weighted averaging

where ϕ is a physical quantity. The gradient quantity of the targeted particle i is expressed by summation of the gradients with all the neighboring particles by a locally weighted averaging as:

$$\nabla\phi\big|_i = \frac{D_s}{n_0}\sum_{j\neq i}\frac{\phi_j-\phi_i}{\left|\boldsymbol{r}_{ij}\right|^2}\boldsymbol{r}_{ij}w\left(\left|\boldsymbol{r}_{ij}\right|\right) \tag{2.2.6}$$

where D_s is the number of spatial dimension and n_0 is the reference particle number density corresponding to the initial particle number density with a regular distribution of neighboring particles. The gradient by Eq. (2.2.5) denotes only a simple one-dimensional gradient along the direction between particles, and then, D_s adjusts the effect of the space dimensionality. As for the reference particle number density n_0 in Eq. (2.2.6), which was originally given by n_i as a summation of kernel function, it is on the assumption that the summation of the kernel function is constantly equal to the reference of that due to the property of incompressible flows.

The gradient model is modified in the pressure gradient term to ensure the numerical stability by deforming the gradient force as a repulsive interaction [9]:

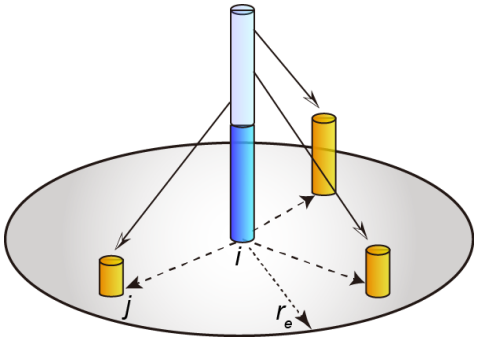

Fig. 2.2.3 Illustration of the Laplacian operation by weighted averaging

$$\langle \nabla p \rangle_i = \frac{D}{n_0} \sum_{j \neq i} \left[\frac{p_j - \hat{p}_i}{|\boldsymbol{r}_{ij}|^2} \boldsymbol{r}_{ij} w(|\boldsymbol{r}_{ij}|) \right] \tag{2.2.7}$$

$$\hat{p}_i = \min_{j \in J} (p_i, p_j), \quad J = \{ j : w(|\boldsymbol{r}_{ij}|) \neq 0 \} \tag{2.2.8}$$

where, $\hat{p}$ is the minimum pressure in the influence area. In the standard gradient model on the basis of purely repulsive force, the repulsive interaction increases infinitely as the particle gets close to the neighboring particle due to the traditional kernel function described in Eq. (2.2.3), so that particles are prevented from overlapping each other effectively. As a result of this, the distribution of particles is kept regular and it brings about a tenacious numerical stability.

While, the divergence is expressed as:

$$\nabla \cdot \boldsymbol{\phi}|_i = \frac{D_s}{n_0} \sum_{j \neq i} \frac{(\boldsymbol{\phi}_j - \boldsymbol{\phi}_i) \cdot \boldsymbol{r}_{ij}}{|\boldsymbol{r}_{ij}|^2} w(|\boldsymbol{r}_{ij}|) \tag{2.2.9}$$

where $\boldsymbol{\phi}$ is a vector of a physical quantity.

As for the Laplacian shown in **Fig. 2.2.3**, it is deduced from the following Taylor series expansion with second order derivative as:

$$r_{ij}^2 \frac{\partial^2 \phi_{ij}}{\partial r_{ij}^2} = 2\varphi_{ij} - 2r_{ij} \frac{\partial \phi_{ij}}{\partial r_{ij}}; \qquad \phi_{ij} = \phi_j - \phi_i, \quad r_{ij} = |r_j - r_i| \tag{2.2.10}$$

Using this, the Laplacian between particles is obtained as:

$$\nabla^2 \phi_{ij} = \frac{1}{r_{ij}^2} \frac{\partial}{\partial r_{ij}} \left(r_{ij}^2 \frac{\partial \phi_{ij}}{\partial r_{ij}} \right) = \frac{2\phi_{ij}}{r_{ij}^2} \tag{2.2.11}$$

The Laplacian at the targeted particle *i* is obtained by summation of each Laplacian with neighboring

particle *j* and a local weighted averaging as:

$$\nabla^2 \phi\Big|_i = \frac{2D_s}{n_0} \sum_{j \neq i} \frac{\left(\phi_j - \phi_i\right)}{\left|\boldsymbol{r}_{ij}\right|^2} w\left(\left|\boldsymbol{r}_{ij}\right|\right) \tag{2.2.12}$$

Here, this equation is modified for consistency with analysis solution from the viewpoint of the increase of variance as:

$$\nabla^2 \phi\Big|_i = \frac{2D_s}{n_0 \lambda} \sum_{j \neq i} \left\{\left(\phi_j - \phi_i\right) w\left(\left|\boldsymbol{r}_{ij}\right|\right)\right\} \tag{2.2.13}$$

$$\lambda = \frac{\sum_{j \neq i} \left\{w\left(\left|\boldsymbol{r}_{ij}\right|\right) \left|\boldsymbol{r}_{ij}\right|^2\right\}}{\sum_{j \neq i} w\left(\left|\boldsymbol{r}_{ij}\right|\right)} \tag{2.2.14}$$

where λ is the variant to equate the increase of variance obtained from discrete calculation points (particles) with the theoretical solution.

2.2.3 Solution process (semi-implicit algorithm)

The MPS method is based on semi-implicit method same as SMAC (Simplified MAC) method, and it applies a Helmholtz-Hodge decomposition to the vector field. The physical variants are estimated by a numerical procedure separating the algorithm into two stages in accordance with the projection scheme as shown in **Fig. 2.2.4**. The velocity vector $\boldsymbol{u}$ and the coordinate vector $\boldsymbol{r}$ at time step k+1 is estimated by two incremental positions and velocities of pseudo time step k+1/2, namely the projection variants in the first stage corresponding to the explicit method and the correction variants in the second stage corresponding to the implicit method as:

$$\boldsymbol{u}_k^* = \boldsymbol{u}_k + \Delta \boldsymbol{u}_k^*, \qquad \boldsymbol{u}_{k+1} = \boldsymbol{u}_k^* + \Delta \boldsymbol{u}_k^{**} \tag{2.2.15}$$

$$\boldsymbol{r}_k^* = \boldsymbol{r}_k + \boldsymbol{u}_k \Delta t + \Delta \boldsymbol{u}_k^* \Delta t, \qquad \boldsymbol{r}_{k+1} = \boldsymbol{r}_k^* + \Delta \boldsymbol{u}^{**} \Delta t \tag{2.2.16}$$

where the subscript ***** denotes the projection variants by the first stage and the subscript ** denotes the correction variants by the second stage. As for the advection term, the particles including their physical quantities are tracked by Lagrangian observation, therefore, the MPS method does not require the advection term causing a numerical diffusion.

Here, the detail of procedures on each calculation stage of the projection scheme is explained.

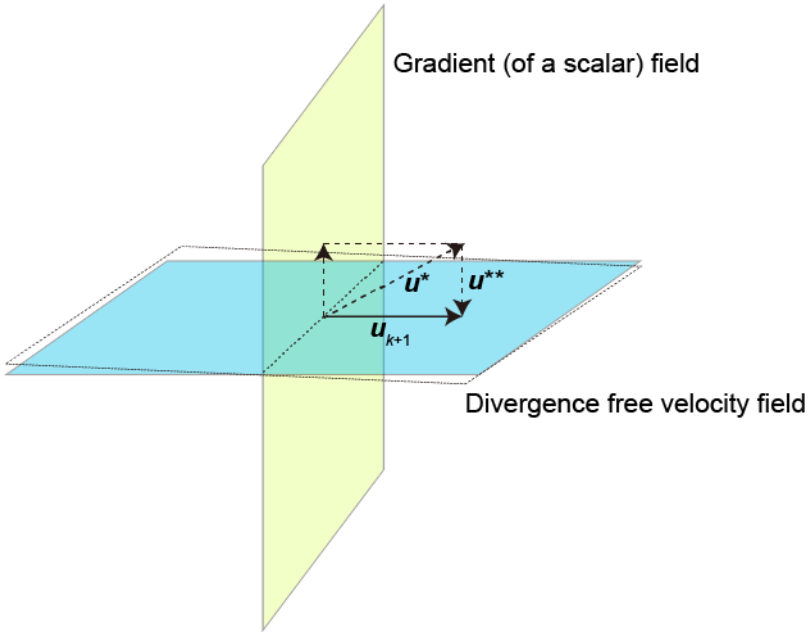

Fig. 2.2.4 Basic concept for derivation of Poisson Pressure Equation in MPS method (Helmholtz-Hodge decomposition)

2.2.3.1 First stage

In the first stage of the projection scheme, the projection velocity vector $\boldsymbol{u}^*$ is explicitly calculated by the external force $\boldsymbol{F}$ and the viscosity term as:

$$\Delta \boldsymbol{u}_k^* = \left(\boldsymbol{F}_k + \nu \nabla^2 \boldsymbol{u}_k \right) \Delta t \tag{2.2.17}$$

where ν is the laminar kinematic viscosity. In the process of numerical discretization, the viscosity term is estimated by the Laplacian model corresponding to Eq. (2.2.13) accommodating a locally weighted averaging value at a centroid of each particle.

2.2.3.2 Second stage

In the first stage of the projection scheme, the mass conservation is not guaranteed. In the second stage, the Continuity equation is introduced into the estimation process of pressure, which is excluded in the first stage. The increment of correction velocity is obtained from the pressure gradient as:

$$\Delta \boldsymbol{u}_k^{**} = -\frac{\nabla p_{k+1}}{\rho} \Delta t \tag{2.2.18}$$

The pressure is derived from the Poisson Pressure Equation given by the Continuity equation. Here, It is assumed that the correction velocities and positions of particles in the second stage satisfy the Continuity equation. Then, on the assumption that the density ρ_i can be approximated to the reference density ρ_0, the Continuity equation to be satisfied in the second stage is rewritten as;

$$\frac{\Delta\rho_{i,k}^{**}}{\Delta t} + \rho_0 \nabla \cdot \Delta \boldsymbol{u}_{i,k}^{**} = 0 \tag{2.2.19}$$

In the MPS method, since the particles represent the physical quantities including their mass and density at their positions, the incompressible condition is satisfied only by keeping the number of particles invariable with a constant particle number density. Therefore, the particle number density must be constant as:

$$n_{i,k}^{*} + \Delta n_{i,k}^{**} = n_0 \left(= n_{i,k+1}\right) \tag{2.2.20}$$

Considering the relation between the particle number density and the density, which are similarly indexes of the incompressible state, here, it is assumed that the particle number density is in proportion to the density. Replacing the density ρ by the particle number density n, the Poisson Pressure Equation is obtained from Eqs. (2.2.18), (2.2.19) and (2.2.20) as:

$$\nabla^2 p_{i,k+1} = -\frac{\rho_0}{\left(\Delta t\right)^2} \frac{n_{i,k}^{*} - n_0}{n_0} \tag{2.2.21}$$

In the numerical discretization procedure, the Laplacian in Eq. (2.2.21) is calculated by using the Laplacian model corresponding to Eq. (2.2.13). After obtaining the pressure p_{k+1} at time step k+1 by Eq. (2.2.21), the increment of correction velocity $\Delta \boldsymbol{u}_k^{**}$ in the second stage is obtained by the pressure gradient corresponding to Eq. (2.2.7).

As a final procedure, the velocity vector $\boldsymbol{u}$ and the coordinate vector $\boldsymbol{x}$ is updated for the next time step k+1 as $\boldsymbol{u}_{k+1}$ and $\boldsymbol{x}_{k+1}$ by using the increments of velocities of each stage ($\Delta \boldsymbol{u}_k^{*}$ and $\Delta \boldsymbol{u}_k^{**}$) as Eqs. (2.2.15) and (2.2.16).

2.2.4 Boundary condition

2.2.4.1 Wall boundary

The Solid boundary for walls or other rigid objects are represented by boundary particles that are forcedly given the proper physical quantities, i.e. zero velocity for the fixed wall. As for the fixed-wall particles at the edge of the calculation domain, such particles would be defined as free surface due to their small particle number densities and given zero pressure forcedly. To avoid this inconsistency, the dummy particles are set behind the wall particles to gain their particle number densities of the boundary particles. The dummy particles are not built into the matrix of the Poisson Pressure Equation and do not have any interaction force with non-dummy particles, but are built into the process for estimation of the particle number density of the non-dummy particles.

2.2.4.2 Free-surface boundary

The free-surface boundary is given to a particle whose particle number density is smaller than reference of that. The definition of free surface is given with a critical constant β as:

$$n_i < \beta n_0 \tag{2.2.22}$$

β is chosen below 1.0 and usually taken 0.97 in the MPS method. The appropriate value of the constant depends on the kernel function. In the Poisson Pressure Equation (PPE), the fee-surface particle is given zero pressure by being excluded from the matrix of the PPE with zero values for the source term and Laplacian of pressure. While, all the non-free-surface particles are built into the matrix and given a coefficient of Laplacian of pressure including that of the free-surface particles also. As for the pressure gradient, zero pressure by the free-surface particle is also given to its neighboring particle around free surface.

The free-surface line is drawn by the free-surface particles defined as Eq. (2.2.22) based on the weighted averaging, therefore, the free surface is seized fuzzily in the influence circle. In particular, the free-surface particle is given zero pressure, and thus, is allowed to overlap other free-surface particles due to the non-interaction force between them in the pressure gradient term. Accordingly, a slight shape of free surface, such as a sloshing flow is difficult to be captured and defined accurately. To resolve this problem, Khayyer et al. [10] proposed a simple and effective criterion for a more accurate assessment of the free surface. Considering the state of free surface, the degree of irregularity of the distribution of neighboring particles around the targeted particle is defined as:

$$\left|\sum_{j\neq i} x_{ij}\right| > \alpha \quad or \quad \left|\sum_{j\neq i} y_{ij}\right| > \alpha; \qquad \alpha = d_0 \tag{2.2.23}$$

This equation is applied together with Eq. (2.2.22). Other accurate scheme of assessment of free surface in the particle method have been proposed by Lee et.al [11] and Ma and Zhou [12].

2.3 Accurate particle method

Despite the fact that the particle methods have an advantage of being free from the numerical diffusion by the advection term, they still involve unphysical behaviors of particles as a significant numerical error mainly associated with unphysical perturbations of pressure. The main cause of this problem is brought by the inaccurate estimation of differential operators. Such a numerical perturbation frequently brings about not only inaccuracy but also numerical instability, and thus, the robustness of the particle methods as one of superior points to Grid-based model is no longer ensured. For the reason of this, this problem is studied widely as a general and most significant issue. In recent years, multitudinous schemes to resolve this problem are developed, and as a result, such perturbation has been suppressed effectively with numerical stability and accuracy. In this section, the existing accurate particle methods are presented.

2.3.1 Overview

The approaches of the accurate particle methods are varied depending on the solutions, such as the momentum conservation, selection of a kernel function, corrected definition of density, re-distribution of particles, the enhancement of gradient operators, interpolation of calculation points, etc. Here, the so-far accurate particle methods including the SPH method are overviewed by classifying them into several concepts.

Here, the accurate particle methods accommodating the projection-based particle method, namely the MPS method are explained for introduction of the DEM-MPS framework.

2.3.1.1 CMPS method (Corrected MPS)

The CMPS method is developed by Khayyer and Gotoh (2008) [13] for enhancement of numerical stability in the pressure gradient term in consideration of mass conservation.

In the standard MPS pressure gradient model, the interaction is on the basis of purely repulsive force to prevent particle from overlapping each other. The gradient force working on the targeted particle *i* from the neighboring partice *j* is calculated by the following formula:

$$\boldsymbol{A}_{j\to i}^{p} = -\frac{mD}{\rho n_0}\frac{p_j - \hat{p}_i}{\left|\boldsymbol{r}_{ij}\right|^2}\left(\boldsymbol{r}_{ij}\right)w\left(\left|\boldsymbol{r}_{ij}\right|\right) \tag{2.3.1}$$

where *m* is the mass of particle. However, the gradient force acting on the particle *j* from particle *i* is estimated as:

$$\boldsymbol{A}_{i\to j}^{p} = -\frac{mD}{\rho n_0}\frac{p_i - \hat{p}_j}{\left|\boldsymbol{r}_{ji}\right|^2}\boldsymbol{r}_{ij}^{*}w\left(\left|\boldsymbol{r}_{ji}\right|\right) \tag{2.3.2}$$

Therefore, the following relation:

$$\boldsymbol{A}_{j\to i}^{p} \neq -\boldsymbol{A}_{i\to j}^{p} \tag{2.3.3}$$

is obtained, and result in failure of anti-symmetric interactions between particles. Consequently, the momentum conservation is not guaranteed, and this drawback possibly brings about the pressure perturbation as particles get close to each other.

The CMPS method sets an imaginary point at the center of particles *i* and *j* as a new calculation point for estimation of the pressure gradient between the particles. Moreover, it replaces the minimum pressures $\hat{p}_i$ and $\hat{p}_j$ by those average $\left(\hat{p}_i + \hat{p}_j\right)/2$ to fulfill a symmetric interaction. Here, the gradient model is modified as:

$$\langle \nabla p \rangle_i = \frac{D}{n_0} \sum_{j \neq i} \frac{p_i + p_j - \left(\hat{p}_i + \hat{p}_j \right)}{\left| \boldsymbol{r}_{ij}^* \right|^2} \boldsymbol{r}_{ij}^* w\left(\left| \boldsymbol{r}_{ij}^* \right| \right) \tag{2.3.4}$$

As a similar approach, the CMPS-based gradient term can be rewritten without the minimum pressures $\hat{p}_i$ and $\hat{p}_j$ as:

$$\langle \nabla p \rangle_i = \frac{D}{n_0} \sum_{j \neq i} \frac{p_i + p_j}{\left| \boldsymbol{r}_{ij}^* \right|^2} \boldsymbol{r}_{ij}^* w\left(\left| \boldsymbol{r}_{ij}^* \right| \right) \tag{2.3.5}$$

Considering the original gradient term, this equation can be rewritten as:

$$\langle \nabla p \rangle_i = \frac{D}{n_0} \left\{ \sum_{j \neq i} \frac{p_j - p_i}{\left| \boldsymbol{r}_{ij}^* \right|^2} \boldsymbol{r}_{ij}^* w\left(\left| \boldsymbol{r}_{ij}^* \right| \right) + \sum_{j \neq i} \frac{2 p_i}{\left| \boldsymbol{r}_{ij}^* \right|^2} \boldsymbol{r}_{ij}^* w\left(\left| \boldsymbol{r}_{ij}^* \right| \right) \right\} \tag{2.3.6}$$

The first term of the right hand side corresponds to the original gradient term and the second term corresponds to the artificial repulsive force term. It is obvious that the second term utilizes a particular variant p_i and the magnitude of the total stabilizing force working on the particle i depends on the distribution of neighboring particles. If the neighboring particles are distributed with a perfectly regular arrangement, no stabilizing force works due to offset of each interaction. While, the stabilizing force enlarges under irregular distributions of particles particularly around the free surface due to the lack of neighboring particles. However, such a particle with an excessive irregular distribution of neighboring particles is given a free-surface condition with zero pressure, and thus, its excessive stabilizing force causing crucial inconsistency with the original gradient is cancelled automatically.

2.3.1.2 MPS-HS method (High-order Souce term)

The MPS-HS method is developed by Khayyer and Gotoh (2009) [14] for accurate estimation of time derivative of the particle number density corresponding to the source term of the Poisson Pressure Equation. In the standard framework, the Continuity equation is written with replacement of the density by the particle number density as:

$$\frac{1}{n_0} \frac{Dn}{Dt} + \nabla \cdot \left(\Delta \boldsymbol{u}_k^{**} \right) = 0 \tag{2.3.7}$$

Here, the first term of the left hand side is usually calculated as:

$$\frac{Dn}{Dt} = \frac{n_0 - n_k^*}{\Delta t} \tag{2.3.8}$$

However, the Poisson Pressure Equation is calculated through a solution process of a matrix, and as a result, some extent errors of convergence may occur. In particular, Eq. (2.3.8) is based on a linear relation of the

particle number density, such errors are apt to be accumulated and bring about pressure perturbation.

For the problem, the CMPS-HS gives a more accurate time derivative of the particle number density as:

$$\frac{Dn}{Dt} = \sum_{j \neq i} \frac{Dw\left(\left|\boldsymbol{r}_{ij}\right|\right)}{Dt} \tag{2.3.9}$$

Using the MPS traditional kernel function, Eq. (2.3.9) is calculated as:

$$\begin{aligned} \frac{Dw\left(\left|\boldsymbol{r}_{ij}\right|\right)}{Dt} &= \frac{Dw_{ij}}{Dt} = \frac{\partial w_{ij}}{\partial \boldsymbol{r}_{ij}} \frac{\partial \boldsymbol{r}_{ij}}{\partial x_{ij}} \frac{dx_{ij}}{dt} + \frac{\partial w_{ij}}{\partial \boldsymbol{r}_{ij}} \frac{\partial \boldsymbol{r}_{ij}}{\partial y_{ij}} \frac{dy_{ij}}{dt} \\ &= -\frac{r_e}{\left|\boldsymbol{r}_{ij}\right|^2} \frac{x_{ij}}{\left|\boldsymbol{r}_{ij}\right|} u_{ij} - \frac{r_e}{\left|\boldsymbol{r}_{ij}\right|^2} \frac{y_{ij}}{\left|\boldsymbol{r}_{ij}\right|} v_{ij} = -\frac{r_e}{\left|\boldsymbol{r}_{ij}\right|^3} \left(x_{ij} u_{ij} + y_{ij} v_{ij}\right) \end{aligned} \tag{2.3.10}$$

where (x_{ij}, y_{ij}) is the relative position of particle i from particle j and (u_{ij}, v_{ij}) is the relative velocity of particle i from particle j. Substituting Eq. (2.3.10) for Eq. (2.2.7), the follow formula:

$$\left\langle \nabla^2 p_{k+1} \right\rangle_i = -\frac{\rho}{n_0 \Delta t} \sum_{j \neq i} \frac{r_e}{\left|\boldsymbol{r}_{ij,k}\right|^3} \left(x^*_{ij,k} u^*_{ij,k} + y^*_{ij,k} v^*_{ij,k}\right) \tag{2.3.11}$$

is obtained. A more accurate handling of the source term of the Poisson Pressure Equation is achieved by this scheme.

2.3.1.3 MPS-HL method (High-order Laplacian)

The MPS-HL method [15] is developed to enhance the accuracy of estimation of Laplacian of pressure in the Poisson Pressure Equation. The Laplacian of a variant of the targeted particle i is deduced from the divergence of its gradient value as:

$$\left\langle \nabla^2 \phi \right\rangle_i = \nabla \cdot \left\langle \nabla \phi \right\rangle_i \tag{2.3.12}$$

Here, referring a definition of the SPH gradient term by Monaghan (1992), the gradient is rewritten as:

$$\begin{aligned} \left\langle \nabla \phi \right\rangle_i &= \frac{1}{\sum_{j \neq i} w_{ij}} \sum_{j \neq i} \left(\phi_j - \phi_i\right) \nabla w_{ij} \\ &= \frac{1}{\sum_{j \neq i} w_{ij}} \sum_{j \neq i} \phi_{ij} \nabla w_{ij}; \quad \phi_{ij} = \phi_j - \phi_i \end{aligned} \tag{2.3.13}$$

Considering the incompressible property, here, it is assumed that the total amount of the averaging weight by the neighboring particle j is invariably equal to the reference particle number density n_0. From Eqs.

(2.3.12) and (2.3.13), the Laplacian at particle *i* is obtained as:

$$\nabla \cdot \langle \nabla \phi \rangle_i = -\frac{1}{n_0} \sum_{j \neq i} \left(\nabla \phi_{ij} \cdot \nabla w_{ij} + \phi_{ij} \nabla^2 w_{ij} \right); \qquad n_0 = (n_i)_0 = \left(\sum_{j \neq i} w_{ij} \right)_0 \tag{2.3.14}$$

The second term in the right hand side of this equation corresponds to a gradient of a relative physical quantity. This term is ignored by the standard Laplacian model, accordingly, the consistency in the Poisson Pressure Equation is not guaranteed with numerical errors.

By the HL scheme, the two-dimensional gradients of relative physical quantity φ_{ij} and kernel function w_{ij} is as follows is written as follows:

$$\nabla \phi_{ij} = \frac{\partial \phi_{ij}}{\partial r_{ij}} \frac{\partial r_{ij}}{\partial x_{ij}} \boldsymbol{i} + \frac{\partial \phi_{ij}}{\partial r_{ij}} \frac{\partial r_{ij}}{\partial y_{ij}} \boldsymbol{j} \tag{2.3.15}$$

$$\nabla w_{ij} = \frac{\partial w_{ij}}{\partial r_{ij}} \frac{\partial r_{ij}}{\partial x_{ij}} \boldsymbol{i} + \frac{\partial w_{ij}}{\partial r_{ij}} \frac{\partial r_{ij}}{\partial y_{ij}} \boldsymbol{j} \tag{2.3.16}$$

Using these equations, the following equation is obtained as:

$$\begin{aligned} \nabla \phi_{ij} \cdot \nabla w_{ij} &= \frac{\partial \phi_{ij}}{\partial r_{ij}} \frac{\partial r_{ij}}{\partial x_{ij}} \frac{\partial w_{ij}}{\partial r_{ij}} \frac{\partial r_{ij}}{\partial x_{ij}} + \frac{\partial \phi_{ij}}{\partial r_{ij}} \frac{\partial r_{ij}}{\partial y_{ij}} \frac{\partial w_{ij}}{\partial r_{ij}} \frac{\partial r_{ij}}{\partial y_{ij}} = \frac{\partial \phi_{ij}}{\partial r_{ij}} \frac{\partial w_{ij}}{\partial r_{ij}} \frac{x_{ij}^2}{r_{ij}^2} + \frac{\partial \phi_{ij}}{\partial r_{ij}} \frac{\partial w_{ij}}{\partial r_{ij}} \frac{y_{ij}^2}{r_{ij}^2} \\ &= \frac{\partial \phi_{ij}}{\partial r_{ij}} \frac{\partial w_{ij}}{\partial r_{ij}} \left(\frac{x_{ij}^2}{r_{ij}^2} + \frac{y_{ij}^2}{r_{ij}^2} \right) = \frac{\partial \phi_{ij}}{\partial r_{ij}} \frac{\partial w_{ij}}{\partial r_{ij}} = \frac{\phi_{ji} - \phi_{ij}}{r_{ij}} \frac{\partial w_{ij}}{\partial r_{ij}} \\ &= \frac{2\phi_{ji}}{\partial r_{ij}} \frac{\partial w_{ij}}{\partial r_{ij}} \end{aligned} \tag{2.3.17}$$

While, the Laplacian of the kernel function is:

$$\begin{aligned} \nabla^2 w_{ij} &= \nabla \cdot \nabla w_{ij} = \frac{\partial}{\partial x_{ij}} \left(\frac{\partial w_{ij}}{\partial r_{ij}} \frac{\partial r_{ij}}{\partial x_{ij}} \right) + \frac{\partial}{\partial y_{ij}} \left(\frac{\partial w_{ij}}{\partial r_{ij}} \frac{\partial r_{ij}}{\partial y_{ij}} \right) \\ &= \frac{\partial^2 w_{ij}}{\partial r_{ij}^2} \left(\frac{\partial r_{ij}}{\partial x_{ij}} \right)^2 + \frac{\partial w_{ij}}{\partial r_{ij}} \frac{\partial^2 r_{ij}}{\partial x_{ij}^2} + \frac{\partial^2 w_{ij}}{\partial r_{ij}^2} \left(\frac{\partial r_{ij}}{\partial y_{ij}} \right)^2 + \frac{\partial w_{ij}}{\partial r_{ij}} \frac{\partial^2 r_{ij}}{\partial y_{ij}^2} \\ &= \frac{\partial^2 w_{ij}}{\partial r_{ij}^2} \left(\frac{x_{ij}^2}{r_{ij}^2} + \frac{y_{ij}^2}{r_{ij}^2} \right) + \left(\frac{2}{r_{ij}} \frac{\partial w_{ij}}{\partial r_{ij}} - \frac{1}{r_{ij}} \frac{\partial w_{ij}}{\partial r_{ij}} \right) \end{aligned} \tag{2.3.18}$$

In Eq. (2.3.18), the following equation is applied with:

$$\frac{\partial^2 r_{ij}}{\partial x_{ij}^2} = \frac{\partial}{\partial x_{ij}}\left(\frac{\partial r_{ij}}{\partial x_{ij}}\right) = \frac{\partial}{\partial x_{ij}}\left(\frac{x_{ij}}{r_{ij}}\right) = \frac{1}{r_{ij}} - \frac{x_{ij}^2}{r_{ij}^3} \tag{2.3.19}$$

From Eqs. (2.3.14), (2.3.17) and (2.3.18):

$$\begin{aligned}\nabla \cdot \langle \nabla \phi \rangle_i &= \frac{1}{n_0}\sum_{j \neq i}\left(\frac{2\phi_{ij}}{r_{ij}}\frac{\partial w_{ij}}{\partial r_{ij}} + \phi_{ij}\frac{\partial^2 w_{ij}}{\partial r_{ij}^2} + \frac{\phi_{ij}}{r_{ij}}\frac{\partial w_{ij}}{\partial r_{ij}}\right) \\ &= \frac{1}{n_0}\sum_{j \neq i}\left(\phi_{ij}\frac{\partial^2 w_{ij}}{\partial r_{ij}^2} - \frac{\phi_{ij}}{r_{ij}}\frac{\partial w_{ij}}{\partial r_{ij}}\right)\end{aligned} \tag{2.3.20}$$

is obtained. Moreover, applying the MPS traditional kernel function to this equation, the high order Laplacian is obtained as:

$$\nabla \cdot \langle \nabla \phi \rangle_i = \frac{1}{n_0}\sum_{j \neq i}\left(\frac{3\phi_{ij} r_e}{r_{ij}^3}\right) \tag{2.3.21}$$

2.3.1.4 MPS-ECS method (Error-Compensating Source)

For suppression of pressure perturbation, it is significant to attenuate the time fluctuation of the particle number density in the correction process of the second stage of the projection scheme. That is, the accuracy depends on the accuracy of estimation of the Source term in the Poisson Pressure Equation. By introduction of the "Error-Compensating terms in the Source term", abbreviated as ECS, into the Source term of the Poisson Pressure Equation, an error of the mass conservation is modified from the viewpoints of both instant and accumulative fluctuation of the particle number density. The Poisson Pressure Equation with ECS is written as:

$$\begin{aligned}\frac{\Delta t}{\rho}\left(\nabla^2 p_{k+1}\right)_i &= \frac{1}{n_0}\left(\frac{Dn}{Dt}\right)_i^* + ECS \\ &= \frac{1}{n_0}\left(\frac{Dn}{Dt}\right)_i^* + func\left[\frac{1}{n_0}\left(\frac{Dn}{Dt}\right)_i^k, \frac{1}{\Delta t}\frac{n^k - n_0}{n_0}\right]\end{aligned} \tag{2.3.22}$$

The first parameter of ECS is a time derivative of the particle number density at time step *k* corresponding to the instant fluctuation. On the other hand, the second parameter is a deviation of the particle number density to that of reference at time step *k* corresponding to the accumulated fluctuation. Kondo・Koshizuka (2010) [16] proposed the following ECS definition as:

$$ECS = \alpha\left[\frac{1}{n_0}\frac{n^k - n^{k-1}}{\Delta t}\right] + \beta\left[\frac{1}{\Delta t}\frac{n^k - n_0}{n_0}\right] \tag{2.3.23}$$

However, constants α and β are chosen on the assumption of a static state with a semi-empirical way, the recommended values is not decided comprehensibility. In addition, the time derivative of the particle number density is based on the first order accuracy, and thus, its application to highly violent flows is difficult due to the error. Khayyer and Gotoh (2011) [17] proposed a comprehensive definition of the parameters α and β accommodating the instant state of the particle number density as:

$$ECS = \alpha\left[\frac{1}{n_0}\left(\frac{Dn}{Dt}\right)_i^k\right] + \beta\left[\frac{1}{\Delta t}\frac{n^k - n_0}{n_0}\right];$$
$$\alpha = \left|\frac{n^k - n_0}{n_0}\right|, \qquad \beta = \left|\frac{\Delta t}{n_0}\left(\frac{Dn}{Dt}\right)_i^k\right| \tag{2.3.24}$$

Categorizing the instant states of the particle number density, the equation can be rewritten as:

$$\frac{\Delta t}{\rho}\left(\nabla^2 p_{k+1}\right)_i = \begin{cases} \frac{1}{n_0}\left(\frac{Dn}{Dt}\right)_i^* \pm \frac{n^k - n_0}{n_0}\left[\frac{2}{n_0}\left(\frac{Dn}{Dt}\right)_i^k\right] & if \quad \left(\frac{Dn}{Dt}\right)_i^k \cdot \frac{n^k - n_0}{n_0} > 0 \\ \frac{1}{n_0}\left(\frac{Dn}{Dt}\right)_i^* & if \quad \left(\frac{Dn}{Dt}\right)_i^k \cdot \frac{n^k - n_0}{n_0} < 0 \end{cases} \tag{2.3.25}$$

The equations contain two indexes accommodating each state of the particle number density, namely the instant and accumulative fluctuations. When both sign of indexes correspond to each other, ECS works. On the other hand, when both sign of indexes are different from each other, ECS equalizes zero and does not work. In either, the Source term is modified to make the particle number density approach the reference of that.

2.3.1.5 MPS-GC method (Gradient Correction)

The MPS gradient model is usually based on purely repulsive force to keep a regular distribution of particles. However, it cannot handle negative pressures, namely the tensile interaction, and thus, cannot reproduce the physical state of the real phenomenon. Khayyer and Gotoh (2011) [17] proposed the Gradient Correction abbreviated as GC for accurate estimation of the gradient term in accordance with the Taylor series expansion. In the Taylor series expansion in 2D dimension, the relation between particles *i* and *j* is written as:

$$p_j = p_i + \left(\frac{\partial p}{\partial x}\right)_i x_{ij} + \left(\frac{\partial p}{\partial y}\right)_i y_{ij} + O\left(h^2\right) \tag{2.3.26}$$

Multiplying both hand sides by $\int \frac{w_{ij}}{r_{ij}}\frac{\boldsymbol{r}_{ij}}{r_{ij}} d\boldsymbol{r}$ as:

$$\int p_j\left(\frac{w_{ij}}{r_{ij}}\frac{x_{ij}}{r_{ij}}dx+\frac{w_{ij}}{r_{ij}}\frac{y_{ij}}{r_{ij}}dy\right)=p_i\int\left(\frac{w_{ij}}{r_{ij}}\frac{x_{ij}}{r_{ij}}dx+\frac{w_{ij}}{r_{ij}}\frac{y_{ij}}{r_{ij}}dy\right)+\left(\frac{\partial p}{\partial x}\right)_i\int x_{ij}\left(\frac{w_{ij}}{r_{ij}}\frac{x_{ij}}{r_{ij}}dx+x_{ij}\frac{w_{ij}}{r_{ij}}\frac{y_{ij}}{r_{ij}}dy\right)$$
$$+\left(\frac{\partial p}{\partial y}\right)_i\int\left(y_{ij}\frac{w_{ij}}{r_{ij}}\frac{x_{ij}}{r_{ij}}dx+y_{ij}\frac{w_{ij}}{r_{ij}}\frac{y_{ij}}{r_{ij}}dy\right)+O\left(h^2\right) \tag{2.3.27}$$

The kernel gradient is written as:

$$\nabla w=\frac{\partial w}{\partial r}\frac{\partial r}{\partial x}\boldsymbol{i}+\frac{\partial w}{\partial r}\frac{\partial r}{\partial y}\boldsymbol{j}\equiv\frac{w_{ij}}{r_{ij}}\frac{x_{ij}}{r_{ij}}\boldsymbol{i}+\frac{w_{ij}}{r_{ij}}\frac{y_{ij}}{r_{ij}}\boldsymbol{j} \tag{2.3.28}$$

Using this form for the gradient model as Eq. (2.3.13), the following equation is given from Eqs. (2.3.27) and (2.3.28) as:

$$\int(p_j-p_i)\left(\frac{w_{ij}}{r_{ij}}\frac{x_{ij}}{r_{ij}}dx+\frac{w_{ij}}{r_{ij}}\frac{y_{ij}}{r_{ij}}dy\right)=\langle\nabla p\rangle_i=\left(\frac{\partial p}{\partial x}\right)_i\int\left(\frac{w_{ij}}{r_{ij}}\frac{x_{ij}}{r_{ij}}dx+\frac{w_{ij}}{r_{ij}}\frac{y_{ij}}{r_{ij}}dy\right)$$
$$+\left(\frac{\partial p}{\partial y}\right)_i\int\left(\frac{w_{ij}}{r_{ij}}\frac{x_{ij}}{r_{ij}}dx+\frac{w_{ij}}{r_{ij}}\frac{y_{ij}}{r_{ij}}dy\right)+O\left(h^2\right) \tag{2.3.29}$$

In consultation with the SPH-based accurate approximation, the following relations should be ensured for linear fields as:

$$\int x_{ij}\frac{w_{ij}}{r_{ij}}\frac{x_{ij}}{r_{ij}}=1.0;\quad\int x_{ij}\frac{w_{ij}}{r_{ij}}\frac{y_{ij}}{r_{ij}}=0;\quad\int y_{ij}\frac{w_{ij}}{r_{ij}}\frac{x_{ij}}{r_{ij}}=0;\quad\int y_{ij}\frac{w_{ij}}{r_{ij}}\frac{y_{ij}}{r_{ij}}=1.0. \tag{2.3.30}$$

This equation can be normalized in a similar manner by Oger et al. as:

$$\sum\boldsymbol{r}_{ij}\otimes\boldsymbol{C}_{ij}\frac{w_{ij}}{r_{ij}}\frac{\boldsymbol{r}_{ij}}{r_{ij}}V_{ij}=\begin{pmatrix}1&0\\0&1\end{pmatrix} \tag{2.3.31}$$

where

$$V_{ij}=\frac{1}{\sum_{j\neq i}w_{ij}} \tag{2.3.32}$$

Eqs. (2.3.31) and (2.3.32) would give $\boldsymbol{C}_{ij}$ in 2D as:

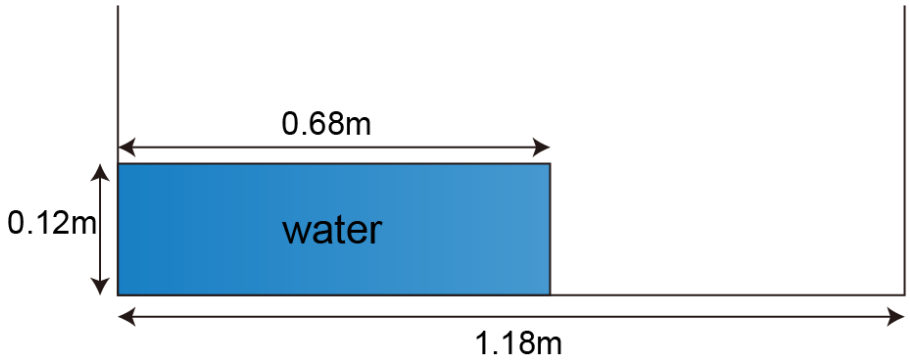

Fig. 2.3.1 Initial condition of the dam breaking simulation

$$\boldsymbol{C}_{ij} = \begin{pmatrix} \sum V_{ij} \dfrac{w_{ij} x_{ij}^2}{r_{ij}^2} & \sum V_{ij} \dfrac{w_{ij} x_{ij} y_{ij}}{r_{ij}^2} \\ \sum V_{ij} \dfrac{w_{ij} x_{ij} y_{ij}}{r_{ij}^2} & \sum V_{ij} \dfrac{w_{ij} y_{ij}^2}{r_{ij}^2} \end{pmatrix}^{-1} \tag{2.3.33}$$

Using $\boldsymbol{C}_{ij}$, The corrected gradient model is obtained as:

$$\langle \nabla p \rangle_i = \frac{D_s}{n_0} \sum_{j \neq i} \frac{p_j - p_i}{\left| \boldsymbol{r}_j - \boldsymbol{r}_i \right|^2} (\boldsymbol{r}_j - \boldsymbol{r}_i) \boldsymbol{C}_{ij} w(\left| \boldsymbol{r}_j - \boldsymbol{r}_i \right|) \tag{2.3.34}$$

2.3.2 Verification of the accurate particle methods

To verify the performance of the accurate particle methods for violent free-surface flows, dam break simulations are implemented. Their performances under more static conditions, such as hydrostatic states, can be referred to Khayyer and Gotoh (2011) [17]. As for the calculation domain is set with its length X = 1.18 m. The water with $X \times Y$ = 0.68×0.12 m is set at the left side in the domain as shown in **Fig. 2.3.1**. The size of the calculation particle is set as d = 0.004 m. This benchmark is implemented by several accurate particle methods as; MPS, CMPS, CMPS-HS, CMPS-HS-HL, CMPS-HS-HL-ECS and MPS-HS-HL-ECS-GC.

Fig. 2.3.2 shows snapshots of simulation results at time t = 0.35 s. MPS has significant perturbations of particle motion particularly around the free surface. While, CMPS improve the stability of the particle motions with more smooth fee-surface line. As for pressure, it is shown from the result of CMPS-HS that HS scheme stunningly enhance the regularity of distribution of pressure, moreover, it reproduce the smoother free surface. The other models with more optional schemes also show the smooth free surface and distribution or pressure. However, in the result of MPS-HS-HL-ECS-GC, despite the fact that it shows the almost perfect regularity in distribution of particles from the zoom-up figure, it includes the instable state of particle motions around the right side wall and the simulation breaks up at time t =0.36 s. MPS-HS-HL-ECS-GC does not include any stabilizing scheme and have difficulty in performing well

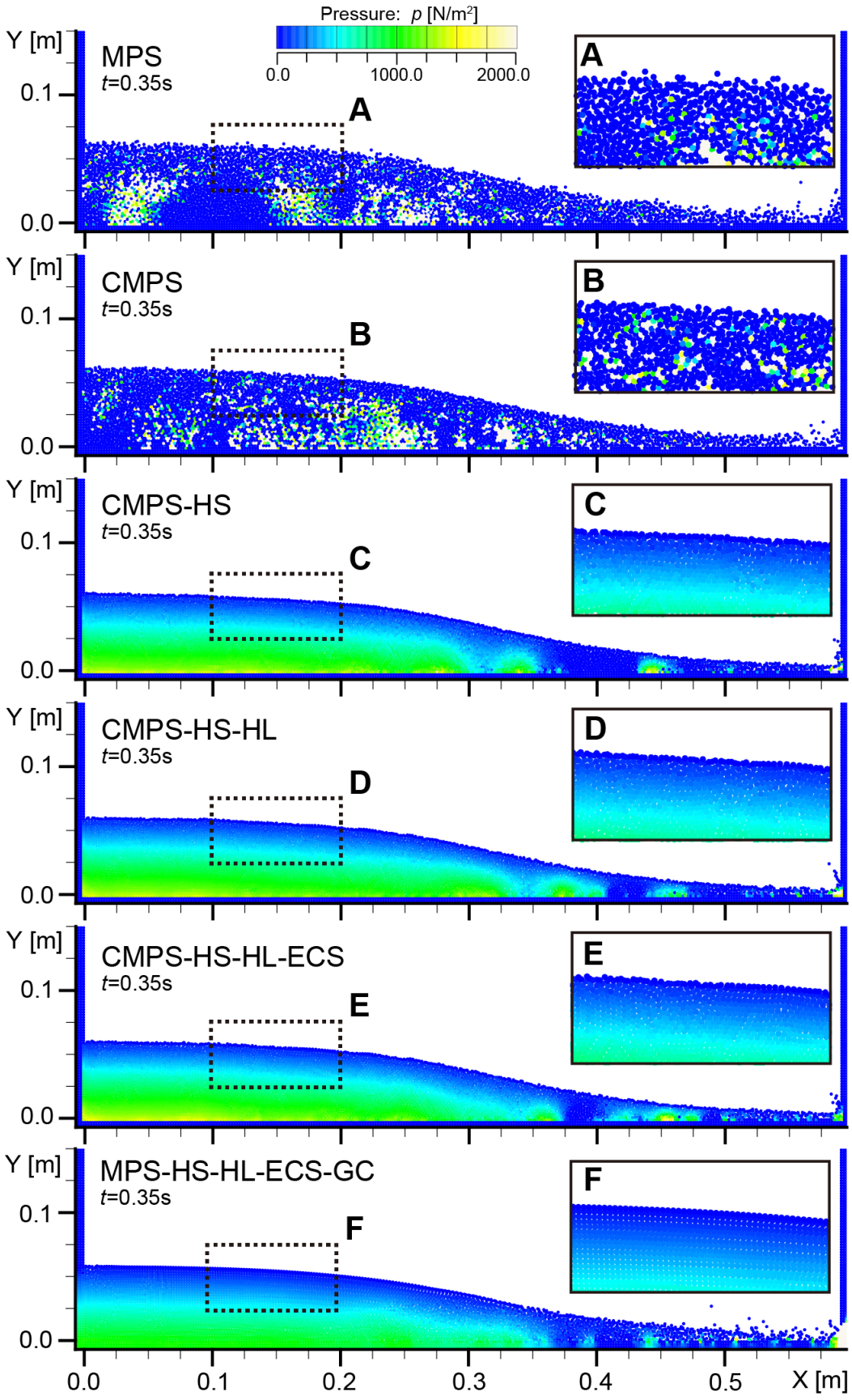

Fig. 2.3.2 Snapshots of the results of dam breaking simulation at t = 0.35 s

under the condition with violent flows. In particular, some repulsive force is necessary for reproduction of bumping into the discontinuous interface, such as walls. The cause of this breaking-up of the simulation corresponds to this matter about the bump. In addition, the GC scheme does not guarantee the momentum conservation due to the correction matrix estimated one by one for each particle by the distribution of the neighboring particles. Therefore, where the particle number density is insufficient, the variance of correction matrixes between neighboring particles increases and may result in the instability mode. This tendency is deteriorated by large deformations of free surface due to the inconsistency in momentum conservation with severe modification by the correction matrixes varying markedly. **Fig. 2.3.3** shows snapshots of simulation results at time t = 0.80 s and 0.92 s. MPS-HS-HL-ECS-GC-DS breaks up before the targeted time, and thus snapshots are shown targeting on the other models. From the snapshots, it is clearly shown that the more accurate particle methods are introduced, the more stable and physical states are obtained. In particular, the effectiveness are obviously found by focusing on the reproducibility of the plunging jet at t = 0.80 s, the splash-up phenomenon t = 0.92 s and the distribution of pressure.

Incidentally, the MPS method occasionally introduces the artificial viscosity term corresponding to the similar concept to the XSPH [18] for prevention of particle-overlapping. Here, the dam break simulations are performed by the previous methods with the XSPH-based artificial viscosity. **Fig. 2.3.4** shows snapshots of simulation results at time t = 0.35 s. By the artificial viscosity, MPS shows a stable state even around the free surface comparing the previous result without the artificial viscosity. Moreover, MPS-HS-HL-ECS-GC is also enhanced in its result without unphysical fluttering of particles. **Fig. 2.3.5** shows snapshots of simulation results at time t = 0.80 s and 0.92 s. Comparing the previous results, all the result obtain more sharp and smooth plunging jets and splash-ups with enhanced pressure field. However, MPS-HS-HL-ECS-GC still lacks the reliable stability against the prominent results shown in the existing studies targeting on more static states. Under the exceedingly violent free-surface flows, another stabilizer is required for this model (refer to Chap.4; **Fig. 4.4.3** and **4.4.4**). This benchmark indicates the effectiveness of the artificial viscosity to some extent. However, this stabilizing viscosity is based on a semi-empirical parameter, and thus, such optional parameters should be appropriately chosen with prudence. Nevertheless, it is difficult to prove the physical meaning of such tuning parameters.

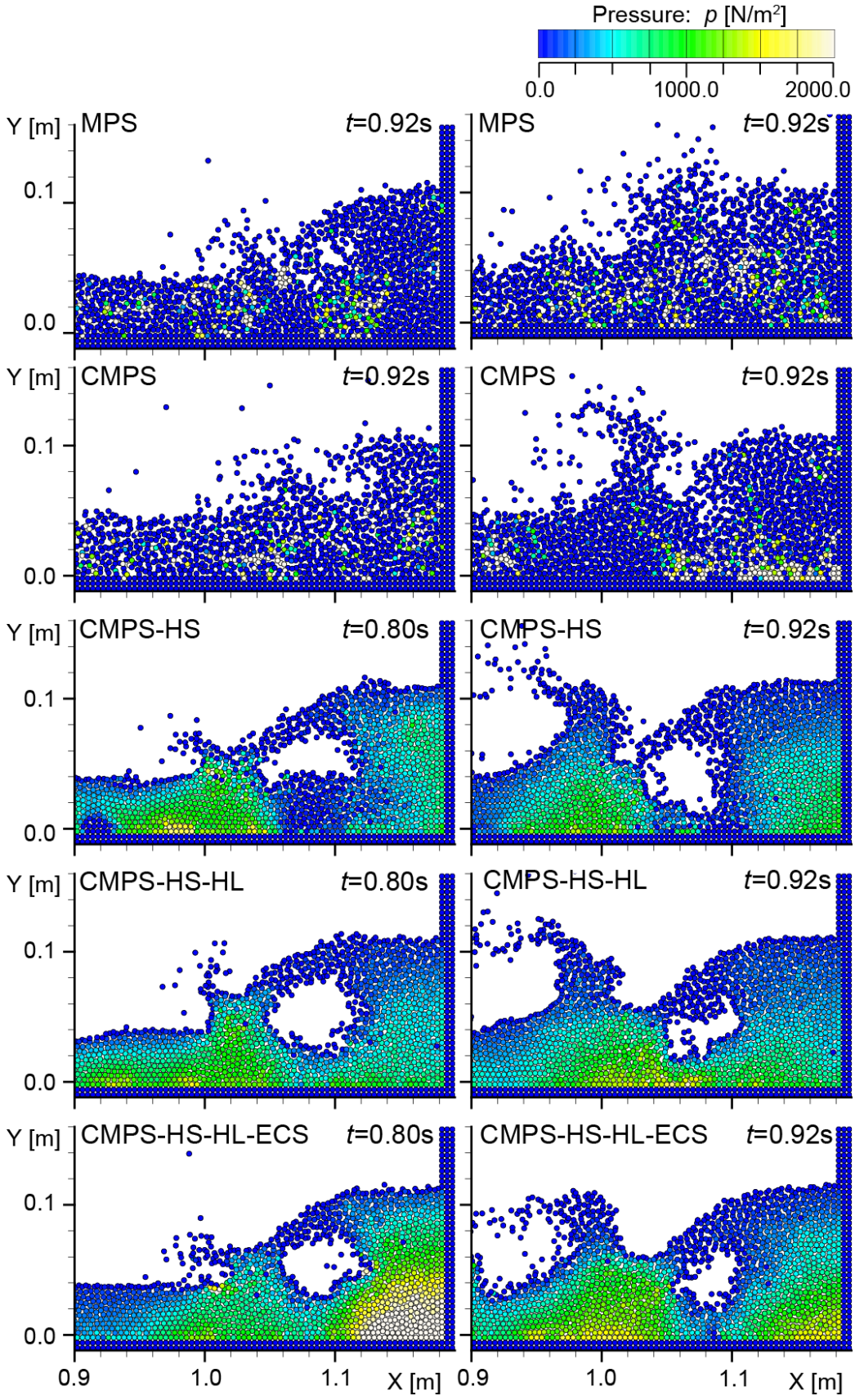

Fig. 2.3.3 Snapshots of results at t = 0.80 s and 0.90 s in dam breaking simulation

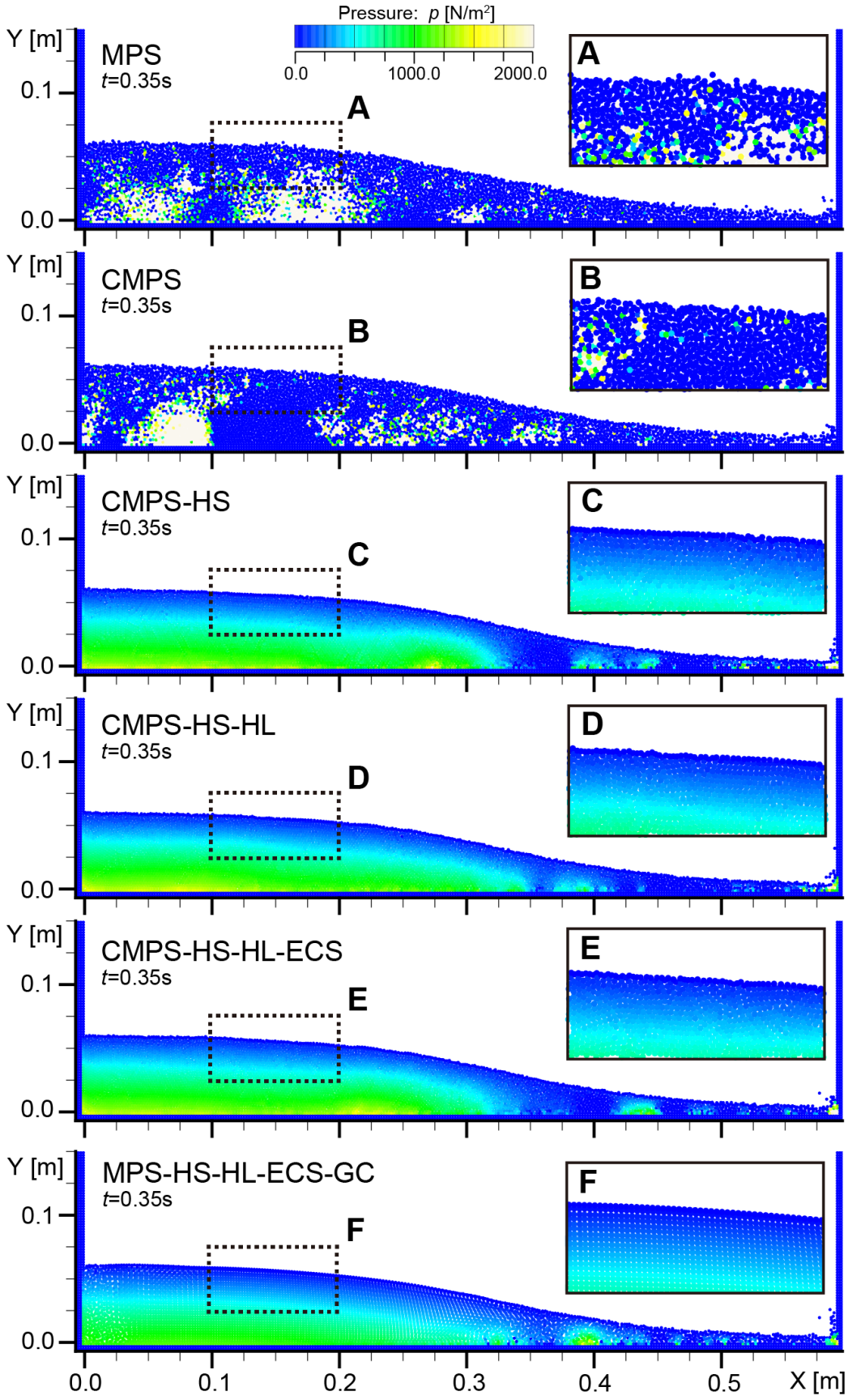

Fig. 2.3.4 Snapshots of results at t = 0.35 s in dam breaking simulation with artificial viscosity

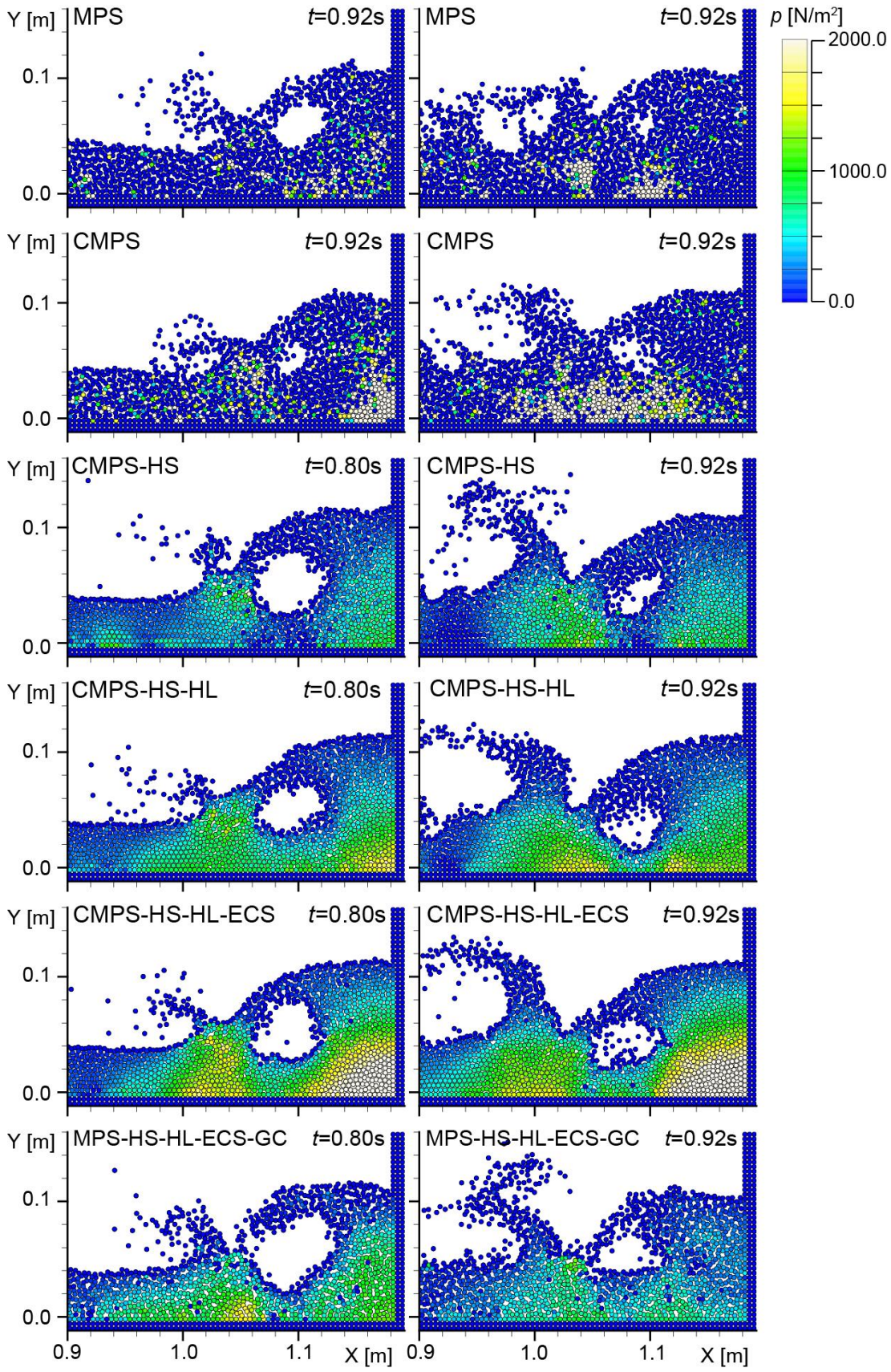

Fig. 2.3.5 Snapshots of results at t = 0.80 s and 0.90 s in dam breaking simulation with artificial viscosity

REFERENCES

[1] B Campbell, C. S., and Brennen, C. E., "Computer Simulation of Granular Shear Flows," *J. Fluid Mech.*, Vol.151, pp.167-188, 1985.

[2] Cundall, P.A. and Strack, O.D.L, "Computer simulation of granular shear flows", J. Fluid Mech., Vol.151, pp.167-188, 1985.

[3] Koshizuka S, Nobe A, Oka Y. "Numerical analysis of breaking waves using the moving particle semi-implicit method", *International Journal for Numerical Methods in Fluids*,Vol.26, pp.751–769, 1998.

[4] Lucy, L. B., "A numerical approach to the testing of the fission hypothesis", *Astron. J.*, vol.82, pp.1013-24, 1977.

[5] Monaghan, J. J., "Simulating free surface flows with SPH", *J. Comput. Phys.* Vol.110, pp.399-406, 1994.

[6] Koshizuka, S. and Oka, Y., "Moving particle semi-implicit method for fragmentation of incompressible fluid", *Nuclear Science and Engineering*, vol.123, pp.421-434, 1996.

[7] Morris J. P., Fox P. J. and Zhu, Y., "Modeling low Reynolds number incompressible flows using SPH", *J. Comput. Phys.*, vol.136, pp.214-226, 1997.

[8] Shao, S. D. and Lo, E. Y. M., "Incompressible SPH method for simulating Newtonian and non-Newtonian flows with a free surface", *Advanced Water Resources*, vol.26 (7), pp.787-800, 2003.

[9] S. Koshizuka, A. Nobe and Y. Oka, "Numerical Analysis of Breaking Waves Using the Moving Particle Semi-implicit Method", International Journal for Numerical Methods in Fluids, 26, 751-769, 1998.

[10] Khayyer, A., Gotoh, H. & Shao, S., "Enhanced predictions of wave impact pressure by improved Incompressible SPH methods", *Applied Ocean Res.*, Vol. 31, pp. 111-131, 2009.

[11] Lee E.S., Moulinec C., Xu R.,Comparisons of weakly compressible and truly incompressible algorithms for the SPH mesh free particle method", *Journal of Computational Physics*, Vol.227(18), pp.8417-8436, 2008.

[12] Ma Q.W. and Zhou J.T., "MLPG-R Method for Numerical Simulation of 2D Breaking Waves", *Computer Modeling in Engineering & Sciences (CMES)*, Vol.43(3), pp.277-304, 2009.

[13] A. Khayyer and H. Gotoh, "Development of CMPS method for accurate water-surface tracking in breaking waves," *Coast. Eng. J.*, 50(2), 179-207, 2008.

[14] A. Khayyer and H. Gotoh, "Modified Moving Particle Semi-implicit methods for the prediction of 2D wave impact pressure", *Coastal Engineering*, 56, 419-440, 2009.

[15] Khayyer, A. and H. Gotoh, "A higher order Laplacian model for enhancement and stabilization of pressure calculation by the MPS method", *Appl. Ocean Res*, Vol. 32 (1), pp. 124–131, 2010.

[16] M. Kondo, S. Koshizuka, "Improvement of stability in moving particle semi-implicit method", *Int. J. Numer. Methods Fluids*, Vol.65, pp.638-654, 2010.

[17] Khayyer, A. and H. Gotoh, "Enhancement of stability and accuracy of the moving particle semi-implicit method", *Journal of Computational Physics*, vol. 230, pp. 3093-3118, 2011.

[18] G.R.Liu and M.B.Liu, "Smoothed Particle Hydrodynamics: a meshfree particle method", *World Scientific*, Singapore, 2003.

CHAPTER 3

Development of the High-resolution DEM-MPS methods

In this chapter, particle-based solid-liquid two-phase coupling schemes, namely DEM-MPS methods are proposed. Firstly, the existing DEM-MPS methods are reviewed, and secondly, three DEM-MPS methods for high-resolution simulations are proposed. The validity of the proposed models is verified by comparison with an experimental result targeting on a solid-liquid two-phase dam breaking. Moreover, one of the proposed models is improved further and applied to a three-dimensional simulation targeting on an experiment of a sedimentation process of numerous blocks.

In many cases, the coastal engineering problems, such as sediment transports and suffering processes of coastal structures comprise unsteady flows caused by violent waves, in particular, the breaker zone includes complicatedly irregular motions of solid structures also in their suffering process. Under such conditions, it is necessary to consider the accurate two-way interactions between solid and liquid phases for precise predictions of the multi-phase flows. For the estimation of the interactions, the following factors should be secured as;

1. Accurate tracking of violent flows including a heavy deformation of the free surface.
2. Accurate tracking of complicated motions of all the solid structures in consideration of the collisions between them as rigid bodies.

Numerous solutions for solid-liquid two-phase flow models are developed particularly by the grid-based model. The characteristic of handling the interface between other phases follows that of tracking the free surface, accordingly, a development of simulation model for accurate tracking free surface contributes to the development of multi-phase flow model in many cases. In the grid-based model, a large number of the proposed models, such as MAC (Marker and cell method) method, VOF (Volume of Fluid) method, C-CUP method, Level-set method, etc. are introduced into the multi-phase flow models indeed. However, coastal engineering problems usually involve heavily violent free-surface flows, and thus, it is difficult to track them accurately with a reliable robustness by such grid-based models due to their distortions of grids. On the other hand, the gridless model, in particular, the particle method has superiority in the robustness for the violent flows and needs only a simple framework without a troublesome reconstruction of the grids. This advantage would be shown in capturing the interface between solid and liquid phases also. Moreover, since the particle method, such as the SPH method and the MPS method are composed of discrete particles for fluid motions with Lagrange tracking like the solid tracking, its compatibility of solid-liquid coupling would be expected.

3.1 Overview

The expansions of the MPS method to solid-liquid two-phase flows have been proposed with various

concepts for coupling of solid-liquid phases. Here, the existing MPS-based solid-liquid two-phase models are overviewed by classifying them into two types for convenience as;

Type 1: Two-fluid-based model, which handles solid and liquid phases as different continuous fluid flows.

Type 2: Two-phase-hybrid model, which handles each phase with an independent discretization space.

3.1.1 Two-fluid-based model

In the two-fluid-based model, the solid phase is regarded as a kind of fluid with the same framework of another continuum phase through the conservative equations of the mass and momentum. The interaction of the liquid phase working on the solid phase, namely the drag force is usually given by the modeling interaction with semi-empirical coefficient of added mass. However, under a simulation condition with a sufficiently high resolution for solid elements, the drag force can be directly estimated without such a modeling procedure by the gradient-diffusion term based on the pressure distribution around the solid elements and the shear stresses on the surface of solid elements. Such interactions between particles related to the pressure gradient and viscosity are originally calculated for each term of the governing equation in the particle method, and thus, this framework is convenient for the program code.

At first, the two-fluid framework was introduced into the MPS method by Gotoh et al. and was applied to a simulation of a process of free-surface waves caused by landslides and debris flows [1], and showed the quantitative effect of the difference of the manner of estimating solid motions by comparison with results of a single-phase-based simulation. The two-fluid model can track the interface between solid and liquid phases accurately even by low-resolution computational set ups, and thus, this model is effective for phenomenon with high concentrations of minute solid elements, such as sediment transport.

However, in the existing two-fluid-based models, the repulsive forces between solid elements including walls were calculated by the pressure gradient and viscosity as fluid flows. Therefore, it involves an excessive loss of kinematic energy in the collision between solid elements, and as a result, it does not obtain the sufficient repulsive force for the solid elements against the real phenomenon. To resolve this, Gotoh et al. (2003) [2] introduced an extra collision force term by the DEM as the two-fluid-based DEM-MPS method. Moreover, they additionally introduced the so-called Passively Moving Solid (PMS) model, which combines the solid elements with each other as components of a bigger structure, and achieved the expansion of the DEM-MPS framework into the multi-scale-link DEM-MPS method. This model can handle multi-scale solid elements with fluid particles, and shows a possibility that fluid particles, which are usually limited as similar scale to the solid phase, can be tracked with a practically high resolution. Similar framework is applied to several engineering problems [3][4].

3.1.2 Two-phase-hybrid model

For estimation of the drag force acting on a drifting solid element in the fluid flow, it is necessary to secure sufficient information of the fluid around the targeted solid elements. However, despite the multi-scale-link DEM-MPS method can achieve the high-resolution tracking of fluid flow around the solid elements, it possibly lacks part of fluid information due to the fact that some fluid particles cannot flow into vacant space between solid elements. This problem is caused by the geometric discrepancy in the spatial

dimension for 2D simulations or the insufficient computational resolution for the liquid phase. Therefore, it is necessary to develop some supplemental manners to express the fluid flowing into the void space. The two-phase-hybrid model is one of the solutions of this problem. This model sets different discretization spaces for each phase and allows the phases to overlap each other. Both discretization spaces are connected to each other through the interaction between solid and liquid phases by utilizing the integral of pressure gradient on the surface of the element or the momentum based on the difference of velocity between the phases.

This model has relatively plenty accomplishments in the MPS method. Firstly, Ikari and Gotoh [5] developed a model based on a semi-empirical solid-liquid interaction with the added mass coefficient model and Gotoh et al. [6] applied the proposed model to a simulation for prediction of motions of coastal armor blocks. Moreover, they introduced the accurate particle methods into the model, and simulated an outbreak process of tsunami caused by a landslide with the proposed model [7]. Sakai et al.[8] proposed the multi-scale DEM-MPS method to reproduce clouds of solid powders from the macroscopic viewpoint by setting macro particles modeling the clouds. In addition, they showed its effectiveness by comparing with the result by the existing MPS-based PMS model [9]. As an expanded model of the multi-scale DEM-MPS method, the group introduced an improved scheme in consideration of the porosity of the solid elements and achieved an application of an optional size of fluid particle with independence from the solid scale. As for another approach of the powder of solid, Ui et al. [10] introduced the turbulent model into the DEM-MPS method. As a study of solid-liquid two-phase dam breaking simulation based on the MPS method, Ahmad and Yee-Chung [11] is also cited as a kind of the two-phase-hybrid model in spite of their framework without DEM. This method tracks the fluid particles as non-Newtonian fluid by utilizing the inter-particle porosity ratio estimated through the kernel function.

3.2 Proposition of the high-resolution DEM-MPS method

In this section, the particle-based numerical solutions for solid-liquid two-phase flows, namely the DEM-MPS methods are proposed [12,13]. Firstly, the details of the three models are explained and their validities are examined by a benchmark targeting on a solid-liquid two-phase dam breaking experiment [14]. Secondly, one of the proposed models is improved, and further, its performance is verified by a simulation targeting on a sedimentation process of numerous blocks dumped from above the water.

The first model is an improved model of the multi-scale-link DEM-MPS method by Gotoh et al. with introduction of the accurate particle methods to track the fluid motions around the solid elements more accurately. The so-far model has a problem about the unphysical hindrance to fluid particles from flowing into vacant space between solid elements. It is expected that the accurate particle methods would help reproducing more physically smooth motions of fluid particles with independence from the geometrical reproducibility of solid elements associated with the resolution.

The second model is an improved two-fluid-hybrid model. Here, the solid elements are set with a bigger diameter than liquid particle for high-resolution tracking of flows. Each discretization space is similarly connected by the solid-liquid interaction, however, the interaction is estimated through their momentum by the gradient-diffusion term. The accurate particle methods are introduced into this model also.

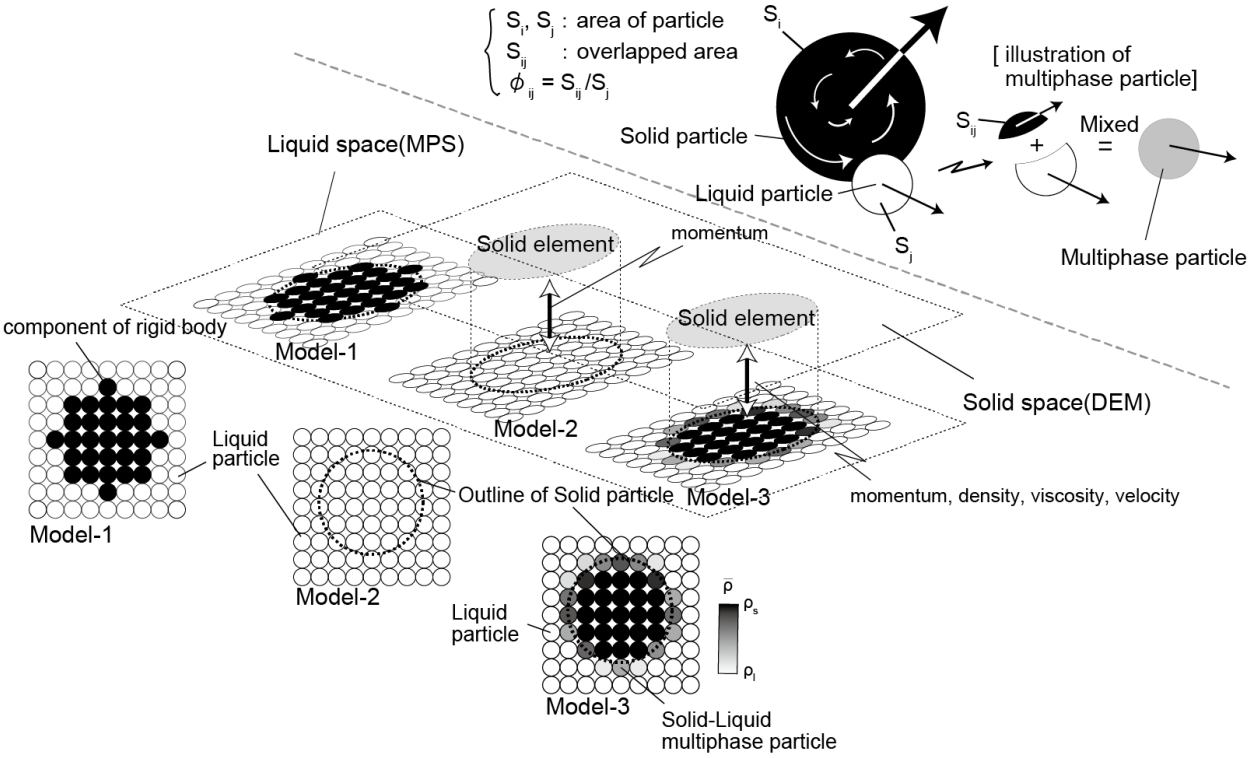

Fig. 3.2.1 Illustration of the concepts of proposed DEM-MPS methods (Model 1, 2 and 3)

As for the third model, the proposed second model is improved further. In addition to the momentum, the velocity and density of solid phase are also considered as a solid-liquid interaction to connect the discretization spaces by projecting them to the liquid particles overlapping the solid elements. Due to this process, not only the volume and momentum, but also the mass is conserved. Moreover, more physical behaviors of the solid elements would be given by the more accurate interaction deduced from the liquid motions reproducing their overlapped solid velocities faithfully. By the projection of the density, the various densities are given to the fluid particles depending on the situation of overlap, and thus, the liquid particles are treated as a kind of multi-phase fluid. From this viewpoint, this model is expansion of the two-fluid-based model, too. Therefore, this model is based on both two-fluid-based model and two-phase-hybrid model. The accurate particle methods are introduced into this model also.

Fig. 3.2.1 shows an illustration of the concept of the proposed three methods.

3.2.1 Model 1: two-fluid-based model

Here, the accurate particle methods corresponding to the CMPS-HS method is introduced into the multi-scale-link DEM-MPS method by Gotoh et al [2] for high resolution tracking of flows [12].

Considering the analogy between solid and liquid phases, the two-fluid-based model is described by a couple of the fundamental equations for fluid motions. The continuity equations are:

$$\frac{D\rho_l}{Dt} + \rho_l \nabla \cdot \boldsymbol{u}_l = 0 \tag{3.2.1}$$

$$\frac{D\rho_s}{Dt} + \rho_s \nabla \cdot \boldsymbol{u}_s = 0 \tag{3.2.2}$$

where ρ is density, t is time, $\boldsymbol{u}$ is the velocity vector. While, the momentum equations are described as:

$$\rho_l \frac{D\boldsymbol{u}_l}{Dt} = -\nabla p_l + \mu_l \nabla^2 \boldsymbol{u}_l + \rho_l \boldsymbol{g} + \boldsymbol{f}_{ls} \tag{3.2.3}$$

$$\rho_s \frac{D\boldsymbol{u}_s}{Dt} = -\nabla p_s + \mu_s \nabla^2 \boldsymbol{u}_s + \rho_s \boldsymbol{g} - \boldsymbol{f}_{ls} + \boldsymbol{f}_{colp} \tag{3.2.4}$$

where p is pressure, μ is viscosity coefficient, $\boldsymbol{g}$ is the vector of gravity acceleration, $\boldsymbol{f}_{ls}$ is the vector of the solid-liquid interaction, $\boldsymbol{f}_{colp}$ is the vector of the solid-solid interaction. The subscripts l, s denote the liquid phase and the solid phase, respectably. The vector of the liquid-liquid interaction vector $\boldsymbol{f}_{ls}$ is calculated as:

$$\boldsymbol{f}_{ls,l} = -\left(-\nabla p_l + \mu_l \nabla^2 \boldsymbol{u}_l\right)_s \tag{3.2.5}$$

$$\boldsymbol{f}_{ls,s} = \left(-\nabla p_s + \mu_s \nabla^2 \boldsymbol{u}_s\right)_l \tag{3.2.6}$$

The process of the update of velocity is composed of two stages similar to the projection-based algorithm for incompressible single-phase flows. The increment of the projection velocity is written as:

$$\Delta \boldsymbol{u}^*_{l,k} = \left(\nu_l \nabla^2 \boldsymbol{u}_l\right)_{k-1} \Delta t + \boldsymbol{g} \Delta t \tag{3.2.7}$$

$$\Delta \boldsymbol{u}^*_{s,k} = \left(\nu_s \nabla^2 \boldsymbol{u}_s\right)_{k-1} \Delta t + \boldsymbol{g} \Delta t \tag{3.2.8}$$

where the subscript * denotes the first stage and the subscript k denotes the time step. While, the increment of the correction velocity in the second stage is written as:

$$\rho_l \Delta \boldsymbol{u}^{**}_{l,k} = -\nabla p_{l,k+1} \Delta t + \boldsymbol{f}_{ls} \Delta t \tag{3.2.9}$$

$$\rho_s \Delta \boldsymbol{u}^{**}_{s,k} = -\nabla p_{s,k+1} \Delta t - \boldsymbol{f}_{ls} \Delta t \tag{3.2.10}$$

where the subscript ** denotes the second stage. Then, by integrating the pressure of both phases, the solid-liquid interaction is eliminated and the following equation is obtained as:

$$\Delta \boldsymbol{u}^{**}_{l,k} + \frac{\rho_s}{\rho_l} \Delta \boldsymbol{u}^{**}_{s,k} = -\frac{1}{\rho_l} \nabla p_{k+1} \Delta t \tag{3.2.11}$$

Since both the solid and liquid phases possess the incompressibility, their mass conservations are guaranteed only by keeping the particle number density equal to the reference of that in the two-fluid-based MPS method also. Considering the fact, the follows is obtained from Eqs. (3.2.9) and (3.2.10) as:

$$\frac{1}{n_0}\Delta n_k^{**} + \nabla\cdot\left(\Delta \boldsymbol{u}_{l,k}^{**} + \frac{\rho_s}{\rho_l}\Delta \boldsymbol{u}_{s,k}^{**}\right)\Delta t = 0 \tag{3.2.12}$$

Moreover, using Eq. (3.2.11), the Poisson Pressure Equation for solid-liquid two-phase flow is obtained as:

$$\nabla^2 p_{k+1} = \frac{\rho_m}{(\Delta t)^2}\frac{n_k^* - n_0}{n_0} \quad (m = l, s) \tag{3.2.13}$$

From this equation, the pressure is obtained, and the corrected velocity is calculated through the following equations by the pressure gradient term are given:

$$\boldsymbol{u}_{s,k}^{**} = \boldsymbol{u}_{s,k} + \Delta \boldsymbol{u}_{s,k}^{*} + \Delta \boldsymbol{u}_{s,k}^{**} \tag{3.2.14}$$

$$\boldsymbol{r}_{s,k}^{**} = \boldsymbol{r}_{s,k} + \boldsymbol{u}_{s,k}\Delta t + \Delta \boldsymbol{u}_{s,k}^{*}\Delta t + \Delta \boldsymbol{u}_{s,k}^{**}\Delta t = \boldsymbol{r}_{s,k} + \boldsymbol{u}_{s,k}^{**}\Delta t \tag{3.2.15}$$

As for the motions of solid elements, in addition to these numerical processes for two-fluid flows, the solid-solid interaction $\boldsymbol{f}_{colp}$ and the rigid connection for expression of solid structures are considered separately. The solid-solid interaction $\boldsymbol{f}_{colp}$ is estimated by the DEM. However, the DEM is based on the explicit method in contrast to the MPS framework characterized by the semi-implicit method, and thus, it needs a more minute time interval Δt_{DEM} than the MPS time interval Δt. Therefore, the DEM calculation is implemented plurally in 1 time step of the MPS calculation to make the time progress equal to that of the MPS calculation. The updated velocity vector of the solid particle $\tilde{\boldsymbol{u}}_k$ and its position $\tilde{\boldsymbol{r}}_k$ at time step k is calculated with the temporary velocity and position estimated by Eqs. (3.2.14) and (3.2.15) as:

$$\tilde{\boldsymbol{u}}_{k+1} = \boldsymbol{u}_{k+1}^{**} + \sum_{a=1}^{N}\Delta\tilde{\boldsymbol{u}}_{k+a/N}; \qquad N = \frac{\Delta t}{\Delta t_{DEM}} \tag{3.2.16}$$

$$\tilde{\boldsymbol{r}}_{k+1} = \boldsymbol{r}_{k+1}^{**} + \sum_{a=1}^{N}\tilde{\boldsymbol{u}}_{k+a/N}\Delta t_{DEM} \tag{3.2.17}$$

where N is the total number of the computational loop procedures by the DEM within 1 time step by the MPS method for fluid flows, a is time step of the DEM calculation and M_s is the mass of the solid particle. The subscript "~" denotes a stage before the modification procedure for the rigid connection. The increment of the modified velocity at each DEM time step is written as:

$$M_s\frac{\Delta\tilde{\boldsymbol{u}}_{k+(a+1)/N}}{\Delta t_{DEM}} = \underbrace{M_s\frac{\Delta\tilde{\boldsymbol{u}}^{*}{}_{k+a/N}}{\Delta t_{DEM}}}_{\boldsymbol{f}colp,k+a/N} + \underbrace{M_s\frac{\Delta\tilde{\boldsymbol{u}}^{**}{}_{k+a/N}}{\Delta t_{DEM}}}_{\boldsymbol{f}connect,k+a/N} \tag{3.2.18}$$

where $\boldsymbol{f}_{connect}$ is the rigid connection force to form the shape of the rigid body. The solid-solid interaction $\boldsymbol{f}_{colp}$ does not act on other components in the same rigid structure. In the numerical process of the DEM, firstly, each solid particles as components of the targeted rigid structure is calculated by the standard DEM

calculation. From the updated position and velocity, the rigid connection is introduced in consideration of the velocity and position of the structure. The behavior of the rigid structure at time step $t+a\Delta t_{DEM}$ is estimated by its translational velocity vector at its centroid $\boldsymbol{T}_{rigid}$ and its angular velocity vector $\boldsymbol{R}_{rigid}$ obtained from the motions of its components as:

$$\boldsymbol{T}_{rigid,k+(a+1)/N} = \frac{1}{L}\sum_{q=1}^{L} \tilde{\boldsymbol{u}}^{*}_{q,k+a/N} \tag{3.2.19}$$

$$\boldsymbol{R}_{rigid,k+(a+1)/N} = \frac{1}{\boldsymbol{I}} \tilde{\boldsymbol{u}}_{q,k+a/N} \times \left(\tilde{\boldsymbol{r}}^{*}_{q,k+a/N} - \boldsymbol{r}_{g,k+(a+1)/N}\right); \qquad \boldsymbol{I} = \sum_{q=1}^{L} \left|\boldsymbol{r}_{q,k+a/N} - \boldsymbol{r}_{g,k+(a+1)/N}\right|^2 \tag{3.2.20}$$

where $\boldsymbol{I}$ is the inertia tensor, $\boldsymbol{L}$ is the total number of the components of the targeted rigid structure. The subscripts g and q denotes the centroid of the rigid structure and the labeled number of the components, respectably. The centroid position of the rigid structure $\boldsymbol{r}_g$ is:

$$\boldsymbol{r}_{g,k+(a+1)/N} = \frac{1}{L}\sum_{q=1}^{L} \tilde{\boldsymbol{r}}^{*}_{q,k+a/N} \tag{3.2.21}$$

The translational velocity vector at its centroid $\boldsymbol{T}_{rigid}$ and its angular velocity vector $\boldsymbol{R}_{rigid}$, the components is updated so as to satisfy the Eqs. (3.2.19) and (3.2.20) (refer to **Fig. 3.2.2**) as:

$$\tilde{\boldsymbol{u}}_{q,k+(a+1)/N} = \boldsymbol{T}_{rigid,k+(a+1)/N} + \left(\tilde{\boldsymbol{r}}^{*}_{q,k+a} - \boldsymbol{r}_{g,k+(a+1)/N}\right) \times \boldsymbol{R}_{rigid,k+(a+1)/N} \tag{3.2.22}$$

From this equation, the position of components q is modified as:

$$\tilde{\boldsymbol{r}}_{q,k+a/N} = \tilde{\boldsymbol{r}}_{q,k+(a-1)/N} + \boldsymbol{u}_{q,k+a/N}\Delta t_{DEM} \tag{3.2.23}$$

Then, the rigid connection force $\boldsymbol{f}_{connect}$ is written as:

$$\boldsymbol{f}_{connect} = M_s \frac{\left(\tilde{\boldsymbol{u}}_{k+(a+1)/N} - \tilde{\boldsymbol{u}}^{*}_{k+a/N}\right)}{\Delta t_{DEM}} \tag{3.2.24}$$

Fig. 3.2.2 illustrates the flowchart of the algorithm of this proposed model.

3.2.2 Model 2: single-phase-flow model

The two-fluid-based model includes the modification procedure by the rigid connection after the solution of the Continuity equation, the solid particles possibly overlap the neighboring liquid particles, and may result in the numerical instability, which cause simultaneously an increase of the computational time due to the

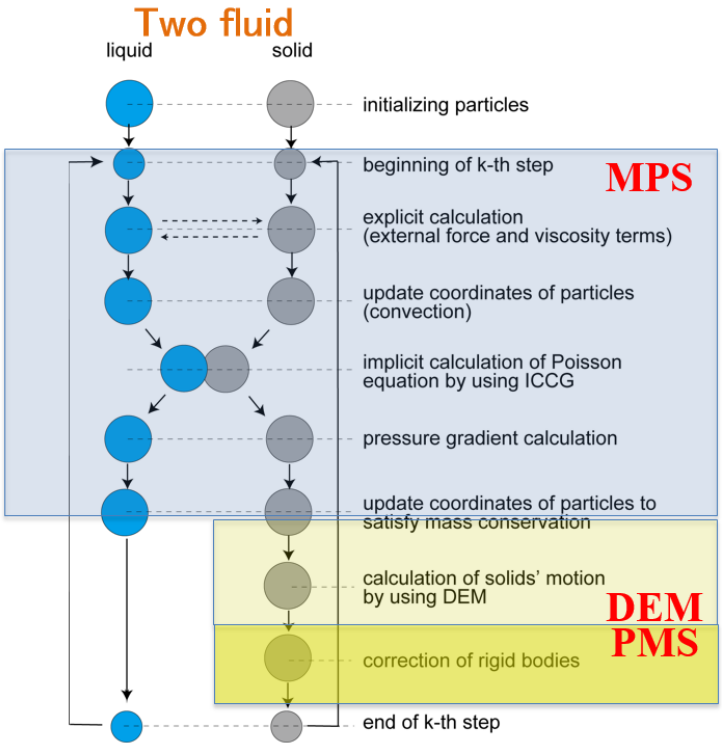

Fig. 3.2.2 Flowchart of the two-fluid-model

instability associated with the disordered matrix of the Poisson Pressure Equation. Moreover, it leaves a problem about ignorant of the solid-liquid interaction acting on the liquid particles, that is an increment of the momentum of the solid particle through the DEM and PMS calculation.

Here, to resolve this problem, another model is proposed [12]. In the new proposed model, solid and liquid particles are tracked in the different discretization space, and the discretization spaces are connected by the solid-liquid interaction. The different point from the existing two-phase-hybrid model is that the solid particle is set with a sufficient bigger diameter than that of the liquid particle. The solid-liquid interaction is estimated by targeting on only the overlapped area between each phase in place of the usage of the influence area with an operation of weighted averaging.

The governing equations of the fluid flow for the liquid particles are described as:

$$\frac{D\rho_l}{Dt} + \rho_l \nabla \cdot \boldsymbol{u} = 0 \tag{3.2.25}$$

$$\rho_l \frac{D\boldsymbol{u}_l}{Dt} = -\nabla p + \mu_l \nabla^2 \boldsymbol{u} + \rho_l \boldsymbol{g} + \boldsymbol{f}_{\text{int}} \tag{3.2.26}$$

where $\boldsymbol{f}_{\text{int}}$ is the vector of the solid-liquid interaction. Then, by handling the solid-liquid interaction $\boldsymbol{f}_{\text{int}}$ as an external force, the computational procedure corresponds to the standard MPS framework for single-phase flows.

The momentum equations of the solid motion are written with the solid-solid interaction $\boldsymbol{f}_{colp}$ as:

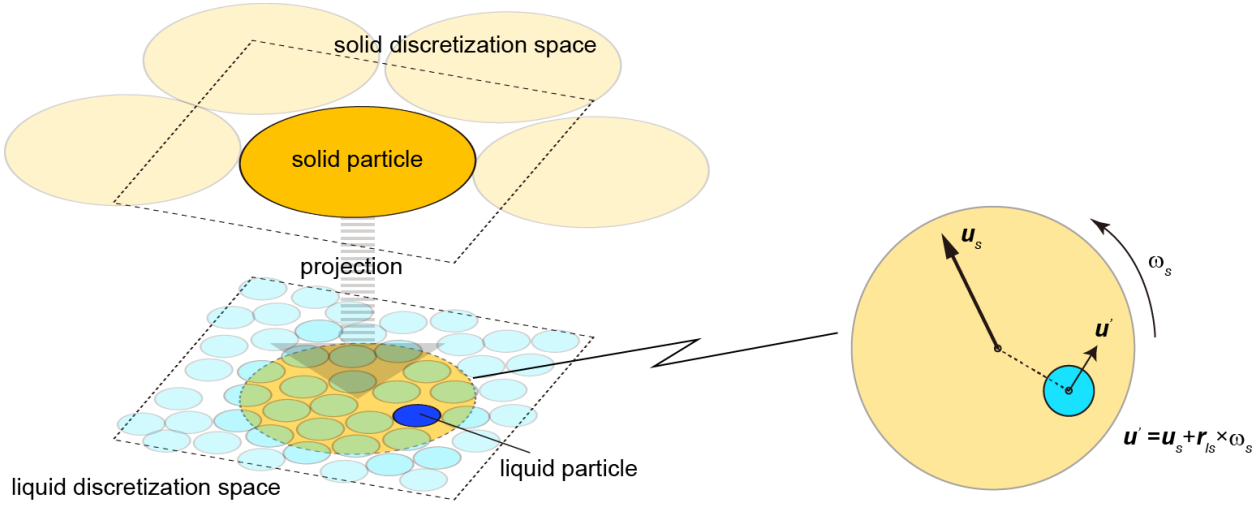

Fig. 3.2.3 Illustration of concept of evaluating projected velocity

$$m_s \frac{d\boldsymbol{u}_s}{dt} = \int_V \left\{ \rho_l \frac{D\boldsymbol{u}_l}{Dt} - \boldsymbol{f}_{\text{int}} + (\rho_s - \rho_l)\boldsymbol{g} \right\} dV + \boldsymbol{f}_{colp} \tag{3.2.27}$$

$$\boldsymbol{I} \frac{d\boldsymbol{\omega}}{dt} = \int_V \boldsymbol{r}_{ls} \times \left(\rho_l \frac{D\boldsymbol{u}_l}{Dt} - \boldsymbol{f}_{\text{int}} \right) dV + \boldsymbol{T}_{colp} \tag{3.2.28}$$

where $\boldsymbol{T}_{\text{colp}}$ is the vector of the torque force by the collision between solid particles, V is the volume of the solid particle. The solid-liquid interaction $\boldsymbol{f}_{\text{int}}$ is given from the difference of the momentums between the overlapped particles belonging to each phase (refer to **Fig. 3.2.3**) as:

$$\boldsymbol{f}_{\text{int}} = \sum \frac{\rho_s \boldsymbol{u}_s' - \rho_l \boldsymbol{u}_l}{\Delta t} \phi \tag{3.2.29}$$

$$\boldsymbol{u}_s' = u_s + \boldsymbol{r}_{ls} \times \boldsymbol{\omega} \tag{3.2.30}$$

where ϕ is the occupation rate of the overlapped area. The momentum equation of the motion of the solid particle i is discretized in consideration of the occupation rate of the overlapped area ϕ between the solid particle i and the liquid particle j as:

$$\sum_{j \in J} \left(\rho_s \phi_{ji,k} \right) \frac{\Delta \boldsymbol{u}_{i,k}}{\Delta t} = \sum_{j \in J} \left[\left\{ \rho_l \frac{\Delta \boldsymbol{u}_{j,k}^{*} + \Delta \boldsymbol{u}_{j,k}^{**}}{\Delta t} - \boldsymbol{f}_{\text{int},j,k} + (\rho_s - \rho_l)\boldsymbol{g} \right\} \phi_{ji,k} \right] + \boldsymbol{f}_{colp} \tag{3.2.31}$$

$$\sum_{j \in J} \left(\rho_s \phi_{ij,k} \left| \boldsymbol{r}_{ij,k} \right|^2 \right) \frac{\Delta \boldsymbol{\omega}_{i,k}}{\Delta t} = \sum_{j \in J} \left[\boldsymbol{r}_{ij,k} \times \left\{ \rho_l \frac{\Delta \boldsymbol{u}_{j,k}^{*} + \Delta \boldsymbol{u}_{j,k}^{**}}{\Delta t} - \boldsymbol{f}_{\text{int},j,k} \right\} \phi_{ij,k} \right] + \boldsymbol{T}_{colp,i} \tag{3.2.32}$$

where

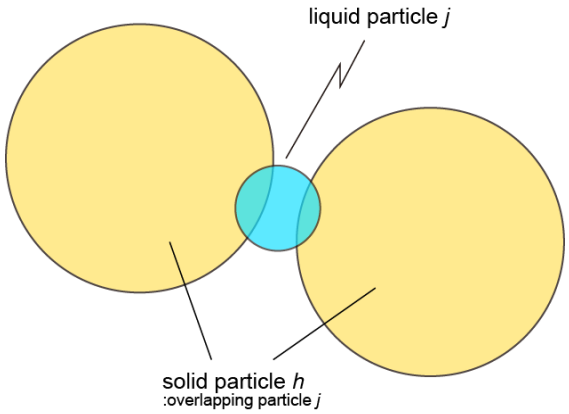

Fig. 3.2.4 Illustration of relation between liquid particle *j* and overlapping solid particle *h*

$$J = \left\{ h : r_{ij,k+1} \le \frac{d_i + d_j}{2} \right\} \tag{3.2.33}$$

The solid-liquid interaction by liquid particle *j* is:

$$\boldsymbol{f}_{\mathrm{int},j,k} = \frac{\sum_{h \in H} \left[\left(\rho_s \boldsymbol{u}'_{h,k+1} - \rho_l \boldsymbol{u}^{**}_{j,k} \right) \phi_{jh,k+1} \right]}{\Delta t}; \qquad H = \left\{ h : r_{hj,k+1} \le \frac{d_h + d_j}{2} \right\} \tag{3.2.34}$$

$$\boldsymbol{u}'_{h,k+1} = \boldsymbol{u}_{h,k+1} + \boldsymbol{r}_{hj,k+1} \times \boldsymbol{\omega}_{h,k+1} \tag{3.2.35}$$

where the subscript *h* denotes the overlapped solid particle *h* to liquid particle *j* (refer to **Fig.3.2.4**).

As for the numerical algorithm, firstly, the liquid particles are tracked by the MPS method. Secondly, utilizing the information of the fluid flows, the drag force is given to the solid particles. By the drag force, the vectors and positions of the solid particles are updated with the solid-solid collision force by the DEM. To guarantee the momentum conservation, the increment of the momentum of the solid particle is projected to the overlapped liquid particles with the occupation rate of the overlap.

This proposed model takes the weak-coupling, and thus, the solid-liquid interaction is estimated practically as;

$$\boldsymbol{f}_{\mathrm{int},j} = \frac{\sum_{h \in H} \left[\left(\rho_s \boldsymbol{u}'_{h,k} - \rho_l \boldsymbol{u}^{**}_{j,k-1} \right) \phi_{hj,k} \right]}{\Delta t}; \qquad H = \left\{ h : r_{hj,k} \le \frac{d_h + d_j}{2} \right\} \tag{3.2.36}$$

Fig.3.2.5 illustrates the flowchart of the algorithm of this proposed model.

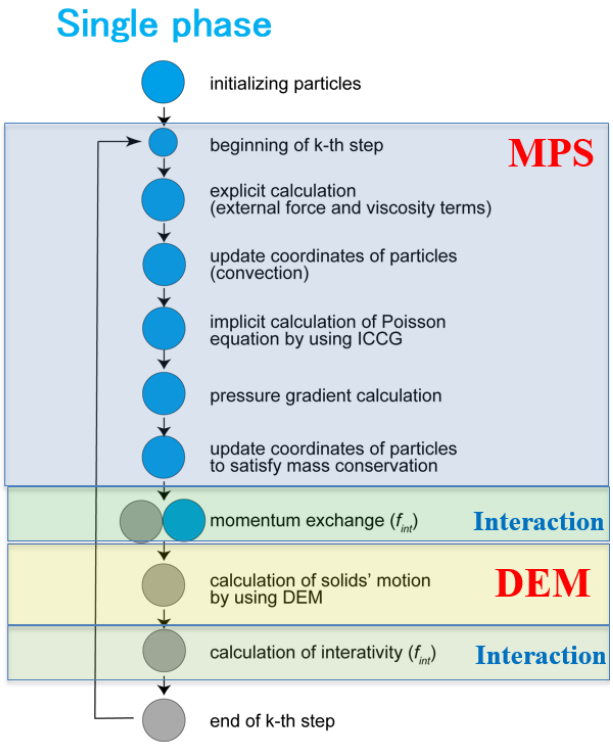

Fig. 3.2.5 Flowchart of the single-phase-flow model

3.2.3 Model 3: multi-phase-flow model

The proposed single-phase-flow model handles all the fluid particles as purely single-phase fluids even for the particles overlapping the solid particles, therefore, it includes inconsistency in the mass conservation of the liquid discretization space against the real phenomenon. To resolve this, an improved model is developed [12]. The newly proposed model projects the physical quantities of the solid particles to the liquid particles overlapping the solid particles, that is each liquid particle is given appropriate density, viscosity and velocity varyingly and treated as a kind of multi-phase liquid particle.

In the calculation process of the fluid flows by the MPS method, the multi-phase liquid particle, to which the physical quantities of solid particles are projected, is introduced. The projection process to define the multi-phase liquid particles is manipulated in consideration of the occupation rate of the overlapped area ϕ between phases:

$$\bar{\theta} = \theta_l\left(1-\sum\phi\right)+\sum\theta_s\phi\left(\theta=\mu,\rho\right) \tag{3.2.37}$$

where θ is a physical quantity. The subscript bar "–" denotes the multi-phase particle. **Fig. 3.2.6** illustrates the concept of the multi-phase-flow model with the occupation ratio of an overlapped area ϕ, the density $\bar{r}$ and the velocity $\tilde{\boldsymbol{u}}_l$ of the multi-phase liquid particle. The velocity of the multi-phase liquid particle overlapping the solid particle is given in consideration of the translational and angular velocity of the overlapped solid particle. The velocity is written in accordance with the occupation rate of the overlapped

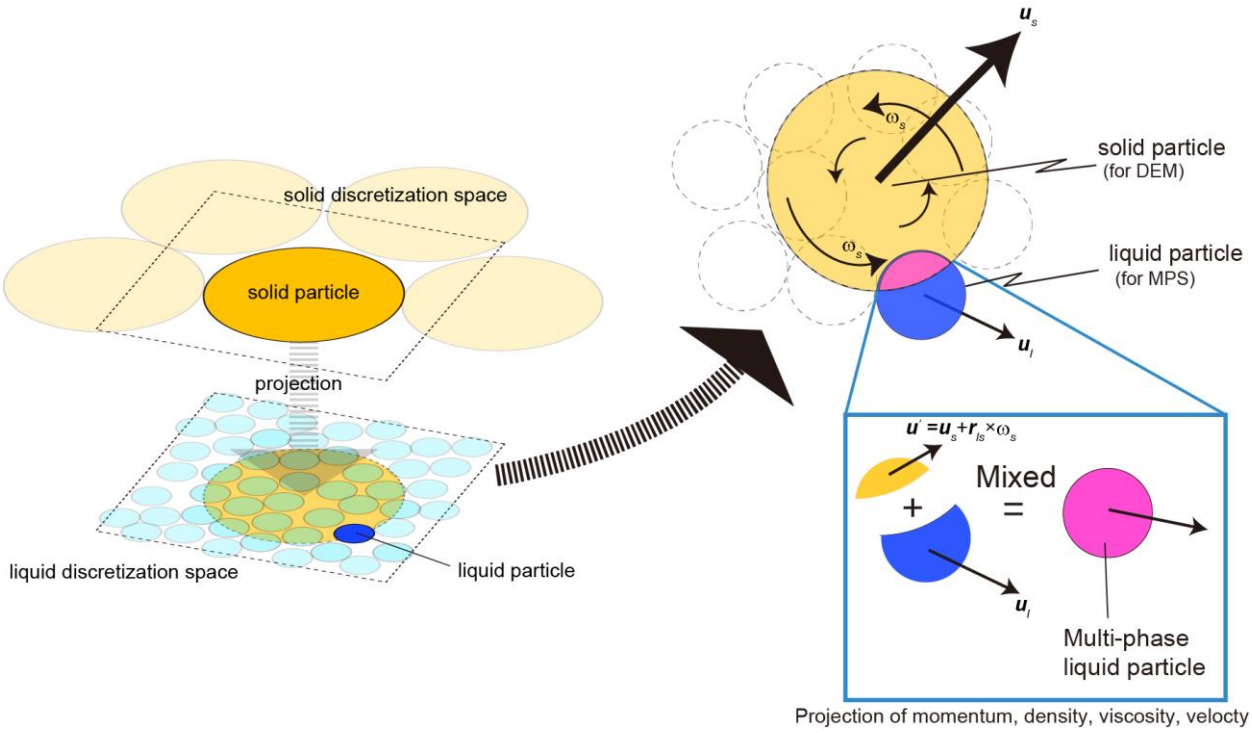

Fig. 3.2.6 Illustration of the concept of the multi-phase-flow model

area ϕ as:

$$\tilde{\boldsymbol{u}}_l = \left(\boldsymbol{u}_s + \boldsymbol{r}_{ls} \times \boldsymbol{\omega}\right) + \boldsymbol{u}_l\left(1-\phi\right); \qquad \boldsymbol{r}_{ls} = \boldsymbol{r}_l - \boldsymbol{r}_s \tag{3.2.38}$$

The governing equations of the multi-phase flow are described as:

$$\frac{D\overline{\rho}}{Dt} + \overline{\rho}\nabla \cdot \tilde{\boldsymbol{u}}_l = 0 \tag{3.2.39}$$

$$\overline{\rho}\frac{D\tilde{\boldsymbol{u}}_l}{Dt} = -\nabla\overline{p} + \overline{\mu}\nabla^2\tilde{\boldsymbol{u}}_l + \overline{\rho}\boldsymbol{g} + \boldsymbol{F}_{int} \tag{3.2.40}$$

where $\boldsymbol{F}_{\text{int}}$ is the vector of the solid-liquid interaction. The momentum equation of the solid motion is written as:

$$m_s\frac{d\boldsymbol{u}_s}{dt} = \int_V\left(\overline{\rho}\frac{D\tilde{\boldsymbol{u}}_l}{Dt} - \boldsymbol{F}_{\text{int}}\right)dV + \boldsymbol{f}_{colp} \tag{3.2.41}$$

$$\boldsymbol{I}\frac{d\boldsymbol{\omega}_s}{dt} = \int_V \boldsymbol{r}\times\left(\overline{\rho}\frac{D\tilde{\boldsymbol{u}}_l}{Dt} - \boldsymbol{F}_{\text{int}}\right)dV + \boldsymbol{T}_{colp} \tag{3.2.42}$$

Similar to the proposed single-phase-flow model, the solid-liquid interaction $\boldsymbol{F}_{\text{int}}$ is estimated as:

$$\boldsymbol{F}_{\text{int}} = \sum \frac{\rho_s \boldsymbol{u}'_s - \tilde{\rho}\,\tilde{\boldsymbol{u}}}{\Delta t} \tag{3.2.43}$$

As for the numerical procedure, firstly, the physical quantities of the multi-phase liquid particles are calculated utilizing Eq. (3.2.37). The increments of the projection velocity and correction velocity by the projection scheme are, respectably written as:

$$\Delta\tilde{\boldsymbol{u}}^{*}_{l,k} = \frac{\bar{\mu}}{\bar{\rho}}\nabla^2\tilde{\boldsymbol{u}}_{l,k}\Delta t + \boldsymbol{g}\Delta t + \boldsymbol{F}_{\text{int}}\Delta t \tag{3.2.44}$$

$$\Delta\tilde{\boldsymbol{u}}^{**}_{l,k} = -\frac{\nabla\bar{p}_{k+1}}{\bar{\rho}}\Delta t + \frac{1}{\bar{\rho}}\sum \boldsymbol{f}_{l,\text{int}} \tag{3.2.45}$$

where $\boldsymbol{f}_{l,\text{int}}$ is the vector of the interaction force from other fluid particles whose densities are different from the targeted particle, namely a kind of another phase in the same MPS discretization space. Similar to the two-fluid-based model, the Poisson Pressure Equation is obtained by integrating each phase (particle) and eliminating the interaction $\boldsymbol{f}_{l,\text{int}}$ as:

$$\nabla^2\bar{p}_{k+1} = \frac{\bar{\rho}}{(\Delta t)^2}\frac{n^*_k - n_0}{n_0} \tag{3.2.46}$$

Utilizing the updated fluid velocity $\tilde{\boldsymbol{u}}^{**}_{l,k}$ obtained from these processes, the motion of the solid particle *i* is calculated as:

$$\sum_j \left(\rho_s \phi_{ji,k}\right)\frac{\Delta\boldsymbol{u}_{i,k}}{\Delta t} = \sum_j \left[\left\{\bar{\rho}_{j,k}\frac{\Delta\tilde{\boldsymbol{u}}^{*}_{j,k} + \Delta\tilde{\boldsymbol{u}}^{**}_{j,k}}{\Delta t} - \boldsymbol{F}_{\text{int},j,k}\right\}\phi_{ji,k}\right] + \boldsymbol{f}_{colp,i} \tag{3.2.47}$$

$$\sum_j \left(\rho_i \phi_{ji,k}\left|\boldsymbol{r}_{ji,k}\right|^2\right)\frac{\Delta\boldsymbol{\omega}_{i,k}}{\Delta t} = \sum_j \left[\boldsymbol{r}_{ji,k} \times \left\{\bar{\rho}_j\frac{\Delta\tilde{\boldsymbol{u}}^{*}_{j,k} + \Delta\tilde{\boldsymbol{u}}^{**}_{j,k}}{\Delta t} - \boldsymbol{F}_{\text{int},j,k}\right\}\phi_{ji,k}\right] + \boldsymbol{T}_{colp,i} \tag{3.2.48}$$

Similar to the single-phase-flow model, the soli-liquid interaction $\boldsymbol{F}_{\text{int}}$ occurred by the weak-coupling between the solid and liquid discretization process is obtained to be given to the velocity of the multi-phase liquid flows as:

$$\tilde{\boldsymbol{u}}_{j,k+1} = \sum_j \left(\boldsymbol{u}_{i,k+1} + \boldsymbol{r}_{ji,k+1}\times\boldsymbol{\omega}_{i,k+1}\right)\phi_{ji,k+1} + \left(1 - \sum_j \phi_{ji,k+1}\right)\tilde{\boldsymbol{u}}^{**}_{i,k} \tag{3.2.49}$$

The solid-liquid interaction is estimated as:

$$\boldsymbol{F}_{\text{int},,j,k} = \frac{\bar{\rho}_{i,k}\tilde{\boldsymbol{u}}_{j,k} - \bar{\rho}_{j,k-1}\tilde{\boldsymbol{u}}^{**}_{j,k-1}}{\Delta t} \tag{3.2.50}$$

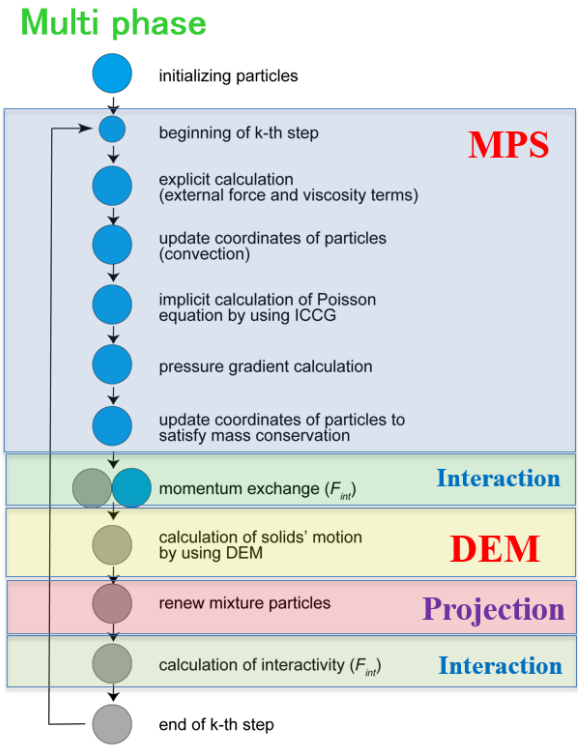

Fig. 3.2.7 Flowchart of the multi-phase-model

Fig. 3.2.7 illustrates the flowchart of the algorithm of this proposed model.

3.2.4 Verification of the proposed DEM-MPS methods

To verify the validity of the proposed three models, 2D numerical simulations targeting on a semi-2D solid-liquid two-phase dam breaking experiment by Shuai Zhang () [] are performed by the proposed models.

3.2.4.1 Experimental condition

The tank in the experiment by Shuai Zhang is set with 26.0 cm in length, 26.0 cm in height and 10.0 cm in depth. As for the initial condition, as shown in **Fig. 3.2.8 (A)**, a gate is set at a distance of 6.0 cm from the left wall of the tank, and 33th cylinders with a diameter d_s = 6.0 cm are piled together with water (12.0 cm in depth) on the left side of the gate. The density of the cylinder is $\rho_s = 2.7\times10^3$ kg/m^3, its diameter is d_s = 6.0 cm and its length is l_s = 9.9cm. The arrangement of the piled cylinders are set as 6th, 5th, 6th, 5th… in order from the bottom of the tank. Firstly, the gate is pulled up rapidly with v = 2.0 m/s, and after, the motions of the cylinders and water in the dam breaking process are shot by a high-speed camera.

3.2.4.2 Simulation condition

The diameter of the liquid particle for the MPS calculation is set as d_l = 0.1 cm in each model. As for the diameter of the solid particle, in Model 2 and 3, it is set as d_s = 1.0 cm corresponding to that of the experiment. While, the Model 1 corresponding to the two-fluid-based model combines solid particles by

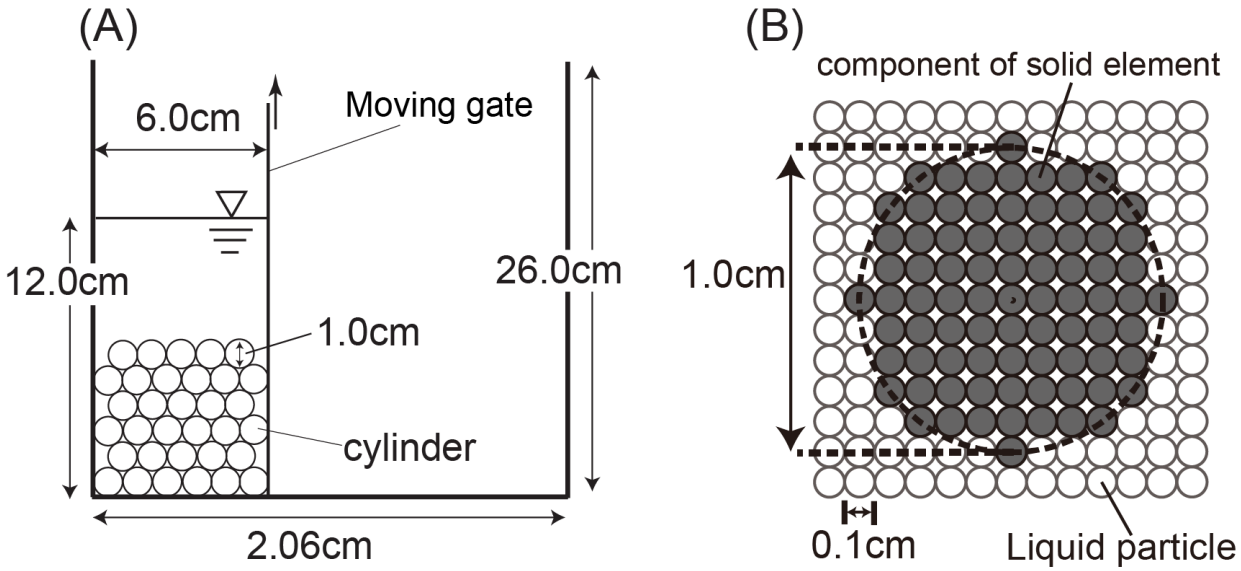

Fig. 3.2.8 Illustration of (A) the initial condition by experiment and numerical simulations and (B) the definition of solid particles of the two-fluid-based model in simulation of solid-liquid two-phase dam breaking

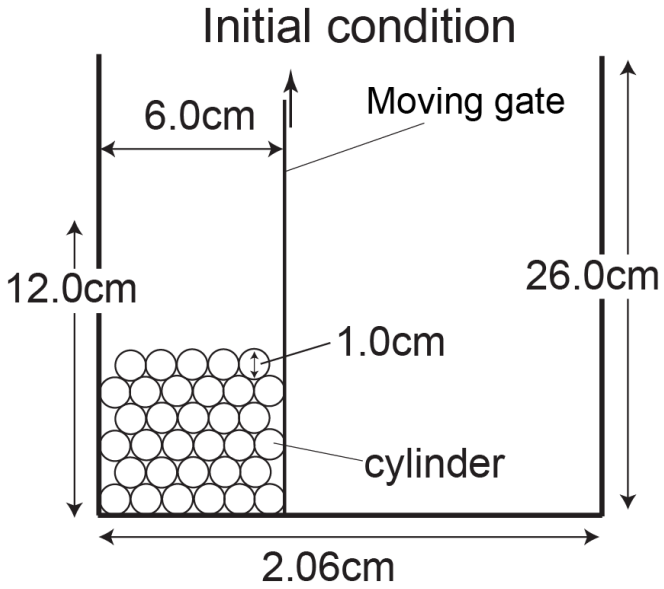

Fig. 3.2.9 Initial condition of cylinder dam breaking by the experiment and simulations by Model 1, 2 and 3

the rigid connection. Here, the particles in the circles with d_c = 1.0 cm distributed at the initial condition as shown in **Fig. 3.2.8 (B)** are defined as components of the solid elements. The other conditions about the size of the tank, water depth and the speed of the gate pulled up are set same as the experiment.

In the DEM calculation, each model needs some tuning parameters for the solid-solid interaction. In this study, targeting on a dam breaking of cylinders without water by Shuai Zhang [14], the parameters are chosen so as to reproduce the experimental result (refer to **Fig. 3.2.9**, **Fig. 3.2.10** and **Table. 3.2.1**).

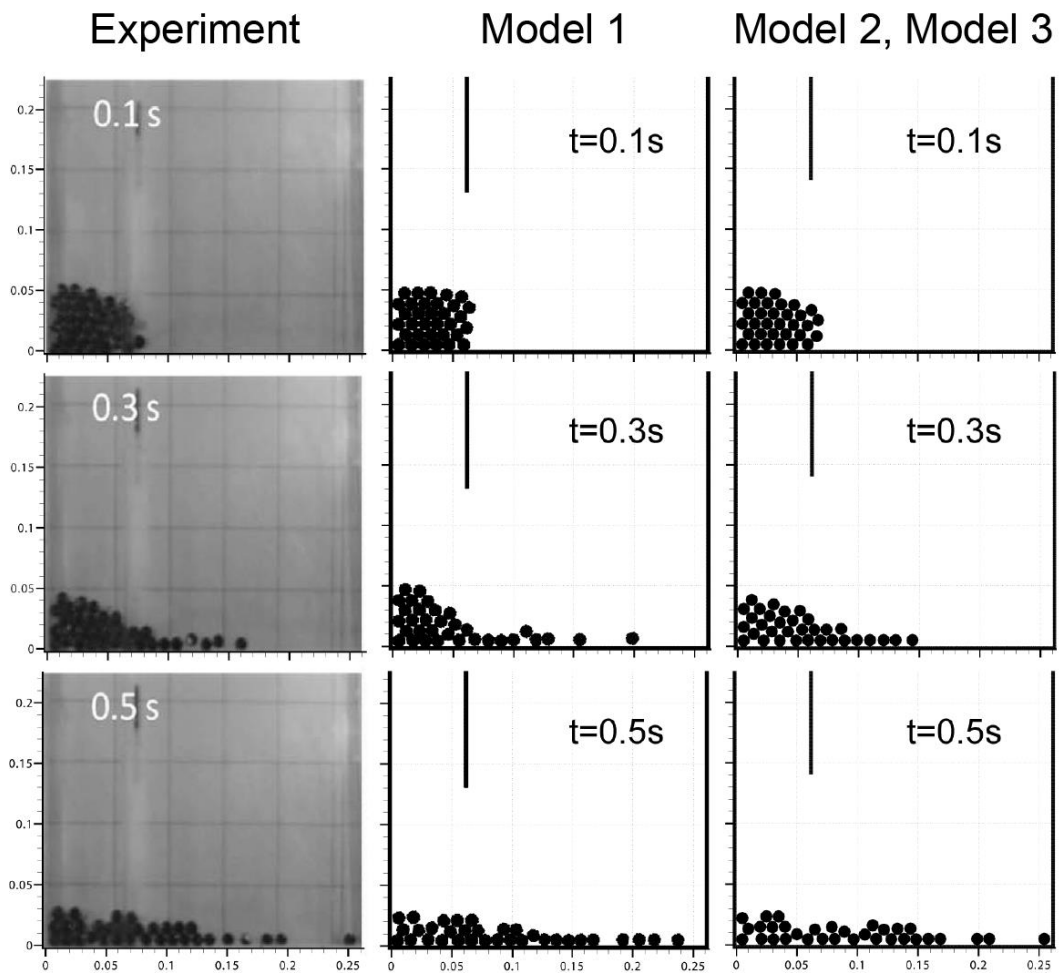

Fig. 3.2.10 Snapshots of the cylinder dam breaking by the experiment and the simulations by Model 1, 2 and 3

Table 3.2.1 Tuning parameters of the DEM

	Model 1	Model 2, Model 3
Young's module	1.0×10^6	7.5×10^5
Friction coefficient of cylinder	0.001	0.270
Friction coefficient of wall	0.06	0.230
Poisson's ratio	0.250	0.250

3.2.4.3 Results of numerical simulation and experiment

Fig. 3.2.11 shows the snapshots of the two-phase dam breaking by the experiment and simulation results by Model 1, 2 and 3 at time t = 0.1 s, 0.3 s and 0.5 s. In the experimental result, the pile of the cylinders collapse gradually from its right edge at time t = 0.1 s. At time t = 0.3 s, the cylinders are classified into three groups; **Group.1** Cylinder driven fast at the right side of the tank, **Group.2** Cylinders driven slowly at the center of the tank and **Group.3** Cylinders settled at the left side of the tank. Moreover, the settled cylinders corresponding to the Group.3 lean to the right. At time t = 0.5 s, the cylinders corresponding to the Group.3 collapse gradually and some of them start to move to right side. On the other hand, the Group.1 and 2 join each other group near the right wall of the tank. At the end, cylinders classified into two groups,

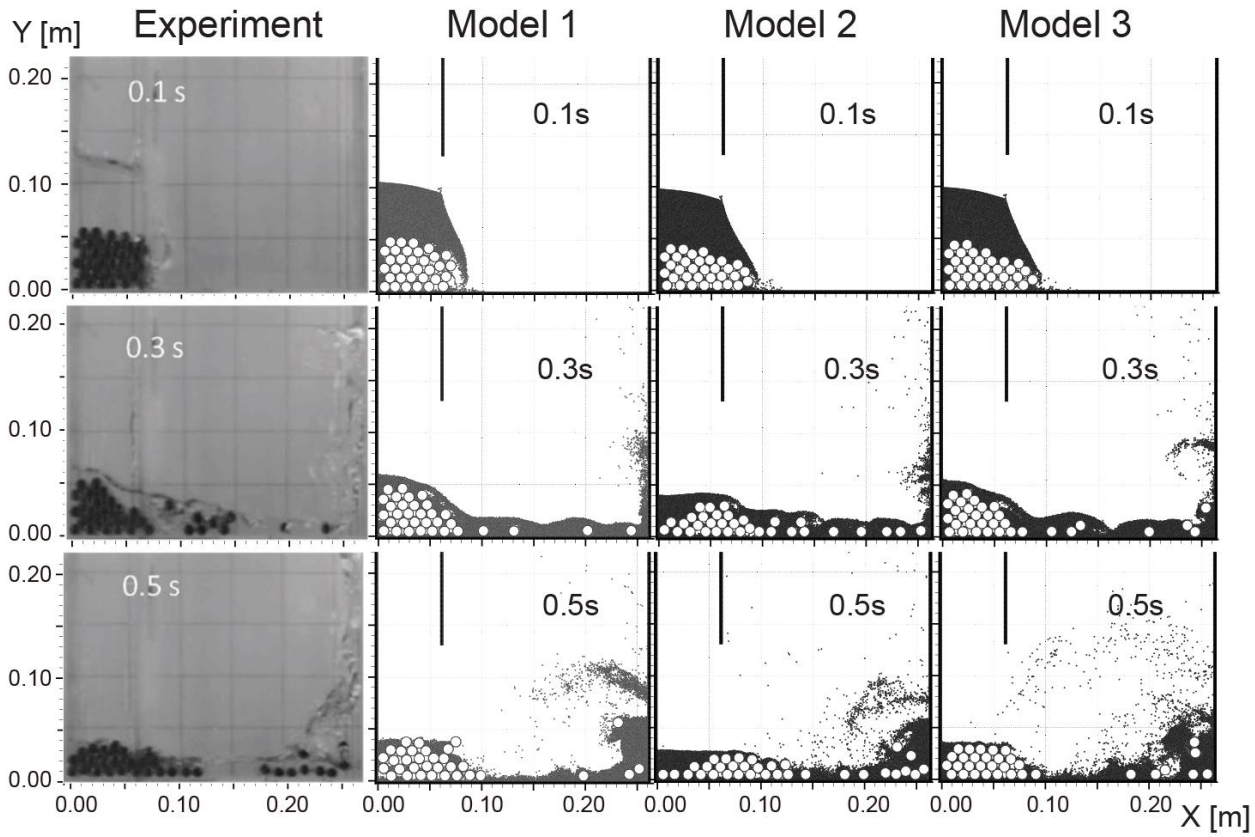

Fig. 3.2.11 Snapshots of the two-phase dam breaking by the experiment and simulations by Model 1, 2 and 3

namely the left side group and the right side group. As for the simulation results, at time t = 0.1 s, all the models show that both cylinder and water moves to the right side excessively. In the experiment, small opening spaces with 0.05cm are set between the cylinders and the both front and back walls, and thus, water flows into the vacant spaces between cylinders as they moving through the opening spaces. While, the simulation based on the two-dimension space cannot give the opening spaces and water is not supplied through the spaces. Consequently, some void spaces occur between moving cylinders where water particles cannot flow into, and may result in the lack of the sufficient solid-liquid interactions. In addition, it might be another cause that surface tension model is not introduced into the proposed models. At time t = 0.3 s, Model 1 and 3 show that their cylinders are clearly classified into three groups as the experimental result, and further, the inclinations of the settled cylinders corresponding to the Group.3 are similar to the experimental result. While, in Model 2, the cylinders move excessively comparing with the experimental result, moreover, the behaviors of the cylinders and the inclination of the settled cylinders near the let wall disagree with that of the experiment. Furthermore, the form of the free surface of water obviously differs from that of the experiment. At time t = 0.5 s, Model 1 and 3 show well-reproductions of the experimental result. In both models, the cylinders are classified into the left side group and the right side group. The shapes of the cluster by the settled cylinders reproduce the slants, which upwards left-to-right and downwards left-to-right, respectable. Moreover, the water-storage near the left wall is also reproduced in both simulation results. Comparing Model 1 with Model 3, the number of the settled cylinders corresponding to the Group.3 is different. In Model 1, the cylinders are expressed by the rigid connection,

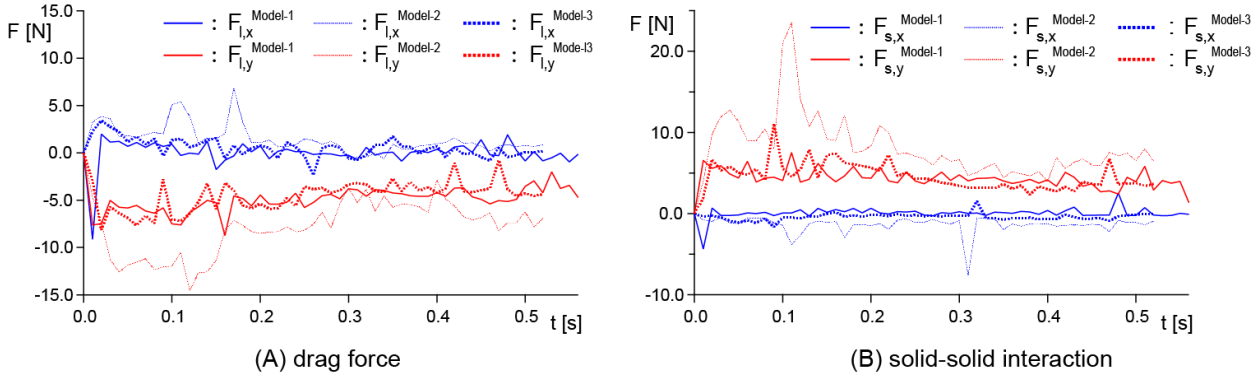

Fig. 3.2.12 Time series of the averaged interaction forces working on solid elements in solid-liquid two-phase dam breaking simulation by Model 1, 2 and 3: (a) Drag force by water and (b) Collision force between solid elements.

accordingly, they contain the unevenness shapes on their surfaces and increase the frictions. As a result, it is supposed that Model 1 disperses the momentum of the cylinder and suppresses the transfer of the cylinders more than Model 3. As for Model 2, it mostly disagrees with the experimental result.

Fig. 3.2.12 shows time series of the averaged interaction forces working on the solid elements (cylinders) in each simulation result. This figure shows (a) the drag force by water and (b) the collision force between the solid elements. From (a) in this figure, Model 2 shows relative small forces $F_{l,y}^{Model2}$ at y direction within time t = 0.01 s - 0.15 s. In Model 2, the solid density is not reflected to the fluid flows, consequently, the motions of the flows are unlikely to be hindered by the solid elements and the mainstream is likely to grow. Therefore, it is supposed that the downward drag force increase for the reason, so that it results in the disagreement with experimental result. On the other hand, Model 1 and Model 3 do not show clear difference between them. It is remarkable that all the interactions of both models almost correspond to each other in spite of the large difference of the tuning parameters between them. This implies that Model 1 and 3 give the comprehensively accurate result only by setting appropriate tuning parameters of the DEM.

3.2.4.4 Concluding remarks

Model 1 and Model 3 show the good reproducibility. However, Model 1 contains the unevenness on the surface of the solid elements, consequently, its excessive friction may possibly bring about unphysical solid-solid interactions. Indeed, in this benchmark, the friction coefficient is set as μ = 0.01 for Model 1, therefore, it seems difficult to be applied to phenomenon with more violent transports of solid elements by the significant friction, such as slide or tumbling. This is a crucial problem.

3.2.5 Model 4: improved two-fluid-based model

Here, the two-fluid-based model proposed in the paragraph 3.2.1 is improved for more accurate calculation of both fluid flow and solid motion [13]. As shown in the previous paragraph, the proposed Model 1 (the two-fluid-based model) has a problem about the reproducibility of friction of solid structures. To resolve this, a new framework for accurate tracking of the rigid structures is proposed. Simultaneously, the steering of the Laplacian for the Poisson Pressure Equation is improved to accommodate the distribution of various

densities for the multi-phase flows. This proposed model is a kind of the mixture model of the two-fluid-flow model and multi-phase-hybrid model.

3.2.5.1 Governing equations

The governing equations are described in a similar manner to the proposed two-fluid-based model (Model 1). The Continuity equations are:

$$\frac{D\rho_l}{Dt} + \rho_l \nabla \cdot \boldsymbol{u}_l = 0 \tag{3.2.51}$$

$$\frac{D\rho_l}{Dt} + \rho_l \nabla \cdot \boldsymbol{u}_l = 0 \tag{3.2.52}$$

The momentum equations of each phase are described as:

$$\rho_l \frac{D\boldsymbol{u}_l}{Dt} = -\nabla p_l + \mu_l \nabla^2 \boldsymbol{u}_l + \rho_l \boldsymbol{g} + \boldsymbol{f}_{ls,l} \tag{3.2.53}$$

$$\rho_s \frac{D\boldsymbol{u}_s}{Dt} = -\nabla p_s + \mu_s \nabla^2 \boldsymbol{u}_s + \rho_s \boldsymbol{g} - \boldsymbol{f}_{ls,s} + \boldsymbol{f}_{colp} \tag{3.2.54}$$

$$\begin{cases} \boldsymbol{f}_{ls,l} = -\left(-\nabla p_l + \mu_l \nabla^2 \boldsymbol{u}_l\right)_s \\ \boldsymbol{f}_{ls,s} = \left(-\nabla p_s + \mu_s \nabla^2 \boldsymbol{u}_s\right)_l \end{cases} \tag{3.2.55}$$

The subscript *l* and *s* denote the liquid phase and the solid phase, respectably. The numerical procedure of the fluid flow by the MPS method is similar to the two-fluid-based model. In this study, for calculation of fluid flows, the accurate particle method corresponding to the CMPS-HS-HL method is introduced. The solid-solid interaction $\boldsymbol{f}_{colp}$ is estimated by the DEM with the PMS model.

3.2.5.2 Improvement of the accurate particle method

In the MPS framework, the Poisson Pressure Equation (PPE) is described with the replacement of the density by the particle number density as:

$$\left\langle \nabla^2 p \right\rangle_i^{k+1} = \frac{\rho}{n_0 \Delta t} \left(\frac{Dn}{Dt} \right)^* \tag{3.2.56}$$

where *k* is time step, r_e is the radius of the influence area, $\boldsymbol{u}_{ij}$ is the vector of the relative velocity of particle *i* from particle *j* as $\boldsymbol{u}_{ij} = \boldsymbol{u}_j - \boldsymbol{u}_i$. The subscript * denotes a projection variant by the first stage of the projection scheme. In the multi-phase flow, the distribution of the density is not uniform in the domain. Here, considering the fact, the divergence of the density is introduced into the HL-based Laplacian of pressure. In the HL scheme [15], a gradient of a physical quantity is expressed as:

$$\langle \nabla \phi \rangle_i = \frac{1}{\sum_{i \neq j} w_{ij}} \sum_{i \neq j} \phi_{ij} \nabla w_{ij} \; ; \qquad \phi_{ij} = \phi_j - \phi_i \tag{3.2.57}$$

where ϕ is a physical quantity, w_{ij} is the kernel function between particles i and j. From this equation, the Laplacian of the variant at particle i is written as:

$$\nabla \cdot \langle \nabla \phi \rangle_i = \frac{1}{n_0} \sum_{i \neq j} \left(\nabla \phi_{ij} \cdot \nabla w_{ij} + \phi_{ij} \nabla^2 w_{ij} \right) \tag{3.2.58}$$

Considering the density in Eq. (3.2.56):

$$\begin{aligned} \nabla \cdot \left\langle \frac{\nabla \phi}{\rho} \right\rangle_i &= \frac{1}{\rho_i} \left(\nabla \cdot \langle \nabla \phi \rangle_i \right) + \nabla \left(\frac{1}{\rho_i} \right) \cdot \langle \nabla \phi \rangle_i \\ &= \frac{1}{n_0} \sum_{i \neq j} \left(\frac{1}{\rho_i} \left(\nabla \phi_{ij} \cdot \nabla w_{ij} + \phi_{ij} \nabla^2 w_{ij} \right) \right) + \frac{1}{n_0} \sum_{i \neq j} \left(\nabla \left(\frac{1}{\rho_i} \right) \cdot \left(\phi_{ij} \nabla w_{ij} \right) \right) \end{aligned} \tag{3.2.59}$$

The gradients of the physical quantity ϕ_{ij} and the kernel function w_{ij} are:

$$\begin{cases} \nabla \phi_{ij} = \dfrac{\partial \phi_{ij}}{\partial \boldsymbol{r}_{ij}} \dfrac{\partial \boldsymbol{r}_{ij}}{\partial x_{ij}} \boldsymbol{i} + \dfrac{\partial \phi_{ij}}{\partial \boldsymbol{r}_{ij}} \dfrac{\partial \boldsymbol{r}_{ij}}{\partial y_{ij}} \boldsymbol{j} + \dfrac{\partial \phi_{ij}}{\partial \boldsymbol{r}_{ij}} \dfrac{\partial \boldsymbol{r}_{ij}}{\partial z_{ij}} \boldsymbol{k} \\ \nabla w_{ij} = \dfrac{\partial w_{ij}}{\partial \boldsymbol{r}_{ij}} \dfrac{\partial \boldsymbol{r}_{ij}}{\partial x_{ij}} \boldsymbol{i} + \dfrac{\partial w_{ij}}{\partial r_{ij}} \dfrac{\partial \boldsymbol{r}_{ij}}{\partial y_{ij}} \boldsymbol{j} + \dfrac{\partial w_{ij}}{\partial \boldsymbol{r}_{ij}} \dfrac{\partial \boldsymbol{r}_{ij}}{\partial z_{ij}} \boldsymbol{k} \end{cases} \tag{3.2.60}$$

By decomposing the second term in the right hand side of Eq. (3.2.59), the following equations are obtained as:

$$\begin{aligned} \nabla \left(\frac{1}{\rho_i} \right) &= \frac{\partial}{\partial \boldsymbol{r}_{ij}} \left(\frac{1}{\rho_i} \right) \frac{\partial \boldsymbol{r}_{ij}}{\partial x_{ij}} \boldsymbol{i} + \frac{\partial}{\partial \boldsymbol{r}_{ij}} \left(\frac{1}{\rho_i} \right) \frac{\partial \boldsymbol{r}_{ij}}{\partial x_{ij}} \boldsymbol{j} + \frac{\partial}{\partial \boldsymbol{r}_{ij}} \left(\frac{1}{\rho_i} \right) \frac{\partial \boldsymbol{r}_{ij}}{\partial z_{ij}} \boldsymbol{k} \\ &= \frac{\frac{1}{\rho_j} - \frac{1}{\rho_i}}{\boldsymbol{r}_{ij}} \frac{\partial \boldsymbol{r}_{ij}}{\partial x_{ij}} \boldsymbol{i} + \frac{\frac{1}{\rho_j} - \frac{1}{\rho_i}}{\boldsymbol{r}_{ij}} \frac{\partial \boldsymbol{r}_{ij}}{\partial y_{ij}} \boldsymbol{j} + \frac{\frac{1}{\rho_j} - \frac{1}{\rho_i}}{\boldsymbol{r}_{ij}} \frac{\partial \boldsymbol{r}_{ij}}{\partial y_{ij}} \boldsymbol{k} \end{aligned} \tag{3.2.61}$$

$$\phi_{ij} \nabla w_{ij\,i} = \phi_{ij} \frac{\partial w_{ij}}{\partial \boldsymbol{r}_{ij}} \frac{\partial \boldsymbol{r}_{ij}}{\partial x_{ij}} \boldsymbol{i} + \phi_{ij} \frac{\partial w_{ij}}{\partial \boldsymbol{r}_{ij}} \frac{\partial \boldsymbol{r}_{ij}}{\partial y_{ij}} \boldsymbol{j} + \phi_{ij} \frac{\partial w_{ij}}{\partial \boldsymbol{r}_{ij}} \frac{\partial \boldsymbol{r}_{ij}}{\partial z_{ij}} \boldsymbol{k} \tag{3.2.62}$$

Therefore, the second term in the right hand side of Eq. (3.2.59) is:

$$\nabla\left(\frac{1}{\rho_i}\right)\cdot\left(\phi_{ij}\nabla w_{ij}\right)=\frac{\phi_{ij}}{\boldsymbol{r}_{ij}}\left(\frac{1}{\rho_j}-\frac{1}{\rho_i}\right)\frac{\partial w_{ij}}{\partial \boldsymbol{r}_{ij}}\left(\frac{\partial \boldsymbol{r}_{ij}}{\partial x_{ij}}\right)^2+\frac{\phi_{ij}}{\boldsymbol{r}_{ij}}\left(\frac{1}{\rho_j}-\frac{1}{\rho_i}\right)\frac{\partial w_{ij}}{\partial \boldsymbol{r}_{ij}}\left(\frac{\partial \boldsymbol{r}_{ij}}{\partial y_{ij}}\right)^2+\frac{\phi_{ij}}{\boldsymbol{r}_{ij}}\left(\frac{1}{\rho_j}-\frac{1}{\rho_i}\right)\frac{\partial w_{ij}}{\partial \boldsymbol{r}_{ij}}\left(\frac{\partial \boldsymbol{r}_{ij}}{\partial z_{ij}}\right)^2$$
$$=\frac{\phi_{ij}}{\boldsymbol{r}_{ij}}\left(\frac{1}{\rho_j}-\frac{1}{\rho_i}\right)\left(-\frac{r_e}{\boldsymbol{r}_{ij}^2}\right)\frac{x_{ij}^{\,2}+y_{ij}^{\,2}+z_{ij}^{\,2}}{\boldsymbol{r}_{ij}^{\,2}}$$
$$=-\frac{\phi_{ij}r_e}{\boldsymbol{r}_{ij}^3}\left(\frac{1}{\rho_j}-\frac{1}{\rho_i}\right) \tag{3.2.63}$$

Moreover, substituting Eq. (3.2.63) into (3.2.59), the following equation is obtained as:

$$\nabla\cdot\left\langle\frac{\nabla\phi}{\rho}\right\rangle_i=\frac{1}{n_0}\left[\sum_{i\neq j}\left(\frac{2\phi_{ij}r_e}{\rho_i\boldsymbol{r}_{ij}^3}\right)+\sum_{i\neq j}\left(-\frac{\phi_{ij}r_e}{\boldsymbol{r}_{ij}^3}\left(\frac{1}{\rho_j}-\frac{1}{\rho_i}\right)\right)\right]$$
$$=\frac{1}{n_0}\left[\sum_{i\neq j}\left(\frac{\phi_{ij}r_e}{\rho_i\boldsymbol{r}_{ij}^3}\left(\frac{3}{\rho_j}-\frac{1}{\rho_i}\right)\right)\right] \tag{3.2.64}$$

Together with the above transform, the Poisson Pressure Equation would possess the anti-symmetric matrix. For this problem, the solving method for the matrix is changed from the widely used solution for the MPS method corresponding to the ICCG method to the BiCGStab method, which can solve the anti-symmetric matrix stably.

As for the viscosity term, the Laplacian is estimated by the standard HL formula:

$$\nabla\cdot\left\langle\nabla\phi\right\rangle_i=\frac{1}{n_0}\sum_{i\neq j}\left(\frac{2\phi_{ij}r_e}{\rho_i r_{ij}^3}\right) \tag{3.2.65}$$

3.2.5.3 Solid model

The solid structure is tracked on the basis of the multi-scale-link DEM-MPS method by Gotoh et al. (2003) to capture the fluid flow with a high resolution. Then, the solid structure is modeled by the Passively Moving Solid model by Koshizuka et al., namely it is composed of plural components corresponding to the solid particles in the MPS discretization space. Therefore, the surface of the structure contains unevenness with the component-scale, which has a bad influence on the accuracy of estimation of solid-solid interactions. To resolve this problem, hereby, an additional DEM particle is set for tracking of the structure with its identical diameter, and the DEM particle is tracked in the different discretization space from the MPS particles for the fluid flow as shown in **Fig. 3.2.13**.

The momentum equations of the translational and rotational motions of the structure are described with the drag force obtained from the MPS particles and the collision force between structures as:

$$m_S\frac{d\boldsymbol{u}_S}{dt}=\sum_N\rho_N\left(\frac{D\boldsymbol{u}_N}{Dt}-\frac{\boldsymbol{f}_{colp}}{\rho_s}\right)+\boldsymbol{F}_{colp};\qquad m_S=\sum_N\rho_N \tag{3.2.66}$$

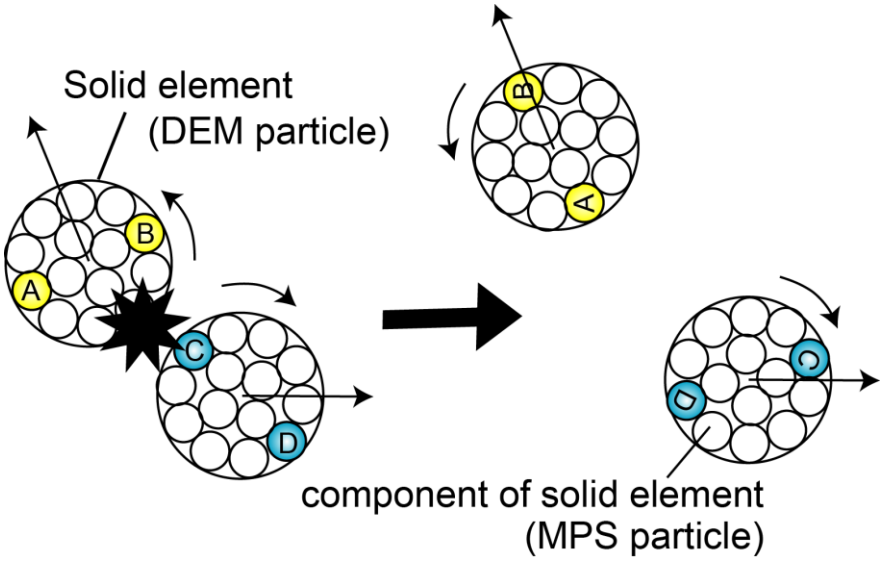

Fig. 3.2.13 Illustration of the concept of the solid-liquid coupling scheme by Model 4

$$\boldsymbol{I}_S \frac{d\boldsymbol{\omega}_S}{dt} = \sum_N \left[\rho_N \boldsymbol{r}_{NS} \times \left(\frac{D\boldsymbol{u}_N}{Dt} - \frac{\boldsymbol{f}_{colp}}{\rho_s} \right) \right] + \boldsymbol{T}_{colp}; \qquad \boldsymbol{I}_S = \sum_N \rho_N \left| \boldsymbol{r}_{NS} \right|^2 \tag{3.2.67}$$

where $\boldsymbol{f}_{colp}$ is the interaction between components of the solid DEM particles as fluids estimated by the MPS method, $\boldsymbol{F}_{colp}$ is the vector of the solid-solid interaction and $\boldsymbol{T}_{colp}$ is the vector of the torque force by the solid-solid collision. The subscripts *S* and *N* denote a DEM particle representing the targeted structure and a MPS particle as a component of the targeted structure for the fluid calculation, respectably. After tracking the solid structures, the velocities and positions of the MPS solid particles are updated by using the translational and rotational velocities of the structures as:

$$\boldsymbol{u}_N^{k+1} = \boldsymbol{u}_N^k + \int_t^{t+\Delta t} \left(\frac{d\boldsymbol{u}_S^k}{dt} + \boldsymbol{r}_{NS} \times \frac{d\boldsymbol{\omega}_S^k}{dt} \right) dt \tag{3.2.68}$$

The solid-solid fluid interaction $\boldsymbol{f}_{colp}$ is defined as:

$$\boldsymbol{f}_{colp} = \rho_s \left(\frac{d\boldsymbol{u}_S}{dt} + \boldsymbol{r}_{NS} \times \frac{d\boldsymbol{\omega}_S}{dt} \right) - \left(-\nabla p_s + \mu_s \nabla^2 \boldsymbol{u}_s + \rho_s \boldsymbol{g} - \boldsymbol{f}_{ls,s} \right) \tag{3.2.69}$$

3.2.6 Verification of the proposed model (Model 4)

To verify the validity, the 3D-based proposed model is employed to solve the violent free-surface flows caused by solid elements dumped into water. The prediction of behaviors of violently deformed free-surface flows is critical issue for coastal engineering problems, such as a construction of settling blocks

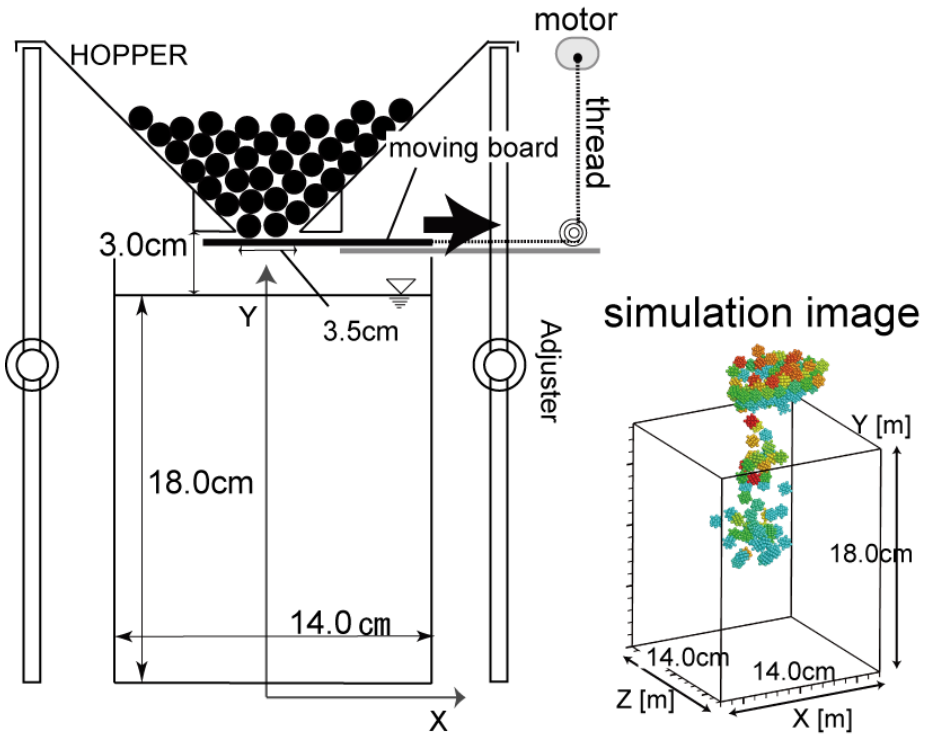

Fig. 3.2.14 Illustration of the initial condition in sedimentation process of dumped blocks by experiment and numerical simulation

from the bottom of a barge-ship. However, the numerical studies seldom focus on complicated eddies around the settling blocks and the violent free-surface flows due to the instability. In this study, the eddy structures around settling particles are investigated from the viewpoint of the computational physics with a high resolution, and additionally, the performance of the newly developed DEM-MPS method is verified by comparison with experimental results for sedimentation.

3.2.6.1 Experimental condition

As shown in **Fig. 3.2.14**, from a hopper set on the top of a tank, 150th circular blocks with diameter d_s = 1.0 cm and density σ =1318.0 kg/m^3 are dumped into the water. The sedimentation process of the dumping particles is shot by a high-speed camera. The size of the tank is set as $X \times Y \times Z$ =14.0 × 18.5 × 14.0 cm^3, and the tank comprises water with 18.0 cm in depth. The gate of the hopper is controlled by a motor and is opened with a speed $\boldsymbol{u}_{\text{gate}}$ = 28.0 cm/s.

3.2.6.2 Simulation condition

The simulation condition is set in equal to the experimental condition. The MPS particles are set with diameter d_m = 0.25 cm for both solid and liquid phases. The calculation domain comprises totally 296,790th MPS particles. The DEM particle are set with diameter d_s = 1.0 cm with correspondence to that of the experiment. As for the tuning parameters for the DEM calculation, they are chosen so as to reproduce the time spending on excretion of all the solid blocks from the inlet of the hopper in the experiment result.

3.2.6.3 Results of simulation and experiment

The **Fig. 3.2.15** shows snapshots of results of the experiment and the numerical simulation. The

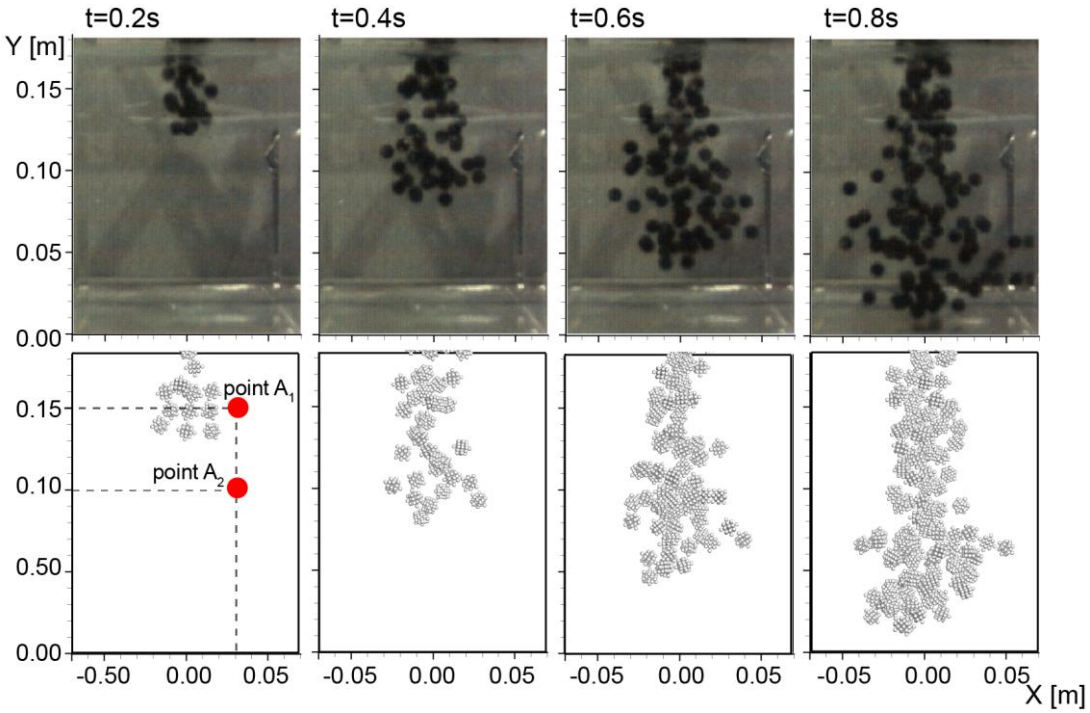

Fig. 3.2.15 Snapshots of sedimentation process of dumped blocks by experiment and numerical simulation

experimental result shows that the settling blocks significantly spread at the front of the bunch of the setting blocks. The simulation result also shows a similar state. Moreover, from the position of the front of the brunch of each result, it is found that the setting velocities and spreading velocities of the blocks in the simulation result agree well with that of experiment. To some extent, the proposed model reproduces the settlement process of blocks in water.

3.2.6.4 Analysis of simulation result

Fig. 3.2.16 shows the time series of the averaged drag force working on each settling block (top: horizontal drag force, bottom: vertical drag force). Considering the fact that settling blocks behave symmetrical motions through the *YZ* plane (X = 0.0 m), only the zone defined as $X \geqq 0.0$ m is targeted for the sampling. The interaction forces are sampled separately in accordance with heights as; A: $0.18 \geqq Y > 0.15$ m, B: $0.15 \geqq Y > 0.10$ m, C: $0.10 \geqq Y > 0.05$ m. From the horizontal drag force, it is found that the group C is given the positive force on the whole, and as a result, its spread is promoted. The zone A, which corresponds to the position nearest the free surface, shows a larger fluctuation of the drag force comparing with other zones. It is supposed that the cause of this stems from the disturbance of the free surface doe to the continuously bumped blocks. The vertical drag force also shows a large fluctuation in the zone A.

Fig. 3.2.17 shows velocity fields and vorticity fields at the *XY* plane ($-0.5d > Z > 0.5d$) in the simulation result. As for the velocity fields, the vortexes appear with a scale of the inlet of the hopper at both sides of the inlet from time t = 0.4 s. It is supposed that the vortexes are induced by the large gradient of velocity between the falling stream grown by the settling blocks and the static surrounding-fluid. These vortexes rapidly grow at time t = 0.4 s ~ 0.6 s, when the front of the bunch of setting blocks reach the height at Y = 0.10 ~ 0.05 m. Since this height corresponds to the zone C showing a significant spread of blocks in **Fig. 3.2.15**, it is grasped that the settling blocks are promoted to spread by the large vortexes. On the other

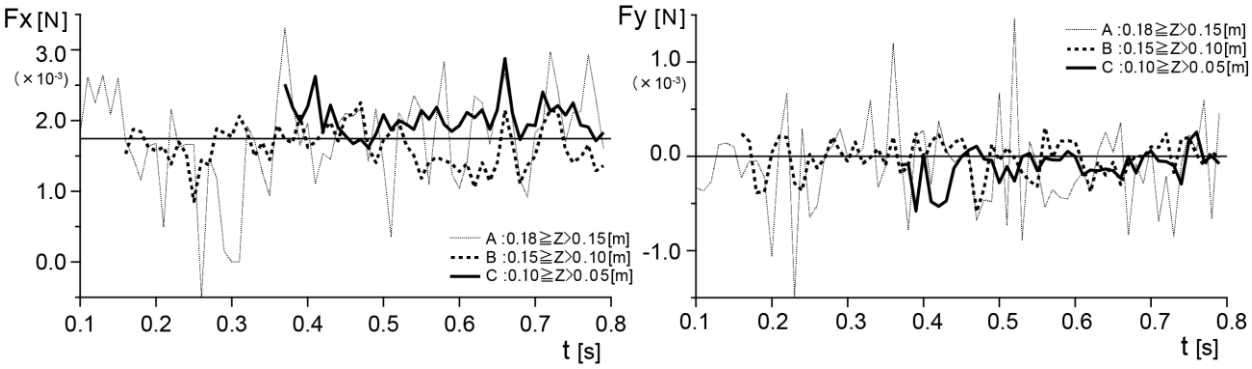

Fig. 3.2.16 Time series of the averaged drag force working on settling blocks in simulation of sedimentation process of dumped blocks: (top) the horizontal drag force and (bottom) the vertical drag force

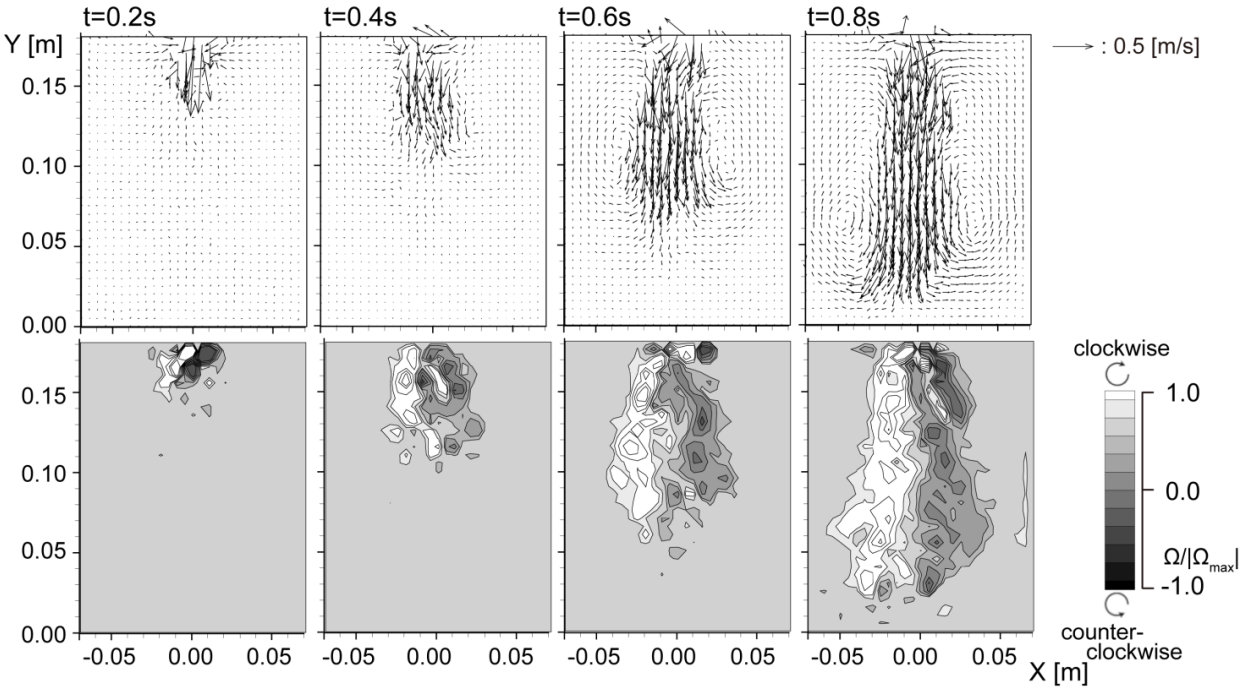

Fig. 3.2.17 Velocity field and velocity field in simulation of sedimentation process of dumped blocks: (top): velocity field at *XY* plane (-0.5*d* > *Z* > 0.5*d*), (bottom) vorticity field at *XY* plane (-0.5*d* > *Z* > 0.5*d*)

hand, any significant vortex is not recognized at the side of the following blocks bumped after time $t = 0.4$ s. In the neighborhood of following blocks except the front of the bunch of the settling blocks, it is clearly shown that the falling stream grows as drawing its surrounding fluid, so that the gradient of velocity between them cannot be grown due to the acceleration by the drawing. As for the vorticity field, vorticity is steeply fluctuated around the settling blocks at any time. In particular, this tendency is obviously appeared around the free surface, and thus, it implies that bumping or settling blocks exchanges the momentum with surrounding fluids actively.

Fig. 3.2.18 shows the time series of horizontal and vertical velocities at the positions A_1 and A_2 (refer to **Fig. 3.2.15**). As for the horizontal velocity u at the position A_1, it shows a fluctuation with time

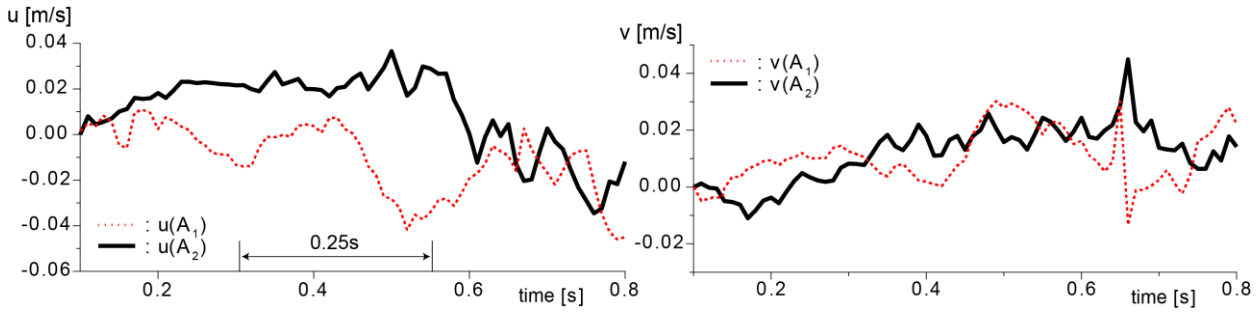

Fig. 3.2.18 Time series of velocities at the positions of A_1 and A_2 (top: Horizontal velocity) and (bottom: vertical velocity)

interval Δt = 0.25 s from time t = 0.3 s. While, at the position A_2, the positive horizontal velocity is reversed to the negative one at time t = 0.6 s. The cause of this is supposed to be the large vortexes at the sides of the front of the bunch of the settling blocks. Noticing the graph of the position A_2, the fine fluctuations are found in the vertical velocity. Watching the movie of the simulation result, it is recognized that it is caused by the settling blocks.

3.2.6.5 Concluding remarks

In this study, a numerical simulation is performed by the proposed DEM-MPS method (Model 4) targeting on an experiment of a sedimentation process of numerous blocks bumped into water. Compering the simulation result with that of the experiment, some extent validity of the proposed model is recognized. From the existing studies, it is known that large vortexes besides the settling blocks are key factors to decide the behaviors of the settling blocks. In this study, such significant vortexes emerge around the free surface and keep the same position against the well-known falling vortexes besides the settling blocks. The simulation result shows their effects quantitatively and has found its significance for prediction of behaviors of settling structures in water.

REFERENCES

[1] Gotoh, H., M., Hayashi, S., Andoh and T., Sakai, "SOLID-LIQUD TWO PHASE FLOW MODEL BASED ON LAGLANGIAN PARTICLE METHOD FOR THE SIMULATION OF WATER WAVE GENERATION DUE TO LANDSLIDES", *Proceedings of JSCE*, Vol.719, pp.31-45, 2002.

[2] Gotoh, H., M., Hayashi, S., Andoh and T., Sakai, "Lagrangian coupling for solid-liquid two phase flow by DEM-MPS method", *Proceedings of hydraulic engineering, JSCE.*, Vol.47, pp.547-552, 2003.

[3] Ikari, H., H., Gotoh and T., Sum, "Computational Mechanics of a blocking of gateless bottom outlet by drift woods", *Proceedings of hydraulic engineering, JSCE.*, Vol.50, pp.793-798, 2006.

[4] OGASAWARA, T., S., KIKUCHI, T., SUNAGAWA and S., SAKAI, "Development of 3D coupling model considered fluid-solid interaction by MPS method", *Proceedings of coastal engineering, JSCE.*, Vol.66, No.1, pp.41-45, 2010.

[5] Ikari, H., and Gotoh, H., "NUMERICAL SIMULATION OF FLOW WITH FLEXIBLE VEGETATION BY PARTICLE METHOD", *Proceedings of hydraulic engineering, JSCE.*, Vol.52, pp.973-978, 2008.

[6] GOTOH, H., H., IKARI, T., YASUOKA and K., OKU, "DEM-MPS model of solid-flow interaction for simulating behavior of armor blocks", *Proceedings of coastal engineering, JSCE.*, Vol.55, pp.836-840, 2008.

[7] GOTOH, H., H., IKARI, T., MATSUBARA and T., ITO, "Numerical Simulation on Tsunami due to Sector Collapse by Solid-Liquid Two-Phase Flow Model Based on Accurate Particle Method", *Proceedings of coastal engineering, JSCE.*,

Vol.67, No.2, pp.196-200, 2011.
[8] Sakai, M., S., Koshizuka and I., Toyoshima, "Numerical Simulation of Solid- Liquid Flows Involving Free Surface by DEM- MPS Method", *J. Soc. Powder Technol., Japan*, Vol.45, pp.466-477, 2008.
[9] SHIGETO, Y., SAKAI, M., MIZUTANI, S., AOKI, T. and SAITO, T., "Development of a Numerical Method of a Solid-Liquid Flow Involving Free Surfaces", *Japanese journal of multiphase flow*, Vol.24, pp.681-688, 2010.
[10] A.Ui, S.Ebata, F.Kasahara, T.Iribe, H.Kikura, H.Aritomi, "study on solid liquid two phase flow on PWR sump clogging issue", *Journal of Nuclear Science and Technology*, Vol.47, No.9, pp.820-828, 2010.
[11] A.Shakibaeinia, Y.C.Jin, "a mesh-free particle Model for simulation of mobile-bed dam break", *Advances in Water Resources*, Vol.34, pp.794-807, 2011.
[12] GOTOH, H., N., Tsuruta, E., Harada, H., IKARI and H., Kubota, "High-resolution DEM-MPS methods for solid-liquid multi-phase flow", *Proc. JSCE*, Vol. B2-68, No.2, pp.21-25.
[13] Tsuruta, N., H., GOTOH, H., IKARI and E., Harada, "Simulation of unsteady settling process of particles by 3D accurate particle method", *Proc. JSCE*, Vol. B2-68, No.2, pp.851-855.
[14] S.Zhang, S.Kuwabara, T.Suzuki, Y.Kawano, K.Morita, K.Fukuda, "simulation of solid-fluid mixture flow using moving particle methods", *J.Comp.Phys.*, Vol.228, pp.2552-2565, 2009.
[15] A. Khayyer and H. Gotoh, "Modified Moving Particle Semi-implicit methods for the prediction of 2D wave impact pressure", *Coastal Engineering*, 56, 419-440, 2009.

Part II

Improved MPS method for unsteady flow around solid phase

CHAPTER 4

Dynamic Stabilization of Moving Particle Semi-implicit Method

This chapter presents a simple and effective scheme for Dynamic Stabilization of MPS method. The new scheme, abbreviated as DS, reproduces meticulously adequate repulsive forces to attenuate the interparticle penetration and thus stabilizes the calculations, even for highly deformed flows characterized by tensile stress states. By performing a set of simple two-phase flow simulations, we also show the inappropriateness of the simplified/anti-symmetric MPS pressure gradient models as they may result in predominant excessive repulsive forces and thus being unable to simulate the main flow features. The DS scheme is shown to provide physically sound and computationally stable simulations of such flows. Furthermore, the DS scheme is introduced into the DEM-MPS methods and shows a good resolution of a problem about the sedimentation process, which is difficult to be handled by the so-far stabilizing schemes. The effectiveness of the DS scheme is shown in some benchmarks.

4.1 Introduction

The MPS (Moving Particle Semi-implicit) method was originally proposed by Koshizuka and Oka [1] for viscous incompressible flow as a Lagrangian mesh-free method. Lagrangian approach in hydraulic flow simulation is free from the non-linear advection term causing numerical diffusion, however, it simultaneously may result in instability due to the maldistribution of calculation points (particles). Up to now, the instability issue, as a general problem of particle method, has been widely studied [2-9]. In MPS-based simulations, the main causes of the maldistribution of particles correspond to either underestimation of interparticle repulsive forces or overestimation of interparticle attractive forces.

Due to the predominance of attractive force overestimation, Koshizuka et al. [10] modified the original MPS gradient model so that the pressure interacting forces would be purely repulsive, and some so-far proposed modifications including the so-called CMPS method [11] are based on this concept. This approach is generally composed of an artificial repulsive force which vanishes for a perfectly symmetric distribution of neighboring particles. As a result, stability and accuracy would depend on the instantaneous distribution of calculation points. The concept of repulsive interparticle forces for enhancement of stability has also been introduced in the SPH framework [4] by incorporating a stress-dependent repulsive force term multiplied by a constant coefficient.

To minimize the tensile instability issue in MPS framework, Khayyer and Gotoh [8] proposed a Gradient Correction (GC) scheme. Nevertheless, this scheme does not resolve the maldistribution of particles and requires a meticulous setting of calculation condition with prudence. In a recent paper, Khayyer and Gotoh [9] showed that multiphase particle-based simulations are prone to become easily destabilized as a result of unphysical perturbations in particle motion and resulting interparticle penetrations.

In brief, a stabilization approach regardless of stress state is required for stable and accurate particle-based simulation. This chapter highlights the particle method related to instability and the unphysical states of so-far proposed MPS methods stabilized by repulsive forces. A modification, namely a Dynamically Stabilized scheme, is proposed to resolve these problems. The new scheme provides meticulously adequate repulsive forces based on the Newton's third law of motion for both compressive and tensile stress states. It is shown to stabilize and adjust the disorder of calculation points for comprehensive MPS applications.

4.2 Problem of the so-far stabilizing schemes

In this section, previous and present gradient terms in the MPS method are explained. Detailed descriptions of other differential operators of standard and improved MPS methods can be referred to [1], [8], [12].
In MPS method, the gradient operator for the pressure gradient [10] is defined as:

$$\langle \nabla p \rangle_i = \frac{D_s}{n_0} \sum_{j \neq i} \frac{p_j - \hat{p}_i}{\left| \boldsymbol{r}_j - \boldsymbol{r}_i \right|^2} (\boldsymbol{r}_j - \boldsymbol{r}_i)\, w\left(\left| \boldsymbol{r}_j - \boldsymbol{r}_i \right| \right) \tag{4.2.1}$$

$$\hat{p}_i = \min_{j \in J} (p_i, p_j), \quad J = \left\{ j : w\left(\left| \boldsymbol{r}_j - \boldsymbol{r}_i \right| \right) \neq 0 \right\} \tag{4.2.2}$$

where p□= pressure, D_s = number of space dimensions, $\boldsymbol{r}$ = coordinate vector, $w(r)$ = the kernel function and n_0 = the reference particle number density. The subscripts i and j correspond to target particle and its neighboring particles, respectively.
The Corrected MPS (CMPS) method [11] modifies Eq. (4.2.1) to enforce interparticle anti-symmetric interactions in consideration of the Newton's third law:

$$\langle \nabla p \rangle_i = \frac{D_s}{n_0} \sum_{j \neq i} \frac{(p_i + p_j) - (\hat{p}_i + \hat{p}_j)}{\left| \boldsymbol{r}_j - \boldsymbol{r}_i \right|^2} (\boldsymbol{r}_j - \boldsymbol{r}_i) w\left(\left| \boldsymbol{r}_j - \boldsymbol{r}_i \right| \right) \tag{4.2.3}$$

Considering the original gradient term [1] and the artificial repulsive force term for stabilization, Eq. (4.2.1) can be rewritten as:

$$\langle \nabla p \rangle_i = \frac{D_s}{n_0} \sum_{j \neq i} \frac{(p_j - p_i)}{\left| \boldsymbol{r}_j - \boldsymbol{r}_i \right|^2} (\boldsymbol{r}_j - \boldsymbol{r}_i) w\left(\left| \boldsymbol{r}_j - \boldsymbol{r}_i \right| \right) + \frac{D_s}{n_0} \sum_{j \neq i} \frac{(p_i - \hat{p}_i)}{\left| \boldsymbol{r}_j - \boldsymbol{r}_i \right|^2} (\boldsymbol{r}_j - \boldsymbol{r}_i) w\left(\left| \boldsymbol{r}_j - \boldsymbol{r}_i \right| \right) \tag{4.2.4}$$

Similarly in the CMPS method corresponding to Eq. (4.2.3) can be rewritten as:

$$\langle \nabla p \rangle_i = \frac{D_s}{n_0} \sum_{j \neq i} \frac{(p_j - p_i)}{\left| \boldsymbol{r}_j - \boldsymbol{r}_i \right|^2} (\boldsymbol{r}_j - \boldsymbol{r}_i) w\left(\left| \boldsymbol{r}_j - \boldsymbol{r}_i \right| \right) + \frac{D_s}{n_0} \sum_{j \neq i} \frac{(p_i - \hat{p}_i) + (p_i - \hat{p}_j)}{\left| \boldsymbol{r}_j - \boldsymbol{r}_i \right|^2} (\boldsymbol{r}_j - \boldsymbol{r}_i) w\left(\left| \boldsymbol{r}_j - \boldsymbol{r}_i \right| \right) \tag{4.2.5}$$

In the right hand sides of both Eqs. (4.2.4) and (4.2.5), because the first term is the mathematical definition of gradient term, the second term can be regarded as the artificial repulsive force term. Focusing on pressure differences in the numerators, we can write:

$$\left|(p_i - \hat{p}_i) + (p_i - \hat{p}_j)\right| \geq \left\{ \begin{array}{c} \left|p_i - \hat{p}_i\right| \\ or \\ \left|p_i - \hat{p}_j\right| \end{array} \right\} \geq \left|p_j - p_i\right| \tag{4.2.6}$$

Therefore, the stability with regard to Eqs. (4.2.1) and (4.2.3) would depend on pressure states and particle distributions. And the artificial repulsive force is clearly predominant in these equations rather than the original gradient. On that account, the gradient operators may result in overestimation of interparticle pressure forces and, as a result, would bring about unphysical fluid motions and perturbations.

4.3 Proposition of the Dynamic stabilization

Here we propose a Dynamically Stabilized (DS) gradient operator comprising of the original Taylor-series consistent gradient model [1] and a meticulously adequate stabilizing force.

$$\langle \nabla p \rangle_i = \frac{D_s}{n_0} \sum_{j \neq i} \frac{(p_j - p_i)}{\left|\boldsymbol{r}_j - \boldsymbol{r}_i\right|^2} (\boldsymbol{r}_j - \boldsymbol{r}_i) w\left(\left|\boldsymbol{r}_j - \boldsymbol{r}_i\right|\right) + \frac{1}{n_0} \sum_{j \neq i} \boldsymbol{F}_{ij}^{DS} w\left(\left|\boldsymbol{r}_j - \boldsymbol{r}_i\right|\right) \tag{4.3.1}$$

$$\begin{cases} \boldsymbol{F}_{ij}^{DS} = 0 & if \quad \left|\boldsymbol{r}_{ji}^*\right| \geq d_{ji} \\ \boldsymbol{F}_{ij}^{DS} = -\rho_i \Pi_{ij} \boldsymbol{e}_{ji,//} & if \quad \left|\boldsymbol{r}_{ji}^*\right| < d_{ji} \end{cases}; \qquad d_{ij} = \alpha_{DS} \frac{d_i + d_j}{2}, \qquad \Pi_{ij} > 0 \tag{4.3.2}$$

where $\boldsymbol{F}_{ij}^{DS}$ = stabilizing force for target particle i from neighboring particle j, ρ = particle density, Π_{ij} = parameter to adjust the magnitude of $\boldsymbol{F}_{ij}^{DS}$, $\boldsymbol{r}_{ji} = \boldsymbol{r}_j - \boldsymbol{r}_i$, $\boldsymbol{e}_{ji,//}$ = the unit vector of $\boldsymbol{r}_{ji}$, d = particle diameter, and α_{DS} = constant for adjusting active range of $\boldsymbol{F}_{ij}^{DS}$. The superscript * refers to a state after the advection by the original gradient term. α_{DS} is decided according to Courant stability condition for a time resolution as:

$$\alpha_{DS} + \alpha_{dt} = 1 \tag{4.3.3}$$

Where α_{dt} = ratio of the time step to Courant number (= 0.1) [13]. In fact, dynamic stabilization is activated if a neighboring particle j overlaps into the target particle i by more than 10 percent of the initial spacing. The intermediate position vector $\boldsymbol{r}^*_{ji}$ can be expressed with the parallel and normal vectors as:

$$\boldsymbol{r}_{ji}^* = \boldsymbol{r}_{ji,//}^* + \boldsymbol{r}_{ji,\perp}^* \tag{4.3.4}$$

Where $\boldsymbol{r}^*_{ji,//}$ = parallel vector of $\boldsymbol{r}^*_{ji}$, and $\boldsymbol{r}^*_{ji,\perp}$ = normal vector of $\boldsymbol{r}^*_{ji}$. The parallel and normal vectors in the above equation can be obtained from the following equations:

$$\begin{cases} \boldsymbol{r}^*_{ji,//} = \boldsymbol{r}_{ji} + \dfrac{\Delta\boldsymbol{r}^*_{ji} \cdot \boldsymbol{r}_{ji}}{\left|\boldsymbol{r}_{ji}\right|} \boldsymbol{e}_{ji,//} \\ \boldsymbol{r}^*_{ji,\perp} = \dfrac{\left|\Delta\boldsymbol{r}^*_{ji} \times \boldsymbol{r}_{ji}\right|}{\left|\boldsymbol{r}_{ji}\right|} \boldsymbol{e}_{ji,\perp} \end{cases} ; \qquad \Delta\boldsymbol{r}^*_{ji} = -\left(\frac{\langle \nabla p \rangle_j}{\rho_j} - \frac{\langle \nabla p \rangle_i}{\rho_i} \right) \Delta t^2 \tag{4.3.5}$$

where $\boldsymbol{e}_{ji,\perp}$= the unit vector of $\boldsymbol{r}_{ji,\perp}$. As shown in **Fig. 4.3.1**, when particles overlap with each other, the stabilizing repulsive force is given to make them separated and verged on each other as the least, that is the adequate repulsive force. The stabilizing forces between particles *i* and *j* act at the opposite directions along the $\boldsymbol{e}_{ji,//}$ respectively to satisfy anti-symmetric relation in accordance with the Newton's third law, that is:

$$\boldsymbol{F}_{ij} = -\boldsymbol{F}_{ji} ; \qquad \boldsymbol{F}_{ij} = \boldsymbol{F}_{ij,//}, \quad \boldsymbol{F}_{ji} = \boldsymbol{F}_{ji,//} \tag{4.3.6}$$

Stabilizing force is based on the instantaneous distribution of particles without any pressure value as:

$$\left|\boldsymbol{r}^*_{ji}\right| = \left|\boldsymbol{r}^*_{ji,//} + \boldsymbol{r}^*_{ji,\perp}\right| < d_{ji} = \left|\boldsymbol{r}^{DS}_{ji}\right| = \left|\boldsymbol{r}^*_{ji,//} + \boldsymbol{r}^*_{ji,\perp} + \Delta\boldsymbol{r}^{DS}_{ji}\right| \tag{4.3.7}$$

where $\boldsymbol{r}_{ij}^{DS}$ = coordinate vector through revision. From Eq. (4.3.7), the following equations can be obtained:

$$\sqrt{d^2_{ji} - \left|\boldsymbol{r}^*_{ji,\perp}\right|^2} = \left|\boldsymbol{r}^*_{ji,//} + \Delta\boldsymbol{r}^{DS}_{ji}\right| \tag{4.3.8}$$

$$\left|\boldsymbol{r}^*_{ji,//}\right| < \left|\boldsymbol{r}^*_{ji,//} + \Delta\boldsymbol{r}^{DS}_{ji}\right| \tag{4.3.9}$$

Therefore,

$$\left|\boldsymbol{r}^*_{ji,//} + \Delta\boldsymbol{r}^{DS}_{ji}\right| = \left|\boldsymbol{r}^*_{ji,//}\right| + \left|\Delta\boldsymbol{r}^{DS}_{ji}\right| \tag{4.3.10}$$

Considering Eq. (4.3.6), revising coordinate vector $\Delta\boldsymbol{r}_{ij}^{DS}$ is derived from Eq. 8:

$$\begin{aligned} \Delta\boldsymbol{r}^{DS}_{ji} = \Delta\boldsymbol{u}^{DS}_{ji}\Delta t = \Delta\boldsymbol{a}^{DS}_{ji}\Delta t^2 &= \left(\frac{\boldsymbol{F}^{DS}_{ji}}{\rho_j} - \frac{\boldsymbol{F}^{DS}_{ij}}{\rho_i} \right)\Delta t^2 = \left(-\frac{\boldsymbol{F}^{DS}_{ij}}{\rho_j} - \frac{\boldsymbol{F}^{DS}_{ij}}{\rho_i} \right)\Delta t^2 \\ &= \left(\frac{\rho_i \Pi_{ij}}{\rho_j} + \frac{\rho_i \Pi_{ij}}{\rho_i} \right)\boldsymbol{e}_{ji}\Delta t^2 = \Pi_{ij}\left(1 + \frac{\rho_i}{\rho_j} \right)\boldsymbol{e}_{ji}\Delta t^2 \end{aligned} \tag{4.3.11}$$

i , j : the present positions

i^* , j^* : the predicted positions derived from the pressure gradient force

i_{ij}^{DS}, j_{ij}^{DS} : the expected positions among i & j adjusted by the stabilizing force F_{ij}^{DS}, F_{ji}^{DS}

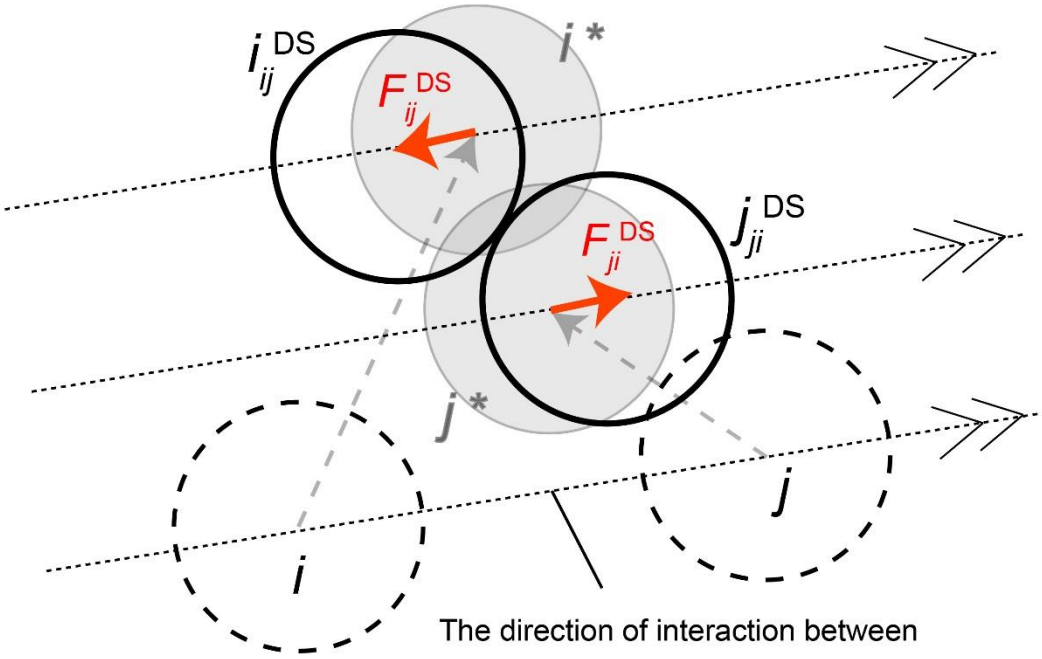

The direction of interaction between i and j in the pressure gradient process

The relationship of vectors between i and j

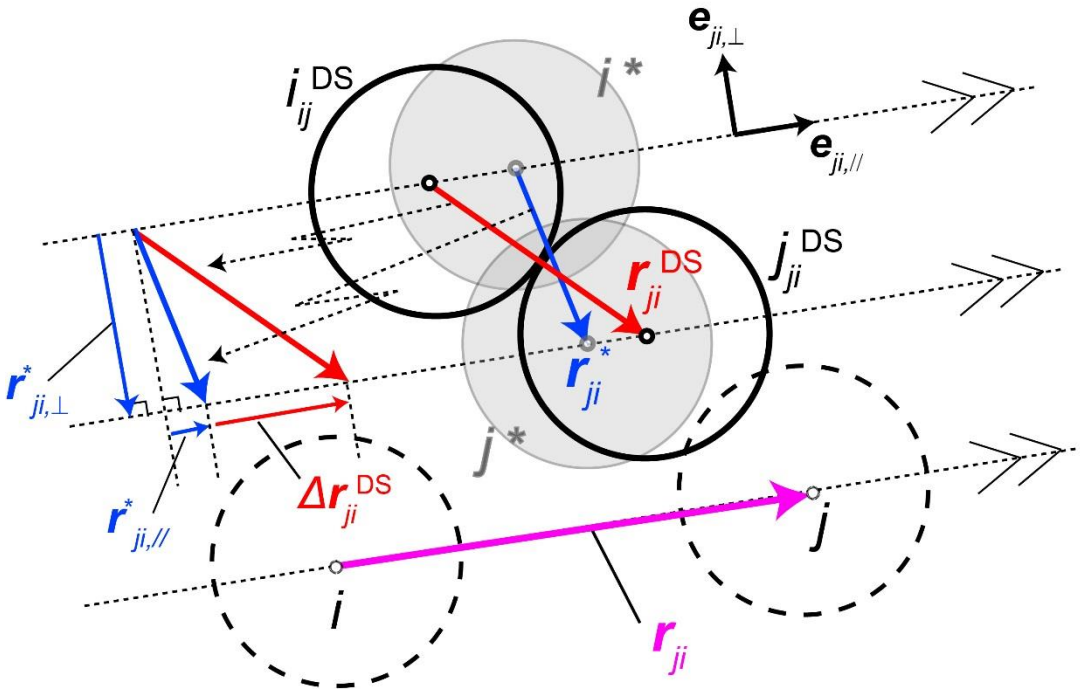

Fig. 4.3.1 A graphical presentation of the concept of the Dynamic Stabilization scheme

From Eqs. (4.3.8), (4.3.10), and (4.3.11):

$$\sqrt{d_{ji}^2-\left|\boldsymbol{r}_{ji,\perp}^*\right|^2}-\left|\boldsymbol{r}_{ji,//}^*\right|=\left|\Delta\boldsymbol{r}_{ji}^{DS}\right|=\left|\Pi_{ij}\left(1+\frac{\rho_i}{\rho_j}\right)\boldsymbol{e}_{ji}\Delta t^2\right|=\Pi_{ij}\left(1+\frac{\rho_i}{\rho_j}\right)\Delta t^2 \tag{4.3.12}$$

Therefore,

$$\Pi_{ij}=\frac{\rho_j}{\Delta t^2\left(\rho_i+\rho_j\right)}\left(\sqrt{d_{ji}^2-\left|\boldsymbol{r}_{ji,\perp}^*\right|^2}-\left|\boldsymbol{r}_{ji,//}^*\right|\right) \tag{4.3.13}$$

The adequate stabilizing forces $\boldsymbol{F}_{ij}^{DS}$ are calculated by the prediction of the particle positions based on the original gradient term corresponding to the first term in the right hand side of Eq. (4.3.1). Firstly, the predicted relative distance between particles i and j is obtained from Eq. (4.3.5). If the particles would penetrate each other in the prediction, parameter Π_{ij} to adjust the magnitude of $\boldsymbol{F}_{ij}^{DS}$ is calculated by Eq. (4.3.13). In this process, $\boldsymbol{F}_{ij}^{DS}$ is considered on the basis of a one-to-one relative position of a target particle i and a neighboring particle j and thus, the pressure gradient at particle i is obtained by considering the distribution of all neighboring particles through a weighted averaging of $\boldsymbol{F}_{ij}^{DS}$ as shown in Eq. (4.3.1).

4.4 Verification of the Dynamic stabilization

4.4.1 Evolution of a square patch of fluid

To test the stability of the proposed scheme in tensile stress states, the evolution of a 2D square patch of water subjected to a rigid rotation is performed. The evolution of the fluid patch is governed by the continuity and Euler equations [14]. In the present simulation, as an initial condition, the square patch is set as 1.0 m in length (L = 1.0 m) comprising of water particles with $d = 2.0\times10^{-3}$ m. The angular velocity is set as $\omega = 1.0\ \mathrm{s}^{-1}$.

Fig. 4.4.1 shows snapshots of water particles and pressure field by MPS-HS-GC and MPS-HS-GC-DS methods. From **Fig. 4.4.1** (**a**), the MPS-HS-GC snapshot at t = 0.84 s is characterized by an unphysical pressure field and dispersed particles in the vicinity of the patch boundaries. The MPS-HS-GC simulation breaks up at this moment. On the other hand, in **Fig. 4.4.1** (**b**), the MPS-HS-GC-DS snapshot shows a stable state without unphysical particle clustering and fragmentation. The MPS-HS-GC-DS simulation continues to run and maintains its stable state tenaciously (shown in **Fig. 4.4.1** (**c**), (**d**)). Hence, the Dynamically Stabilized scheme provides a fully stable simulation of a highly deformed free-surface flow characterized by a tensile stress state.

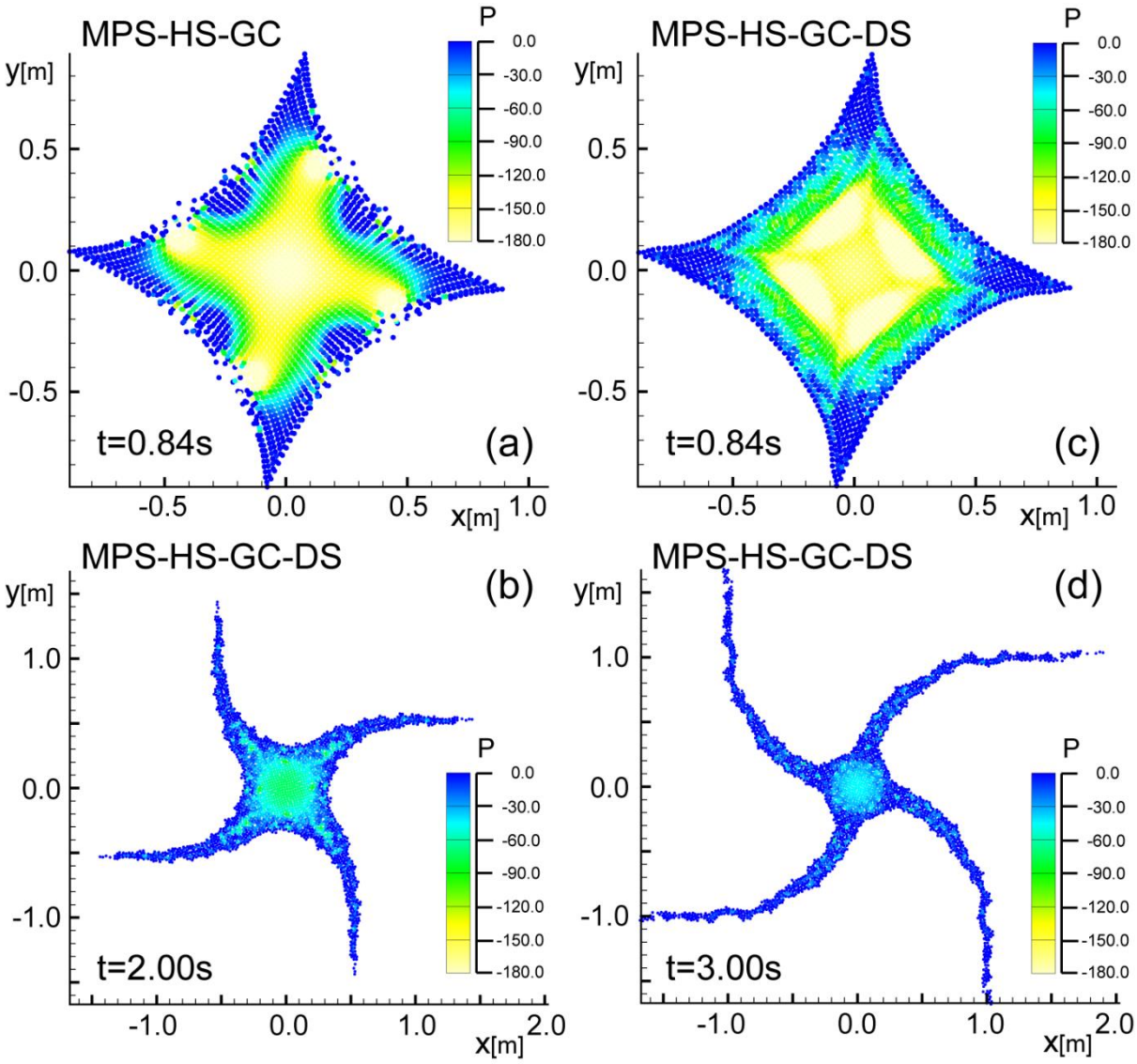

Fig. 4.4.1 Snapshots of water particles together with pressure field by the MPS-HS-GC and the MPS-HS-GC-DS methods in simulation of an initially square patch of fluid

4.4.2 Dam breaking

In this section, dam breaking simulations are implemented to verify the performance of the proposed stabilizer for the violent free-surface flow. As for the numerical condition, the calculation domain is set with its length X = 1.18 m. The water with $X \times Y$ = 0.68×0.12 m is set at the left side in the domain as shown in **Fig. 4.4.2**. The size of the calculation particle is set as d = 0.004 m. This benchmark is implemented by the MPS-HS-HL-ECS-GC method and the MPS-HS-HL-ECS-GC-DS method. The MPS-HS-HL-ECS-GC method does not include any stabilizing scheme and have difficulty in simulating violent flows including large deformations of free surface without the prudent simulation setting. Therefore, the artificial viscosity characterized by the XSPH [15] framework is introduced additionally.

Fig. 4.4.3 shows snapshots of simulation results at time t = 0.35 s by the MPS-HS-HL-ECS-GC

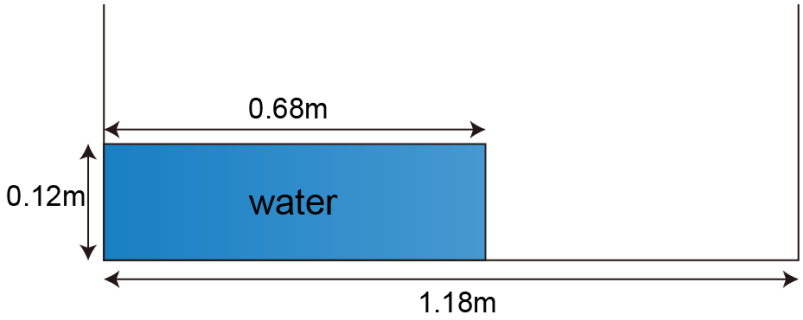

Fig. 4.4.2 Initial condition of the dam breaking simulation

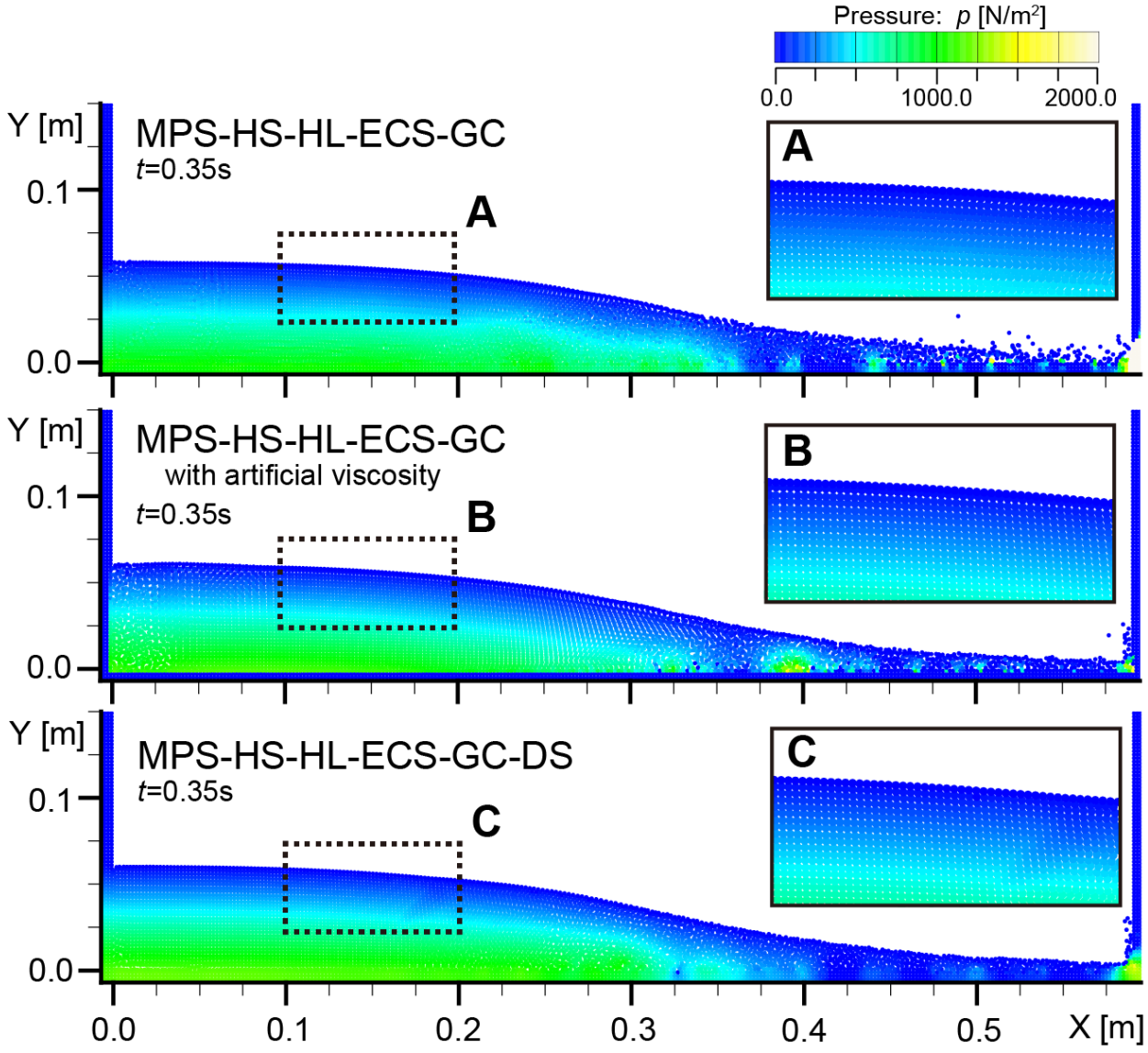

Fig. 4.4.3 Snapshots of simulation results by the MPS-HS-HL-ECS-GC method (with and without the artificial viscosity) and the MPS-HS-HL-ECS-GC-DS method at t = 0.35 s in dam breaking simulation

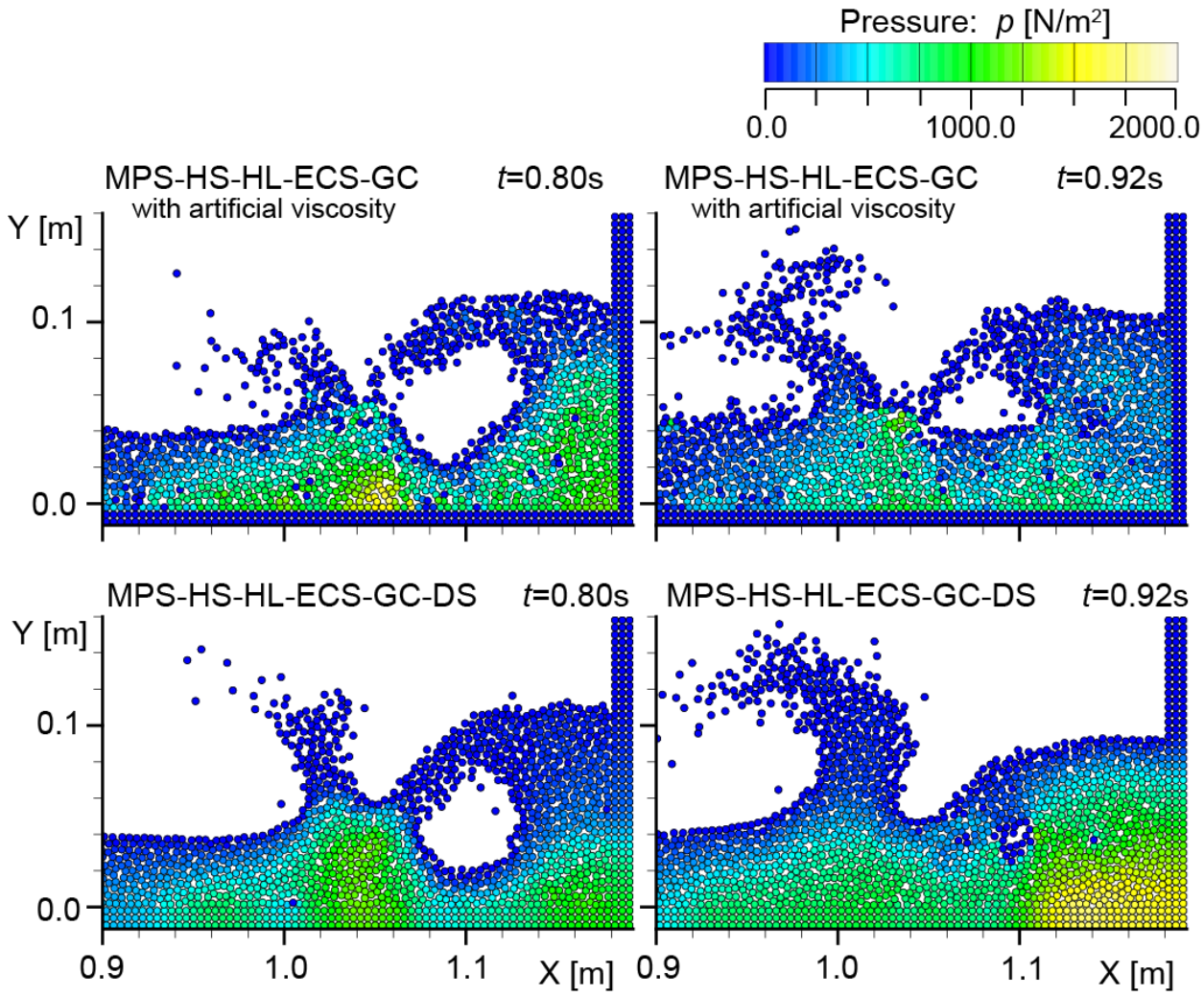

Fig. 4.4.4 Snapshots of simulation results by the MPS-HS-HL-ECS-GC method with artificial viscosity and the MPS-HS-HL-ECS-GC-DS method at t = 0.80 s and 0.90 s in dam breaking simulation

methods (with and without artificial viscosity) and the MPS-HS-HL-ECS-GC-DS method. The MPS-HS-HL-ECS-GC without artificial viscosity shows the instability mode around the right side wall and the simulation breaks up at time t =0.36 s. While, in the MPS-HS-HL-ECS-GC with artificial viscosity shows an enhanced stability even around the right side wall. The MPS-HS-HL-ECS-GC-DS shows the most highly stable state with the smoothest distribution of pressure.

Fig. 4.4.4 shows snapshots of simulation results at time t = 0.80 s and 0.92 s by the MPS-HS-HL-ECS-GC with artificial viscosity and the MPS-HS-HL-ECS-GC-DS. From the snapshots, it is clearly shown that the MPS-HS-HL-ECS-GC-DS enhance the reproduction of the free-surface line. In addition, the distribution of pressure also improved significantly. The GC scheme does not guarantee the momentum conservation due to the correction matrix estimated one by one for each particle by the distribution of the neighboring particles. Therefore, the GC scheme has a problem that the perturbation or motions of free-surface particles are not suppressed under the excessively violent flows without prudent simulation settings and stabilizers. This benchmark indicates that the DS scheme is effect for both the stabilization and accuracy, comparing with the existing stabilizer based on a semi-empirical parameter.

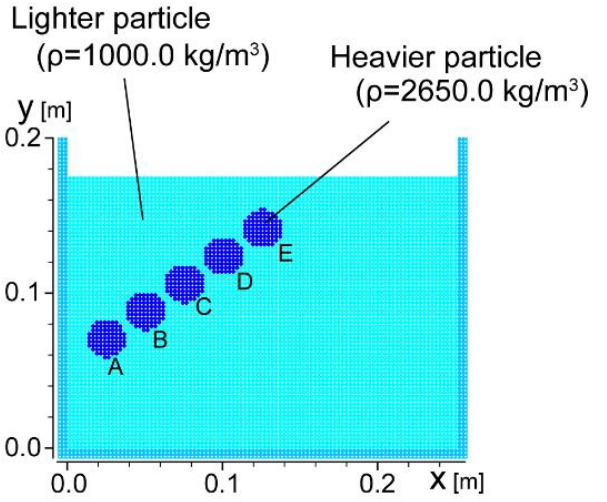

	X [m]	Y [m]
A	0.025	0.071
B	0.050	0.088
C	0.075	0.106
D	0.100	0.124
E	0.125	0.141

Coordinates of the central point of each heavier particle group

*The diameter of each heavier particle group: d_g=0.025m

Fig. 4.4.5 Initial condition of fluid particles in simulation of a two-phase flow for settlement of heavier fluid

4.4.3 Numerical simulation of two-phase flows

In this section, the stability and performance of the proposed scheme in reproduction of multi-phase flows are examined through some benchmark numerical tests. For comparison, these numerical tests are implemented by three numerical models listed as follows.

1. **CMPS-HS**: An improved particle method using the CMPS gradient scheme [11] and a Higher order Source of Poisson Pressure Equation [12], which is effective in enhancing the numerical stability (and can treat only repulsive interaction between particles).
2. **MPS-HS-GC**: An enhanced particle method utilizing the HS scheme [12] and a Gradient Correction (GC) [8], which is effective in improvement of accuracy (and can treat both repulsive and tensile interactions).
3. **MPS-HS-GC-DS**: An enhanced particle method using the HS [12], GC [8] and the newly DS scheme.

4.4.3.1 Settlement of heavier fluid in water

Numerical simulation of a simple typical two-phase flow, i.e. settlement of heavier fluid particles in water, is performed with CMPS-HS, MPS-HS-GC and MPS-HS-GC-DS methods. The initial condition is set as shown in **Fig 4.4.5**. The tank is 0.25 m in length and 0.2 m in height, and is filled with 7,000 fluid particles with $d = 2.5\times10^{-3}$ m, resulting in a water depth of 0.175 m. The densities of the lighter particles ρ_L and the heavier particles ρ_H are set as ρ_L = 1000.0 kg/m^3 and ρ_H = 2650.0 kg/m^3, respectively. From **Fig 4.4.6**, the CMPS-HS method reproduces a stable free-surface, however, vectors of velocity are unphysical with

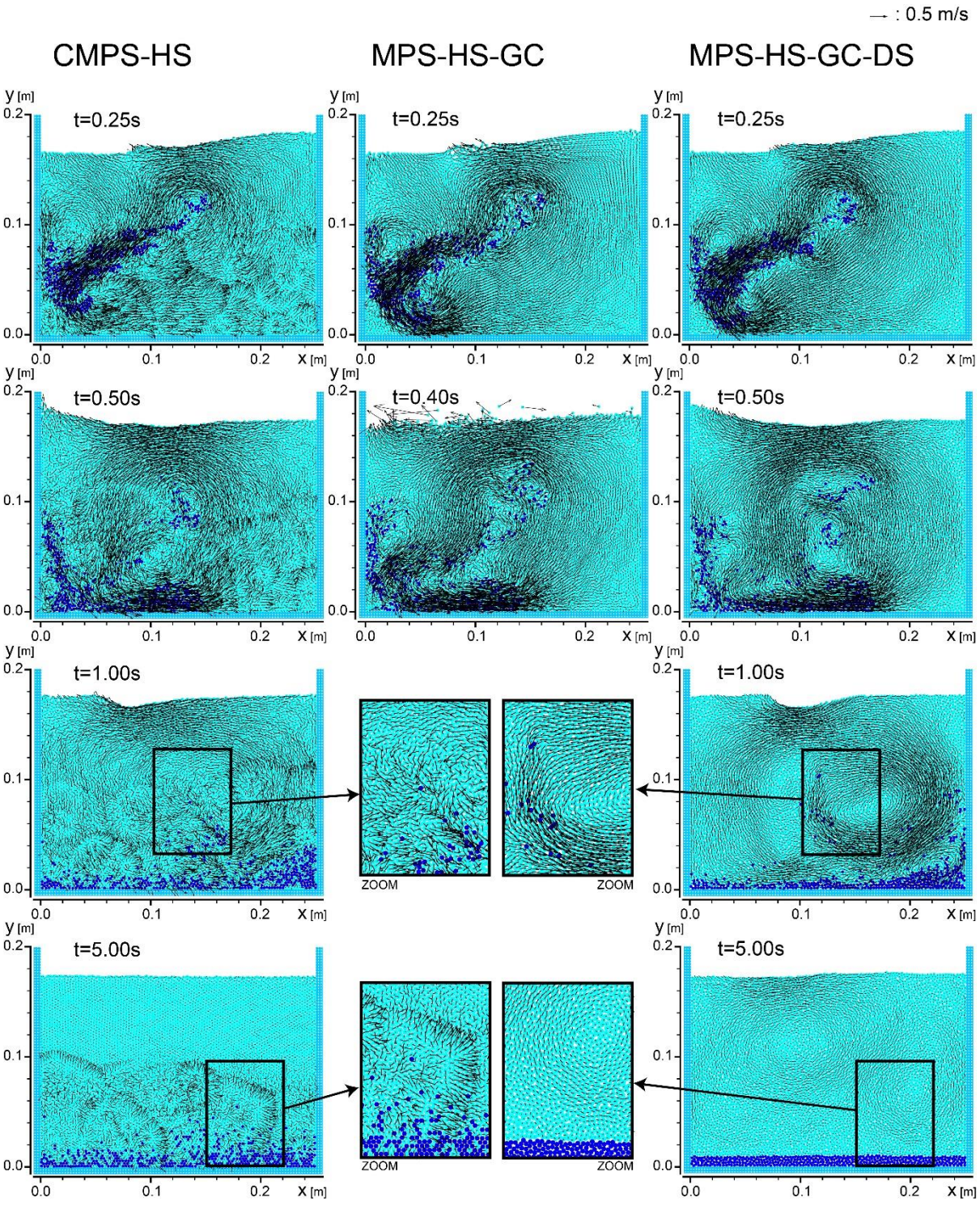

Fig. 4.4.6 Snapshots of fluid particles together with velocity vectors by the MPS-HS, CMPS-HS and the MPS-HS-GC-DS methods in simulation of a two-phase flow for settlement of heavier fluid

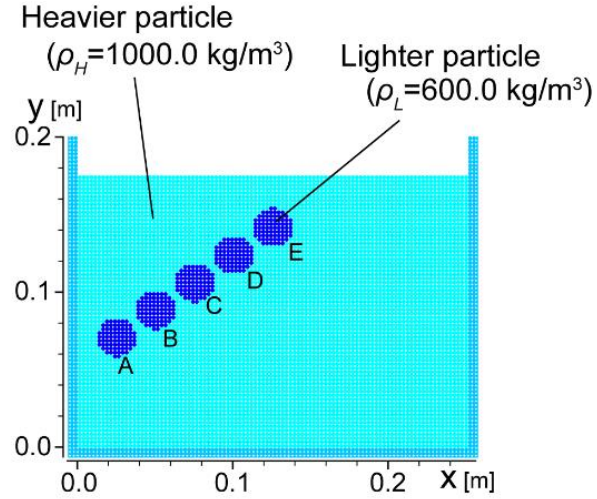

	X [m]	Y [m]
A	0.025	0.071
B	0.050	0.088
C	0.075	0.106
D	0.100	0.124
E	0.125	0.141

Coordinates of the central point of each lighter particle group

*The diameter of each lighter particle group: d_g=0.025m

Fig. 4.4.7 Initial condition of fluid particles in simulation of a two-phase flow for surfacing of lighter fluid

perturbations. In addition, some heavier particles do not settle down and are fully bounded within the lighter fluid particles. The cause of this unphysical result is likely brought about by a too strong stabilizing force (Eq. (4.2.5)). The results by MPS-HS-GC are characterized by an unstable free-surface, in particular, at t = 0.4 s. This unphysical reproduction leads to numerical instability at t = 0.41 s. On the other hand, MPS-HS-GC-DS portrays a physically sound reproduction of the phenomenon. The snapshots by this method show a smooth free-surface with reproducing the circulating flow driven by the settlement of heavier fluid. The settlement of heavier fluid particles is well simulated by this method.

4.4.3.2 Surfacing of lighter fluid in water

Simulation of a two-phase flow with surfacing of lighter fluid particles in water is performed (**Fig. 4.4.7**) with CMPS-HS, MPS-HS-GC and MPS-HS-GC-DS methods. The initial set up of calculation corresponds to that in Section 4.4.2.1, except for replacing a fluid lighter than water with ρ_L = 600.0 kg/m^3 in place of the previously heavier fluid. As shown in **Fig. 4.4.8,** in spite of the smooth free-surface line, CMPS-HS recurrently shows unphysical perturbation of velocity even in the static state at t = 10.00 s. Further, lighter particles stay in water, or are bounded within heavier (water) particles. While, MPS-HS-GC reproduces rather smoother velocity field, surface particles behave unstably and the simulation breaks up at t = 0.35 s. The MPS-HS-GC-DS shows a good reproduction in both velocity field (circulating flow driven by surfacing of particles) and behavior of particles. This scheme resolves all problems shown in the results of the other schemes.

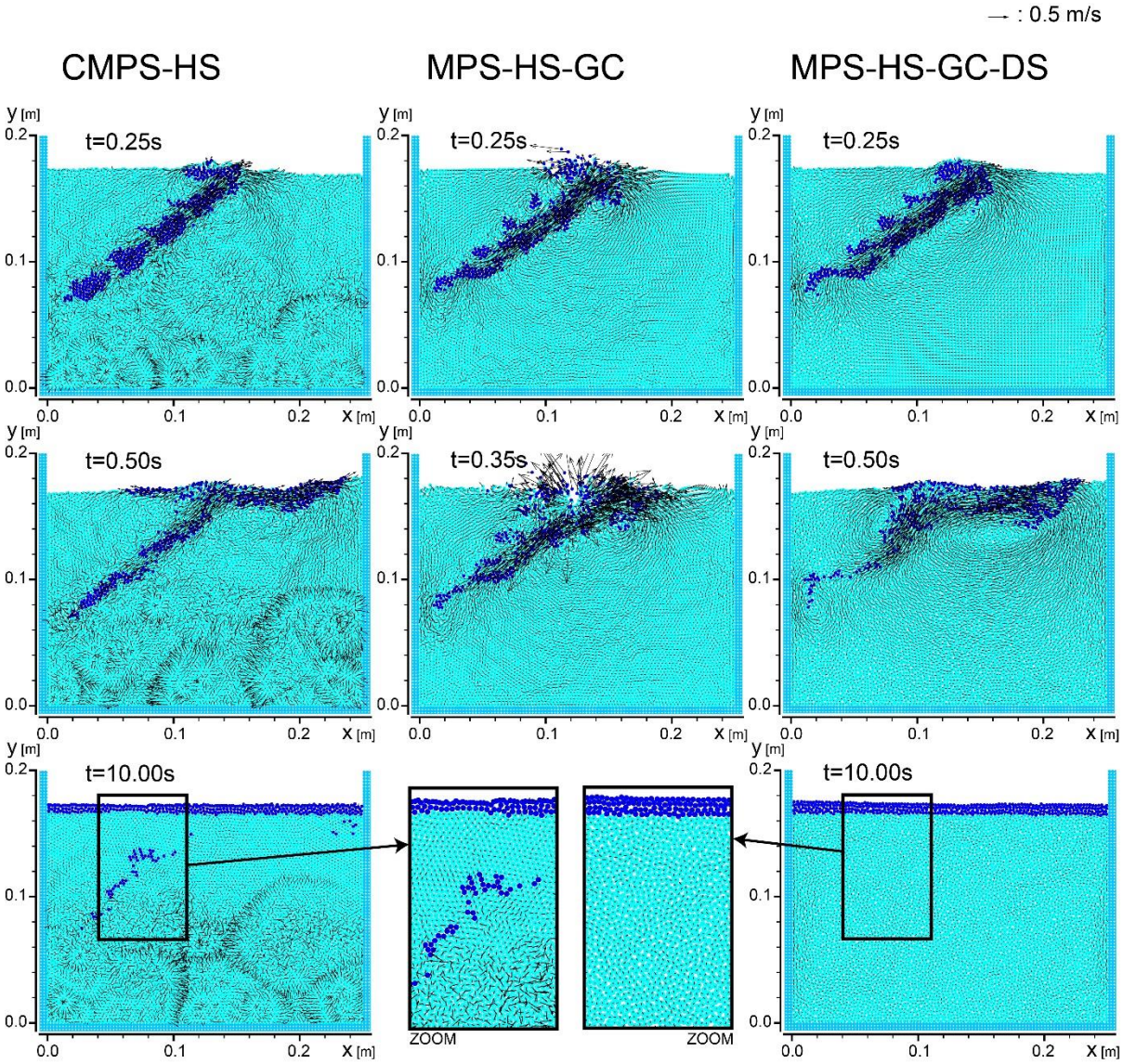

Fig. 4.4.8 Snapshots of fluid particles together with velocity vectors by the MPS–HS, CMPS–HS and the MPS–HS–GC–DS methods in simulation of a two-phase flow for surfacing of lighter fluid.

4.4.4 Concluding Remarks

A novel scheme is proposed for dynamic stabilization of a particle method, namely, the MPS method. The new scheme, abbreviated as DS, provides precisely adequate repulsive interparticle forces based on the instantaneous distribution of particles to eliminate the interparticle penetration, which is the main cause of instability in particle methods. A few numerical tests, namely, evolution of a square patch of fluid and a set of simple two-phase flow simulations have been performed to show the stabilizing and enhancing effects of the DS scheme. Despite the fact that this paper focuses on Dynamic Stabilization of 2D MPS-based simulations, the major finding and developments can be easily applied and extended to 3D simulations as well as other particle methods, i.e. the SPH method.

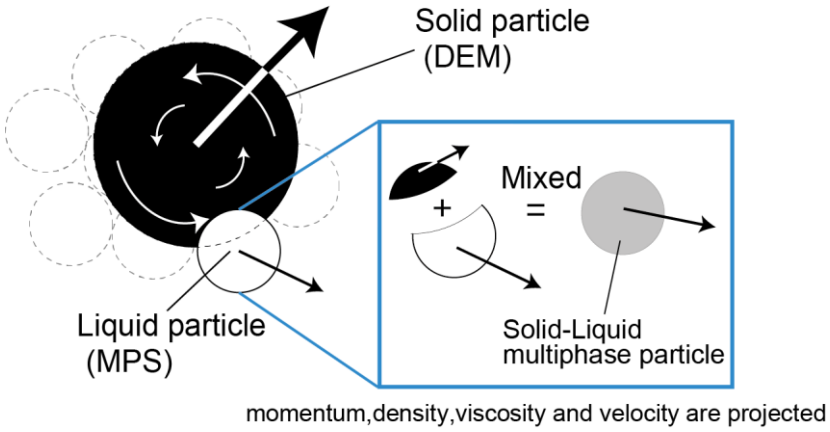

Fig. 4.5.1 Illustration of the concept of a solid-liquid multi-phase particle by the multi-phase-flow model

4.5 Introduction of the Dynamic Stabilization into the DEM-MPS method

In this section, the Dynamic Stabilization (DS) is introduced into the DEM-MPS method. The adaptability of the DS scheme to each DEM-MPS framework is verified by benchmarks targeting on a sedimentation process of solid particles dumped into water, which is significant for coastal constructions.

4.5.1 Introduction

When armor stones are dumped into water from a hopper above a water surface, a violent motion of water surface may arise from violent entries of stones. Although there are some studies targeting on the sedimentation process, the comprehension of the process including the free surface is insufficient due to the difficulty in handling the violent free-surface flows. These violent behaviors bring a problem of numerical instability even in computation by particle methods. A stability of semi-implicit schemes, such as MPS or ISPH, depends on control of unphysical pressure fluctuations. Hence accurate particle methods are necessary in computation of solid-liquid two-phase flow with violent motion of water surface. In particular, around interface of solid and liquid phases, a pressure fluctuation is apt to be locally high. In this section, the DS (Dynamic Stabilization) scheme is introduced into the DEM-MPS method in order to resolve the problem, and its validity is examined by some numerical benchmark tests through the comparison with results of the previous DEM-MPS method.

4.5.2 Solid-liquid Coupling model (DEM-MPS coupling model)

4.5.2.1 Solvers for fluid flow

Herewith, the solvers for fluid flows are constructed with accurate particle methods, namely the MPS-HS-HL-ECS-GC-DS method. As for the GC scheme [16], in spite of its prominent effectiveness to reproduce the corrected gradient, the momentum conservation is not guaranteed due to the correction

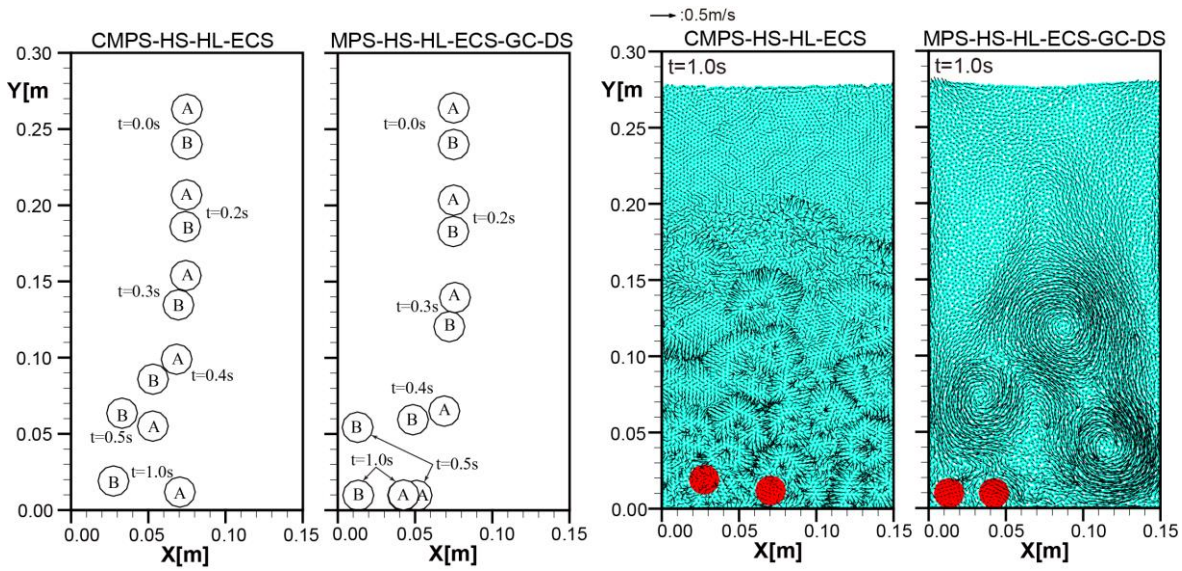

Fig. 4.5.2 (left) Snapshots of a track of the solid particles and (B) snapshots of all the particles with their velocities at *t* = 1.0 s in DKT simulation by DEM-MPS methods

matrix deduced from distribution of neighboring particles one by one. Therefore, it is generally difficult to apply the GC scheme to single-phase flow simulations with violent free-surface deformations on the account of the numerical instability caused by the inapplicability of the GC scheme to exceedingly irregular distribution of particles (e.g. around the free surface). However, thanks to the DS scheme, its comprehensive application including violent free-surface flows has been achieved. And, it is expected that the combination of GC scheme and DS scheme works well even for solid-liquid two-phase violent flows by the DEM-MPS framework.

4.5.2.2 DEM-MPS coupling scheme

Here, the DEM-MPS coupling schemes are adopted as follows:

A. Multi-phase-flow model (Gotoh et al., 2012 [17]):

As shown in **Fig. 4.5.1**, DEM-particles and MPS-particles are set on different discretization spaces, and each space is connected to each other by projecting the physical quantities (e.g. momentum, density and velocity).

B. Two-fluid-based model (Gotoh et al., 2003 [18]):

This model, the solid-solid interaction estimated by the DEM is additionally introduced into the governing equations of two-fluid-based MPS framework.

More detail of these coupling schemes can be referred to Chap.3.

4.5.3 Verification of the proposed models about settlement problems

4.5.3.1 DKT (Drafting, Kissing and Tumbling)

To investigate the influence of the artificial stabilizing force, numerical simulations targeting on a DKT phenomenon characterized by sedimentation of particles are performed by the existing repulsion-based

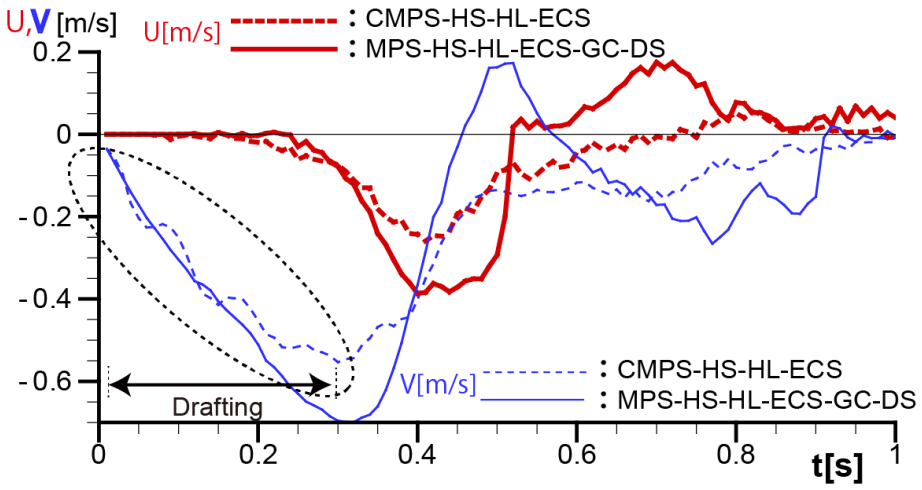

Fig. 4.5.3 The transfer velocities of the solid particle B

model (DEM-CMPS-HS-HL-ECS method) and the proposed model (DEM-MPS-HS-HL-ECS-GC-DS method). As for the DEM-MPS coupling scheme, the multi-phase-flow model is applied in this test. Two solid particles with diameter as d_s=0.02m and density as ρ_s=2,650kg/m^3 are settled down in water from the initial position as; particle A: (0.075, 0.264 m), particle B: (0.075, 0.240 m). The tank is set with its size as (x, y) = (0.3, 0.1 m) and filled with water with 0.28 m depth. The water particle is set with its diameter d_l=0.0025m and density ρ_s=1,000kg/m^3.

Fig. 4.5.2 shows (A) snapshots of the solid particles in the settlement processes and (B) snapshots of all the particles with the velocity field at time t=1.0 s, when the sedimentation process has completed, in the DKT simulations. From the snapshot (A), DEM-CMPS-HS-HL-ECS simulation shows that the motions of the solid particles suddenly falls into inactive states from time t=0.4s, and the particle B do not settle down completely after all. In addition, from the velocity field given by the snapshot (B), unphysical noises of velocity are clearly recognized. On the other hand, the DEM-MPS-HS-HL-ECS-GC-DS simulation does not show such unphysical cessations of motions of solid particles and unphysical noises in the velocity field.

Fig. 4.5.3 shows a time series of the transfer velocity of the solid particle B. In the DEM-MPS-HS-HL-ECS-GC-DS simulation, unphysical noise of vertical velocity within during the Drafting process (t < 0.3s) is relatively small comparing with the DEM-CMPS-HS-HL-ECS simulation. This implies the effectiveness of the proposed accurate particle method for suppression of the numerical noises.

Fig. 4.5.4 shows a ratio of the original pressure gradient force to the artificial stabilizing force. The DEM-CMPS-HS-HL-ECS simulation shows that the artificial stabilizing force is inconsistently predominant and implies that the particle motions are calculated apart from the original governing equation. While, in the DEM-MPS-HS-HL-ECS-GC-DS simulation, the artificial stabilizing force is sufficiently small and thus, it is implied that the solid motions are calculated faithfully along the governing equation.

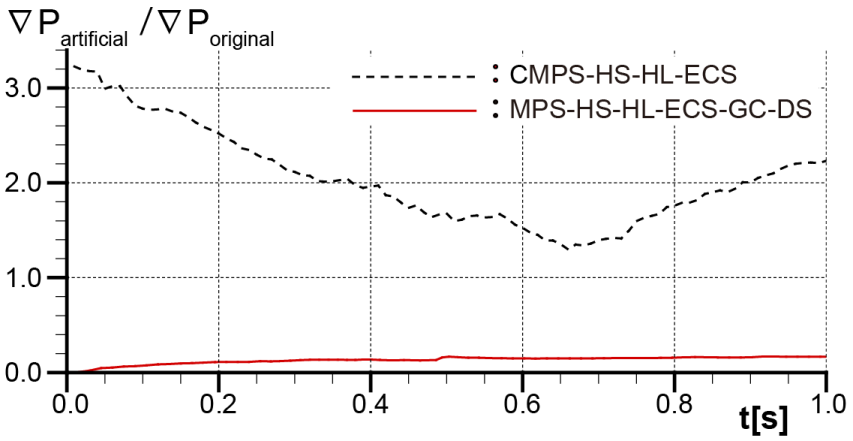

Fig. 4.5.4 Ratio of the original gradient force to the artificial stabilizing force working on the solid particles

4.5.3.2 Settlement of solid particles dropped from above water

To verify the validity of the proposed model from a more practical viewpoint, a simulation is performed targeting on a settlement of solid particles dumped from above water on the assumption of a coastal construction to settle rubble-mounds from barge-ship. Similar to the previous benchmark, the multi-phase-flow model is applied with the DEM-CMPS-HS-HL-ECS method (sim.B) and the DEM-MPS-HS-HL-ECS-GC-DS method (sim.C). The solid particle is set with its diameter d_s=0.01m and density ρ_s = 2,650kg/cm^3. While, the water particle is set with its diameter d_l=0.0025m and density ρ_l = 1,000kg/cm^3. At the initial, the solid particles are set on a hopper and the water particles are set in a tank as shown in **Fig. 4.5.5 (A)**. The solid particles are dumped into water as the hopper gate opening.

Fig. 4.5.5 (B and C) shows the snapshots of simulation results with the velocity field in a dumping and sedimentation process of the solid particles. At time t=0.4s, the unphysical noises of velocities are effectively suppressed in sim.C in contrast to sim.B. Moreover, sim.C shows that a spread state of the front of the bunch of the settling particles is faithfully reproduced, which is generally shown in experiments of sedimentation process of solid particles. At the end of the sedimentation process corresponding to time t=2.0s, sim.B leaves solid particles at a standstill in water. While, in sim.C, the problem is resolved so that all the solid particles are settled down completely and deposited at the bottom of the tank. Up to now, unphysical motions of the settled particles are one of a crucial problem for MPS simulations, particularly in a place where the pressure is locally high, such as a neighborhood of wall. The unphysical behaviors of particles are significant also around free surface, where the particle number densities of particles are small. However, from this benchmark, it is expected that the proposed Dynamic Stabilization is, to some extent, comprehensively effective for avoid such problems.

4.5.3.3 Sedimentation process of heavier particles in water

In the previous benchmarks, the proposed problem about an unphysical standstill of settling solid particles is examined by focusing on the artificial stabilizing force. To illustrate that the problem is generally found with independence from DEM-MPS coupling schemes, here, a simulation targeting on a sedimentation process of heavier particles are performed by the commonly used model, namely the two-fluid-model by Gotoh et al. (2003) [18]. As shown in **Fig. 4.5.6 (A)**, a tank is set with its size as 0.25×0.13 m and filled with water with 0.12 m in depth. In the static water, heavier liquid particles with density ρ_L=2,650 kg/m^3

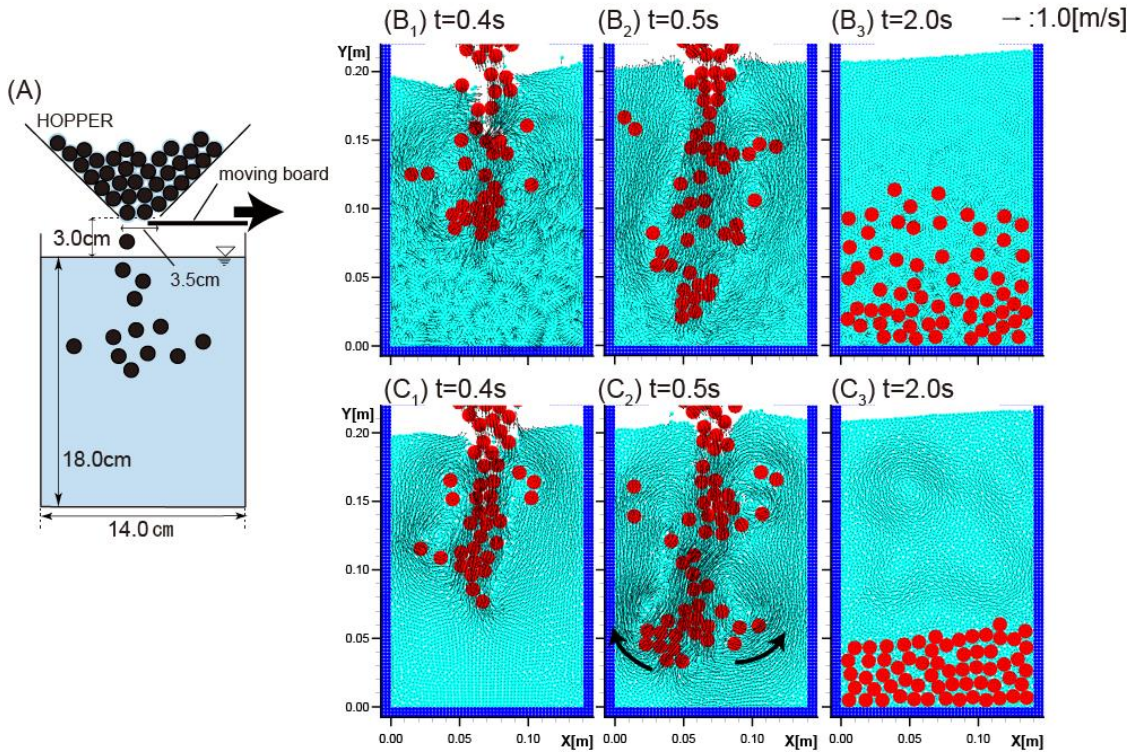

Fig. 4.5.5 Illustration of (A) the initial condition and (B and C) snapshots of simulation results with velocity field in simulation of a dumping and sedimentation process of the solid particles

corresponding to the group L and solid particles with density ρ_S=2,650 kg/m^3 corresponding to the group S are set. Their sedimentation processes are tracked. Similar to the previous tests, the DEM-CMPS-HS-HL-ECS method (sim.B) and the DEM-MPS-HS-HL-ECS-GC-DS method (sim.C) are used for this test. All the particles including the lighter liquid particles with density ρ_W=1,000 kg/m^3 are set with diameter d=0.0025 m.

Fig. 4.5.6 (B) and (C) shows the snapshots of simulation results with velocity field. Same as the previous simulations by the multi-phase-flow model, sim.B shows significant numerical noises in the velocity field and unphysical motions of settling particles with an unphysical standstill. On the other hand, sim.C shows an improvement about the unphysical states of velocity and motions of settling particles.

Fig. 4.5.7 shows the ratio of the original gradient force to the artificial stabilizing force working on the settling heavier particles. In these simulations also, unphysical predominance of the stabilizing force is shown in sim.B, and it is implied that the motions of the particles are calculated apart from the original governing equation. Moreover, in sim.B, it is found that the solid particles (group S) comprising the DEM process for the solid-solid interaction are given more predominant stabilizing force than the heavier liquid particles (group L). The problem is deteriorated by the DEM process. On the other hand, sim.C shows that the problem about unphysical predominance of the artificial stabilizing force is suppressed effectively in both group L and S.

In this benchmark, the fluid-phase-flow also shows the common problem about an unphysical standstill of settled particles, and simultaneously, shows a good resolution of the problem in a simulation by the proposed accurate particle method for the high-resolution DEM-MPS-based simulation.

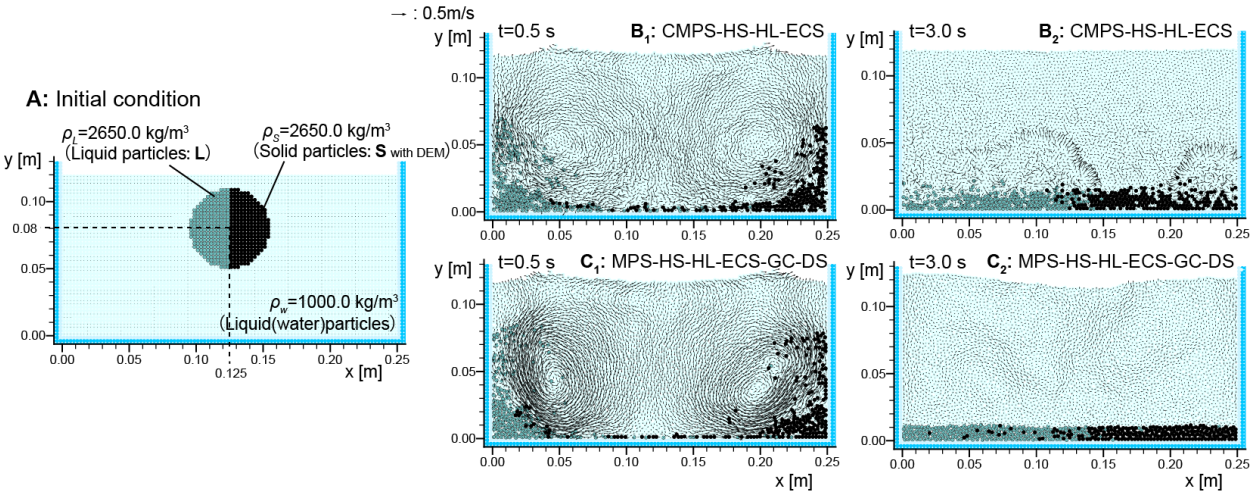

Fig. 4.5.6 Illustration of (A) the initial condition and (B and C) Snapshots of the simulation results with velocity fields in simulations targeting on a sedimentation process of heavier particles

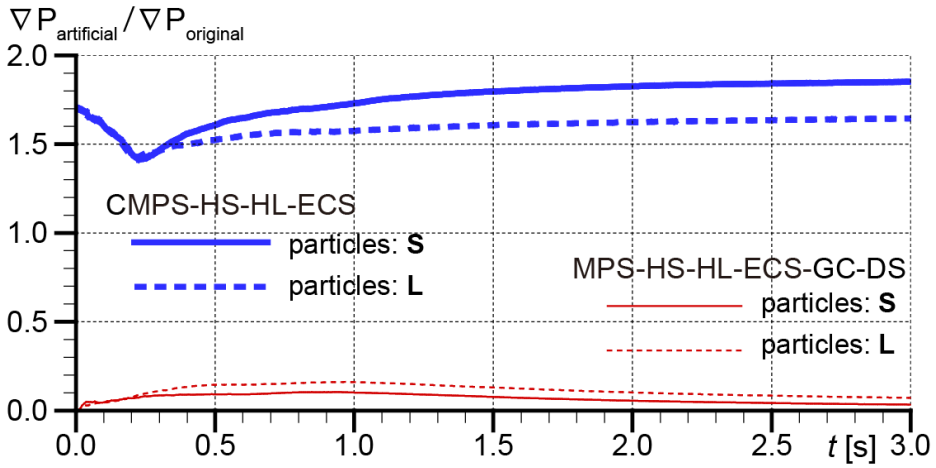

Fig. 4.5.7 The ratio of the original gradient force to the artificial stabilizing force working on the settling heavier particles

4.5.4 Concluding remarks

In this study, the proposed stabilizing scheme, namely the Dynamic Stabilization is introduced into the DEM-MPS frameworks. Through simple benchmarks, a common problem in simulation of sedimentation process of solid particles is disclosed. By the existing stabilizers characterized by semi-empirical stabilizing forces depending on distribution of pressure, the settled particles inevitably involves an unphysical behavior with a standstill and significant noises in the velocity field with independence from the DEM-MPS coupling schemes. However, by performed benchmarks, it is shown that the proposed Dynamic Stabilization suppresses such problems effectively.

REFERENCES

[1] Gotoh, H., M., Hayashi, S., Andoh and T., Sakai, "SOLID-LIQUD TWO PHASE FLOW MODEL BASED ON LAGLANGIAN PARTICLE METHOD FOR THE SIMULATION OF WATER WAVE GENERATION DUE TO LANDSLIDES", *Proceedings of JSCE*, Vol.719, pp.31-45, 2002.

[2] Gotoh, H., M., Hayashi, S., Andoh and T., Sakai, "Lagrangian coupling for solid-liquid two phase flow by DEM-MPS method", *Proceedings of hydraulic engineering, JSCE.*, Vol.47, pp.547-552, 2003.

[3] Ikari, H., H., Gotoh and T., Sum, "Computational Mechanics of a blocking of gateless bottom outlet by drift woods", *Proceedings of hydraulic engineering, JSCE.*, Vol.50, pp.793-798, 2006.

[4] OGASAWARA, T., S., KIKUCHI, T., SUNAGAWA and S., SAKAI, "Development of 3D coupling model considered fluid-solid interaction by MPS method", *Proceedings of coastal engineering, JSCE.*, Vol.66, No.1, pp.41-45, 2010.

[5] Ikari, H., and Gotoh, H., "NUMERICAL SIMULATION OF FLOW WITH FLEXIBLE VEGETATION BY PARTICLE METHOD", *Proceedings of hydraulic engineering, JSCE.*, Vol.52, pp.973-978, 2008.

[6] GOTOH, H., H., IKARI, T., YASUOKA and K., OKU, "DEM-MPS model of solid-flow interaction for simulating behavior of armor blocks", *Proceedings of coastal engineering, JSCE.*, Vol.55, pp.836-840, 2008.

[7] GOTOH, H., H., IKARI, T., MATSUBARA and T., ITO, "Numerical Simulation on Tsunami due to Sector Collapse by Solid-Liquid Two-Phase Flow Model Based on Accurate Particle Method", *Proceedings of coastal engineering, JSCE.*, Vol.67, No.2, pp.196-200, 2011.

[8] Sakai, M., S., Koshizuka and I., Toyoshima, "Numerical Simulation of Solid- Liquid Flows Involving Free Surface by DEM- MPS Method", *J. Soc. Powder Technol., Japan*, Vol.45, pp.466-477, 2008.

[9] SHIGETO, Y., SAKAI, M., MIZUTANI, S., AOKI, T. and SAITO, T., "Development of a Numerical Method of a Solid-Liquid Flow Involving Free Surfaces", *Japanese journal of multiphase flow*, Vol.24, pp.681-688, 2010.

[10] A.Ui, S.Ebata, F.Kasahara, T.Iribe, H.Kikura, H.Aritomi, "study on solid liquid two phase flow on PWR sump clogging issue", *Journal of Nuclear Science and Technology*, Vol.47, No.9, pp.820-828, 2010.

[11] A.Shakibaeinia, Y.C.Jin, "a mesh-free particle Model for simulation of mobile-bed dam break", *Advances in Water Resources*, Vol.34, pp.794-807, 2011.

[12] GOTOH, H., N., Tsuruta, E., Harada, H., IKARI and H., Kubota, "High-resolution DEM-MPS methods for solid-liquid multi-phase flow", *Proc. JSCE*, Vol. B2-68, No.2, pp.21-25.

[13] Tsuruta, N., H., GOTOH, H., IKARI and E., Harada, "Simulation of unsteady settling process of particles by 3D accurate particle method", *Proc. JSCE*, Vol. B2-68, No.2, pp.851-855.

[14] S.Zhang, S.Kuwabara, T.Suzuki, Y.Kawano, K.Morita, K.Fukuda, "simulation of solid-fluid mixture flow using moving particle methods", *J.Comp.Phys.*, Vol.228, pp.2552-2565, 2009.

[15] G.R.Liu and M.B.Liu, "Smoothed Particle Hydrodynamics: a meshfree particle method", *World Scientific*, Singapore, 2003.

[16] Khayyer, A. and H. Gotoh, "Enhancement of stability and accuracy of the moving particle semi-implicit method", *Journal of Computational Physics*, vol. 230, pp. 3093-3118, 2011.

[17] GOTOH, H., N., Tsuruta, E., Harada, H., IKARI and H., Kubota, "High-resolution DEM-MPS methods for solid-liquid multi-phase flow", *Proc. JSCE*, Vol. B2-68, No.2, pp.21-25.

[18] Gotoh, H., M., Hayashi, S., Andoh and T., Sakai, "Lagrangian coupling for solid-liquid two phase flow by DEM-MPS method", *Proceedings of hydraulic engineering, JSCE.*, Vol.47, pp.547-552, 2003.

CHAPTER 5

The Space Potential Particles

Particle methods have been seldom verified by a Karman vortex simulation, which is commonly performed as a typical benchmark in Computational Fluid Dynamics. This is mainly due to a difficulty in suppression of occurrence of unphysical voids manifested usually in a strong vortex on account of definition of free surface by the Lagrangian tracking framework with inconsistency in volume conservation. This paper presents a simple and effective scheme as a free-surface boundary condition of projection-based particle methods, namely MPS method [1] and ISPH method [2] to handle the free surface with consistency in volume conservation. The new scheme is introduced into the Poisson Pressure Equation (PPE) in consideration of a potential in void space as Space Potential Particle, abbreviated as SPP, to reproduce physical motions of particles around free surface through a particle-void interaction. The accuracy of SPP scheme in volume conservation is investigated by performing a set of simple benchmarks, and SPP scheme shows a good resolution of the problem, that the existing models cannot overcome. Moreover, Karman vortex simulations are implemented by the SPP scheme. Then, the accuracy and stability of the simulations are investigated from the viewpoint of time resolution, and a problem of a commonly used stabilizing scheme is found. SPP scheme resolves the problem and shows good reproductions of Karman vortex simulations with avoiding unphysical voids and its tenacious stability.

5.1 Introduction

The MPS (Moving Particle Semi-implicit) method was originally proposed by Koshizuka and Oka [1] for viscous incompressible free-surface flow so that even violent flows such as breaking waves can be easily analyzed [3,4]. Due to the superiority in tracking violent flows, the MPS method is applied to various engineering problems. However, in spite of its robustness backed up with pragmatic uses, verification of its validity by the so-called Karman vortex [5-11], which is commonly targeted as a typical benchmark [12,13] to examine the credibility of schemes in violently complicated flows, is insufficient [14], and so is the SPH (Smoothed Particle Hydrodynamics) method [15-18] as a similar particle method. The main reason of this stems from its difficulty to suppress occurrence of unphysical voids (e.g. in a strong vortex), and thus unphysical free surface, in contrast with its prominence in handling free surface itself physically. The causes of this problem can be classified roughly into two matters. The first is the particle-based definition of free surface. The second corresponds to the setting of boundary condition of the outlet flow. The latter is often discussed [14,17-18] for the volume conservation in the domain, but the former [18] is ignored more often, seeing that a rigorous simulation inherently excludes any free surface in the Karman vortex benchmark. However, the fact is that in the projection-based particle methods the voids' surrounding particles are erroneously considered as free-surface. Therefore, whether voids exist in an output of calculation results, steering of free surface is independently significant for accuracy, and accordingly, influences the emergence of inaccurate voids.

This chapter shows that the existing schemes have a problem about consistency between mathematical expression and physical description related to unphysical voids and a free-surface condition in the numerical process. A novel definition of free-surface condition, namely, the Space Potential Particles, abbreviated as SPP, is proposed to resolve the inconsistency, considering a potential of interactions in the void space where particles are not distributed. It shows that unphysical voids caused by unclear free surface capturing is restrained effectively in the Karman vortex simulations even at a relative high Reynolds number.

5.2 Space Potential Particles

5.2.1 Overview of so-far interaction models

The so-far applied schemes in handling the unphysical voids in particle method simulation are briefly reviewed. As a classical and most popular approach for unphysical voids in the MPS method, the standard gradient model [20] or its improved model (CMPS) [21] based on repulsive inter-particle forces are commonly used. The purely repulsive interaction works so as to get rid of unphysical voids in a process that particles around the voids likely move towards the voids by being pushed from the opposite position where particles and their repulsive forces exist. Nevertheless, unphysical voids still arise from this indirect compensation process in a strong vortex.

As for another approach of this matter, tensile interaction is introduced. It sounds appropriate to diminish directly a dilating cavity between particles, which is a cause of unphysical voids, and assuredly, sounds congruous to reproduce veritable states of real phenomenon also. In the light of the current studies, the gradient model is improved mainly targeting on tensile interaction for accuracy and stability in accordance with the Taylor series by reconstructing distributions of evaluated interactions [22-24]. Significant achievements of this approach are shown in the SPH method (e.g. see [25-30]), meanwhile, this scheme was also introduced in the MPS method by Khayyer and Gotoh [31]. However, even recent accurate schemes still leave unphysical voids usually at the centroid of a vortex under a high-Reynolds number condition. These treatments are constructive for restraints of unphysical voids [31,32]. However, once voids occur, it is difficult to remove them because particles around the voids tend to be pulled apart from the voids by neighboring particles to compensate their particle-number-density deficiency.

In general, the MPS framework sets a free-surface boundary for a particle whose particle number density is below a threshold; giving it zero pressure forcedly, and the matrix of the Poisson Pressure Equation (PPE) is solved by using this boundary condition. Therefore, the Continuity equation is not enforced for a free-surface particle, and as a result, the volume conservation is not guaranteed around the free surface. In addition, since the free-surface boundary is set as a fixed boundary in the PPE, it is premised that particles (or fluids) do not flow into a void space, for which no interaction with particles is defined. Such a calculation process without any direct information of existence of voids misses a potential of voids and brings about inconsistency in “mathematical space” for the numerical solution with “physical space” as an expression of real phenomenon. Consequently, unphysical voids occurring as an error cannot be removed efficiently. In brief, the following two factors are noted for free surface;

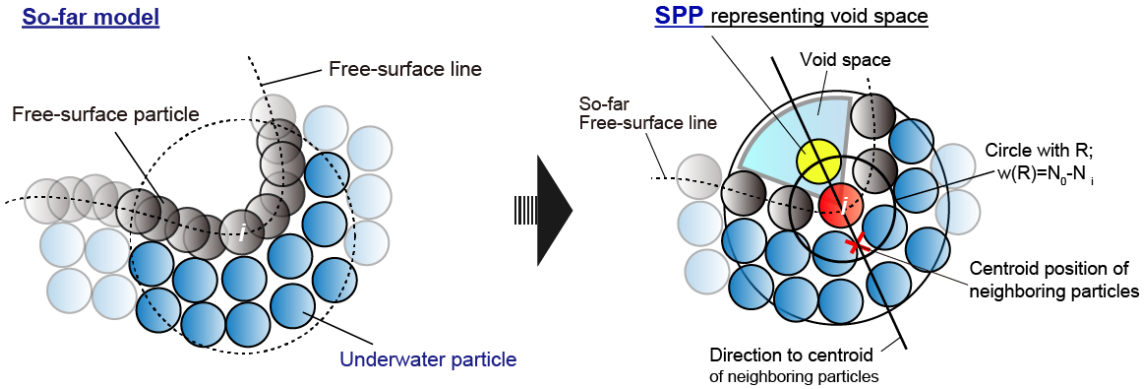

Fig. 5.2.1 Graphical presentation of the concept of the Space Potential Particle scheme

1. Substance potential (e.g. mass, volume) for volume conservation: Free-surface boundary should not be given to fluid particles with a potential to change the substance states.
2. Space potential for degree of freedom in motions of particles: Fluid particles around free surface should be given a fluid-void interaction to keep a physical mobility of fluid flow.

Hereby, a new boundary condition is set to give information of the "mathematical void space" in the calculation process as "Space Potential" so that moving particles can flow into voids by introduction of an additional virtual free-surface boundary particle in the calculation process. This technic achieves that all the fluid particles can be handled as pure fluids with consistency in the Continuity equation.

5.2.2 Introduction of SPP

The precondition for estimation of the differential operation of a targeted particle requires a uniform distribution of neighboring particles in the influence area. However, particles around free surface do not have sufficient neighboring particles around them. Here, it is interpreted that the influence area of such a free-surface particle is filled up with particles representing flows as both substance-and-space and voids corresponding to mere space. To satisfy the requisite condition of the differential operation, Space Potential Particles abbreviated as SPP are distributed to represent the void space. As shown in **Fig. 5.2.1**, SPP is set for all the particles around free surface one by one considering the particle number density of the targeted particle *i* as:

$$w_i^{spp} = \begin{cases} n_0 - n_i & if \quad n_0 > n_i \\ 0 & if \quad n_0 \le n_i \end{cases} \tag{5.2.1}$$

where w_i^{spp} is an averaging weight given by SPP for *i*, n_i is the particle number density of the targeted particle *i* and n_0 is the reference particle number density. In the MPS method, the weighting function *w* is commonly adopted the following function:

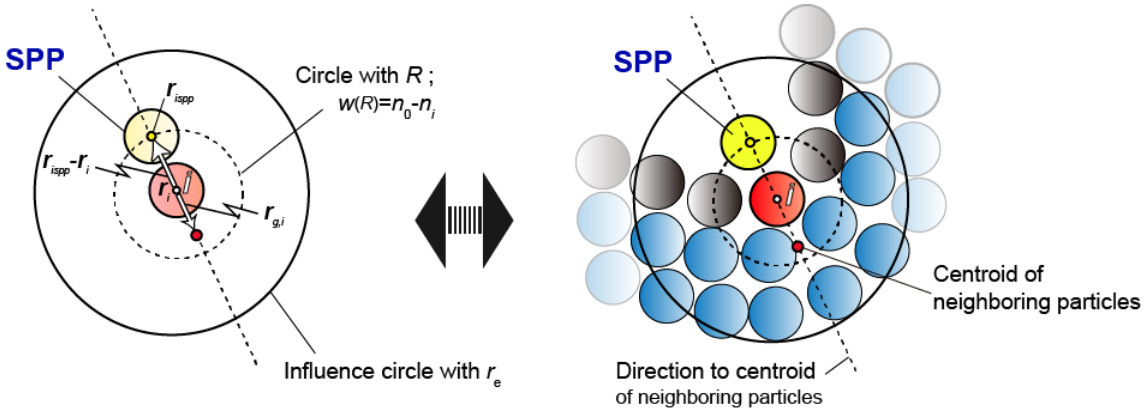

Fig. 5.2.2 Graphical presentation of the relationship of each vector for the Space Potential Particles scheme

$$w\left(\left|\boldsymbol{r}_{ij}\right|\right)=\begin{cases}\dfrac{r_e}{\left|\boldsymbol{r}_{ij}\right|}-1 & if \quad r_e>\left|\boldsymbol{r}_{ij}\right| \\ 0 & if \quad r_e\le\left|\boldsymbol{r}_{ij}\right|\end{cases} \tag{5.2.2}$$

where $\boldsymbol{r}_{ij}$ is a relative coordinate vector of a neighboring particle j to the targeted particle i ($\boldsymbol{r}_{ij}=\boldsymbol{r}_j-\boldsymbol{r}_i$; $\boldsymbol{r}_i$, $\boldsymbol{r}_i$ is the coordinate vector of particle i and j, respectively) and r_e is the radius of the influence circle. As shown in **Fig. 5.2.2**, defining the coordinate vector of SPP for particle i as $\boldsymbol{r}_{ispp}$, the distance between the SPP and particle i corresponding to $|\boldsymbol{r}_{ispp}-\boldsymbol{r}_i|$ is obtained from Eqs.1 and 2 as:

$$\left|\boldsymbol{r}_{ispp}-\boldsymbol{r}_i\right|=\frac{r_e}{w_i^{spp}+1}=\frac{r_e}{n_0-n_i+1} \qquad \left(\because w_i^{spp}=\frac{r_e}{\left|\boldsymbol{r}_{ispp}-\boldsymbol{r}_i\right|}-1\right) \tag{5.2.3}$$

Then, the centroid of neighboring particles is calculated to decide the coordinate of SPP;

$$\boldsymbol{r}_{g,i}=\sum_{j\in J}\boldsymbol{r}_{ij}w\left(\left|\boldsymbol{r}_{ij}\right|\right); \qquad J=\left\{j\neq i \quad and \quad j\neq ispp\right\} \tag{5.2.4}$$

where $\boldsymbol{r}_{g,i}$ is the relative coordinate vector of the centroid of neighboring particles to particle i. Considering the maldistribution of particles due to the void, SPP is set in the opposite direction to the centroid of neighboring particles from particle i. As an expression of the direction of the position of SPP from particle i, the following equation is obtained;

$$\frac{\boldsymbol{r}_{ispp}-\boldsymbol{r}_i}{\left|\boldsymbol{r}_{ispp}-\boldsymbol{r}_i\right|}=-\frac{\boldsymbol{r}_{g,i}}{\left|\boldsymbol{r}_{g,i}\right|} \tag{5.2.5}$$

The position of SPP is defined as a point where conditions of Eqs. (5.2.3) and (5.2.5) are satisfied. As shown in **Fig. 5.2.2**, the position $\boldsymbol{r}_{ispp}$ is at an intersection of a circumference with a radius $R=|\boldsymbol{r}_{ispp}-\boldsymbol{r}_i|$ by Eq.

(5.2.3) and a line crossing the centroid of the particle i with its gradient as Eq. (5.2.5). Concretely, its coordinate vector $\boldsymbol{r}_{ispp}$ is written as:

$$\boldsymbol{r}_{ispp} = \boldsymbol{r}_i - \frac{\left|\boldsymbol{r}_{ispp} - \boldsymbol{r}_i\right|}{\left|\boldsymbol{r}_{g,i}\right|}\boldsymbol{r}_{g,i} \tag{5.2.6}$$

A nd, in accordance with the free-surface boundary condition, SPP velocity is defined not to give any shear stress to the targeted particle i as:

$$\boldsymbol{u}_{ispp} = \boldsymbol{u}_i \tag{5.2.7}$$

where $\boldsymbol{u}$ is the particle velocity. In the PPE, SPP is treated as a fee-surface particle with zero pressure, and thus, SPP is excluded from the matrix of the PPE being given zero values for the source term and Laplacian of pressure. While, all the fluid particles are built into the matrix, in particular, particles around free surface are given a coefficient of Laplacian of pressure including that of SPP also. Surely, a pressure gradient by SPP is also given to its targeted fluid particle around free surface. SPP is set for each particle around free surface one by one, and as a result, its interaction works only for the targeted particle and is not shared between fluid particles. Due to this process, each fluid particle around free surface is given appropriate boundary condition.

5.3 Validation of the proposed models

5.3.1 Verification of the reimposition of unphysical voids

In this section, simple benchmarks for the SPP scheme are implemented to verify its performance of restrainer and reimposition to unphysical voids in a whirling water flow in a rotating tank without gravity. To make it clear, the accuracy of the proposed scheme is examined by comparison with results of so-far models. The targeted models are as follow;

1. The improved repulsion-based model: CMPS-based model (CMPS-SBV-HS-HL-ECS method [21,31,33,34])
2. The improved corrected-gradient model, which can treat accurately tensile interaction also: GC-based model (MPS-SBV-HS-HL-ECS-GC-DS method [31,33,34,35])
3. The proposed model: GC-SPP-based model (MPS-SBV-HS-HL-ECS-GC-DS-SPP method [31,33,34,35])

The Dynamic Stabilization (DS) [35] is a stabilizing scheme to enhance the numerical stability for the purely Taylor-series consistent gradient force such as GC scheme [31]. While, the repulsion-based model on the basis of the CMPS model [21] introduces a kind of a stabilizer into the gradient term directly, and thus, the DS scheme cannot be applied to the model simultaneously (refer to [35]). The tank is set as 0.1 m in length comprising water particle with d = 0.002 m. Initially, all the particles including the water particles

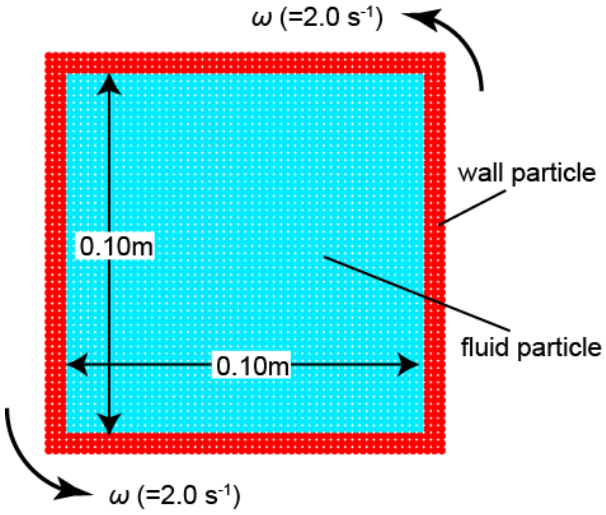

Fig. 5.3.1 Initial condition of particles in simulation of a whirling flow with a regular distribution of particles

are given the angular velocity ω = 2.0 s^{-1}. Moreover, the angular velocity of the tank is constantly given as ω = 2.0 s^{-1} at all the time. Here, since the gravity acceleration is not applied, edges of wall touching outside should be given zero pressure. Therefore, the dummy particles, which are usually set behind the wall particles for solution of the PPE with zero pressure, are needless and replaced by the wall particles in the tests.

5.3.1.1 Test 1: whirlpool with regular distribution of particles

F Firstly, the durability of each model to suppress occurrence of unphysical voids is verified. Water particles are distributed regularly at the initial condition as shown in **Fig. 5.3.1**. **Fig. 5.3.2** shows snapshots of water particles with their pressures and particle number densities by each numerical simulation at t = 0.5 s. In the improved repulsion-based model, an unphysical void space occurs at the center of the tank by the centrifugal force. And it shows an unphysical pressure field with perturbation. While, the improved corrected-gradient model keeps a regular distribution of particles without the hole at the center and shows a smoothed pressure field. The proposed SPP model also maintains the regular distribution of particles with a physical pressure field. These results suggest that tensile force plays a key role to reproduce a physical distribution of particles and keep the volume conservation in whirl flows.

5.3.1.2 Test 2: whirlpool with irregular distribution of particles

The performance of reimposition of unphysical voids by each model is verified in the Test.2. As an initial condition, the same number of fluid particles as Test.1 is set with a different arrangement keeping a hole at the center of the tank. As shown in **Fig. 5.3.3**, particles are firstly distributed regularly as the initial condition of Test1. Then, particles in a 0.04 m range from the center of the tank are forcedly jammed to make room for a hole with a radius r_c = 0.003m. The adjusted positions of jammed particles is written as;

$$\boldsymbol{r}_i^{t2init} = \begin{cases} \boldsymbol{r}_i^{regul}\left(1-\dfrac{r_c}{R_c}+\dfrac{r_c}{\left|\boldsymbol{r}_i^{regul}\right|}\right) & if \quad \left|\boldsymbol{r}_i^{regul}\right| \le R_c \\ \boldsymbol{r}_i^{regul} & if \quad \left|\boldsymbol{r}_i^{regul}\right| > R_c \end{cases} \tag{5.3.1}$$

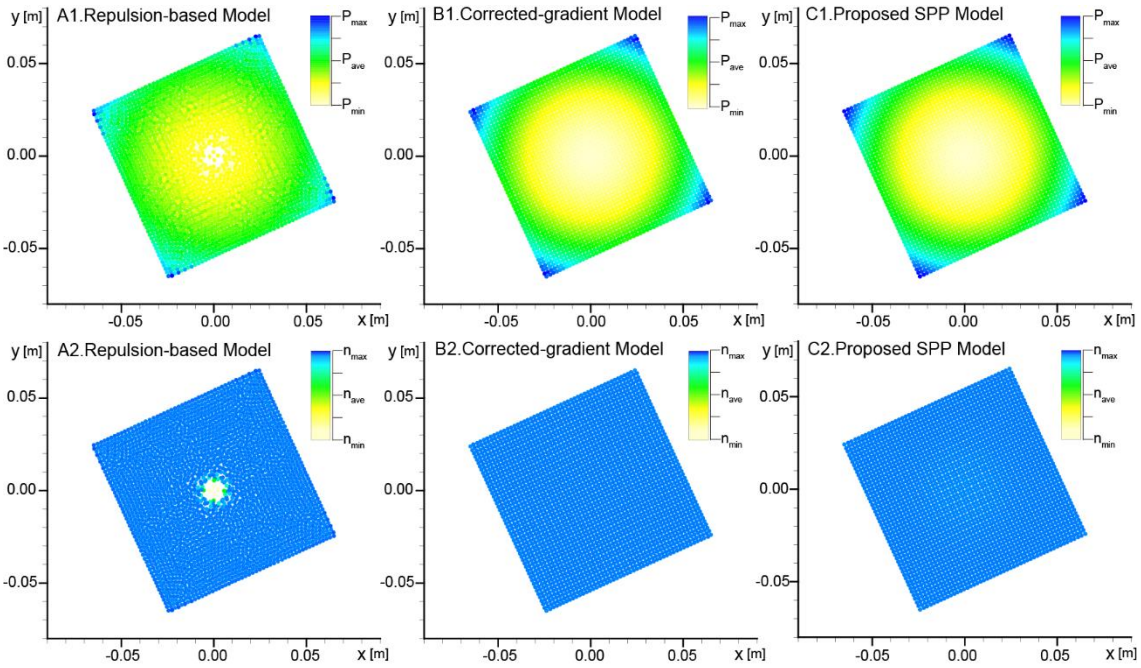

Fig. 5.3.2 Snapshots of water particles at *t*=0.5s together with (A) pressure field and (B) distribution of particle number densities by (1) improved repulsion-based model, (2) improved corrected-gradient model and (3) improved proposed SPP model in simulation of a whirling flow with a regular distribution of particles

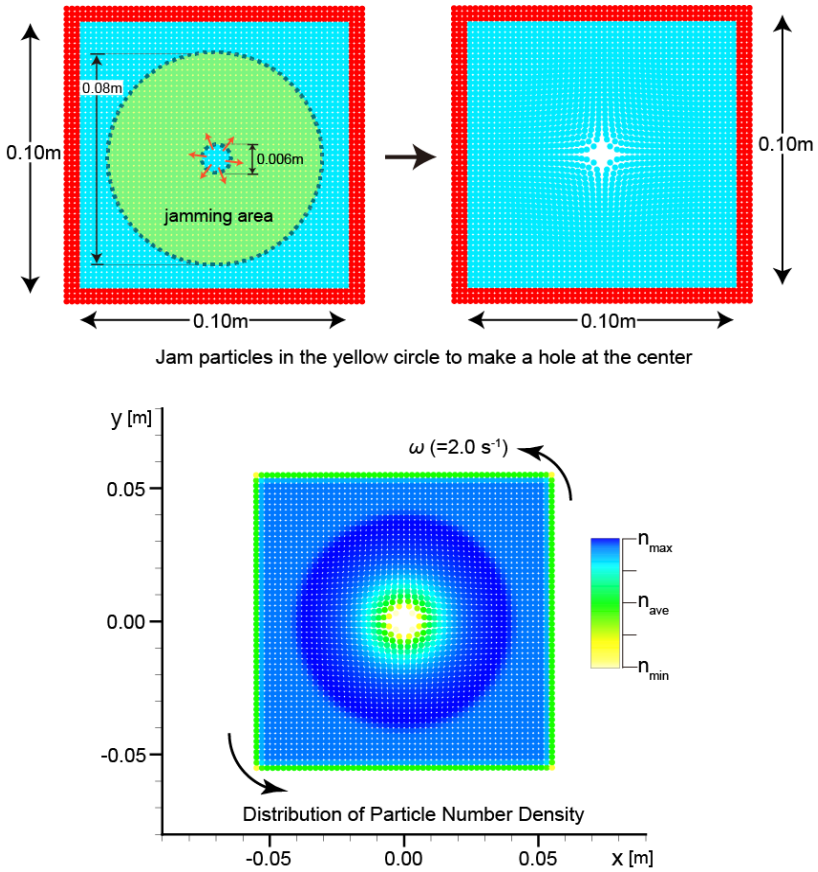

Fig. 5.3.3 Initial condition of particles in simulation of a whirling flow with an irregular distribution of particles

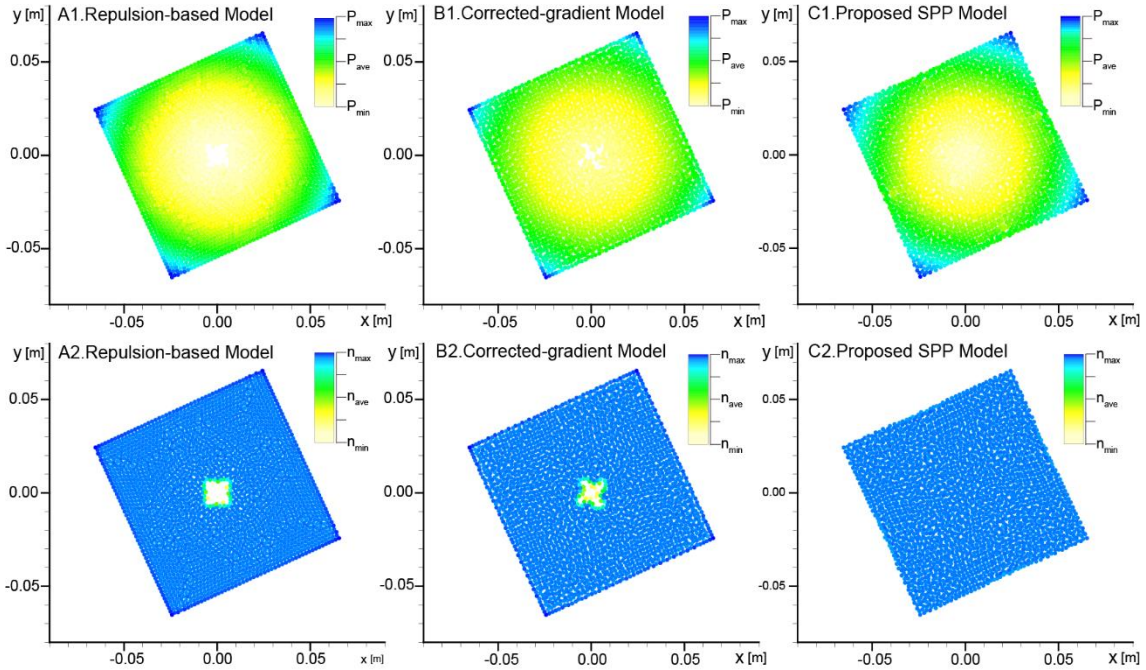

Fig. 5.3.4 Snapshots of water particles at t=0.5s together with (A) pressure field and (B) distribution of particle number densities by (1) improved repulsion-based model, (2) improved corrected-gradient model and (3) improved proposed SPP model in simulation of a whirling flow with an irregular distribution of particles

where $\boldsymbol{r}^{t2init}$ is the newly modified coordinate vector of particles as an initial condition of the Test.2, $\boldsymbol{r}^{regul}$ is the coordinate vector of particles corresponding to the initial condition of the Test.1 and R_c is the radius of the jamming area (R_c = 0.04 m). Since the number of employed particles of Test.2 corresponds to that of Test.1, which comprises water particles fully in the tank, the artificial hole at the center would be packed by particles in a rigorous simulation result. **Fig. 5.3.4** shows snapshots of water particles at t=0.5 s with their pressures and particle number densities of the simulation results. The improved repulsion-based model shows a remained hole at the center as Test.1. The improved corrected-gradient model also leaves the hole at the center with inconsistency of the volume conservation. On the other hand, the proposed SPP model packs particles into the hole and the tank is full with water particles. The improved corrected-gradient model does not have any interactions between the hole and particles, therefore, free-surface particles around the hole may be pulled towards each other to gain their small particle number density by closing to the nearby particles. To begin with, the improved corrected-gradient model and the improved repulsion-based model give a free-surface boundary condition to free-surface particles directly without consideration of volume of the particles, and as a result, the volume of water in the tank is defined lower than the total amount of all the water particles initially.

5.3.2 The Karman vortex simulation

Here, the proposed SPP model is applied to the 2D Karman vortex simulations to show its efficiency for suppression of unphysical voids. Similar to the benchmarks in Chap.3, numerical models are adopted as; the improved repulsion-based model, the improved corrected-gradient model and the proposed SPP model.

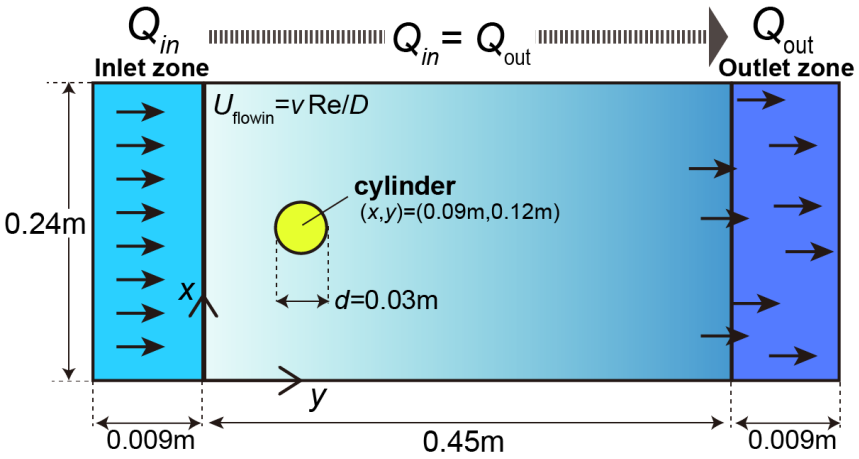

Fig. 5.3.5 Initial condition of Karman vortex simulation.

5.3.2.1 Simulation condition

The calculation set up is shown in **Fig. 5.3.5**. The calculation domain is set as a channel with 0.45 m in length and 0.24 m in width, and filled with water particles with d=0.003 m. A cylinder with its diameter D = 0.03 m is set at a position (x, y) = (0.09 m, 0.12 m). The diameter of the cylinder is ten times larger than that of water particles. Water particles are constantly flown in the channel from the inlet zone with a velocity accommodating with targeted Reynolds numbers, and water particles flow out from the outlet zone. In the MPS method, the moving particles around the outlet are defined as free-surface particles due to their lower particle number densities than the reference n_0. As a result of that, outflow particles cannot reproduce the physical flows, which would be extended more in the real channel. To resolve this, an outlet condition is set to guarantee the volume conservation in the calculation domain as:

$$\sum_{i\in I}\boldsymbol{u}_i = \sum_{j\in J}\boldsymbol{u}_j\,; \qquad I=\{i : x_i < 0.00m\}\,, \quad J=\{j : x_j > 0.45m\} \tag{5.3.2}$$

where I corresponds to the inlet zone and J corresponds to the outlet zone. This condition reproduces a similar flux of the outflow to that of the inflow. As for a condition of inflow, considering the numerical stability, the flow-in particles are given a slow velocity initially and it is increased by degrees within the first 0.5 s. During this period also, Eq. (5.3.2) is applied to the outflow particles to keep the volume conservation in the calculation domain.

5.3.2.2 Verification of time resolution

Particle methods express the fluid motions by Lagrangian tracking, therefore, they do not require the advection term, which is a cause of numerical diffusion. Instead, a regular distribution of particles should be kept for numerical stability and accuracy associated with differential operations. Therefore, some stabilizing schemes are usually introduced for the problem by utilizing an artificial repulsive force to prevent particles from overlapping each other [35]. Considering the original gradient term [1] and the artificial repulsive force term for stabilization, the pressure gradient terms can be generally rewritten as:

$$\langle\nabla p\rangle_i = \frac{D_s}{n_0}\sum_{j\neq i}\frac{(p_j - p_i)}{|\boldsymbol{r}_{ij}|^2}\boldsymbol{r}_{ij}w_{ij} + \boldsymbol{F}_i^{stability} \tag{5.3.3}$$

where p is pressure, D_s is the number of space dimension and $\boldsymbol{F}_i^{stability}$ is the stabilizing force. The first term on the right hand side of Eq. (5.3.3) corresponds to the original gradient term in accordance with the Taylor series, and the second term correspond to the artificial repulsive force term. As for the standard gradient model [20] written as:

$$\langle \nabla p \rangle_i = \frac{D_s}{n_0} \sum_{j \neq i} \frac{(p_j - \hat{p}_i)}{|\boldsymbol{r}_{ij}|^2} \boldsymbol{r}_{ij} w_{ij} \; ; \qquad \hat{p}_i = \min_{j \in J} (p_i, p_j), \quad J = \{ j : w_{ij} \neq 0 \} \tag{5.3.4}$$

This equation can be rewritten [35] by Eq. (5.3.3) as:

$$\langle \nabla p \rangle_i = \frac{D_s}{n_0} \sum_{j \neq i} \frac{(p_j - p_i)}{|\boldsymbol{r}_{ij}|^2} \boldsymbol{r}_{ij} w_{ij} + \boldsymbol{F}_i^{\,stability}; \qquad \boldsymbol{F}_i^{\,stability} = \frac{D_s}{n_0} \sum_{j \neq i} \frac{(p_i - \hat{p}_i)}{|\boldsymbol{r}_{ij}|^2} \boldsymbol{r}_{ij} w_{ij} \tag{5.3.5}$$

This kind of transformation to enhance the numerical stabilization is generally adopted in the particle methods including the SPH method [36]. In the numerical models cited in this study also, the stabilizing schemes are adopted for the pressure gradient term. First, in the repulsion-based model, the pressure gradient is based on the Corrected MPS (CMPS) method [21] and written as:

$$\langle \nabla p \rangle_i = \frac{D_s}{n_0} \sum_{j \neq i} \frac{(p_i + p_j) - (\hat{p}_i + \hat{p}_j)}{|\boldsymbol{r}_{ij}|^2} \boldsymbol{r}_{ij} w_{ij} \tag{5.3.6}$$

Considering the original gradient term and the artificial repulsive force term, this equation can be rewritten [35] as:

$$\langle \nabla p \rangle_i = \frac{D_s}{n_0} \sum_{j \neq i} \frac{(p_j - p_i)}{|\boldsymbol{r}_{ij}|^2} \boldsymbol{r}_{ij} w_{ij} + \boldsymbol{F}_i^{\,stability}; \qquad \boldsymbol{F}_i^{\,stability} = \frac{D_s}{n_0} \sum_{j \neq i} \frac{(p_i - \hat{p}_i) + (p_i - \hat{p}_j)}{|\boldsymbol{r}_{ij}|^2} \boldsymbol{r}_{ij} w_{ij} \tag{5.3.7}$$

On the other hand, the corrected-gradient model and the proposed model are commonly applied with the Gradient Correction (GC) scheme [31] and the Dynamic Stabilization (DS) scheme [35] as:

$$\langle \nabla p \rangle_i = \frac{D_s}{n_0} \sum_{j \neq i} \frac{(p_j - p_i)}{|\boldsymbol{r}_{ij}|^2} \boldsymbol{r}_{ij} \boldsymbol{C}_{ij} w_{ij} + \boldsymbol{F}_i^{\,stability}; \qquad \boldsymbol{F}_i^{\,stability} = \frac{1}{n_0} \sum_{j \neq i} \boldsymbol{F}_{ij}^{\,DS} w_{ij} \tag{5.3.8}$$

where $\boldsymbol{C}_{ij}$ is a corrective matrix by the GC scheme and $\boldsymbol{F}_{ij}^{DS}$ is a minimum required stabilizing force by the DS scheme. DS scheme reproduces meticulously adequate repulsive forces to provide physically sound and computationally stable simulations of main flow features. In general, the more minute a time-interval is, the more precisely a regular distribution of particles is reproduced due to the frequent correction of the distribution of particles. An adequate time resolution is significant for reproduction of a regular distribution of particles.

Here, targeting on a Reynolds number as Re=1200, the Karman vortex simulation is performed

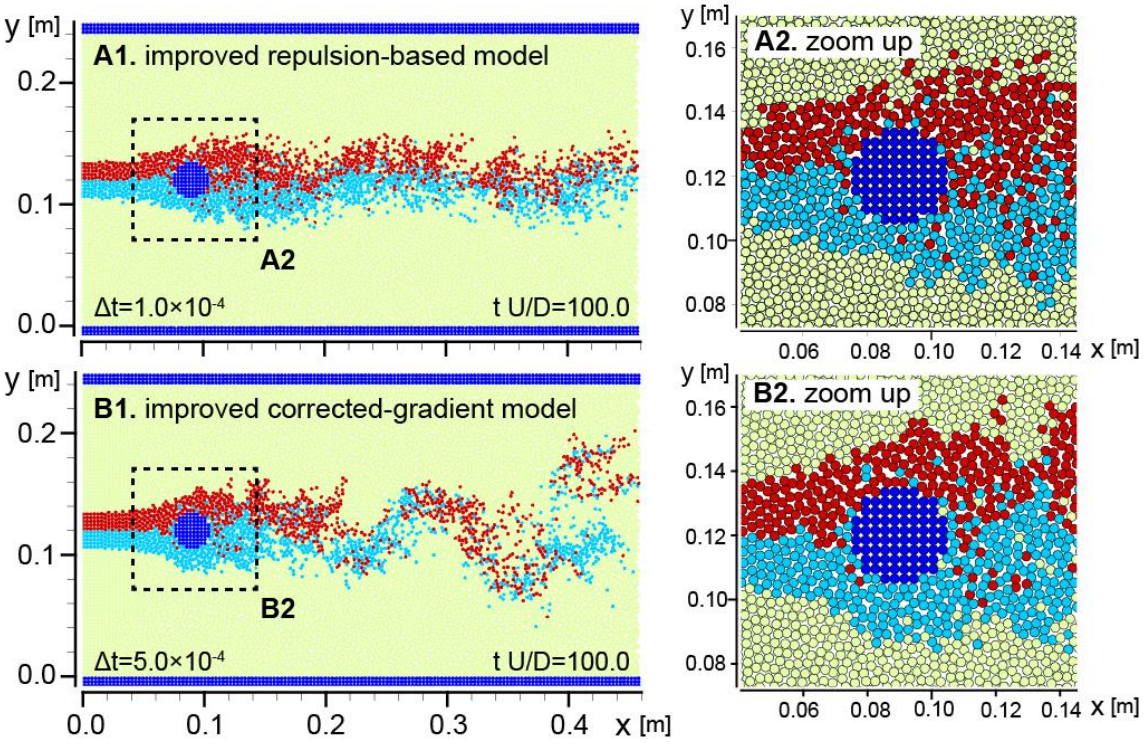

Fig. 5.3.6 Snapshots of particles at together with flow lines obtained tracking the flow-in particles at the same height of the cylinder by (A) improved repulsion-based model and (B) improved corrected-gradient model in simulation of a Karman vortex under Re=1200 with a minute time resolution

with a sufficiently minute time-interval. Firstly, the improved repulsion-based model and the improved corrected-gradient model are applied to the simulation to verify the efficiency of the stabilizers for unphysical voids. To exclude unphysical voids completely, the improved repulsion-based model needs a time-interval $\Delta t = 1.0\times10^{-4}$ s, while, the improved corrected-gradient model needs $\Delta t = 5.0\times10^{-4}$ s. **Fig. 5.3.6** shows the simulation results with flow lines obtained tracking the flow-in particles at the same height of the cylinder by each simulation model. Both simulation results do not show obvious unphysical voids and keep regular distributions of particles, however, flow lines by the flow-in particles are noisily scattered and a significant Karman vortex cannot be found.

Fig. 5.3.7 shows the simulation results with velocity fields by each simulation model. This figure clearly shows considerable numerical noises in the velocity fields. The distributions of particles are exactly modified regularly by setting a minute time-interval in both simulation results. However, since the artificial stabilizing forces are fundamentally unrelated with the original gradient, an excess amount of the stabilizing force brings about inaccurate velocity fields. A lower time resolution is necessary not to interfere the original gradient force and reproduce the accurate velocity field.

Then, the Karman vortex simulation is performed with fifth times longer time-intervals than the previous test; the improved repulsion-based model is applied with a time-interval $\Delta t = 5.0\times10^{-4}$ s, and the improved corrected-gradient model is applied with $\Delta t = 2.5\times10^{-3}$ s. **Fig. 5.3.8** shows the simulation results with flow lines obtained tracking the flow-in particles at the same height of the cylinder by each simulation model. And, **Fig. 5.3.9** shows their velocity fields. From **Fig. 5.3.8**, it is found that unphysical voids occur around the cylinder and centroids of vortices in both simulation models. Moreover, the simulation by the repulsion-based model breaks up at $t = 30.25$ s ($t' = 40.33$, $t' = t\,U/R$) due to the unstable state around the

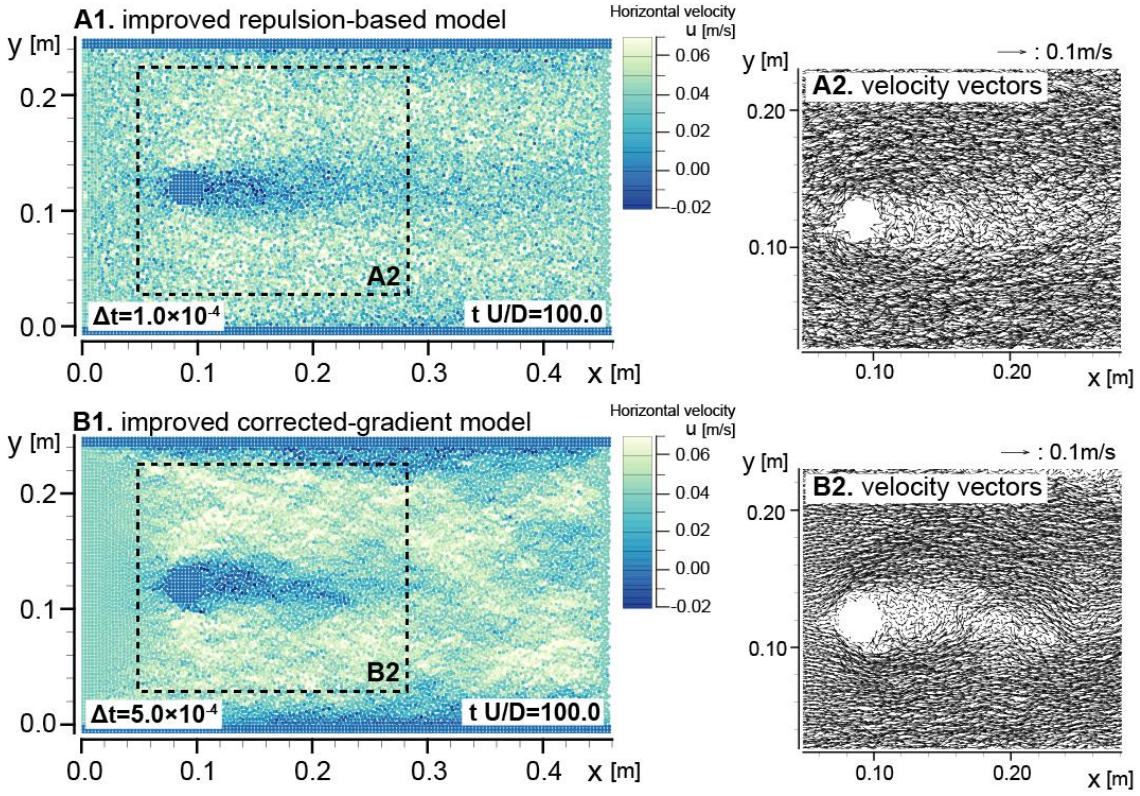

Fig. 5.3.7 Snapshots of particles together with velocity field by (A) improved repulsion-based model and (B) improved corrected-gradient model in simulation of a Karman vortex under Re=1200 with a minute time resolution

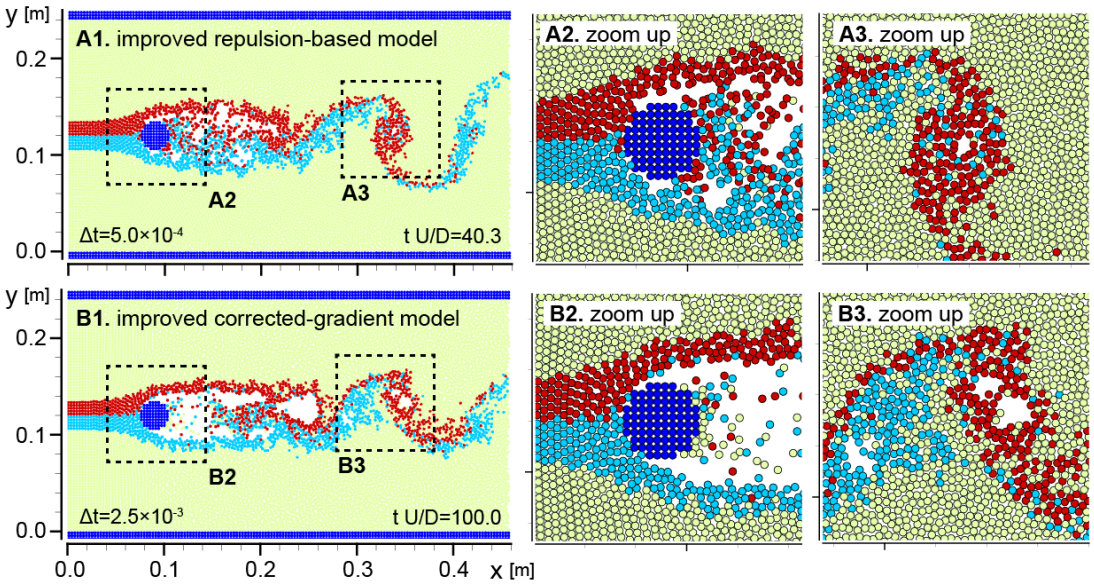

Fig. 5.3.8 Snapshots of particles together with flow lines obtained tracking the flow-in particles at the same height of the cylinder by (A) improved repulsion-based model and (B) improved corrected-gradient model in simulation of a Karman vortex under Re=1200 with a low time resolution

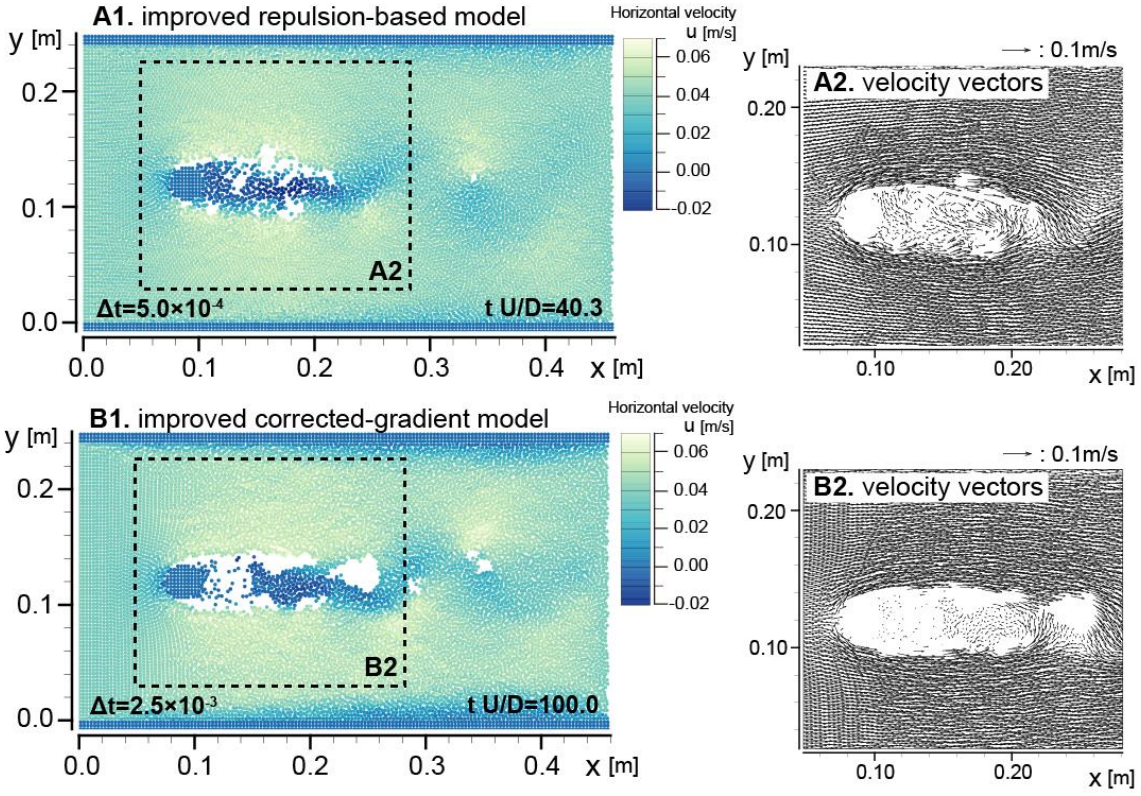

Fig. 5.3.9 Snapshots of particles together with velocity field by (A) improved repulsion-based model and (B) improved corrected-gradient model in simulation of a Karman vortex under Re=1200 with low numerical time-intervals

voids. While, noises of particle velocities are restrained in **Fig. 5.3.9**. From these results, another stabilizing approach is essential for both physical velocity field and regular distribution of particles, that is numerical accuracy and stability.

5.3.2.3 Introduction of the SPP scheme

Here, the proposed SPP scheme is applied to the corrected-gradient model for the Karman-vortex (Re=1200) simulation with the time resolution $\Delta t = 2.5\times10^{-3}$ s. **Fig. 5.3.10** shows the simulation result with a flow line. The unphysical voids shown in the previous simulation results are not found and the flow line shows a clear Karman vortex. In **Fig. 5.3.11** showing the velocity field, numerical noises of velocity are also restrained effectively. In particular, the velocity field is distributed smoothly comparing with previous simulation results without the SPP scheme. **Fig. 5.3.12** shows a simulation result with a particle flow line by the proposed SPP model with a lower time-resolution $\Delta t = 5.0\times10^{-3}$ s. This result also shows a well-reproduction of the Karman vortex without any unphysical void. These simulation results by each model are summarized in **Table.5.3.1**. Comparing with the repulsion-based model, even though the proposed SPP model requires longer calculation time for each time step, it simulates the Karman vortex at Re=1200 more accurately and stably with, at least, a ten-times lower time resolution. Accordingly, the SPP scheme is significantly effective for both accuracy and computational cost.

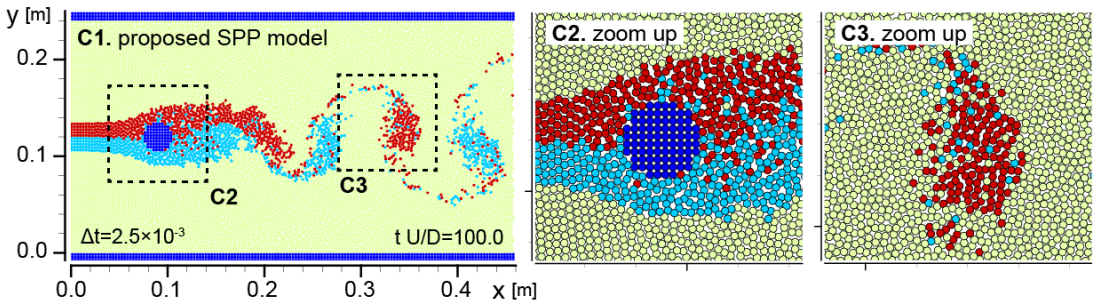

Fig. 5.3.10 Snapshots of particles together with flow lines obtained tracking the flow-in particles at the same height of the cylinder by the proposed SPP model in simulation of a Karman vortex under Re=1200

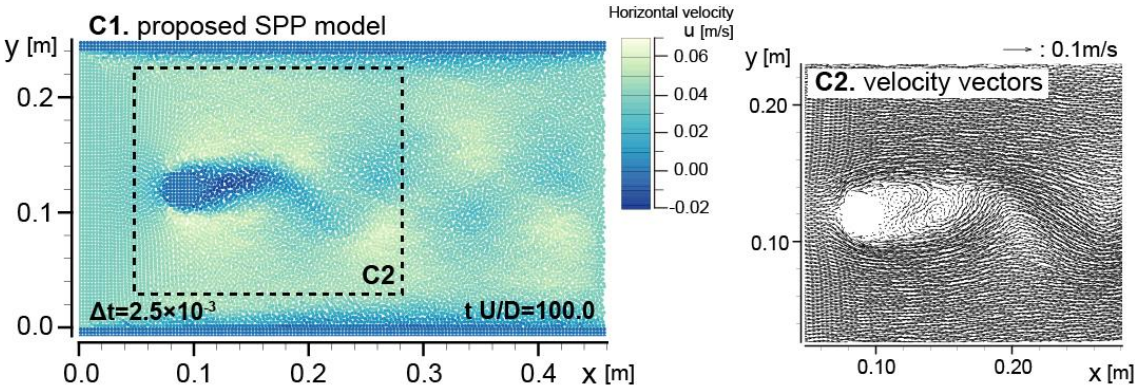

Fig. 5.3.11 Snapshots of particles together with velocity field by the proposed SPP model in simulation of a Karman vortex under Re=1200

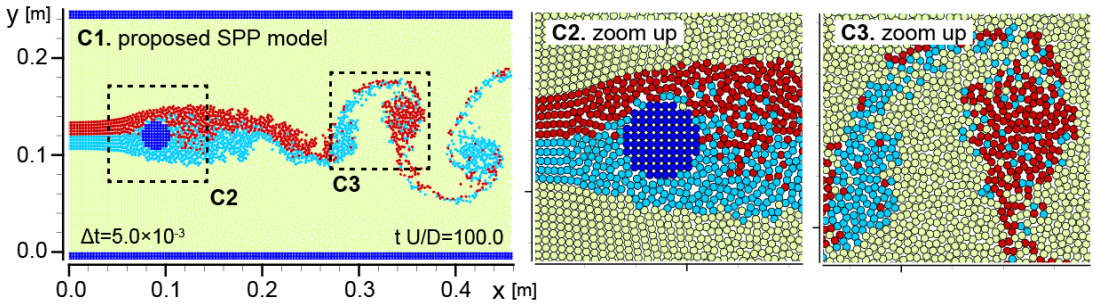

Fig. 5.3.12 Snapshots of particles together with flow lines obtained tracking the flow-in particles at the same height of the cylinder by the proposed SPP model in simulation of a Karman vortex under Re=1200 with a low time resolution

5.3.2.4 Karman vortex simulation at Re=120 by the SPP scheme

Targeting on a relative low Reynolds number as Re=120, a Karman vortex simulation is performed by the proposed SPP model. **Fig. 5.3.13** shows the simulation result with flow lines obtained tracking the flow-in particles at the same height of the cylinder. This figure shows a good reproduction of Karman vortex without any unphysical void in this simulation, and it shows a smoother Karman vortex street than the results under the higher Reynolds number condition, corresponding to the physical state of the real phenomenon.

Table. 5.3.1 Comparison of numerical results in simulation of Karman vortex with Re=1200

Model	Time-interval	Velocity field	Unphysical voids	Number of Time-steps*2 /min	Simulation-time*2 /min
Improved Repulsion-based model (CMPS-HS-HL-ECS)	$\Delta t = 1.0\times10^{-4}$ s	noisy	none	170.3 steps/min	0.017 sec/min
	$\Delta t = 5.0\times10^{-4}$ s	smooth	exist*1	107.4 steps/min	0.054 sec/min
Improved corrected-gradient model (MPS-HS-HL-ECS-GC-DS)	$\Delta t = 5.0\times10^{-4}$ s	noisy	none	100.0 steps/min	0.050 sec/min
	$\Delta t = 2.5\times10^{-3}$ s	smooth	exist	119.0 steps/min	0.298 sec/min
Proposed SPP model (MPS-HS-HL-ECS-GC-DS-SPP)	$\Delta t = 2.5\times10^{-3}$ s	smooth	none	71.3 steps/min	0.178 sec/min
	$\Delta t = 5.0\times10^{-3}$ s	smooth	none	66.1 steps/min	0.330 sec/min

*1 The simulation breaks up at $t = 30.25$s ($t' = 40.33$: $t' = t\ U/R$)

*2 CPU spec: Intel® Xenon® Processor E3-1270 V2 @ 3.50GHz

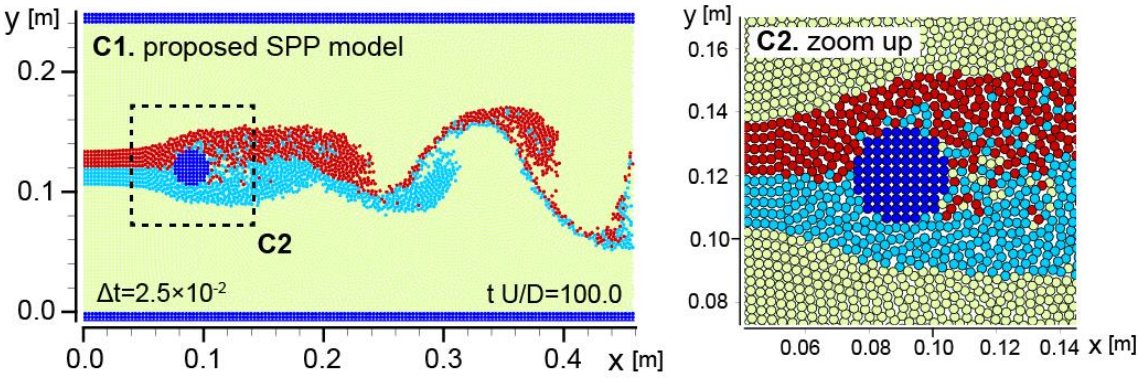

Fig. 5.3.13 Snapshots of particles together with flow lines obtained tracking the flow-in particles at the same height of the cylinder by the proposed SPP model in simulation of a Karman vortex under Re=120

5.4 Concluding remarks

A novel scheme is proposed as a surface boundary condition of projection-based particle methods, namely, the MPS and ISPH methods to resolve a so-far encountered problem of inconsistency in the volume conservation around free surface. From numerical tests by a whirling water flow in a rotating tank, the efficiency of the restrainer and reimposition to unphysical voids by the proposed SPP scheme is demonstrated. Moreover, the SPP scheme is applied to the Karman vortex simulations. In general, it was difficult for the particle methods to suppress the unphysical voids under moving strong vortices without minute time-intervals for the simulation processes, which may bring about a numerical noise by stabilizer. However, from simulation results performed in this study, it is shown that such difficulties are resolved easily by introduction of the proposed SPP scheme.

Despite the fact that this paper focuses on unphysical voids as an error of unphysical free surface, this scheme can be introduced to the physical free surface also, for its volume conservation tracked obscurely up to now. Moreover, even a multi-phase flow simulation which does not have any free surface inherently,

e.g. gas and liquid flow, also has possibly unphysical voids in the calculation process [37], and thus, it is expected that the proposed scheme would work effectively for the numerical accuracy and stability of multiphase particle methods as well.

REFERENCES

[1] Koshizuka, S. and Y. Oka, "Moving particle semi-implicit method for fragmentation of incompressible fluid", *Nuclear Science and Engineering*, 123, pp. 421-434, 1996.

[2] Shao, S. D. and E.Y.M. Lo, "Incompressible SPH method for simulating Newtonian and non-Newtonian flows with a free surface", *Advances in Water Resources*, vol.26, pp. 787–800, 2003.

[3] Gotoh, H. and T., Sakai, "Key Issues in the Particle Method for Computation of Wave Breaking", *Coastal Eng.*, Vol. 53, No. 2-3, pp.171-179, 2006.

[4] Gotoh, H., "Lagrangian Particle Method as Advanced Technology for Numerical Wave Flume", *International Journal of Offshore and Polar Engineering*, Vol. 19, No.3, pp.161-167, 2009.

[5] Zdravkovich, M.M., "Smoke observations of the formation of a Karman vortex street", *J. Fluid. Mech*, vol.37, pp. 491–496, 1969.

[6] Williamson, C.H.K. and A. Roshko, "Vortex formation in the wake of an oscillating cylinder", *Journal of Fluids and Structures*, Volume 2, Issue 4, pp. 355–381, 1988.

[7] Williamson, C.H.K., and A. Roshko, "Vortex Dynamics in the Cylinder Wake", *Annual Review of Fluid Mechanics*, Vol. 28, pp. 477–539, 1996.

[8] Anderson, J.M., Streitlien, K., Barrett, D.S., "Triantafyllou, M.S., Oscillating foils of high propulsive efficiency", *Journal of Fluid Mechanics*, Volume 360, pp. 41-72, 1998

[9] Schumm, M., E. Berger and P. A. Monkewitz, "Self-excited oscillations in the wake of two-dimensional bluff bodies and their control", *Journal of Fluid Mechanics*, Volume 271, pp. 17-53, 1994.

[10] Gopalkrishnan, R., M. S. Triantafyllou, G. S. Triantafyllou and D. Barrett, "Active vorticity control in a shear flow using a flapping foil", *Journal of Fluid Mechanics*, Volume 274, pp. 1-21, 1994.

[11] Noack, R., K. Afanasiev, M. Morzynski, G. Tadmor and F. Thiele, "A hierarchy of low-dimensional models for the transient and post-transient cylinder wake", *Journal of Fluid Mechanics*, Volume 497, pp. 335-363, 2003.

[12] Breuer, M., "A challenging test case for large eddy simulation: high Reynolds number circular cylinder flow", *International Journal of Heat and Fluid Flow*, Volume 21, Issue 5, pp. 648–654, 2000.

[13] Kim, J.W. and D.J. Lee, "Generalized Characteristic Boundary Conditions for Computational Aeroacoustics", *AIAA Journal*, Vol. 38, No. 11, pp. 2040-2049, 2000.

[14] Hori, C., Gotoh, H., Khayyer, A. & Ikari, H., "Simulation of flip-through wave impact by cmps method with sps-turbulence model", *Proc. Coastal Structures 2011*, Yokohama, on CD-ROM, 2011.

[15] Takeda, H.; Miyama, S. M.; Sekiya, M., "Numerical Simulation of Viscous Flow by Smoothed Particle Hydrodynamics", *Progress of Theoretical Physics*, Vol. 92, No. 5, pp. 939-960, 1994.

[16] Lee, E.-S., C. Moulinec, R. Xu, D. Violeau, D. Laurence, P. Stansby, "Comparisons of weakly compressible and truly incompressible algorithms for the SPH mesh free particle method", *Journal of Computational Physics*, Volume 227, Issue 18, Pages 8417–8436, 2008.

[17] Lastiwka, M., M. Basa, N. J. Quinlan, "Permeable and non-reflecting boundary conditions in SPH", *International Journal for Numerical Methods in Fluids*, Volume 61, Issue 7, pp. 709–724, 2009.

[18] Marrone, S., A. Colagrossi, M. Antuono, G. Colicchio, G. Graziani, "An accurate SPH modeling of viscous flows around bodies at low and moderate Reynolds numbers" *Journal of Computational Physics*, Volume 245, pp. 456–475, 2013.

[19] Federico, I., S. Marrone, A. Colagrossi, F. Aristodemo, M. Antuono, "Simulating 2D open-channel flows through an

SPH model", *European Journal of Mechanics - B/Fluids*, Volume 34, pp. 35–46, 2012.
[20] Koshizuka, S., Nobe, A. and Y. Oka "Numerical Analysis of Breaking Waves Using the Moving Particle Semi-implicit Method", *International Journal for Numerical Methods in Fluids*, vol. 26, pp. 751-769, 1998.
[21] Khayyer, A. and H. Gotoh, "Development of CMPS method for accurate water-surface tracking in breaking waves", *Coast. Eng. J.*, 50(2), pp. 179-207, 2008.
[22] Nayroles, B., G. Touzot and P. Villon. "Generalizing the finite element method: diffuse approximation and diffuse elements", *Comput. Mech.*, Vol.10, pp. 307-318, 1992.
[23] Belytschko, T., L. Gu and Y.Y. Lu, "Fracture and crack growth by element-free Galerkin methods", *Modelling Simul. Mater. Sci. Eng*, Vol.2, pp. 519-534, 1994.
[24] Lancaster, P., and K. Salkauskas, "Surfaces generated by moving least squares methods", *Math. Comp.*, vol. 37, pp. 141-158, 1981.
[25] Liu, W.K., S. Jun and Y.F. Zhang, "Reproducing kernel particle methods", *Int. J. Numer. Methods Engrg*, Vol. 20, pp. 1081-1106, 1995.
[26] Bonet, J. and T.-S.L. Lok, "Variational and momentum preservation aspects of smooth particle hydrodynamics formulations", *Comput. Meth. Appl. Mech. Eng*, Vol. 180, pp. 97–115, 1999.
[27] Dilts, G.A., "Moving-least-squares-particle hydrodynamics - I. Consistency and stability", *International Journal for Numerical Methods in Engineering*, vol.44, pp. 1115–1155, 1999.
[28] Colagrossi, A. and Maurizio L., "Numerical simulation of interfacial flows by smoothed particle hydrodynamics", *Journal of Computational Physics*, Volume 191, Issue 2, pp. 448–475, 2003.
[29] Oger, G., M. Doring, B. Alessandrini, P. Ferrant, "An improved SPH method: towards higher order convergence", *J. Comput. Phys.*, Vol. 225 (2), pp. 1472–1492, 2007.
[30] Schwaiger, H.F., "An implicit corrected SPH formulation for thermal diffusion with linear free surface boundary conditions", *Int. J. Numer. Methods Eng*. Vol. 75, pp. 647–671, 2008.
[31] Khayyer, A. and H. Gotoh, "Enhancement of stability and accuracy of the moving particle semi-implicit method", *Journal of Computational Physics*, vol. 230, pp. 3093-3118, 2011.
[32] Colagrossi, A., "A meshless Lagrangian method for free-surface and interface flows with fragmentation", PhD Thesis, Universita di Roma, La Sapienza, 2003.
[33] Khayyer, A. and H. Gotoh, "Modified Moving Particle Semi-implicit methods for the prediction of 2D wave impact pressure", *Coastal Engineering*, 56, 419-440, 2009.
[34] Khayyer, A. and H. Gotoh, "A higher order Laplacian model for enhancement and stabilization of pressure calculation by the MPS method", *Appl. Ocean Res*, Vol. 32 (1), pp. 124–131, 2010.
[35] Tsuruta, N., A. Khayyer and H. Gotoh, "A Short Note on Dynamic Stabilization of Moving Particle Semi-implicit Method", *Computers & Fluids*, Vol. 82, pp.158–164, 2013.
[36] Monaghan JJ., "SPH without a tensile instability", *Journal of Computational Physics*, vol.159(2), pp.290–311, 2000.
[37] Khayyer, A. and H. Gotoh, "Enhancement of performance and stability of MPS mesh-free particle method for multiphase flows characterized by high density ratios", *Journal of Computational Physics*, Vol. 242, pp. 211-233, 2013.

CHAPTER 6

Investigation of Kernel function

6.1 Overview

In the Particle methods, fluid motions are calculated by Lagrangian tracking of calculation points (particles) and the governing equation is solved by modeling locally weighted interactions between particles with the kernel function. In addition to an amount of the total interaction acting the targeted particle, its acting direction is also decided by the weighted averaging operation. Consequently, it is essential to keep regularity of distribution of particles to reproduce the correct acting force for numerical stability and accuracy in particle simulations. However, the perfect regularity is not reproduced except static areas expressed by fixed particles or the initial condition due to transfer of the moving particles, and a little error is allowed in practical processes of particle simulations. Instead, as solutions of the problem, some stabilizing schemes have been developed to minimize the irregular distribution of estimation, such as introduction of the stabilizing repulsive force as an artificial viscosity (corresponding to Chap.4) to keep a permissible minimum distance between particles, solving the higher-order derivative (corresponding to the HS and HL schemes), applying the correction matrix to the gradient operation (corresponding to the GC scheme) to modify irregular distribution of estimation, handling the appropriate free-surface boundary (corresponding to Chap.5) for unphysical voids caused by the maldistribution of particles and etc. As a common manner of these approaches, they are applied with the kernel function as long as the particle method is based on the locally weighted estimation. That is, the kernel function is one of the most significant factors to guarantee stable particle simulations.

Investigations of kernel functions are performed particularly in the SPH method. In the SPH framework, density is estimated through the weighted averaging process by the kernel function, and hence, the kernel function is often focused on as a first issue for the solution of governing equations in the numerical procedure. Discussing the stability by each kernel function, firstly, the order of polynomial in the kernel functions are taken as a key factor to decide its continuity property with the convergence, namely smooth distribution of weighting in differential operators [1]. In the projection-based particle method, the second derivative is contained in the Poisson Pressure Equation (PPE), and thus, it was reported that at least 3^{rd} order of polynomial is necessary for the numerical stability. In recent years, the higher-order kernels are introduced into the particle method and well-stabile results are gotten in their studies. As for the candidates, the higher-order B-spline kernels (Schoenberg, 1946 [2], Monaghan and Lattanzio, 1985 [3]) corresponding to quartic spline and quantic spline [4], HOCT4 kernel [5], Wendland (Wendland, 1995 [6]) kernel, etc. are widely used. In the instability mode by particle methods, clumping of particles by tensile force are often found. It is known that this tensile instability with the clumping state is inevitable and deteriorated in the smoothing operation by centroid-increasing kernel functions in contrast to a state by repulsive interactions (Khayyer and Gotoh, 2011 [7]). As for this influence, the continuity of derivatives at the origin was noticed and its influence was examined by comparing some kernels [8]. While, Walter and

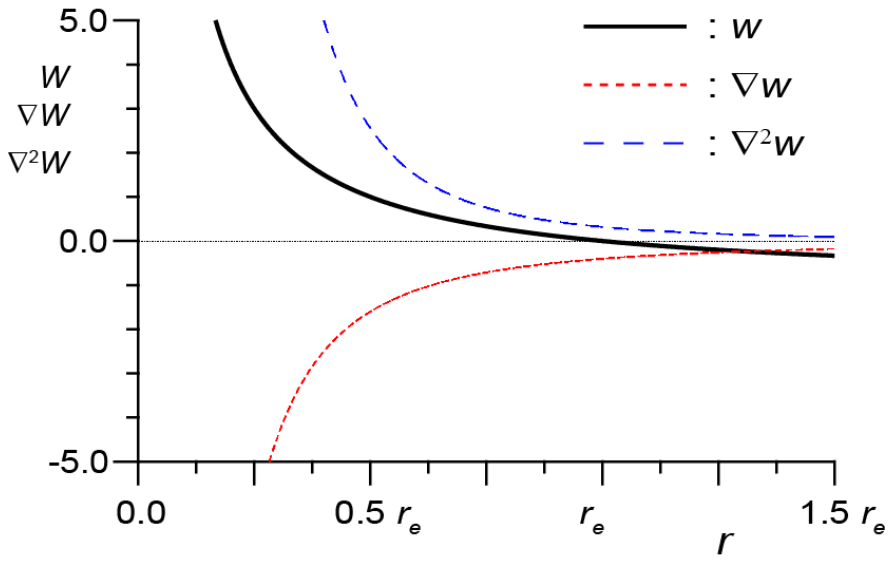

Fig. 6.2.1 Traditional kernel function

Hossam (2012) [9] found that instability of the kernel function depends on its Fourier transform, and proved that the negative Fourier transform predominantly causes the instability mode rather than the traditional ideas about the origin of the instability.

On the other hand, the MPS method originally targets on incompressible flows and places emphasis on the incompressibility characterized by a non-overlapped-particle state. Therefore, the traditional gradient model is composed of purely repulsive interactions and the traditional kernel function is chosen so as to assist the repulsive interaction suitably. The traditional kernel function w is written as:

$$w\left(\left|\boldsymbol{r}_{ij}\right|\right)=\frac{r_e}{\left|\boldsymbol{r}_{ij}\right|}-1; \qquad \boldsymbol{r}_{ij}=\boldsymbol{r}_j-\boldsymbol{r}_i \tag{6.1.1}$$

where $\boldsymbol{r}$ is the coordinate vector of a particle, r_e is the radius of the influence area and subscripts i and j denote the targeted particle i and its neighboring particle j, respectably. **Fig. 6.2.1** shows the illustration of the traditional kernel. By this function, the repulsive force enlarges infinitely as particles getting close to each other and avoidance of overlapped-particle states is guaranteed.

However, nowadays, the accurate particle methods have been developed with introduction of the tensile interactions. Being incidental to them, interaction formula representing each term in the governing equations are reshaped, consequently, the tendency of the adaptability of kernel function has been changed. In this chapter, the applicability of the traditional kernel function for the accurate particle method is investigated by focusing on the convergence along the Gauss's theorem in the kernel function. Additionally, one of the higher-order kernel function, that is the Wendland kernel as a reliable kernel function proved by the existing studies is introduced into the accurate particle method to enhance numerical stability in the MPS simulations, and its validity is examined through some benchmarks by comparison with experimental results and simulation results by the traditional kernel function.

6.2 Consistency in convergence for locally weighted averaging

In the MPS method, the gradient operation is expressed by interactions between neighboring particles as:

$$\langle \nabla \phi \rangle_i = \frac{1}{n_0} \sum_{j \neq i} \nabla \phi_{ij} w_{ij}; \qquad \phi_{ij} = \phi_j - \phi_i, \quad w_{ij} = w(|\boldsymbol{r}_{ij}|) \tag{6.2.1}$$

where ϕ is a physical quantity and n_0 is the reference particle number density. Where the kernel resolution scale is fully sufficient, the number of the sampling interactions is approximated to the infinite, and thus, the summation formula in Eq. (6.2.1) can be substituted by an integral formula laying a same foundation as the SPH framework. By the SPH kernel function W, the gradient of a physical quantity $\nabla\phi W$ at position $\boldsymbol{x}$ with its neighboring calculation point $\boldsymbol{\xi}$ is written as [10]:

$$\nabla \phi(\boldsymbol{\xi})|_{\boldsymbol{\xi}} W(|\boldsymbol{r}|, h) = \nabla \{\phi(\boldsymbol{\xi}) W(|\boldsymbol{r}|, h)\}|_{\boldsymbol{\xi}} + \phi(\boldsymbol{\xi}) \nabla W(|\boldsymbol{r}|, h)|_{\boldsymbol{x}} \tag{6.2.2}$$

where h is the smoothing scale. Moreover, applying Gauss's theorem to the integral of Eq. (6.2.2), the local weighted averaging gradient at position $\boldsymbol{x}$ is obtained as:

$$\nabla \phi(\boldsymbol{x})|_{\boldsymbol{x}} = \iiint_{\Omega} \nabla \phi(\boldsymbol{\xi})|_{\boldsymbol{\xi}} W(|\boldsymbol{r}|, h) dV = \iint_{S} \phi(\boldsymbol{\xi}) W(|\boldsymbol{r}|, h) \boldsymbol{n} dS + \iiint_{\Omega} \phi(\boldsymbol{\xi}) \nabla W(|\boldsymbol{r}|, h)|_{\boldsymbol{x}} dV \tag{6.2.3}$$

While, the local weighted averaging divergence at position $\boldsymbol{x}$ is:

$$\nabla \cdot \boldsymbol{\phi}(\boldsymbol{x})|_{\boldsymbol{x}} = \iiint_{\Omega} \nabla \cdot \boldsymbol{\phi}(\boldsymbol{\xi})|_{\boldsymbol{\xi}} W(|\boldsymbol{r}|, h) dV = \iint_{S} \boldsymbol{\phi}(\boldsymbol{\xi}) W(|\boldsymbol{r}|, h) \cdot \boldsymbol{n} dS + \iiint_{\Omega} \boldsymbol{\phi}(\boldsymbol{\xi}) \cdot \nabla W(|\boldsymbol{r}|, h)|_{\boldsymbol{x}} dV \tag{6.2.4}$$

The local weighted averaging Laplacian at position $\boldsymbol{x}$ is:

$$\begin{aligned} \nabla^2 \phi(\boldsymbol{x})|_{\boldsymbol{x}} &= \iint_{S} \nabla \cdot \{\phi(\boldsymbol{\xi}) W(|\boldsymbol{r}|, h) \boldsymbol{n}\} dS + \iiint_{\Omega} \nabla \cdot \{\phi(\boldsymbol{\xi}) \nabla W(|\boldsymbol{r}|, h)|_{\boldsymbol{x}}\} dV \\ &= \iint_{S} \{\nabla \phi(\boldsymbol{\xi})|_{\boldsymbol{x}} W(|\boldsymbol{r}|, h) \cdot \boldsymbol{n} + \phi(\boldsymbol{\xi}) \nabla W(|\boldsymbol{r}|, h)|_{\boldsymbol{x}} \cdot \boldsymbol{n} + \phi(\boldsymbol{\xi}) W(|\boldsymbol{r}|, h) \nabla \cdot \boldsymbol{n}|_{\boldsymbol{x}}\} dS \\ &\quad + \iiint_{\Omega} \{\nabla \phi(\boldsymbol{\xi})|_{\boldsymbol{x}} \cdot \nabla W(|\boldsymbol{r}|, h)|_{\boldsymbol{x}} + \phi(\boldsymbol{\xi}) \nabla^2 W(|\boldsymbol{r}|, h)|_{\boldsymbol{x}}\} dV \end{aligned} \tag{6.2.5}$$

Considering the computational cost, the influence area, in which neighboring positions are sampled for estimation of the interactions, is limited to an infinite area in practical processes. Accordingly, prudent consideration of consistency in the Gauss's theorem at the discontinuous edge of the influence area is required. Herewith, the consistency of the traditional kernel function for the accurate particle method in convergence of each operation is investigated from on the basis of Eqs. (6.2.3), (6.2.4) and (6.2.5).

6.2.1 Consistency in convergence of the Source term of PPE

Firstly, consistency in convergence of the Source term of PPE by the traditional MPS kernel function for the accurate particle method corresponding to the HS scheme is examined. The Continuity equation is written as:

$$\frac{1}{n_0}\frac{Dn_i}{Dt} + \nabla \cdot \boldsymbol{u}_i = 0 \tag{6.2.6}$$

where n is the particle number density and $\boldsymbol{u}$ is the velocity vector. In two-dimension space by the HS scheme, the first term in the left hand side of Eq. (6.2.6) is obtained through the Lagrangian derivative as:

$$\begin{aligned}
\frac{1}{n_0}\frac{Dn_i}{Dt} &= \frac{1}{n_0}\sum_{j\neq i}\frac{Dw_{ij}}{Dt} \\
&= \frac{1}{n_0}\sum_{j\neq i}\left(\frac{\partial w_{ij}}{\partial r_{ij}}\frac{\partial r_{ij}}{\partial x_{ij}}\frac{\partial x_{ij}}{\partial t} + \frac{\partial w_{ij}}{\partial r_{ij}}\frac{\partial r_{ij}}{\partial y_{ij}}\frac{\partial y_{ij}}{\partial t}\right) = \frac{1}{n_0}\sum_{j\neq i}\left(\frac{\partial w_{ij}}{\partial r_{ij}}\frac{\partial r_{ij}}{\partial x_{ij}}u_{ij} + \frac{\partial w_{ij}}{\partial r_{ij}}\frac{\partial r_{ij}}{\partial y_{ij}}v_{ij}\right) \\
&= \frac{1}{n_0}\sum_{j\neq i}\left(\boldsymbol{u}_{ij}\cdot\nabla_{ij}w_{ij}\right) \;; \qquad \left(\nabla_i = \left(\frac{1}{\partial x_i}, \frac{1}{\partial y_i}\right), \quad \nabla_{ij} = \left(\frac{1}{\partial x_{ij}}, \frac{1}{\partial y_{ij}}\right)\right) \\
&= -\frac{1}{n_0}\sum_{j\neq i}\left(\boldsymbol{u}_{ij}\cdot\nabla_i w_{ij}\right); \qquad \left(\nabla_i = -\nabla_{ij} \quad \because \frac{1}{\partial x_i} = \frac{1}{\partial x_{ij}}\frac{\partial x_{ij}}{\partial x_i} = \frac{1}{\partial x_{ij}}(-1)\right)
\end{aligned} \tag{6.2.7}$$

where $\boldsymbol{r}$ is defined as $\boldsymbol{r} = (x, y)$ and $|\boldsymbol{r}| = r$. Here, for examination of its convergence, the left hand side of this equation is deformed to an integral formula by transforming each variant as: particle $i \rightarrow$ position $\boldsymbol{x}$ and neighboring particle $j \rightarrow$ position $\boldsymbol{\xi}$, and defining a vector $\boldsymbol{\phi}$ as: $\boldsymbol{\phi}(\boldsymbol{\xi}) = \boldsymbol{u}(\boldsymbol{\xi}) - \boldsymbol{u}(\boldsymbol{x})$. Then, the following equation is obtained as:

$$\begin{aligned}
&\frac{1}{n_0}\sum_{j\neq i}\left(\boldsymbol{u}_{ij}\cdot\nabla_i w_{ij}\right) \\
&\rightarrow \iiint_\Omega \boldsymbol{\phi}(\boldsymbol{\xi})\cdot\nabla W\left(|\boldsymbol{r}|, h\right)\big|_x dV = \iiint_\Omega \boldsymbol{u}(\boldsymbol{\xi})\cdot\nabla W\left(|\boldsymbol{r}|, h\right)\big|_x dV - \iiint_\Omega \boldsymbol{u}(\boldsymbol{x})\cdot\nabla W\left(|\boldsymbol{r}|, h\right)\big|_x dV
\end{aligned} \tag{6.2.8}$$

As for the second term in the right hand side of this equation, $\boldsymbol{u}(\boldsymbol{x})$ is constant in the influence domain of position $\boldsymbol{x}$, and the integration of derivative of the kernel $\nabla W|_{\boldsymbol{x}}$ is given zero due to offset by the symmetric distribution of the samples $\boldsymbol{\xi}$. Therefore, this term is decided as:

$$\iiint_\Omega \boldsymbol{u}(\boldsymbol{x})\cdot\nabla W\left(|\boldsymbol{r}|, h\right)\big|_x dV = 0 \tag{6.2.9}$$

Then, from Eqs. (6.2.7), (6.2.8) and (6.2.9), the follows:

$$\frac{1}{n_0}\frac{Dn_i}{Dt} \to -\iiint_\Omega \boldsymbol{u}(\xi)\cdot\nabla W(|\boldsymbol{r}|,h)\big|_x\, dV \tag{6.2.10}$$

is obtained. While, the second term in the left hand side of Eq. (6.2.6) is simply given from Eq. (6.2.4) as:

$$\begin{aligned}&\nabla\cdot\boldsymbol{u}_i\\ &\to \nabla\cdot\boldsymbol{u}(\boldsymbol{x})\big|_x = \iint_S \boldsymbol{u}(\xi)W(|\boldsymbol{r}|,h)\cdot\boldsymbol{n}dS + \iiint_\Omega \boldsymbol{u}(\xi)\cdot\nabla W(|\boldsymbol{r}|,h)\big|_x\, dV\end{aligned} \tag{6.2.11}$$

Applying Eqs. (6.2.10) and (6.2.11) to the Continuity equation (6.2.5), we get the following transformed equation as:

$$\begin{aligned}&\frac{1}{n_0}\frac{Dn_i}{Dt} + \nabla\cdot\boldsymbol{u}_i\\ &\to -\iiint_\Omega \boldsymbol{u}(\xi)\cdot\nabla W(|\boldsymbol{r}|,h)\big|_x\, dV + \left\{\iint_S \boldsymbol{u}(\xi)W(|\boldsymbol{r}|,h)\cdot\boldsymbol{n}dS + \iiint_\Omega \boldsymbol{u}(\xi)\cdot\nabla W(|\boldsymbol{r}|,h)\big|_x\, dV\right\}\\ &\quad = \iint_S \boldsymbol{u}(\xi)W(|\boldsymbol{r}|,h)\cdot\boldsymbol{n}dS\end{aligned} \tag{6.2.12}$$

Therefore, it gets obvious that the requisite condition for convergence of the Continuity equation (6.2.6) is:

$$\iint_S \boldsymbol{u}(\xi)W(|\boldsymbol{r}|,h)\cdot\boldsymbol{n}dS = 0 \tag{6.2.13}$$

In practical processes of MPS simulations, the influence area is not set as the infinite area, but a finite area defined by limiting the sampling targets to the neighboring zone as $r \leqq r_e$, and the following definition is given as:

$$w(r_e) = 0 \tag{6.2.14}$$

This can be transformed as:

$$w(r_e) = 0 \quad \to \quad W(h,h) = 0 \tag{6.2.15}$$

Consequently, Eq. (6.2.13) is clearly satisfied and the convergence in application of the HS scheme by the traditional kernel function is proved.

6.2.2 Consistency in convergence of Laplacian of pressure

Secondly, consistency of the Laplacian of pressure in PPE is examined in application of the HL scheme. From Eqs. (6.2.3) and (6.2.13), the gradient operator can be transformed in consideration of the symmetric distribution of neighboring particles as:

$\nabla\phi_i$

$$\rightarrow \nabla\phi(\boldsymbol{x})\big|_{\boldsymbol{x}} = \iiint_{\Omega} \phi(\boldsymbol{\xi}) \nabla W(|\boldsymbol{r}|, h)\big|_{\boldsymbol{x}} dV$$

$$\rightarrow \frac{1}{n_0}\sum_{j\neq i}\left(\phi_j \nabla_i w_{ij}\right) = \frac{1}{n_0}\sum_{j\neq i}\left(\phi_{ij}\nabla_i w_{ij}\right) + \frac{1}{n_0}\sum_{j\neq i}\left(\phi_i \nabla_i w_{ij}\right) \tag{6.2.16}$$

$$= \frac{1}{n_0}\sum_{j\neq i}\left(\phi_{ij}\nabla_i w_{ij}\right)$$

The HL scheme is deduced from divergence of the gradient by using Eq. (6.2.16) as:

$$\nabla^2\phi_i = \nabla\cdot\nabla\varphi_i = \nabla_i\cdot\left\{\frac{1}{n_0}\sum_{j\neq i}\left(\phi_{ij}\nabla_i w_{ij}\right)\right\} = \frac{1}{n_0}\sum_{j\neq i}\left(\nabla_i\phi_{ij}\cdot\nabla_i w_{ij} + \phi_{ij}\nabla_i{}^2 w_{ij}\right) \tag{6.2.17}$$

$$\left(or \quad \frac{1}{n_0}\sum_{j\neq i}\left(\nabla_{ij}\phi_{ij}\cdot\nabla_{ij} w_{ij} + \phi_{ij}\nabla_{ij}{}^2 w_{ij}\right)\right)$$

While, the integral formula of Laplacian is obtained from Eqs. (6.2.5) and (6.2.14) as:

$\left\langle\nabla^2\phi\right\rangle_i$

$$\rightarrow \nabla^2\phi(\boldsymbol{x})\big|_{\boldsymbol{x}} = \iint_S \left\{\nabla\phi(\boldsymbol{\xi})\big|_{\boldsymbol{x}} W(|\boldsymbol{r}|, h)\cdot\boldsymbol{n} + \phi(\boldsymbol{\xi})\nabla W(|\boldsymbol{r}|, h)\big|_{\boldsymbol{x}}\cdot\boldsymbol{n} + \phi(\boldsymbol{\xi})W(|\boldsymbol{r}|, h)\nabla\cdot\boldsymbol{n}\big|_{\boldsymbol{x}}\right\}dS$$

$$+ \iiint_{\Omega}\left\{\nabla\phi(\boldsymbol{\xi})\big|_{\boldsymbol{x}}\cdot\nabla W(|\boldsymbol{r}|, h)\big|_{\boldsymbol{x}} + \phi(\boldsymbol{\xi})\nabla^2 w(|\boldsymbol{r}|)\big|_{\boldsymbol{x}}\right\}dV$$

$$= \iint_S \left\{0^* + \phi(\boldsymbol{\xi})\nabla W(|\boldsymbol{r}|, h)\big|_{\boldsymbol{x}}\cdot\boldsymbol{n} + 0^*\right\}dS \qquad (*Applying\ Eq.(6.2.15)) \tag{6.2.18}$$

$$+ \iiint_{\Omega}\left\{\nabla\phi(\boldsymbol{\xi})\big|_{\boldsymbol{x}}\cdot\nabla W(|\boldsymbol{r}|, h)\big|_{\boldsymbol{x}} + \phi(\boldsymbol{\xi})\nabla^2 W(|\boldsymbol{r}|, h)\big|_{\boldsymbol{x}}\right\}dV$$

$$= \iint_S \left\{\phi(\boldsymbol{\xi})\nabla W(|\boldsymbol{r}|, h)\big|_{\boldsymbol{x}}\cdot\boldsymbol{n}\right\}dS$$

$$+ \iiint_{\Omega}\left\{\nabla\phi(\boldsymbol{\xi})\big|_{\boldsymbol{x}}\cdot\nabla W(|\boldsymbol{r}|, h)\big|_{\boldsymbol{x}} + \phi(\boldsymbol{\xi})\nabla^2 W(|\boldsymbol{r}|, h)\big|_{\boldsymbol{x}}\right\}dV$$

Similarly, Eq. (6.2.17) can be transformed to an integral formula in consideration of the symmetric distribution of neighboring particles as Eq. (6.2.9):

$$\frac{1}{n_0}\sum_{j\neq i}\left(\nabla_i\phi_{ij}\cdot\nabla_i w_{ij} + \phi_{ij}\nabla_i{}^2 w_{ij}\right) = \frac{1}{n_0}\sum_{j\neq i}\left(\nabla_i\phi_j\cdot\nabla_i w_{ij} + \phi_j\nabla_i{}^2 w_{ij}\right) - \frac{1}{n_0}\sum_{j\neq i}\left(\nabla_i\phi_i\cdot\nabla_i w_{ij} + \phi_i\nabla_i{}^2 w_{ij}\right)$$

$$= \frac{1}{n_0}\sum_{j\neq i}\left(\nabla_i\phi_j\cdot\nabla_i w_{ij} + \phi_j\nabla_i{}^2 w_{ij}\right) \tag{6.2.19}$$

$$\rightarrow \iiint_{\Omega}\left\{\nabla\phi(\boldsymbol{\xi})\big|_{\boldsymbol{x}}\cdot\nabla w(|\boldsymbol{r}|)\big|_{\boldsymbol{x}} + \phi(\boldsymbol{\xi})\nabla^2 w(|\boldsymbol{r}|)\big|_{\boldsymbol{x}}\right\}dV$$

It is shown that the requisite condition to correspond Eq. (6.2.19) to Eq. (6.2.18) is:

$$\iint_S \left\{\phi(\boldsymbol{\xi})\nabla W(|\boldsymbol{r}|, h)\big|_{\boldsymbol{x}}\cdot\boldsymbol{n}\right\}dS = 0 \tag{6.2.20}$$

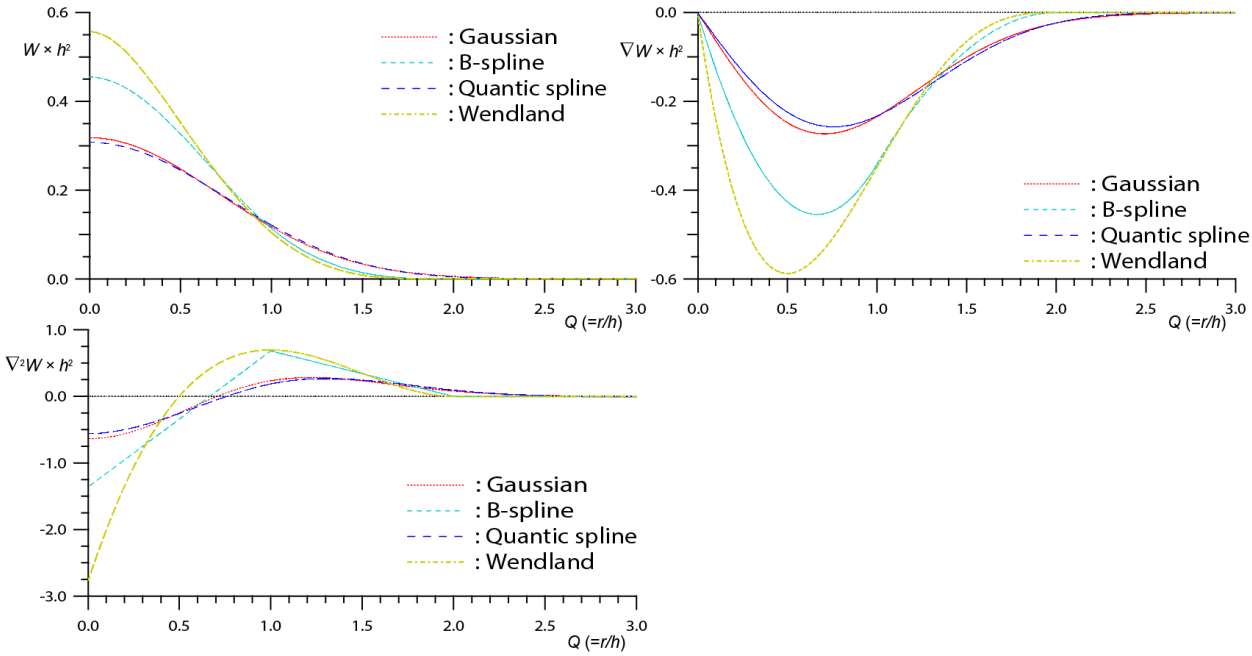

Fig. 6.3.1 (A)Widely used Kernels, (B) their first derivatives and (C) their second derivatives

In the finite area, namely the influence area by practical simulation processes, the following condition is required for Eq. (6.2.20) as:

$$\nabla w(r_e) = 0 \tag{6.2.21}$$

However, the traditional kernel function is defined as:

$$\nabla w(r_e) = -\frac{1}{r_e} \tag{6.2.22}$$

Consequently, the traditional kernel function does not satisfy with the requisite condition (Eq. (6.2.20)) for the HL scheme. In brief, the traditional kernel function has a problem of continuity of the second derivative around the edge of the influence circle. By resolving this inconsistency, it is expected that the numerical stability and accuracy would be enhanced.

6.3 Introduction of the Wendland kernel

Herewith, the Wendland kernel (shown in **Fig. 6.3.1**) whose reliance is proved by existing studies is newly introduced into the MPS method to resolve the problem disclosed in the previous section. The Wendland kernel consists of relative high order polynomials of 5th degree and satisfies with Eqs. (6.2.14) and (6.2.21). The equation of the function is as follows:

$$W(q,h)=\alpha_{Ds}\begin{cases}\left(1-\frac{q}{2}\right)^4(1+2q) & if \quad 0\le q\le 2\\ 0 & if \quad 2<q\end{cases};\qquad q=\frac{r}{h},\quad \alpha_{Ds}=1.0 \tag{6.3.1}$$

where α_{Ds} is the normalization constant. Since the MPS framework originally includes the normalization constant with the particle number density n_0, α_{Ds} is not required, and here, set as α_{Ds} =1.0.

6.4 Verification of efficacy of Wendland kernel

To verify the adaptability of the Wendland kernel function, three benchmarks are performed with simulations by the traditional kernel function and the Wendland kernel function. Here, pressure stability of water is focused on to show the effectiveness of the Wendland kernel function for suppression of pressure perturbation. Benchmarks target on a hydrostatic state, a water state under a vibrated gravity and a sloshing phenomenon, respectably.

6.4.1 Hydrostatic state

Targeting on a hydrostatic state in a tank as shown in **Fig. 6.4.1**, the stability of pressure is examined by comparing 2-D numerical simulations based on the traditional kernel function and the Wendland kernel function. The tank is set with 0.3 m in height and 0.6 m in length with a measuring point A at the center of the bottom of the tank. The tank comprises water with 0.1 m in depth. The calculation particle is set with its diameter as d_0=0.005 m and its density as ρ_0=1000.0 kg/m^3. As for the accurate particle method, each numerical simulation utilizes the MPS-HS-HL-ECS-GC-DS method.

Fig. 6.4.2 shows a time series of pressure at the measuring point in numerical simulations by the traditional kernel function and the Wendland kernel function. Both results show noises of pressure at the beginning. This noise is generally shown at the beginning of simulations until the weight of water has been propagated to the bottom and the repulsive pressure from the bottom has been completely propagated to the free surface as the distribution of pressure approaching the analytical solution. However, in the traditional kernel, a repulsion of the first noise appears just after it. While, the Wendland kernel does not show such a noise and settles in a stable state promptly. Seeing the zoom-up figures, the traditional kernel shows an unphysical perturbation of pressure from time t= 0.06 s with the excess pressure comparing with the analytical solution. On the other hand, the Wendland kernel does not have any perturbation of pressure and shows a good agree with the analytical solution.

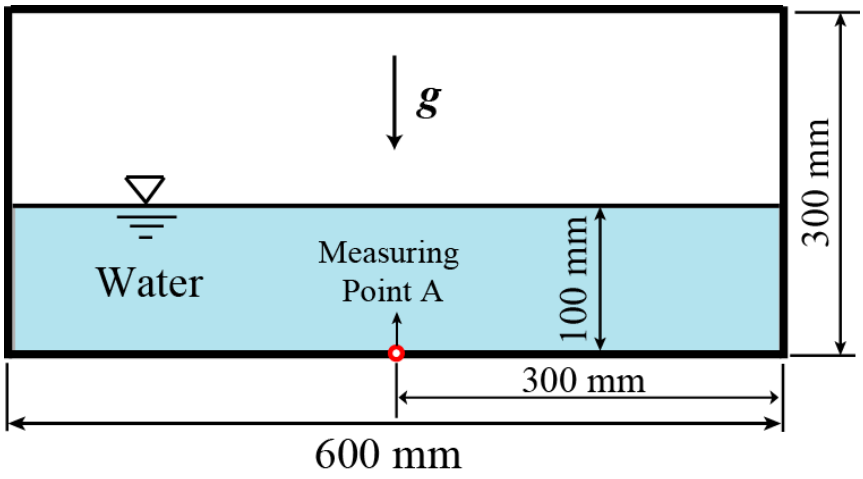

Fig. 6.4.1 Illustration of the initial condition in simulation of hydrostatic state

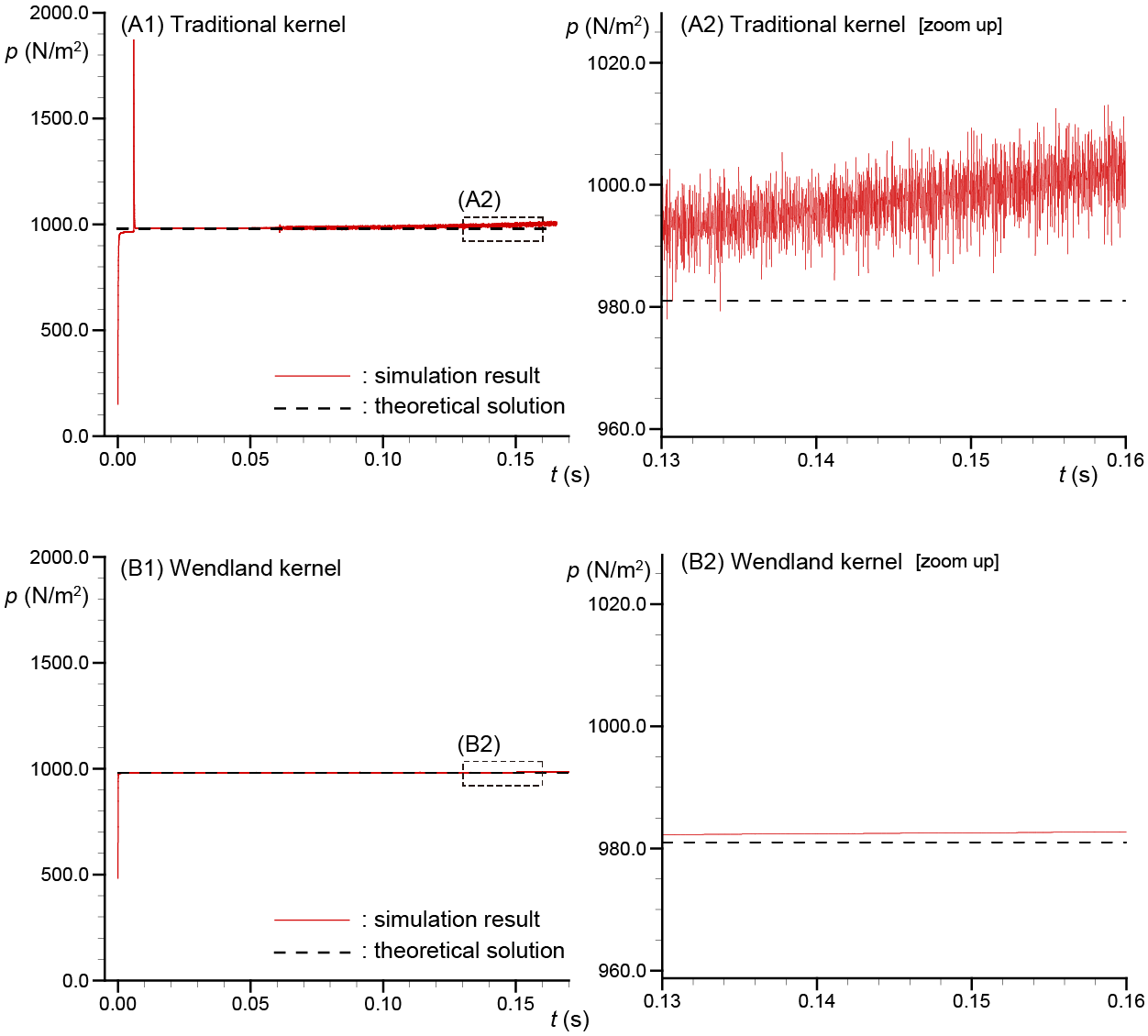

Fig. 6.4.2 Time series of pressure at the measurement point in in simulations of hydrostatic state by the traditional kernel function and the Wendland kernel function

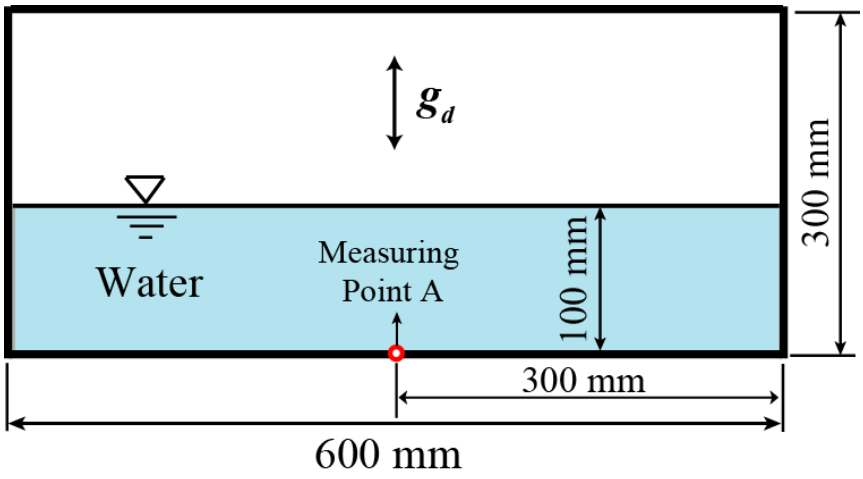

Fig. 6.4.3 Illustration of the initial condition in simulation of water under vibrated gravity

6.4.2 Vibrated gravity

Secondly, simulations targeting on a state of water under a vibrated gravity with a sinusoidal oscillation are performed by the traditional kernel function and the Wendland kernel function. The sinusoidal oscillation is defined as:

$$\boldsymbol{g}_d = 2\boldsymbol{g} + 0.4\boldsymbol{g}\,\exp\left(0.05\pi t / T\right)\sin\left(2\pi t / T\right) \tag{6.4.1}$$

where T is the period of the excitation set as $T = 0.01$ s. The tank and water are set same as the previous test as shown in **Fig. 6.4.3**. The simulation condition about the calculation particle and the accurate particle method are also set similarly to the previous test. This test also examines pressure stability at the measuring position A at the center of the bottom of the tank.

Fig. 6.4.4 shows a time series of pressure at the measuring point A in the simulations under the vibrated gravity by the traditional kernel function and the Wendland kernel function. At the beginning of the simulations, both results show the first noises. Focusing on the noise, the Wendland kernel shows a better convergence to the stable state with fewer time-steps than the traditional kernel. Moreover, the traditional kernel shows a repulsive pressure just after this first noise in this test also, while, the Wendland kernel does not shows such a oscillation with the rapid settlement of pressure. From the zoom-up figures, unphysical noises are found at the tip of the excitation in the result by the traditional kernel. In addition, at the lower tip of the excitation, gaps with the analytical solution are significant. Meanwhile, the Wendland kernel shows a better agreement to the analytical solution without any unphysical noises at each tip of the excitation.

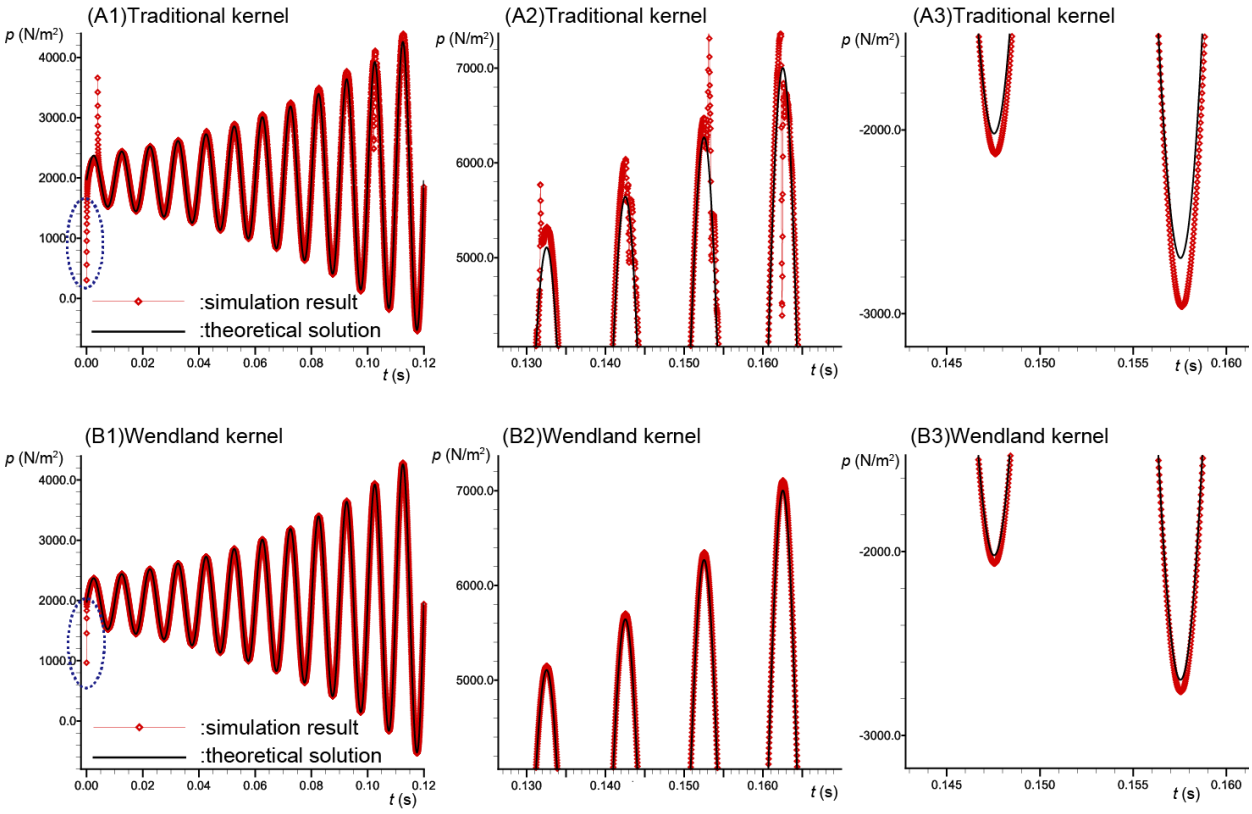

Fig. 6.4.4 Time series of pressure at the measurement point A in simulations of water under vibrated gravity by the traditional kernel function and the Wendland kernel function

6.4.3 Sloshing

The sloshing phenomenon is simulated by the traditional kernel function and the Wendland kernel function. The size of the tank is identical to the previous tests. The tank is oscillated by:

$$A(t) = A_0 + A_{\max} \sin(2\pi t / T) \tag{6.4.2}$$

where A is the parallel position of the tank, A_0 is the initial parallel position of the tank, the $A_{\max}$ is the maximum amplitude of the excitation with $A_{\max}$ = 0.5 m. The period of the excitation T is set as T = 1.5 s. The water depth is set as 0.12 m and the calculation particle is set with its diameter as d_0=0.003 m and its density as ρ=1000.0 kg/m^3. The accurate particle method is utilized same as the previous tests corresponding to the MPS-HS-HL-ECS-GC-DS method. The measuring point B of pressure is set at the left wall of the tank with its height position h_B = 0.1 m as shown in **Fig. 6.4.5**. This benchmark was performed by Khayyer and Gotoh (2013) [] with an almost similar set of the accurate particle methods (but DS scheme was not used), and they have already gotten a good result with a significantly enhanced pressure trace in a better agreement with the experiment by the traditional kernel. Therefore, in this study, a lower time resolution $\Delta t = 2.5\times10^{-4}$ s is set to display the clear difference between the kernels.

Fig. 6.4.6 shows a time series of pressure at the measuring point B in simulations of sloshing by the traditional kernel function and the Wendland kernel function. In spite of the little gap with the

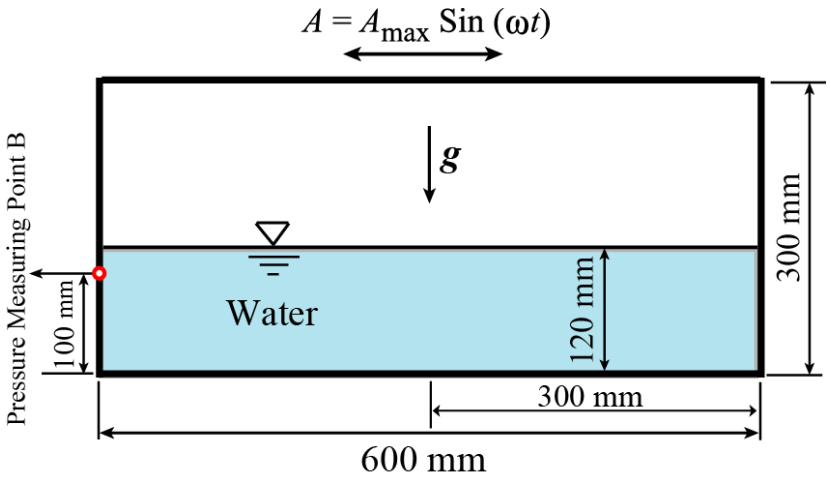

Fig. 6.4.5 Illustration of the initial condition in simulation of sloshing

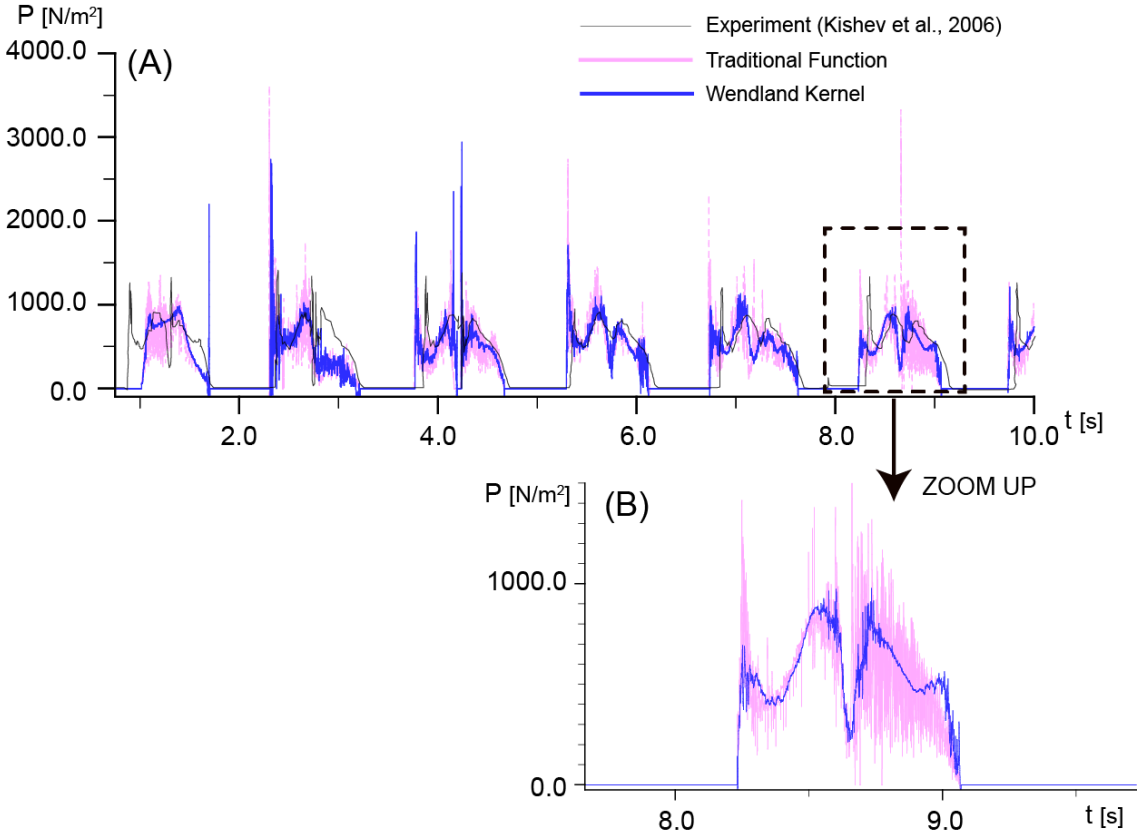

Fig. 6.4.6 Time series of pressure at the measurement point in simulation of sloshing by the traditional kernel function and the Wendland kernel

experimental result on the account of the simulation condition with two-dimension space, the Wendland kernel shows better agreement to the experimental result. In particular, from the zoom-up figure, it is found that the perturbation of pressure is significantly suppressed comparing with the result by the traditional kernel function.

6.5 Concluding remarks

In this study, the consistency in convergence of each differential operation by the traditional kernel function is investigated. From the examination by the mathematical description of differential operators, it is disclosed that the second derivative used for estimation of the Laplacian of pressure in PPE has a problem due to its discontinuity at the edge of the influence circle. To resolve this problem, the Wendland kernel function is introduced into the MPS method with the accurate particle method. And its validity is examined by simple benchmarks targeting on a hydrostatic state, a water state under a vibrated gravity and a sloshing phenomenon through comparison with the analytical solutions or experimental result and the simulation results by the traditional kernel function. From the benchmarks, the effectiveness of the Wendland kernel function for suppression of numerical instability is shown by focusing on the pressure stability.

REFERENCES

[1] Morris J. P., 1996, Pub. Astr. Soc. Aust., 13, 97

[2] Schoenberg, I. J., "Contribution to the problem of approximation of equidistant data by analytic functions", *Quart. Appl. Math.* Vol.4, pp.45–99, pp.112–141, 1946.

[3] Monaghan, J. J. and Lattanzio, J. C., "A refined particle method for astrophysical problems", *A&A*, vol.149, pp.135–143, 1985.

[4] Morris, J.P., "Analysis of Smoothed Particle Hydrodynamics with Applications", (doctor's thesis, Department of Mathematics, Monash University), 1996.

[5] Read J. I., Hayfield T., Agertz O., MNRAS, 405, 1513, 2010.

[6] Wendland, H., "Piecewise polynomial, positive denite and compactly supported radial functions of minimal degree", *Adv. Comput. Math.*, Vol.4, pp.389-396, 1995.

[7]

[8] Swegle, J.W., D.L., Hicks and S.W., Attaway, "Smoothed particle hydrodynamics stability analysis", *J. Comput. Phys.*, Vol.116, pp.123-134, 1995.

[9] Dehnen, W. and Aly, H., "Improving convergence in smoothed particle hydrodynamics simulations without pairing instability", *MONTHLY NOTICES OF THE ROYAL ASTRONOMICAL SOCIETY*, Vol.425 (2), pp.1068-1082, 2012.

[10] Gotoh, H., Okayasu, A. and Watanabe, Y., "COMPUTATIONAL WAVE DYNAMICS", published by *World Scientific*, 234 pages.

CHAPTER 7

Conclusions and future works

7.1 Major findings

The aim of this study is to establish and improve comprehensive solid-liquid two-phase flow models for practical applications with the reliable accuracy, stability and ease by high-resolution tracking. To achieve the purpose, the Distinct Element Method (DEM; Cundall and Strack, 1979) and the Moving Particle Semi-implicit (MPS; Koshizuka and Oka, 1996) method have been chosen to construct the particle-based comprehensive solid-liquid two-phase flow model, namely the high-resolution accurate DEM-MPS method for various complicated boundary conditions. This study has focused on development of the DEM-MPS coupling scheme for high-resolution simulations and improvement of the MPS framework for more accurate tracking with a reliable stability for its practical applications. The major findings of this study are as follows:

I. Development of the high-resolution DEM-MPS methods [Chap. 3]:

Four DEM-MPS methods have been proposed and verified their performances through some benchmarks. The propositions are as follows:

[Model 1. Two-fluid-based model] The accurate particle methods for solid-liquid two-phase flows are proposed on the basis of the two-fluid-based model. This model has superiority in the ease of its simple code and calculation setups even for complicated boundary conditions.

[Model 2. single-phase-flow model] This model is based on the two-phase-hybrid model, and is composed of two separated discretization space accommodating each phase connected by the solid-liquid interaction based on the momentum. As an advantage of this model, the algorithm of the coupling scheme for the solid-liquid phases is orthodox and easy to understand.

[Model 3. multi-phase-flow model] This model improves Model 2 in consideration of additional physical quantities (e.g. velocity and density) by projecting them to each phase. By this projection procedure, the appropriate density is given to the MPS particle with the mass conservation. Consequently, This model treats the multi-phase flows in the MPS discretization space, and thus, it is suppose that this model is based on the two-fluid model and multi-phase-hybrid model.

[Model 4. improved two-fluid-based model] This model improves Model 1 to resolve a problem related to the computational space resolution to reproduce the solid shape. Setting another solid particle for the DEM procedure, the smoothed shape of the solid element is guaranteed in estimation of solid-solid interactions.

II. Improvement of the MPS method for unsteady flow around solid phase [Chap. 4, 5 and 6]:

The MPS method has been improved with some proposed schemes to enhance the numerical stability and accuracy. The enhanced schemes are as follows:

[Dynamic Stabilization (DS): Chap.4] A new stabilizing scheme for the pressure gradient term, namely DS scheme has been developed. Through the investigation of the mathematical description of the existing pressure gradient model, it was found that the so-far artificial stabilizing forces are predominant rather than the original pressure gradient force and would fail to reproduce faithful gradient forces to the governing equation. For this reason, in the multi-phase flow simulations, surfacing or settling particles are confined fully within water particles against the real phenomenon. While, the proposed stabilizer (DS) gives the adequate repulsive force based on the Newton's third law of motion for both compressive and tensile stress states. It was shown to stabilize and adjust the disorder of calculation points for comprehensive MPS applications with more accurate velocity fields and motions of particles. In addition, the DS scheme can be applied to the GC-based gradient term without hindrance to the advantaged characteristics of the GC scheme. More comprehensive application of GC scheme is achieved by introduction of the DS scheme.

[Space Potential Particles (SPP) : Chap.5] A new free-surface boundary condition, namely the SPP scheme has been proposed for consistency of definition of the free-surface particle in the mathematical and physical properties. The SPP scheme presents a new virtual particle given the free-surface boundary for unphysical void space with liquid-void interactions, and succeeded in clearly capturing the free surface with volume conservation, which is defined obscurely in the particle methods until now. Moreover, in a Karman vortex simulation under the uniform flow with a fixed cylinder, it was shown that the SPP scheme effectively suppresses unphysical voids, that are generally found behind the cylinder in particle-based simulations. Furthermore, this scheme gains a significant enhancement of the numerical stability and saves computational costs remarkably with lower time resolution.

[Introduction of the Wendland kernel: Chap.6] The convergence of the kernel function has been investigated. From an examination of the mathematical descriptions of each term and differential operators of the particle methods, it was found that the continuity of the first derivative of the kernel at the edge of the influence area is necessary for the consistency in convergence of application of the high order Laplacian. To achieve this requisite condition, a higher order and reliable kernel function, namely the Wendland kernel has been introduced. The Wendland kernel showed its good performance to suppress the pressure perturbation effectively in some simple benchmarks including a sloshing simulation.

7.2 Future works

This study focuses on developments and improvements of particle-based accurate and stable frameworks for solid-liquid two-phase flows with high resolution. The proposed schemes have achieved to enhance the numerical stability with more accuracy and remarkably save the computational cost by their applicability to low time resolution. However, the high-resolution multi-phase simulations under violent flows require enormous computational costs particularly under 3D simulation setups. Therefore, considering the computational limitation in practical uses, it is still unrealistic to reproduce the sufficient circumstances, such as sediment transportation and minute eddies caused by their motions. To resolve this, some lower-resolution models must be introduced in order to capture the behaviors of the minute elements and the Sub-Particle-Scale (SPS; Gotoh et al, 2001) turbulence smaller than calculation particles.

As for the SPS turbulence, so far, the effect and physical meaning of the implicitly expressed turbulence out of control, such as unexpected perturbations of particle motions is not studied fully. However, thanks to the developments of the existing accurate particle methods including achievements of this study for more faithful solver to the original governing equation (Navier-Stokes equation), the clear definition of the turbulence is being disclosed and the unexpected perturbations of particle motions are removed by degrees. Thus, the future target should be introduction and improvement of the SPS turbulence model.

As for the accurate tracking of the minute solid elements (e.g. sediments on the seabed) with high space resolution, Chap.5 shows a possibility to resolve the difficult problem of the calculation cost. Despite the fact that the SPP scheme was applied to only unphysical voids in this study, it implies that the appropriate boundary conditions can be given dynamically depending on the states without stationed calculation points. If it is succeeded in setting more comprehensively dynamical boundary condition even for fixed and moving boundary with a similar framework to the SPP scheme, the whole calculation particles distributed over them will be saved. In addition, it is expected to enhance the accuracy of capturing the interface between phases by such a dynamic boundary condition accommodating with its shape.

As another approach for practical applications with moderate calculation cost, my current interest is development of the multi-scale particle method. Calculation particles are generally given a uniform size in the domain to secure the numerical stability with an identical weighted-averaging-operation. Up to now, there are few applications of multi-scale particle method due to the difficulty in keeping consistency in the derivative operations with varying scale. This problem is based on a fundamental and general issue of the particle methods, which is characterized by the locally weighted averaging operation with maldistribution of calculation particles. This significant matter is related to all the topics taken in this dissertation, such as convergence of the kernel function, the faithful velocity to the original governing equation, handling the voids between particles and the SPS turbulence also. Being engaged in this issue would give fortuitous ideas by deliberating the synthesized factors with from various angles.